SPECTROSCOPY OF NiCCH AND OsSi, AND THE BOND ENERGIES OF VC, VS, AND VN

by

Eric Loren Johnson

A dissertation submitted to the faculty of
The University of Utah
in partial fulfillment of the requirements for the degree of

Doctor of Philosophy

Department of Chemistry

The University of Utah

December 2016

The University of Utah Graduate School

STATEMENT OF DISSERTATION APPROVAL

The dissertation of **Eric Loren Johnson**

has been approved by the following supervisory committee members:

Michael D. Morse	, Chair	**08/01/2016** Date Approved
Peter B. Armentrout	, Member	**08/01/2016** Date Approved
Ryan P. Steele	, Member	**08/01/2016** Date Approved
Richard D. Ernst	, Member	**08/01/2016** Date Approved
Shanti Deemyad	, Member	**08/01/2016** Date Approved

and by **Cynthia J. Burrows** , Chair of

the Department of **Chemistry**

and by David B. Kieda, Dean of The Graduate School.

ABSTRACT

Optical spectra of the supersonically cooled NiCCH radical have been recorded in the 530-650 nm region using the resonant two-photon ionization method, and five of the observed bands have been rotationally resolved. The rotationally resolved studies demonstrate that the ground state of NiCCH is of $\tilde{X}\ ^2\Delta_{5/2}$. Most of the observed bands are assigned to the $\tilde{A}\ ^2\Delta_{5/2} \leftarrow \tilde{X}\ ^2\Delta_{5/2}$ electronic transition, which shows a progression in the Ni-C stretching mode, ν_3. In addition, single excitations of the modes ν_2 (C≡C stretch), ν_4 (C≡C-H bend), and ν_5 (Ni-C≡C bend) are observed, allowing these vibrational intervals to be determined for the $\tilde{A}\ ^2\Delta_{5/2}$ state. Hot bands also allow the determination of ν_5 in the ground $\tilde{X}\ ^2\Delta_{5/2}$ state.

The optical spectrum of diatomic OsSi has been investigated for the first time. Two electronic band systems have been identified along with a number of unclassified bands. Nine bands have been investigated at rotational resolution, allowing the ground state to be identified as X $^3\Sigma^-_{0+}$, arising from the $1\sigma^2 1\pi^4 2\sigma^2 3\sigma^2 1\delta^2$ configuration. The ground X $^3\Sigma^-_{0+}$state is characterized by r_e = 2.1207(27) Å and $\Delta G_{1/2}$" = 516.315(4) cm^{-1} for the most abundant isotopologue, $^{192}Os^{28}Si$ (38.63%). The A1 excited electronic state is characterized by T_0 = 15 727.7(7) cm^{-1}, ω_e = 397.0(7) cm^{-1}, and r_e = 2.236(16) Å for $^{192}Os^{28}Si$. The B1 excited electronic state is characterized by T_0 = 18 468.71 cm^{-1}, $\Delta G_{1/2}$ = 324.1 cm^{-1}, and r_e = 2.1987(20) Å for $^{192}Os^{28}Si$.

The abrupt onset of predissociation in the congested electronic spectra of jet-cooled VC, VN, and VS has been observed using resonant two-photon ionization spectroscopy. Using this method, bond dissociation energies of D_0(VC) = 4.1086(25) eV, D_0(VN) = 4.9968(20) eV, and D_0(VS) = 4.5353(25) eV are obtained. These values are compared to previous measurements and to computational results. The precision of these bond dissociation energies makes them good candidates for testing computational chemistry methods, particularly those that employ density functional theory.

For my mother and father, thank you for your support

The essence of science: ask an impertinent question, and you are on the way to a pertinent answer.

Jacob Bronowski (1908-74)

TABLE OF CONTENTS

LIST OF TABLES

LIST OF FIGURES

ACKNOWLEDGEMENTS

During my six years at the University of Utah, there have been many people who helped me. First and foremost, I would like to thank my research advisor, Dr. Michael Morse, for his help. Dr. Morse was always willing to lend a hand or make a suggestion when I was having trouble in lab. He was also a great teacher and his respect for his students is something I plan to emulate myself as a professor.

I am also very thankful for the Morse group members past and present who assisted me greatly; Alonzo Martinez, Olha Krechkivska, Dan Matthew, Sergei Aksyonov, Quincy Davis, Sang Hoon Oh, Andrew Sevy, and Jason Sorensen. I would in particular like to thank Maria Garcia, who trained me on the R2PI instrument and helped me even after she had left the group. In addition, I owe a lot to Dan Matthew. He got me started on the R2PI instrument and put up with me asking him a ton of questions and asking for his help with many things in the lab.

I would also like to thank Dennis Romney and Tom Gudmundson in the machine shop, and Dale Heisler in the electronics shop. Without their help, I would not have been able to complete my experiments.

Finally, I would like to thank my friends and family for their encouragement and love. I could not have done this without you.

CHAPTER 1

INTRODUCTION

1.1 Introduction

Spectroscopy, which may be defined as the study of the interaction between light and matter, has played a major role in chemistry, physics, and astronomy. Spectroscopy was founded in the 17th century, when many physicists started to use prisms to look at the spectra of the sun and the stars. Most famously, Isaac Newton found that by using a prism, white light could be split into its component colors. Furthermore, a second prism could recombine the component colors to make white light.[1] After Newton's discovery, physicists investigated the spectra and found that each element had a distinct pattern of colors. This original work used a prism as the dispersing element. The next major step in the development of spectroscopy was the invention of the diffraction grating spectroscope by Joseph von Fraunhofer in 1814.[2-3] The spectroscope was invented by replacing a prism with a diffraction grating. Fraunhofer's diffraction grating was constructed using wires to form a series of slits that are closely spaced together. When the light impinges on the diffraction grating, the separate components of the light will emerge at different angles. The development of the spectroscope allowed spectra to be collected with better resolution and enabled the wavelengths of the radiation to be measured. Fraunhofer used this to analyze the dark lines in the spectrum of the sun,

which arise from absorption of the continuum emitted by the sun at the specific absorption wavelengths of elements that are present in the solar atmosphere. These absorptions lines are now known as the Fraunhofer lines. After the development of the spectroscope, scientists started to measure lines emitted by the elements. Gustav Kirchhoff and Robert Bunsen, in particular, used the diffraction grating developed by Fraunhofer and a new flame source developed by Bunsen, now known as the Bunsen burner, to prove that every element has a unique set of emission lines.[2]

Although the studies mentioned above helped develop the field of spectroscopy, scientists were still confused about how exactly light and matter interacted with one another. To clarify this confusion, Kirchhoff introduced the idea of a blackbody as a material that absorbs and emits all radiation frequencies at any temperature. The radiation emitted from a blackbody is the simplest case for the interaction between light and matter because in a blackbody cavity the radiation does not depend on the material of the cavity. Lord Rayleigh and J. H. Jeans modeled blackbody radiation using classical electromagnetic theory, as developed by Maxwell, and obtained

$$\rho_\nu(T)d\nu = \frac{8\pi k_B T}{c^3}\nu^2 d\nu. \tag{1.1}$$

Here $\rho_\nu(T)d\nu$ is the radiant energy density per unit frequency, k_B is the Boltzmann constant, T is the temperature, c is the speed of light, and ν is the frequency. This is known as the Rayleigh-Jeans law. It accurately modeled the blackbody radiation frequency distribution at low frequencies but fails miserably at high frequencies.[4-6] The deviation could not be explained by classical physics and led to the development of

quantum mechanics. Only by requiring that energy could be added to or removed from the radiation field in increments of hν was it possible to obtain the correct blackbody formula. This insight by Max Planck introduced a new fundamental concept, Planck's constant, and led to the the Planck blackbody law:

$$\rho_\nu(T)d\nu = \frac{8\pi h}{c^3}\frac{\nu^3 d\nu}{e^{h\nu/k_BT}-1}. \quad (1.2)$$

Here *h* is Planck's constant.[5-6] Its value was originally determined by fitting the experimental data to the form of the Planck law given above. In his derivation, Planck assumed that the electrons in the blackbody material had energies that were discrete, or as they are now known, quantized energies, and proportional to an integral multiple of the frequency. Although this leap of faith ultimately led to the correct answer and the development of quantum mechanics, many scientists did not accept Planck's work. However, only a few years after Planck, Albert Einstein used Planck's hypothesis to explain the photoelectric effect.

Heinrich Hertz, a German physicist, discovered the photoelectric effect. He found that ultraviolet light causes electrons to be emitted from a metallic surface.[6-7] The photoelectric effect deviates from the expectations of classical physics in two ways: first, in classical physics, the kinetic energy of the electrons that are ejected from the metal should be dependent on the intensity of the radiation, but they are not. Second, the photoelectric effect would be expected to occur at any frequency as long as the light is intense enough. However, in experiments it was found that the kinetic energy of the electrons was independent of the intensity of the radiation and that there was a threshold

frequency, below which the electrons could not be ejected from the metallic surface. To explain these observations, Einstein took Planck's hypothesis and expanded it. As mentioned above, Planck used the quantization of energy in the absorption and emission mechanics of the electrons in the blackbody, but assumed that the radiation acted like a classical wave. In effect, he assumed that the energy in the electromagnetic field was not quantized, but would take on any magnitude. Einstein proposed that the radiation itself actually consisted of small packets of energy, known as photons, and that it behaved like a particle. By using this assumption, it was easy for Einstein to show that the kinetic energy of an ejected electron is equal to the energy of the incoming light minus the minimum energy required to eject an electron from a specific metal, also known as the work function. This explanation can be easily seen in the following equation

$$KE = h\nu - \phi \tag{1.3}$$

where *KE* is the kinetic energy of the ejected electron, ν is the radiation frequency, and ϕ is the work function.[4-6] Even though both Planck's and Einstein's solutions accurately modeled these experiments that could not be explained by classical physics, it took many years before quantum mechanics was fully developed as a theory and accepted by the scientific community as a whole.

Although the history of spectroscopy is fascinating, that is not the focus of this dissertation. The previous paragraphs were used to demonstrate why spectroscopy is important and how it was established. Once the field was well established, it was used to explain how matter acted on a molecular, atomic, and subatomic level.

Over the last several decades, scientists have used spectroscopy to investigate the structure and characteristics of molecules. Some classic examples include ultraviolet-visible molecular absorption spectroscopy, infrared spectroscopy, microwave spectroscopy, Raman spectroscopy, and nuclear magnetic resonance (NMR) spectroscopy. However, if spectroscopy is being performed on highly reactive compounds, a custom spectrometer needs to be built. In the Morse group, the focus is on unsaturated transition-metal compounds, which are highly reactive, therefore the resonant two-photon ionization (R2PI) spectrometer was constructed. The design and implementation of the R2PI spectrometer is described in Chapter 2. It is used to characterize small transition-metal-containing compounds that would be much more difficult to investigate using other techniques.

In the R2PI spectrometer, lasers are used to probe the molecules. Not every type of spectroscopy uses lasers, but they are fairly common. When the laser was first invented, it had a fixed frequency, which severely limited the studies that scientists could undertake. With development of tunable lasers, including dye lasers and optical parametric oscillator (OPO) lasers, scientists have been able to expand the scope of their studies significantly. One of the major advantages of laser light is that it has high intensity and can be produced with narrow linewidths. This allows scientists to investigate the electronic, vibrational, and rotational structure of molecules in greater detail than ever before. By investigating the electronic spectrum of a molecule, one can elucidate the electronic structure of the system. Investigating the vibrational spectra of molecules has permitted measurements of the forces between atoms in the molecule. Finally, the rotational structure of molecules is used to determine the rotational constant,

which is inversely related to the moment of inertia and can be used to find the bond lengths and bond angles in polyatomic molecules. In a diatomic molecule, it is only the bond length that may be determined. The rotational structure of the spectrum can also be used to determine the total electronic angular momentum around the axis of the molecule, known as Ω. This quantity often provides a great deal of insight into the electronic structure of the molecule.

In the Morse group, we use the R2PI spectrometer to investigate transition metal compounds and to determine their ground and excited electronic states, bond lengths, vibrational frequencies, and bond energies. The goal of the research is to gain knowledge about these molecules and pass along the information to other chemists so they can accurately model systems that cannot be readily investigated experimentally.

1.2 Dissertation Outline

This thesis is separated into six chapters and two appendices. The first chapter explains the history and importance of these studies along with an outline of the dissertation. Chapter 2 focuses on the design and implementation of the R2PI spectrometer. This chapter was written with a person who has little to no spectroscopic experience in mind. The studies that were collected by this author using the R2PI spectrometer are described in the following three chapters.

In Chapters 3 and 4, R2PI spectroscopy was used to study NiCCH[8] and OsSi,[9] respectively. For NiCCH, I found that the ground state is $\widetilde{X}\ ^2\Delta_{5/2}$. In my investigation of NiCCH, I only found one excited state, $\widetilde{A}\ ^2\Delta_{5/2}$. I determined the rotational constants for both the ground and excited states. Finally, multiple vibrational frequencies were

experimentally determined for the excited state. For OsSi, the ground state was found to be X $^3\Sigma_{0^+}^-$. Two excited states were investigated, A1, which is assigned as $^3\Pi_1$, and B1, which is assigned as $^1\Pi_1$.

In Chapter 5, I describe how the bond dissociation energies of VC, VN, and VS were determined using R2PI spectroscopy.[10] This study used an OPO laser because it has a much wider scanning range than the dye laser that is typically used in the Morse group. The bond dissociation energies in Chapter 5 are more accurate than those found in previous investigations into VC, VN, and VS.

The final chapter, Chapter 6, concludes the dissertation and looks forward to how these data can be used. The final sections of this thesis contain Appendices A and B, which provide detailed spectroscopic data, compiled into tables and figures, for the nickel acetylide and osmium silicide molecules.

1.3 References

1. Newton, I. New Theory about Light and Colors. *Phil*. *Trans*. *Roy*. *Soc*. **1672,** *80*, 3075-3087.

2. Brand, J. C. D. *Lines of light : the sources of dispersive spectroscopy, 1800-1930*. Amsterdam; Luxembourg : Gordon and Breach: 1995.

3. Condon, E. U.; Shortley, G. H. *The Theory of Atomic Spectra*. 2nd ed.; University Press: Cambridge, 1970; p 441.

4. Pauling, L. *Introduction to quantum mechanics : with applications to chemistry*. 1st ed.. ed.; New York, London : McGraw-Hill book company: 1935.

5. McQuarrie, D. A. *Physical Chemistry : A Molecular Approach*. Sausalito, Calif. : University Science Books: 1997.

6. Blinder, S. M. *Introduction to Quantum Mechanics : In Chemistry, Materials Science, and Biology*. Academic Press: Amsterdam, 2004.

7. Hertz, H. Über einen Einfluß des ultravioletten Lichtes auf die electrische Entladung. *Ann*. *Phys*. **1887,** *267* (8), 983-1000.

8. Johnson, E. L.; Morse, M. D. The $\tilde{A}\ ^2\Delta_{5/2}$-$\tilde{X}\ ^2\Delta_{5/2}$ electronic band system of nickel acetylide, NiCCH. *Mol*. *Phys*. **2015,** *113* (15-16), 2255-2266.

9. Johnson, E. L.; Morse, M. D. Resonant Two-Photon Ionization Spectroscopy of Jet-cooled OsSi. *J*. *Chem*. *Phys*. **2015,** *143* (10), 104303/1-104303/12.

10. Johnson, E. L.; Davis, Q. C.; Morse, M. D. Predissociation Measurements of Bond Dissociation Energies: VC, VN, and VS. *J*. *Chem*. *Phys*. **2016,** *144* (23), 234306/1-234306/9.

CHAPTER 2

THE EXPERIMENTAL METHOD

2.1 Introduction

In this dissertation, spectroscopy is used to study the ground- and excited-state characteristics and bond dissociation energies of transition-metal-containing molecules. The purpose of the research is to map the energy levels of the molecule of interest. By measuring the energy levels, one may also determine the rotational constants, bond lengths, and vibrational frequencies for the ground and excited states of the species of interest. More importantly, rotationally resolved spectra allow the ground- and excited-state electronic symmetries to be deduced, and from that information the molecular orbital configurations of the upper and lower states may often be determined. Resonant two-photon ionization (R2PI) spectroscopy is the particular spectroscopic method that was used to study the molecules reported here. This method came into common use with the combination of tunable lasers, pulsed ultraviolet lasers, supersonic expansion techniques, and time of flight mass spectrometry.[1-2] The tunable laser allows one to scan the spectrum and the pulsed ultraviolet laser allows the excited state to be ionized. Supersonic expansion cools the molecules to their ground electronic, vibrational and lowest rotational states. This greatly reduces the spectral congestion that occurs when many low-lying excited states are populated, making the spectra much easier to interpret.

Spectral congestion is a particular problem for molecules with many low-frequency vibrations, or when rotational structure is complicated by overlapping branches at higher temperatures. By studying these molecules at low temperatures, typically around 5 K, the spectra are generally much less congested and far easier to assign.

Another advantage of R2PI spectroscopy is that the molecule of interest is ionized after being excited with the dye laser, and the resulting ion is detected. This is a form of action spectroscopy, in which the absorption of a photon is not detected directly, but is inferred by some action that is induced by the absorption. In this case, it is an ionization event. In another example, laser-induced fluorescence spectroscopy, the absorption of a photon is detected by the fluorescence that follows. Detection of ions is advantageous for two primary reasons. First, it is in principle possible to detect nearly 100% of the ions that are produced. This contrasts with laser-induced fluorescence (LIF) spectroscopy, in which a superb light collection system may collect 10% of the emitted photons, and an excellent photomultiplier may detect only 30% of the incident photons. The net detection of only 3% of the emitted photons seems like very poor performance, but it is close to the best that can be achieved by LIF spectroscopy. A second advantage is that ions can be detected using a mass spectrometer, providing unambiguous identification of the carrier of the spectroscopic transition. This is particularly helpful when the sample contains many different chemical species. In fact, the mass spectrum permits the spectra of individual isotopic combinations to be separately recorded without requiring the use of isotopically enriched samples. In addition, the background signal in the mass spectrum is frequently very low because off-resonant two-photon ionization processes can often be minimized by reducing the laser intensity.

In the Morse group, the majority of molecules that are studied contain a transition metal molecule. Most often, the group studies transition metal dimers, such as Pt_2[3] or TiFe.[4] However, transition metal atoms attached to ligands are also frequently studied in the group, with chromium tungsten, CrW,[5] iridium silicide, IrSi,[6-7] and copper acetylide, CuCCH,[8] being three recent examples. Although infrequent, the group has also studied molecules that do not contain transition metals, such as Al_2,[9] Al_3,[10] Bi_3.[11]

2.2 Source Chamber

Figure 2.1 shows a drawing of the instrument that was used in all of these studies. As can be seen in the figure, there are two major chambers: the source chamber, which is on the left, and the analytical chamber, also known as the A chamber, is on the right. The source chamber is 71 cm wide by 41 cm high and 46 cm deep, enclosing a volume of about 108 L. It is evacuated by a three-stage vacuum system. First, the chamber is evacuated to 1 torr or less using an Edwards E2M80 mechanical pump, then an Edwards EH500 Mechanical Booster pump is used to evacuate the chamber to about 20 mtorr. Finally, a 10-inch Varian VHS-10 diffusion pump is turned on, which pumps the chamber down to its final pressure, which is around 6×10^{-7} torr. The Edwards mechanical and turbo pumps back the diffusion pump. The source chamber and the diffusion pump are separated by a pneumatic 10-inch gate valve.

2.3 Analytical Chamber

The analytical chamber, which is commonly referred to as the A-chamber, is to the right of the main chamber in the drawing in Figure 2.1. It is isolated from the main

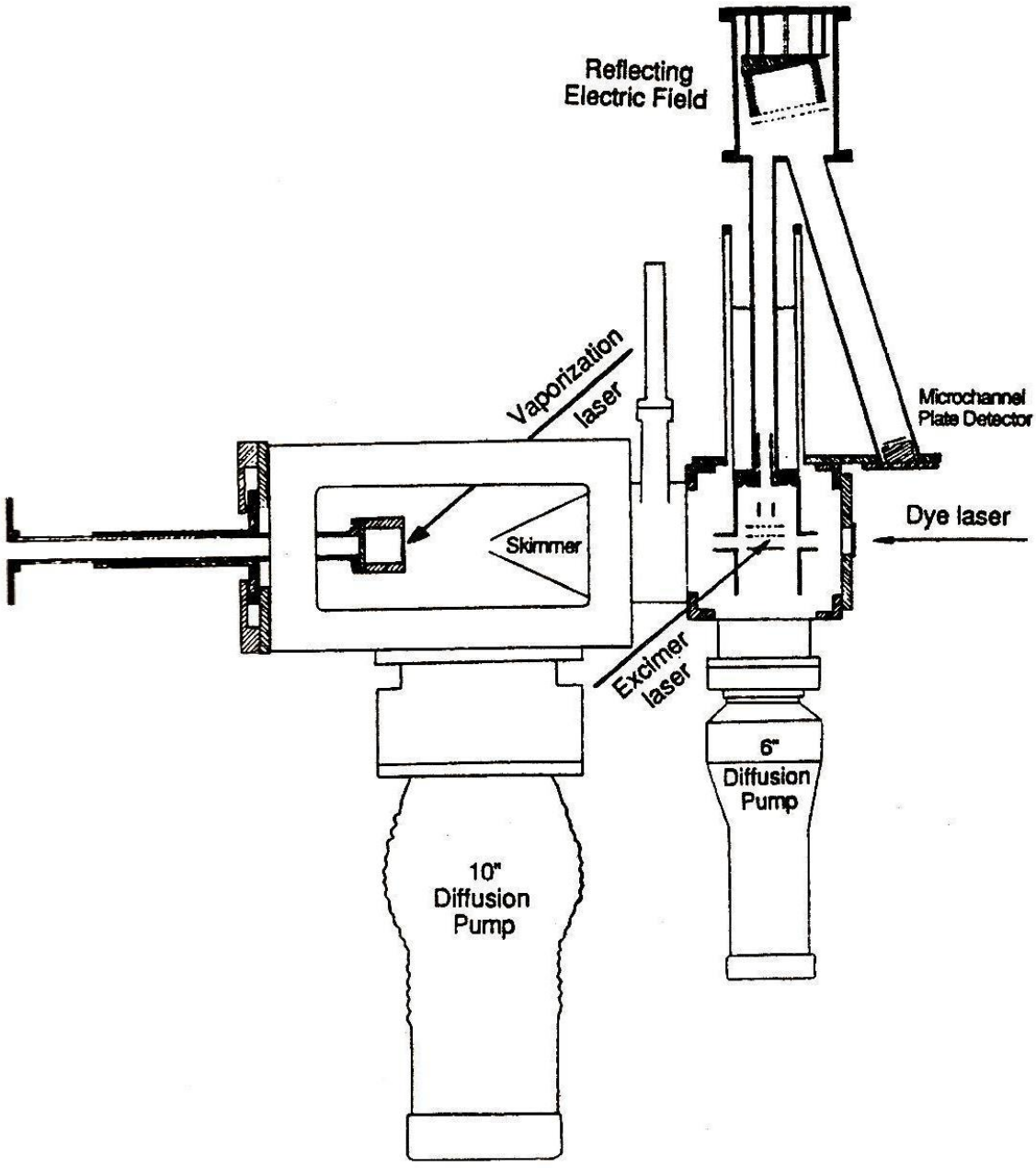

Figure 2.1 Schematic of the resonant two-photon ionization instrument.

chamber by a 4-inch pneumatic gate valve. This chamber is where the tunable dye laser and the ionization laser probe the molecules. The molecular beam enters the chamber from the left in Figure 2.1; the other three sides of the chamber are sealed with circular flanges with a 2-inch optical window in the center of each flange. The A chamber consists of two pieces: the bottom portion, which is a cube about 27 cm on each side that encloses about 14 L of volume; and the time of flight tube, which is composed of a 5 cm diameter tube that extends upwards about 61 cm, terminating at a cylinder that is approximately 20 cm in diameter and 25 cm in height. This cylinder houses the reflecting electric field assembly. Extending down from this cylinder at an angle of about 18 degrees is a 7.6 cm diameter tube with a length of about 62 cm, which terminates at the housing for the microchannel plate detector.

The analytical chamber is first evacuated to approximately 20 mtorr by an Edwards RV12 mechanical pump. Then, an Edwards Diffstak 160 Series diffusion pump is turned on to pump the chamber out to approximately 2×10^{-7} torr. The interface between the analytical chamber and the diffusion pump is a butterfly valve that is controlled by a pneumatic Edwards BRV25 valve. Unlike the main chamber, the analytical chamber is constantly maintained under vacuum to prevent water vapor from being adsorbed on the microchannel plate detector, which causes swelling and eventually cracking of the microchannel plates.

2.4 Molecular Source

When investigating the spectra of a stable molecule, it is often possible to purchase the compound from a chemical company. The molecules studied in the Morse

group, however, are generally highly reactive and must be created in the instrument. A major issue is that it can be difficult to produce the molecule of interest because although the molecule is stable in isolation, it can easily react with water or oxygen or can readily form larger clusters. In fact, clusters are regularly seen in the mass spectrum of a typical experiment because clustering is exothermic. To obtain the best molecular signal, some trial and error tweaking of experimental conditions is generally required. If the species being studied is a transition metal attached to a ligand, a reaction gas is needed to supply the ligand. The ablated metal will then react with the gas to produce the target molecule along with other species. For example, silane gas is used to produce transition metal silicides. Other common examples include methane to produce carbides, acetylene to produce acetylides, ammonia to produce nitrides, and hydrogen sulfide to produce sulfides. There are two important components of the R2PI instrument that help to form the target species: laser ablation and supersonic expansion, both of which occur in the source chamber.

The metal sample that is used is usually either pure metal or an alloy disk with a diameter between 1.5 and 3 cm. To make a consistent quantity of the molecule, the sample must be homogenous and smooth. Any irregularities in the sample can lead to fluctuations in the mass spectrum, which can make experiments very difficult if not impossible. The metal sample disk is mounted to a sample holder that is attached to an assembly that has a series of gears, pulleys, and cams, all of which are driven by an external motor. The sample is pressed up against the vaporization block so that no gas can escape between the sample and the block as the sample is being ablated. A schematic of the sample holder is shown in Figure 2.2. The sample is rotated and translated to

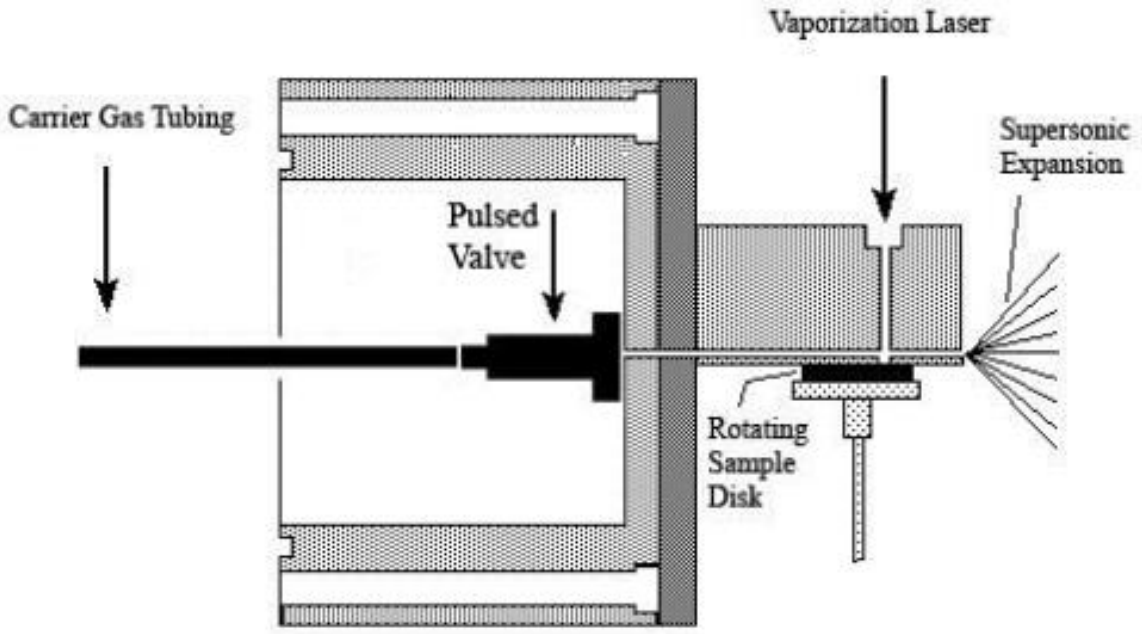

Figure 2.2 The molecular source.

prevent holes from being drilled in the sample and to reduce or eliminate fluctuations in the molecular signal. The stainless steel or brass vaporization block measures 5 cm × 5 cm × 2.5 cm and has two perpendicular channels that are drilled completely through the block. One channel provides a path for the vaporization laser to ablate the metal sample. This channel has a diameter of 2 mm and a length of 2.5 cm. The other channel is used to direct the carrier gas, which can be seeded with a reactive gas, to flow over the ablated metal and carry it toward the expansion orifice. In the Morse group, a variety of expansion blocks have been machined to allow the diameter of the expansion orifice to vary from 1 mm to 5 mm. The diameter of the expansion orifice can dramatically affect the species that are produced in the reactions, as well as changing the temperature of the molecules at the position where they are probed. Larger diameter expansion orifices cause the molecules to exhibit higher rotational temperatures.

The molecules described in this dissertation were produced using a Quantel Brilliant pulsed Nd:YAG laser (3^{rd} harmonic radiation, 355 nm) to ablate the metal sample at a rate of 10 Hz. The beam profile measures approximately 5 mm in diameter at the laser aperture, but was focused onto the sample using a 50 cm focal length lens, leading to a beam diameter of about 0.5 mm at the sample. One important way to optimize the molecular signal is to vary the timing between the pulse of the gas valve and the firing of the vaporization laser so that sample ablation occurs during the most intense part of the gas pulse.

The short duration of the laser pulse combined with the small focus diameter causes the vaporization laser to have a high power density. This causes the sample to heat up rapidly and atoms are ejected into the gas phase, which leads to the formation of a

plasma. The plasma that is formed consists of atomic ions, neutral atoms, and electrons.[12] A pulsed valve is attached to a flange directly behind the vaporization block, and is timed to fire prior to when the vaporization laser is fired. This guarantees that the high-pressure carrier gas mixture will be above the metal surface when the laser is fired. The point of ablation is about 3.7 cm downstream from where the carrier gas enters the vaporization block. Downstream from the ablation channel, the metal plasma products are entrained in the carrier gas and collisions with reactive molecules lead to the formation of a wide variety of molecules, including both neutral and ionic molecules, as well as clusters. Unfortunately, the chemistry involved in this process is not selective, so it takes trial and error to make a strong signal of the molecule of interest. In a typical experiment, one must get the signal for the molecule of interest to be as strong as possible while also maintaining a low signal for competing molecules. The most important parameters to vary are the concentration of reactant gas that is mixed with the carrier gas, the backing pressure, the duration of the gas pulse, the vaporization laser energy, and the diameter and length of the channel through which the gas pulse is directed.

2.5 Supersonic Expansion

Supersonic expansion is a key component of R2PI because it allows the molecules to be cooled to around 5 K. If one were not to cool the molecules, their spectra would be much more difficult to assign, if not impossible. In addition, a hot molecule has a multitude of states that are populated, which reduces the intensity of any given spectroscopic feature, leading to a poor signal-to-noise ratio. Most of the cooling of the plasma that results from the vaporization of the metal sample takes place in the 12.5 mm

long channel prior to supersonic expansion. Here, ions are recombined with electrons, and chemical reactions with the added reactant gas lead to production of a variety of molecules. The high pressure of the carrier gas, typically 1-10 atm of helium with a small percentage of reactant gas, leads to a large number of collisions as the molecules flow down the channel. We believe that in this high-pressure zone molecules are cooled to close to room temperature. However, even room temperature molecules can have spectra that are hard to assign due to spectral congestion. To cool to extremely low temperatures, supersonic expansion is employed.

Supersonic expansion is achieved by expanding a gas from a high-pressure (1 atm to 13.6 atm) reservoir at a temperature *T* (300 K in these experiments) into a low-pressure environment through an orifice that is much larger than the mean free path between collisions. The gas is introduced through a pulsed gas valve, which directs the gas flow over the sample. In the high-pressure environment within the narrow channel, molecules are formed via two different routes. Clustering processes involve the combination of two pre-existing species (such as two metal atoms, or a metal cluster and another metal atom). In these processes, the dissociation of the newly formed cluster will occur unless energy is removed by a collision. Thus, clustering reactions require three-body collisions to stabilize the product. An example is the three-body collision between two metal atoms and a helium atom, leading to metal dimer formation. Another kind of reactive process is the reaction of the metal atom (possibly in an excited electronic state) with a reactant gas. In this type of process, products can be formed by a two-body collision, because other atoms may depart to carry off the excess energy. An example would be the reaction of a metal atom with CH_4 to form $MC + 2H_2$. The clustering reaction to form metal dimers

requires a high helium pressure in order to stabilize the product, while the formation of metal-ligand complexes such as those studied in this dissertation may be formed with a much lower carrier gas pressure. In either case, a trial and error procedure is needed to optimize the concentration of the species of interest.

Supersonic expansion occurs through a small circular orifice into the source chamber. The diameter of the expansion orifice in most of the experiments is 1 mm, so the mean free path (λ) between the helium collisions must be much smaller than the diameter (D) of the expansion orifice. The mean free path of helium was calculated using the gas kinetic equation

$$\lambda_0 = \frac{RT}{2^{1/2} N_A \pi d^2 P}, \tag{2.1}$$

where R is the gas constant in $J \cdot K^{-1} \cdot mol^{-1}$, T is the temperature in K, d is the molecular diameter and P is the pressure in Pascals. For supersonic expansion, the mean free path must be much smaller than the diameter of the expansion orifice, thereby allowing the gas to maintain thermal equilibrium during the expansion. Since the source pressure is high, gas viscosity and heat transfer may be neglected. Therefore, the gas flow may be treated as an adiabatic, isentropic expansion. This expansion of the gas is called a supersonic expansion, as is explained below.

In an adiabatic, isentropic expansion, the sum of the enthalpy and kinetic energy of the gas is conserved, so that

$$H(x) + \frac{1}{2} m u(x)^2 = constant. \tag{2.2}$$

Here H is the molar enthalpy, m is the molar mass, u is the flow velocity and x is the distance downstream from the expansion orifice.[1]

As the flow velocity increases, equation (2.2) requires that the enthalpy of the gas must decrease. This cools the translational degrees of freedom of the carrier gas. The various degrees of freedom of the molecules that are carried along in the flow are cooled by their immersion in the cold translational bath.[13] The energy levels with the closest spacing, which are the rotational energy levels, are the most readily cooled, and these continue to be cooled farther downstream of the expansion orifice than the other degrees of freedom. Electronic and vibrational degrees of freedom, which have larger gaps between energy levels, are not cooled as effectively in supersonic expansion and cooling of these degrees of freedom does not continue as far downstream as rotational cooling. In fact, most electronic and vibrational cooling takes place in the channel prior to expansion because there are higher energy collisions with the helium carrier gas in the channel. The supersonic expansion causes the rotational degrees of freedom to be cooled close to the translational temperature, while the electronic and vibrational energy levels are less effectively cooled.

The maximum velocity of the molecular beam is determined by the mass of the carrier gas and the temperature of the reservoir. The source pressure does not affect supersonic expansion unless the pressure is too low to achieve a fully developed supersonic expansion. The ultimate flow velocity of the carrier gas occurs when all of the enthalpy is converted into directed mass flow, and is given by

$$u_{max} = \sqrt{\frac{2C_p T_0}{m}}\,. \tag{2.3}$$

Here C_p is the constant pressure molar heat capacity, m is the molar mass, and T_0 is the temperature of the reservoir of the monatomic ideal gas.[1] The most common carrier gas that is used in the Morse group is helium. For a monatomic gas, C_p equals 5/2 R, where R is the gas constant. The typical reservoir temperature is around 300 K, which produces a terminal velocity of 1.77×10^5 cm/s.

The expansion of the molecular beam is known as supersonic because the ratio of the beam velocity to the speed of sound is greater than one. This ratio is also known as the Mach number and is given by

$$M(x) = \frac{u(x)}{a}. \tag{2.4}$$

Here $u(x)$ is the flow velocity at a downstream distance from the orifice given by x, and a is the speed of sound, which is given by

$$a = \sqrt{\frac{\gamma kT}{m}}. \tag{2.5}$$

Here $\gamma = \frac{C_p}{C_v} = \frac{C_p}{C_p - R}$, k is Boltzmann's constant, T is the temperature in Kelvin, and m is the mass of one molecule.

After the molecules exit the expansion orifice and undergo supersonic expansion into the source chamber, a highly divergent expansion jet is obtained. To conduct experiments that depend on mass spectrometry for detection, the beam is passed through a skimmer into the analytical chamber. The skimmer limits gas flow into the second

chamber, allowing conditions conducive to mass spectrometry to be maintained. It also collimates the molecular beam so that good overlap with the probing laser beams may be achieved. The skimmer employed in these experiments has a 1 cm opening, allowing a good match between the diameter of the molecular beam and the diameters of the unfocussed laser beams. For ease of operation, a pneumatic gate valve is installed between the source and analytical chambers. This allows the user to keep the analytical chamber under high vacuum while maintenance is performed (changing metal samples, etc.) inside the source chamber.

2.6 Resonant Two-Photon Ionization Process

After the molecular beam enters the analytical chamber, it is first probed by either a dye laser (Lamba Physik Scanmate Pro) or an OPO laser (Continuum Horizon). The key part of R2PI is that after being probed by the first laser, the molecular beam is then probed by a second laser to ionize the molecules.

2.6.1 Ionization Process and One-Photon Ionization Process

When employing R2PI spectroscopy as a spectroscopic method, it is crucial that none of the lasers employed can ionize the molecule of interest in a one-photon process. Thus, all photon energies employed must be less than the ionization energy of the molecule. If this requirement is not followed, the molecule will undergo one-photon ionization, which is schematically illustrated in Figure 2.3 (a). The number of ions generated by a one-photon ionization process is vastly greater than the ion signal produced by any other process, making other processes unobservable under these

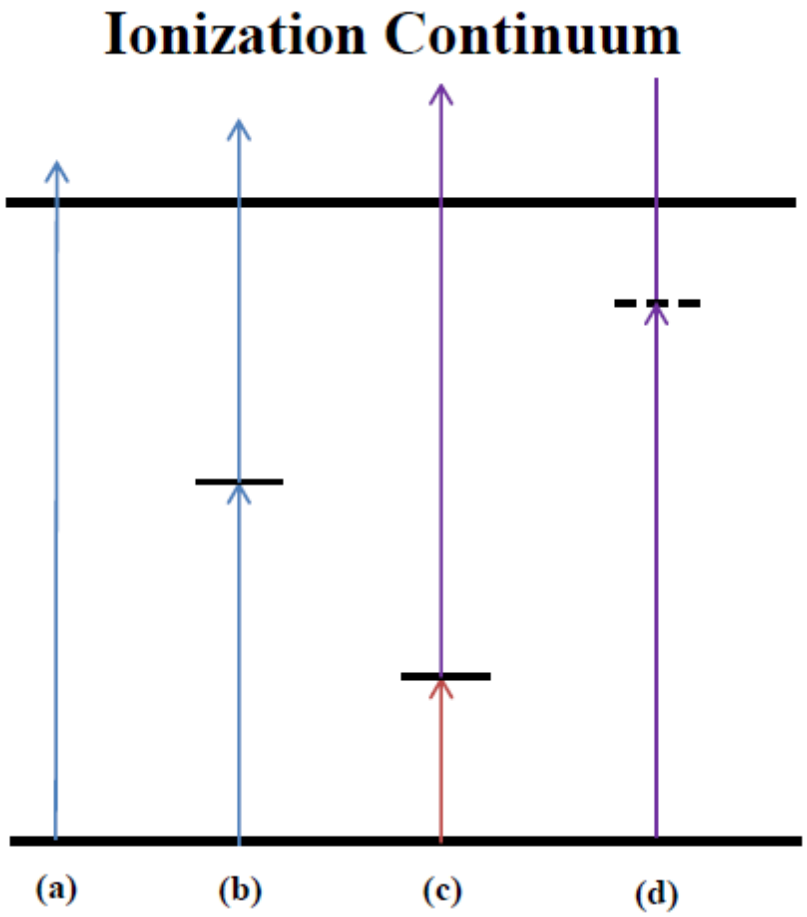

Figure 2.3 Ionization processes in the R2PI experiment, which include (a) one-photon ionization, (b) one-color, two-photon ionization, (c) two-color, two-photon ionization, and (d) a two-color, two-photon ionization through a virtual state.

conditions.

Typically, the processes investigated in the Morse group employ a visible photon for excitation and an ultraviolet photon to ionize the molecules that have been excited by absorption of the first photon. A second case that leads to spectroscopic failure occurs when the wavelength of the ionization laser is resonant with a transition in the molecule. When this occurs, the absorption of two ultraviolet photons can very effectively ionize the molecule, leading to a large molecular signal that is independent of the visible photon wavelength, as depicted in Figure 2.3 (b). When this occurs, it can be very difficult or impossible to pick out transitions induced by the visible wavelength against the large background due to absorption of two ionization laser photons. If the ionization laser wavelength is resonant with a transition in the molecule of interest, it is generally necessary to move to a different ionization wavelength.

In the experiments presented in this dissertation, the ionization photon was supplied from an excimer laser (GAM 100/125). This has the advantage that by filling the laser with different gases, the output wavelength can be varied substantially. In the Morse group, three gases were typically used in the excimer laser: KrF (248 nm, 4.66 eV), ArF (193 nm, 6.42 eV), and F_2 (157 nm, 7.90 eV). Using KrF and ArF gas in the excimer is straightforward, but using F_2 gas is more difficult because 157 nm is in the vacuum ultraviolet region of the electromagnetic spectrum and is easily absorbed by both molecular oxygen and fused silica. Therefore, when using F_2 gas in the excimer laser, the fused silica window through which the excimer radiation passes is replaced with an MgF_2 window and a purge tube is attached between the excimer laser and the A-chamber. The tube is purged of O_2 using a constant flow of nitrogen. This allows the 157 nm vacuum

ultraviolet radiation to be transmitted to the MgF_2 window, which admits it to the chamber.

2.6.2 Two-Photon Ionization Processes

The ideal ionization process in a typical experiment in the Morse group is a two-photon ionization process in which the sum of the excitation laser and the ionization laser photon energies is greater than the ionization energy of the molecule. This is depicted in Figure 2.3(c) and may be termed a resonant two-color, two-photon ionization process, because the two photons involved in the process have different frequencies. The rate of adsorption for a two-photon process is given by [14]

$$W_{f\leftarrow i} = \frac{2\pi}{\hbar^4}\left|\sum_n \frac{(\boldsymbol{E}_2\cdot\boldsymbol{\mu}_{fn})(\boldsymbol{\mu}_{ni}\cdot\boldsymbol{E}_1)}{\omega_{ni}-\omega_1} + \frac{(\boldsymbol{E}_1\cdot\boldsymbol{\mu}_{fn})(\boldsymbol{\mu}_{ni}\cdot\boldsymbol{E}_2)}{\omega_{ni}-\omega_2}\right|^2 \delta(\omega_{fi}-\omega_1-\omega_2), \qquad (2.6)$$

where *i* and *f* represent the initial and final states of the molecule and *n* is the intermediate state. In Equation 2.6, $\boldsymbol{E}_1$ and $\boldsymbol{E}_2$ represent the amplitudes of the electric field vectors of the two laser sources, with their respective frequencies denoted by ω_1 and ω_2. In addition, $\boldsymbol{\mu}_{fn}$ and $\boldsymbol{\mu}_{ni}$ represent the transition dipole integrals between the final and intermediate state and the intermediate and initial state, respectively. The energy difference between the intermediate state and the initial state is given by $\hbar\omega_{ni}$. The sum over all *n* covers all possible intermediate states, and these various pathways to ionization can interfere constructively or destructively. The delta function $\delta(w_{fi}-w_1-w_2)$ expresses the conservation of energy, so that the energy of the overall molecular transition must be equal to the sum of the two photon energies. In R2PI experiments, the final state lies in

the ionization continuum so this condition can always be met. The denominators of the two terms go to zero when the excitation to a particular intermediate state matches the photon energy, which is termed a resonance. An additional imaginary term in the denominator, associated with the lifetimes of the intermediate states, n, prevents these terms from actually going to zero and blowing up, but this detail is omitted here. In practice, because of the separation in time between the two laser pulses, it is only the first term that is relevant to our experiments, because excitation always occurs using ω_1, which is the frequency of the excitation laser.

In addition to providing an undesirable source of background signal when the ionization wavelength is resonant with a transition, the process depicted in Figure 2.3(b) can be a useful means of obtaining an R2PI spectrum if the ultraviolet laser can be scanned. In Figure 2.3(c), two photons of the same wavelength have sufficient energy to ionize the molecule, so as the laser is scanned, whenever an absorption resonance is reached, absorption of the second photon occurs readily, carrying the molecule to the ionization continuum and producing ions. This is termed a resonant, one-color two-photon ionization process. This mechanism is not commonly utilized in the Morse group, because we are generally investigating spectra that are in the visible region, and nearly all of the species investigated have ionization potentials that are too high to be reached by the absorption of two visible photons. In the bond dissociation energy studies that are discussed later in this dissertation, however, the excitation photon lies in the ultraviolet (UV). For the VC, VN, and VS molecules that were studied, two photons of the excitation wavelength provided sufficient energy to ionize the molecule, and the one-color, resonant two-photon ionization process was readily observed.

If the laser that produces the tunable output is fired earlier than the fixed-frequency ultraviolet laser, it is straightforward to separate the ion signals generated by absorption of two tunable laser photons from the ion signal caused by absorption of one photon of each frequency, or of two photons of the fixed-frequency laser. This is because the separation in time between the firing of the two lasers leads to a slightly earlier production of ions when the ion is formed by absorption of two tunable laser photons. The ions that are produced earlier in time arrive slightly earlier at the detector, leading to a doubling of the mass peak in the spectrum. By monitoring the peak that appears at the slightly lower mass, we can monitor ions produced by the absorption of two tunable laser photons. Conversely, by monitoring the second peak we are able to record the spectrum that is obtained by excitation with the tunable laser followed by ionization with the fixed-frequency laser. In fact, if the timing between the ionization laser and the tunable OPO laser is increased, the first peak moves towards lighter masses; the opposite occurs if the timing between the lasers is decreased. Figure 2.4 shows the mass spectrum of VS, which will be described in more detail later in this dissertation, with the tunable OPO and fixed-frequency excimer lasers firing. The one-color, two-photon ionization peak caused by absorption of two OPO laser photons occurs at slightly lower apparent mass than the peak caused by the two-color, two-photon process.

Another method to determine if a molecular signal arises from a one-color, two-photon process is to simply omit the second laser. Any transitions that are observed are then of necessity caused by one-color, two-photon ionization processes.

The final two-photon ionization process is displayed in Figure 2.3(d). This occurs when the first photon is not resonant with an absorption in the molecule. It is said that the

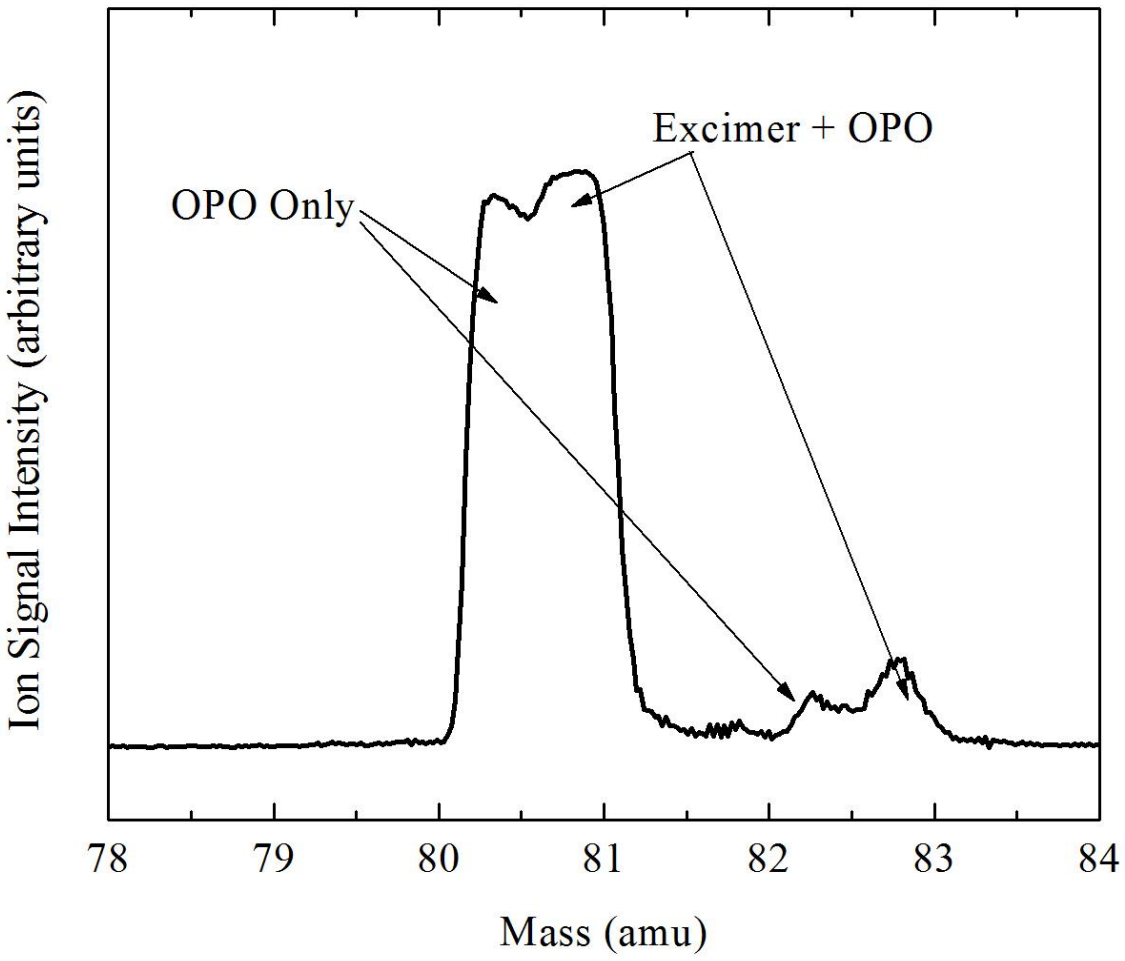

Figure 2.4 The mass spectrum with the OPO and excimer laser firing. Two peaks are typically observed: the one to the left is due to one-color, two-photon ionization from the OPO laser and the one to the right is due to two-color, two-photon ionization from the OPO and excimer lasers.

transition goes through a "virtual state". This corresponds to the situation in which no intermediate state, *n*, in Equation (2.6) causes the denominator to approach zero. As a result, it is possible for several molecular eigenstates to make significant contributions to the summation in this equation. The extent to which a given molecular eigenstate will make a contribution to the sum is governed by the magnitudes of the transition dipole moments between the state in question and the initial and final states, and the energy defect, which defines how far away from resonance the state lies. Because several intermediate states can contribute to the sum, it is sometimes said that a virtual state is a superposition of molecular eigenstates. This in indicated in Figure 2.3(d) by the dashed line.

In principle, ionization through a virtual state can always occur, although if the molecular eigenstates that contribute to the sum are far from resonance, the net rate of ionization will be small. We frequently observe this effect when a high intensity of fixed-frequency excimer laser radiation is employed, and thus monitoring this signal provides a convenient way to optimize the concentration of the molecule of interest. To obtain a spectrum with a good signal-to-noise ratio, however, this nonresonant background signal must be reduced. This is easily done by simply reducing the intensity of the excimer laser, which is done by either reducing the operating voltage of the laser or by placing low-quality fused silica filters between the laser output and the analytical chamber. Filtering the excimer laser allows the intensity of the background signal due to the nonresonant virtual state ionization processes to be reduced compared to the resonant two-photon ionization signals. This occurs because the nonresonant ionization process requires the absorption of two excimer laser photons, causing its probability to be

proportional to the laser intensity squared. In contrast, the resonant ionization process requires absorption of only one excimer laser photon, causing these signals to be proportional to the excimer laser intensity raised to the first power. If the excimer laser intensity is reduced excessively, however, both the virtual state transitions and the resonant transitions will disappear.

Figure 2.5 displays the enhancement that occurs in a resonant two-color, two-photon ionization process. In Figure 2.5 (a), the mass spectrum of ^{58}NiCCH (mass 83) and ^{60}NiCCH (mass 85) is shown with only the excimer laser firing. The larger signals correspond to ^{58}Ni·HCCH and ^{60}Ni·HCCH, which are probably one-photon ionized with this choice of excimer laser wavelength (157 nm, 7.9 eV). This NiCCH molecular signal observed in Figure 2.5(a) is due to the one-photon ionization process that was described above. Figure 2.5 (b) shows the same mass spectrum but with both the dye laser and excimer laser beams intersecting the molecular beam. The increase in molecular signal is due to the two-color, two-photon ionization process depicted in Figure 2.3(b). This figure clearly demonstrates why the two-photon processes are so important to the experiments performed in the Morse group. It also demonstrates the utility of a mass-resolved detection system: this allows the weak ion signals due to NiCCH to be readily distinguished from the much stronger signals due to Ni·HCCH.

2.7 Time-of-Flight Mass Spectrometry (TOFMS)

After the molecules are ionized, they are accelerated in the ion source region of the time-of-flight mass spectrometer, which is used to separate the ions by mass. Because the ions are singly charged, if they are produced in a region with an electrostatic potential

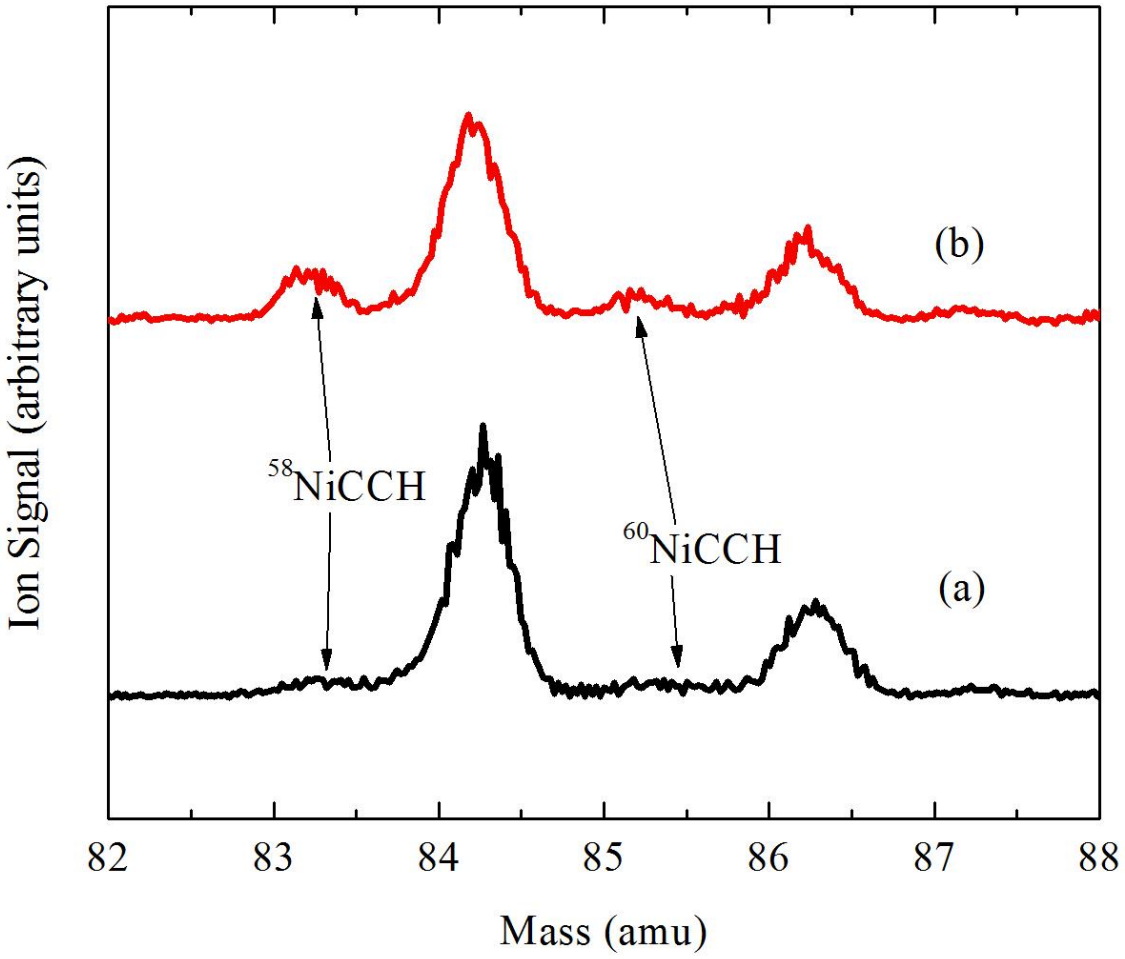

Figure 2.5 Mass spectrum with (a) just the excimer laser firing and (b) the dye and excimer lasers firing, with the dye laser tuned to a transition.

V_0 and are accelerated to ground potential, they develop a kinetic energy of eV_0. After acceleration, the ions travel up a flight tube and are then reflected down a second flight tube to the detector. Because the kinetic energy is the same for all ions, independent of mass, the equation

$$KE = \frac{mv^2}{2} \tag{2.7}$$

implies that ions of small mass, *m*, will compensate by achieving a higher velocity, thereby reaching the detector after a short time. Heavier ions will strike the detector at a later time. This is the basis of the time-of-flight mass spectrometric method.

2.7.1 Wiley-McLaren Ion Source Design

When TOFMS was first developed, ions were accelerated in a single region characterized by a uniform electric field. With this arrangement, however, the mass resolution was very poor. By breaking up the acceleration region into two regions with different electric field strengths, however, it is possible to obtain much better mass resolution. This is the technique employed in the Morse group R2PI spectrometer. In the Morse group, the ion source employs the Wiley-McLaren design,[15] which breaks the acceleration region into an extraction region and an acceleration region. This employs three elements to control the electric field. The electrode farthest away from the flight tube is known as the repeller and is set to a fixed voltage of +2000 volts. The electrode closest to the flight tube is grounded and is therefore set to 0 volts. The intermediate electrode, which lies between the repeller and the ground electrode, is known as the

draw-out grid (DOG). This electrode can be adjusted to optimize the resolution of the mass spectrum. Its function is to position the spatial focus of the ion packets at the planar front surface of the detector, so that all of the ions of a given mass reach the detector at the same time. This electrode design is known as the Wiley-McLaren design.[15] This design is advantageous because with the three electrodes there is a smooth decrease in the voltage potential, which allows for much better mass resolution than one electrode acceleration.

As seen in Figure 2.1, the TOFMS used in the experiments in this dissertation employs additional ion optics to reflect the ion packet down a second flight tube. Non-linear TOFMS designs, such as this, can be advantageous because they allow some imperfections in the linear design to be corrected. They also allow a longer flight path to be achieved in a smaller amount of space. However, with any nonlinear design, additional ion optics are required to reflect the ions into the next portion of the flight tube.

Along with these extraction, acceleration, and reflection ion optics, two additional electrodes are required to steer the ions through the TOFMS to the detector. As described previously, when helium is the carrier gas, the velocity of the molecular beam is 1.77×10^5 cm/s. This forward velocity is unaffected by the acceleration imparted by the extraction and acceleration electric fields, because these fields are orthogonal to the forward velocity vector. If the forward velocity is not reduced or halted, the ions will crash into the wall of the flight tube and never reach the detector. Therefore, two electrodes, known as the deflector, are placed above the Wiley-McLaren ion extraction/acceleration region. The deflector plates are used to halt the forward motion of

the ions and direct them toward the detector. The voltage on the deflector plates can be adjusted to make minor improvements on the mass resolution and to optimize the transmission of the desired ion to the detector.

2.7.2 Reflectron

When employing a single-stage ion extraction/acceleration assembly, the local electrostatic potential at the point of ion production, V(z), determines the ultimate kinetic energy of the ion and therefore its velocity in the flight tube. The resulting flight velocity is given by

$$v = \sqrt{\frac{2eV(z)}{m}} \tag{2.8}$$

where *V(z)* is the electrostatic potential at the position where the ion is created, *z*, *e* is the electron charge, and *m* is the mass of the ion. It is assumed that the ion is singly charged, which is the case for the species produced by the R2PI process. As can be seen, there is a correlation between the position where the ions are formed (z) and the resulting ion velocity, v. Because the ions produced at a higher potential are farther away from the detector, they also develop a higher velocity and will begin to catch up with the more slowly moving ions that were formed farther from the repeller plate. At a certain position, the faster ions will catch up with the slower ions in front of them, and the ion packet will be compressed to a plane. This point is known as the spatial focus and after it, the ions will diverge again. In the experiments performed in this dissertation, a reflectron was installed to improve the mass resolution by ensuring that the spatial focus

of the ion of interest occurs at the detector.[16] The design of the reflectron is similar to the Wiley-McLaren design in that there are three electrodes in the reflectron. The first electrode that the ions encounter is the ground electrode, which is set at 0 V. The final electrode the ions encounter in the reflectron is the reflector, which, like the repeller, is always set at +2000 V. Between the ground and reflector electrodes is the retarder electrode. Much like the DOG electrode, the retarder electrode can be adjusted to change the spatial focus of the ions and adjust the mass resolution. When the ions enter the reflectron, the faster ions penetrate farther into it than slower ions. Therefore, it will take longer for faster ions to be reflected than the slower ions. After the reflectron, the slower ions will exit first but the faster ions will catch up eventually at a second spatial focus.

The flight tube is designed with the second portion at an angle of 18 degrees relative to the first flight tube, so when undergoing reflection the ions are turned 162 degrees. The vector that is perpendicular to the electrodes in the reflectron is oriented at a 9 degree angle relative to the first and second portions of the flight tube, so that the angle of incidence is equal to the angle of reflection. Finally, the planar surface of the microchannel plate detector is aligned so that its surface normal is parallel to the second portion of the flight tube.

2.8 The Detector

A chevron configuration dual microchannel plate (MCP) detector is located at the end of the flight tube. The two microchannel plates each consist of an array of tiny continuous dynode electron multipliers. Each microchannel is approximately 10 μm in diameter and etched at a 12 degree bias angle to the surface normal. This prevents the

ions from passing through the microchannels without hitting the walls. The first surface of the first plate of the MCP is charged to -2000 V to attract the ions so that they strike the surface with nearly 4000 eV of kinetic energy. The bottom surface of the second plate is charged to -50 V. The two microchannel plates have matched resistances, so the interface between the two is at roughly -1000 V. This ensures that each microchannel plate provides roughly the same gain. When the ions collide with the front of the MCP, electrons are dislodged from the surface of the MCP. These electrons then travel down the channels and hit the walls. When the primary electrons collide with the walls of the channels, several secondary electrons are ejected, and these collide with the wall of the channel further down, leading to a tremendous net gain. The typical gain for the dual-plate MCP is 10^7.

The MCP is connected to a 50 Ω terminated anode[17] that is coupled to a 350 MHz SR445 A Stanford Research preamplifier with 5× amplification per channel, with 4 total channels available, which may be chained in sequence for a total of 625× amplification. In practice, we usually operate with only two channels chained in sequence, providing 25× amplification. The output voltage waveform is digitized by a National Instruments scope card. The digitized signal is then read and manipulated using a Windows 7-based PC, using a program developed by the Morse group in the LabView programming language. The signal-to-noise ratio is improved by summing 30 time-of-flight waveforms before measuring the intensities of the molecule of interest, which averages out shot-to-shot fluctuations. The entire experimental cycle repeats at a rate of 10 Hz so the collection of one mass spectrum takes 3 seconds of laboratory time.

2.9 Data Collection

2.9.1 The Mass Spectrum

After the molecules are created, cooled by supersonic expansion, skimmed, probed by the two lasers, and the resulting ions pass through the TOFMS and impact the detector, the mass spectrum is displayed on the computer screen. The mass spectrum can be used to verify that the molecule of interest is being formed. This can be done by setting the ionization laser to a high fluence, so that nonresonant two-photon ionization can occur. Viewing the mass spectrum over a period of time allows the user to determine whether or not the molecular signal is stable. If a particular molecular signal is not stable, this will show up in the R2PI spectrum of the molecule as fluctuations. These could be due to inhomogeneous metal alloy sample, a sample that seals poorly on the vaporization block, a poorly functioning pulsed valve, fluctuating vaporization or ionization laser power, or a multitude of other issues. Another advantage of the mass spectrum is that it can be used to align the dye laser into the analytical chamber. This is done by first collecting the mass spectrum with just the ionization laser firing, which gives a baseline for the molecular signal. Then the mass spectrum is collected with both the ionization laser and the dye or OPO firing. The molecular signal will increase due to the two-color, two-photon ionization process described above if the tunable laser is tuned to an absorption wavelength. The optics that direct the light from the OPO or dye laser can then be adjusted while monitoring the mass spectrum so that this light interacts with the highest density of molecules. This gives the largest increase in signal and should give the strongest transitions, provided the ion signal on resonance is much larger than the background signal due to the ionization laser alone. For example, Figure 2.5(a) displays a

mass spectrum with just the ionization laser firing, and Figure 2.5(b) displays the same mass spectrum with the ionization laser and dye laser firing, with the dye laser tuned to an absorption band. The increase in signal in the mass spectrum is what is monitored in a R2PI experiment.

One final advantage of the mass spectrum collected in the Morse group using time-of-flight mass spectrometry is that multiple peaks (corresponding to different chemical species, or different isotopic modifications of a given species) can be monitored while scanning the tunable laser. This makes the experiment more efficient because transitions in different molecules can be observed in one scan. For example, if the molecule of interest has multiple masses due to different isotope combinations, these masses can be monitored in one scan. This scan can then be used to determine the isotope shift between the different masses.

2.9.2 Low-Resolution Spectra

For a typical experiment in the Morse group, after the mass channels are assigned, a low-resolution scan is collected by scanning a tunable laser while the frequency of the ionization laser is fixed. As mentioned above, the ionization laser in the experiments discussed in this dissertation is an excimer laser so it is easy to fix its frequency. There are two tunable lasers used in these experiments: Lambda Physik Scanmate Pro dye laser or Horizon OPO laser. The dye laser is pumped by a Continuum Surelite III Nd:YAG laser and the OPO is pumped by a Continuum Surelite II Nd:YAG laser.

The dye laser has a low-resolution linewidth of 0.15 cm^{-1}. The diffraction grating is controlled by using a program in LabView using VIs provided by Lambda Physik. The

dye laser can be scanned from 11000 cm^{-1} to 25000 cm^{-1} and is covered by a large variety of dyes. The dyes can be separated into two regions: the red region, which goes from 543 nm to 900 nm, and the blue region, which goes from 400 to 563 nm. Depending on the region, the dye laser is pumped either with second harmonic (532 nm, red dyes) light or third harmonic (355 nm, blue dyes) light from the Nd:YAG laser.

The OPO has linewidths that range from 5 cm^{-1} to 15 cm^{-1}. The crystals and prisms in the OPO are also controlled using a program in LabView. The OPO can be scanned from about 3700 cm^{-1} to about 52,000 cm^{-1}. The advantage of the OPO is that dyes are not needed so one does not have to worry about switching between dyes. The OPO laser is pumped by both 1064 nm and 355 nm light from the Nd:YAG pump laser. The 355 nm pump radiation is split into a signal beam (wavelengths shorter than 710 nm) and an idler beam (wavelengths longer than 710 nm). The photon energies of the signal and idler beams always add up to the energy of the 355 nm pump photons. The 1064 nm fundamental radiation of the Nd:YAG laser is used to create UV light in the regions from 292 to 400 nm and from 193 to 208 nm. Overall, the laser can generate wavelengths in five different regions via different mechanisms. From 709.4 nm to 2700 nm, the idler beam is used. From 400 nm to 709.4 nm, the signal beam is used. From 292 nm to 400 nm, the signal beam is summed with the 1064 nm Nd:YAG fundamental radiation using a sum frequency generation crystal. From 208 nm to 292 nm, the signal beam is frequency doubled using one of two different second harmonic generation crystals. Finally, from 208 nm to 193 nm, the signal beam is first frequency doubled and then mixed with the 1064 nm Nd:YAG fundamental beam. Naturally, the output energy that may be obtained varies significantly between these different wavelength regions. The laser linewidth

varies significantly as well.

Figure 2.6 shows an example of a low-resolution spectrum as is typically collected with the dye laser. The figure displays the vibronically resolved spectrum of ^{58}NiCCH from 15,500 cm^{-1} to 18,500 cm^{-1}. This region is not very congested but there are multiple transitions from the v"=0 and v"=1 levels in the ground electronic state that terminate at the same excited level but excite different vibrational modes in NiCCH. The vibronically resolved spectra can be fitted using the following equation

$$\nu = T_0 - \omega_5^{''}\nu_5^{''} + \omega_2'\nu_2' + \omega_3'\nu_3' + \omega_4'\nu_4' + \omega_5'\nu_5' + x_{33}'(\nu_3'^2 + \nu_3') + x_{23}'\left(\nu_2'\nu_3' + \frac{\nu_2'+\nu_3'}{2}\right) + x_{34}'\left(\nu_3'\nu_4' + \frac{\nu_3'+\nu_4'}{2}\right) + x_{35}'\left(\nu_3'\nu_5' + \frac{\nu_3'+\nu_5'}{2}\right) \quad (2.9)$$

where T_0 is the term energy of the excited state, ω_r' is the vibrational frequency of the rth vibrational mode and x_{rs}' is the anharmonicity between the rth and sth vibrational modes.

With the OPO laser, the low-resolution spectra are collected to find the bond dissociation energy of a molecule, although it can also be used like the dye laser to obtain a vibronically resolved spectrum, albeit at a lower resolution than may be obtained using the dye laser. Figure 2.7 displays a scan over the bond dissociation energy of ^{51}VC. Here, below 33,138 cm^{-1} the excited vibronic levels are long lived because the only decay pathway is fluorescence. Above this threshold, however, the molecule has the additional decay channel of dissociation available, leading to a much shorter excited state lifetime. The net result is that above 33,138 cm^{-1}, the molecule falls apart before it can absorb a second photon and be ionized. This allows the sharp cut-off in the spectrum to be assigned as the bond dissociation energy of VC. Unlike the widely spaced vibronic

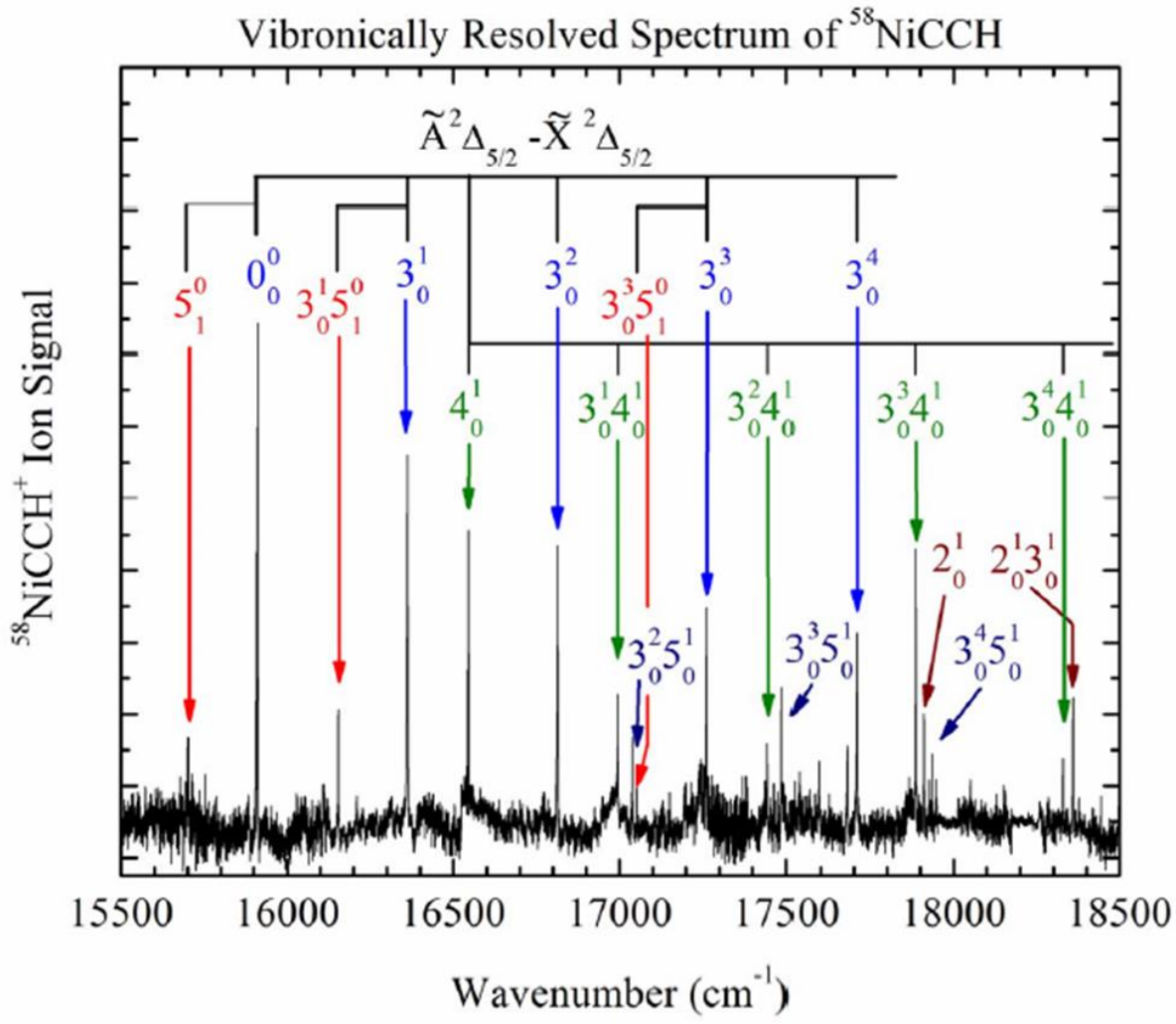

Figure 2.6 Vibronically resolved spectrum of ^{58}NiCCH.

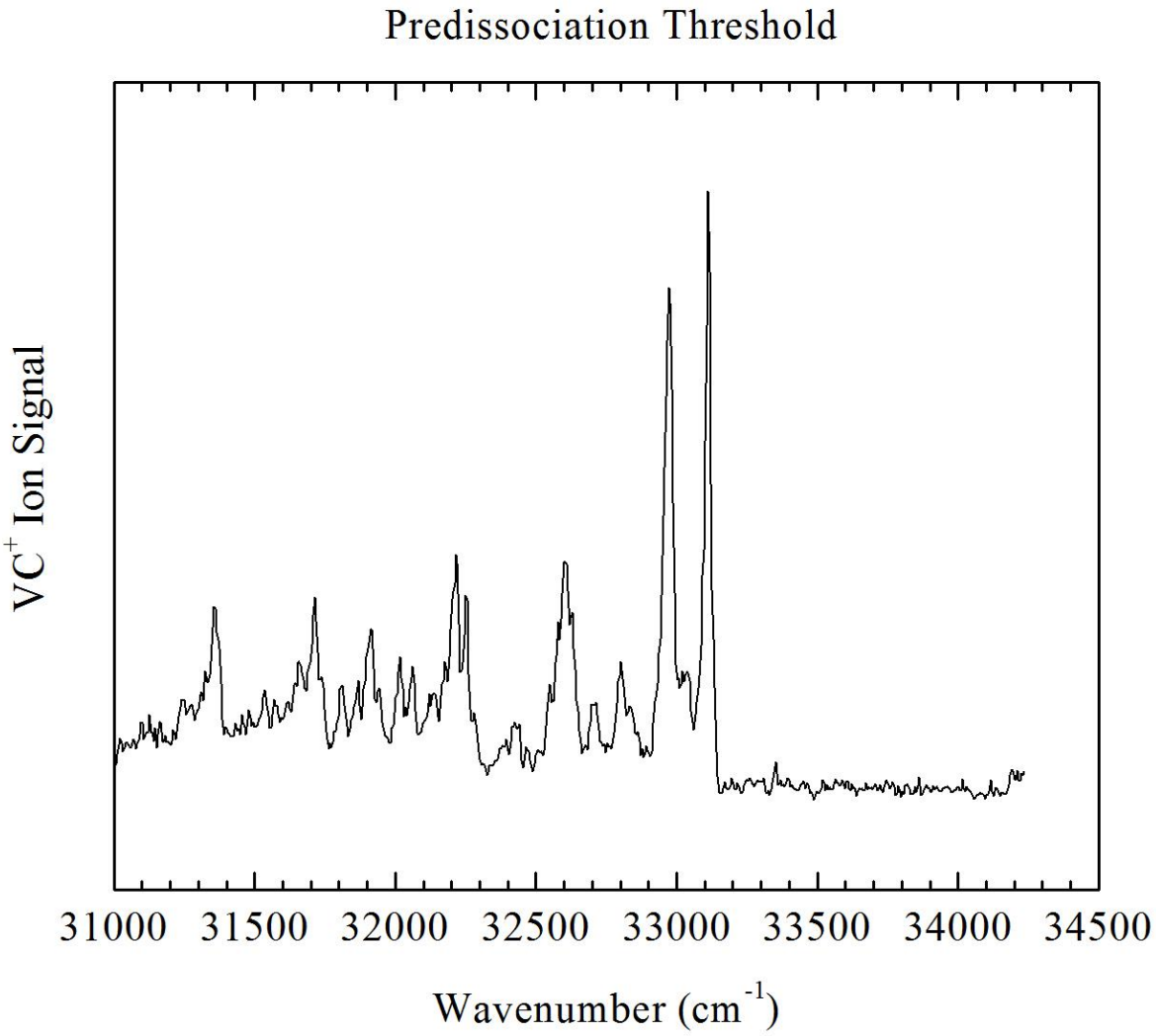

Figure 2.7 Predissociation threshold in ^{51}VC.

features of Figure 2.6, the spectrum of VC corresponds to a structured continuum. This is due to the high density of vibronic levels near the dissociation limit, and is characteristic of many transition metal molecules near this limit.

2.9.3 High-Resolution Spectra

Although the vibronically resolved spectra collected in low-resolution scans contain a great deal of useful information, the goal of the Morse group is to determine fundamental information of transition metal molecules, such as bond lengths and ground electronic state symmetries. To obtain this information, rotationally resolved spectra must be collected. To do so, an air spaced intracavity étalon with a free spectral range of 1.0 cm^{-1} is placed inside the dye laser oscillator in a sealed cavity that also contains the diffraction grating. The étalon increases the resolution of the dye laser to 0.04 cm^{-1}. When the étalon is placed inside the oscillator, it is aligned so that only one étalon mode lies under the transmission range of the diffraction grating. This is done using a hand-held étalon while making adjustments to the dye laser until one set of fringes are observed in the hand-held étalon. Once a single étalon mode is observed, the laser cavity is sealed and evacuated using an Alcatel rotary vane vacuum pump until the pressure is reduced to 15 torr.

After confirming that a single fringe pattern is still seen at this low pressure, the laser cavity is then slowly pressurized to atmospheric pressure with sulfur hexafluoride (SF_6) while the diffraction grating and étalon are held in place. By introducing sulfur hexafluoride slowly, the index of refraction of the medium in the oscillator cavity is slowly increased, which causes the speed of light to decrease. As the speed of light

decreases, the frequency is also decreased based on the following relationship

$$\nu = \frac{c_m}{\lambda}. \tag{2.10}$$

Here c_m is the speed of light in the medium, ν is the frequency, and λ is the wavelength. Sulfur hexafluoride is used because its index of refraction (1.000723 at 633 nm, 1 atm, 300 K)[18] is among the highest of readily available gases. The slow introduction of SF_6 into the oscillator cavity is known as pressure scanning. The diffraction grating and étalon serve to select a wavelength, which remains fixed within the dye laser oscillator cavity. As the pressure increases, however, the speed of light within the medium decreases as the index of refraction is slowly changed from 1.000000 to 1.000723 (at 1 atm pressure, 633 nm). As the speed of light decreases, the output frequency also decreases. Because the photon energy is given by E=hν, the photon energy also decreases during a pressure scan, allowing the spectrum to be recorded over a limited range. In the work described in this dissertation, a pressure scan typically covered a range from 15 torr to 760 torr, corresponding to about 15 cm^{-1} in the blue region and 10 cm^{-1} in the red region of the spectrum. Multiple scans were typically recorded, individually calibrated, and averaged together to improve the signal-to-noise ratio. If the rotational structure of a given molecular band spanned a broader range than 10-15 cm^{-1}, the dye laser could be moved to a slightly different wavelength and scanned again using pressure scanning, and the calibrated final scans could be pieced together to allow the high-resolution spectrum of the overall band to be examined. The calibration process is discussed later in this chapter, in Section 2.9.4.

As mentioned above, the goal of these scans is to obtain the rotational structure of the vibronically resolved peaks that were found in the low-resolution spectrum. Figure 2.8 displays the rotationally resolved spectrum for the 3_0^1 band of the $\tilde{A}\ ^2\Delta_{5/2} \leftarrow \tilde{X}\ ^2\Delta_{5/2}$ band system of the ^{58}NiCCH molecule. This is a good example of a typical high-resolution spectrum that is collected in the Morse group.

2.9.4 Calibration

Although the dye laser provides narrow linewidth tunable radiation, the precise output wavenumber is not accurately known. For this reason, it is important to calibrate the high-resolution spectra. In order to calibrate the high-resolution spectra, a beamsplitter is used to pick off the dye laser light and send about 5% of the radiation toward a cell filled with a reference gas and 5% to an étalon with the free spectral range of 0.22 cm^{-1}. Two photodiodes are placed after the cell and the étalon to record the reference gas transmission spectrum and the étalon transmission fringes, respectively. The fringes are used to linearize the high-resolution spectrum and the reference gas is used to calibrate the spectrum. The reference gas is either isotopically enriched tellurium ($^{130}Te_2$) or iodine ($^{127}I_2$). Isotopically enriched $^{130}Te_2$ in a heated cell is used if the scan is between 18,500 cm^{-1} and 24,000 cm^{-1}.[19-20] I_2 is used to the red of 18,500 cm^{-1}, although the iodine has to be heated if the scan is to the red of 14,100 cm^{-1}.[21-23] Either Te_2 or I_2 can be used between 18,500 cm^{-1} and 19978 cm^{-1}, but I_2 is easier to use because it does not have to be heated in this region.

For the bond dissociation energies reported in this dissertation, a different calibration method was used. Because the OPO has a much worse resolution than the dye

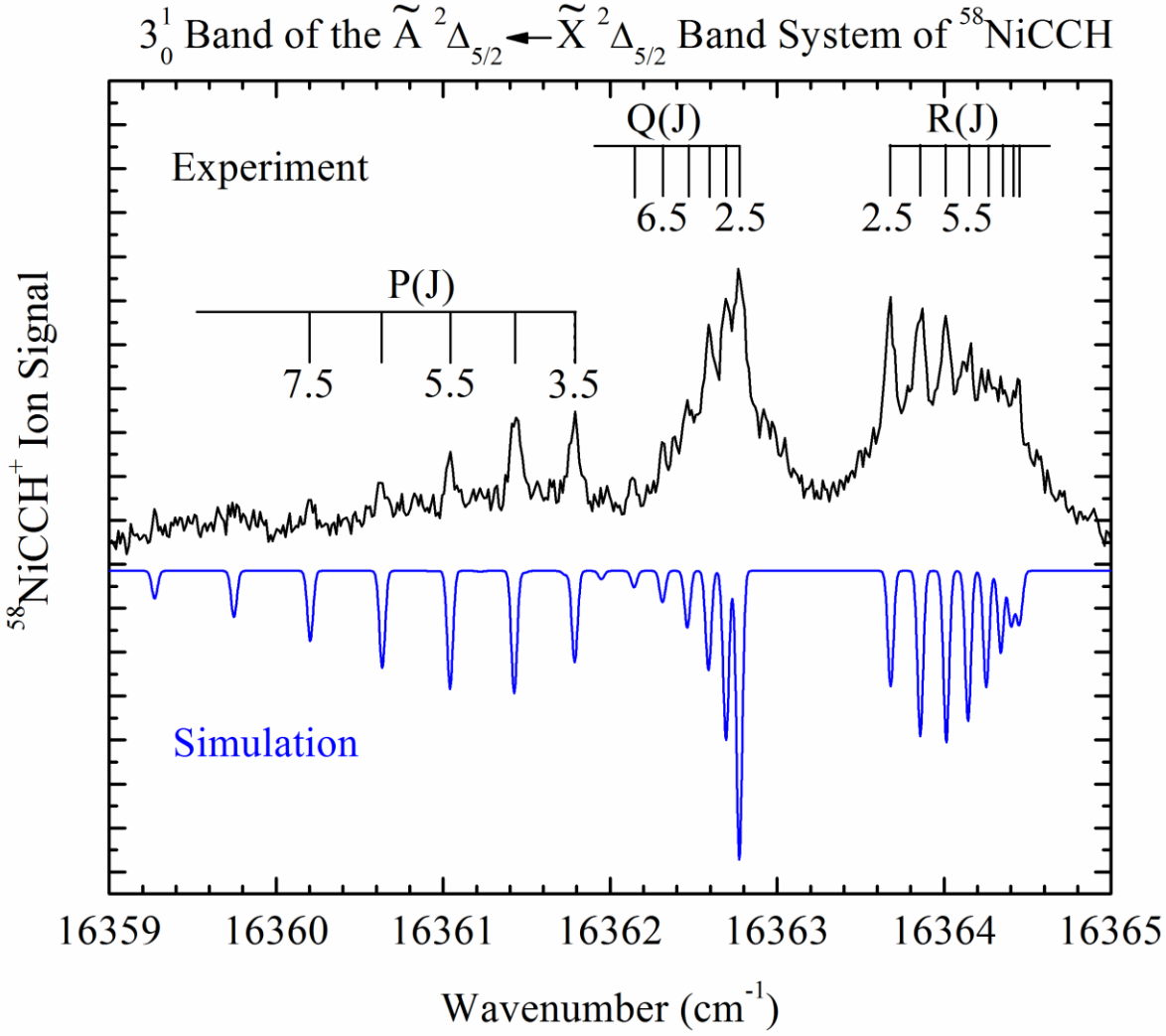

Figure 2.8 High-resolution spectrum of the 3_0^1 band in the $\tilde{A}\ ^2\Delta_{5/2} \leftarrow \tilde{X}\ ^2\Delta_{5/2}$ band system of ^{58}NiCCH. The upper spectrum is the collected spectrum and the lower spectrum is simulated.

laser, the iodine/tellurium and étalon method could not be used. Instead, the atomic signals of certain elements were monitored while scanning over the bond dissociation threshold. Figure 2.9 shows the scan over the bond dissociation energy of VC, along with the atomic signals of Mo and V. For this example, a vanadium-molybdenum alloy was used as the metal sample, so both atomic V and Mo were present, and their signals could be separately recorded. Using the known lines in the atomic spectra of V and Mo,[24] the VC bond dissociation threshold could be accurately calibrated.

After the high-resolution spectra are collected and calibrated, a minor correction has to be made. Due to how the dye laser enters the chamber, the molecules move toward the dye laser at the terminal velocity of helium (1.77×10^5 cm/s). This means that the molecules interact with dye laser light that is shifted slightly to the blue due to the Doppler effect. The correction that must be added to the apparent dye laser wavenumber is given by $\Delta\nu = \nu \times (v/c)$, where v is the velocity of the gas, ν is the wavenumber of the peak in the spectrum, c is the speed of light, and $\Delta\nu$ is the correction. This correction usually ranges from 0.1 cm^{-1} to 0.2 cm^{-1}.

2.9.5 Excited State Lifetimes

As mentioned above, the low- and high-resolution scans can be used to extract a great deal of information about the molecule under study. However, neither the low-resolution nor the high-resolution scan can provide the decay lifetime of a particular excited state. The lifetime curve is collected by setting the excitation laser to the desired transition and randomly varying the time at which the tunable laser fires with respect to the ionization laser, which is fixed in time. As the excitation laser is varied in time, ion

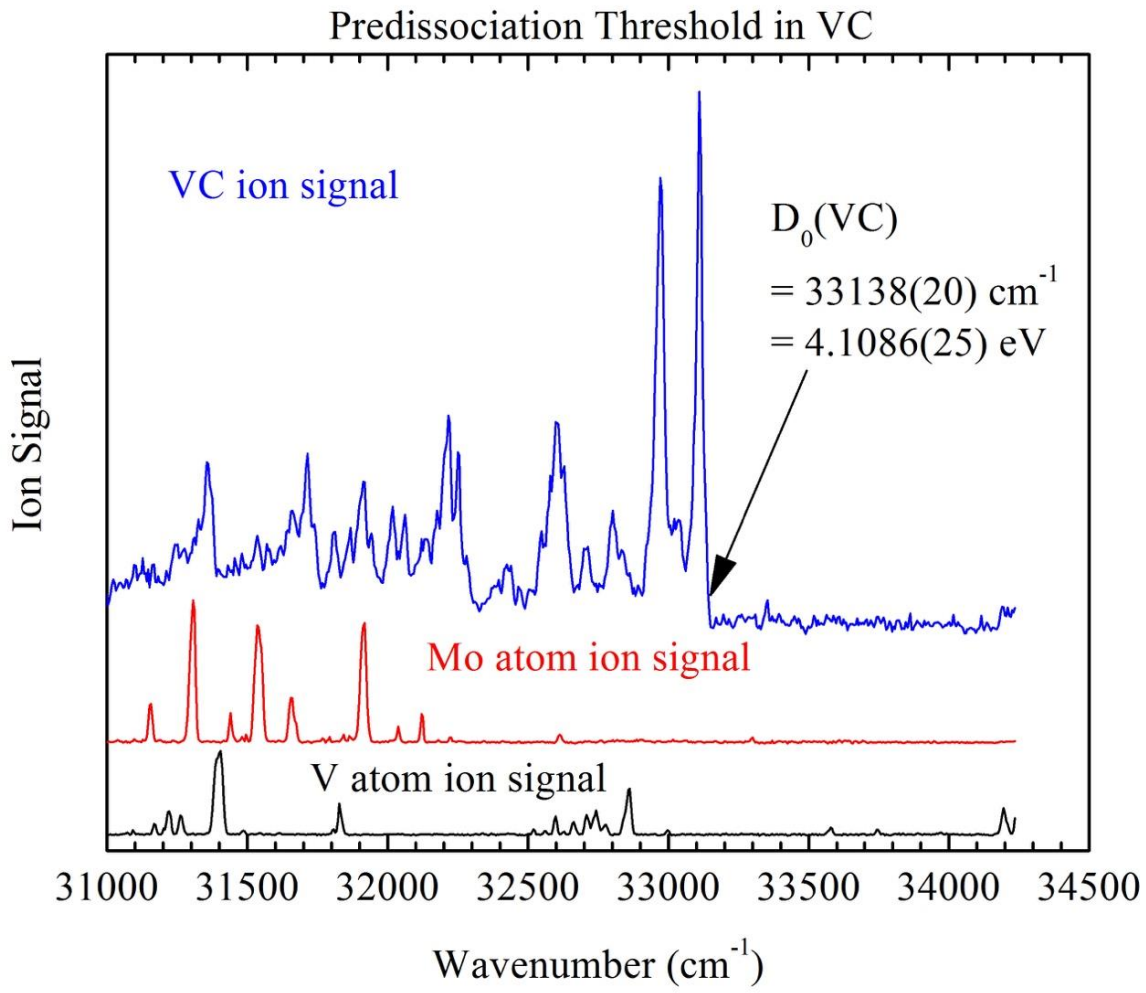

Figure 2.9 Predissociation threshold in VC (blue), Mo atomic signal (red), and V atomic signal (black). The spectra were recorded using an OPO laser in conjunction with KrF excimer radiation, which provided the second, ionizing photon. The dense continuum of transitions terminates at 33,138 cm^{-1}, allowing the bond dissociation energy of VC to be determined as $D_0(VC) = 4.1086 \pm 0.0025$ eV and the heat of formation to be $\Delta H_f^0(VC) = 822.70 \pm 0.51$ kJ/mol.

ion signals are accumulated for the various excitation-ionization time intervals. After sufficient datapoints have been collected and averaged, an ion signal versus delay time curve is generated. The exponential decay lifetime, τ, is then extracted from the data using the Levenberg-Marquardt nonlinear least-squares algorithm.[25] The lifetime may be used to confirm if a series of vibrational bands correspond to different vibrational levels in the same excited state, since then the vibrational levels would be expected to have similar lifetimes. Similarly, if the excited state decays primarily by fluorescence to the ground state, the oscillator strength of the transition can be deduced from the upper state lifetime. Finally, an abrupt shortening in the lifetimes of vibronic levels as a function of level energy can be used as an indicator that predissociation sets in above the threshold energy. Figure 2.10 demonstrates a typical lifetime curve collected in the Morse group. This figure shows the lifetime of the 0^0 level of the $\tilde{A}\ ^2\Delta_{5/2}$ state of NiCCH. If we assume that the decay is purely due to fluorescence to the ground state, the lifetime can be used to determine the absorption oscillator strength using the equation

$$f = \left(1.499 \frac{s}{cm^2}\right) \frac{\lambda^2}{\tau}\ , \tag{2.11}$$

where *f* is the absorption oscillator strength and λ is the wavelength. Even if fluorescence to other states occurs or if other decay processes, such as predissociation, are present, the absorption oscillator strength calculated using this formula will provide an upper limit.

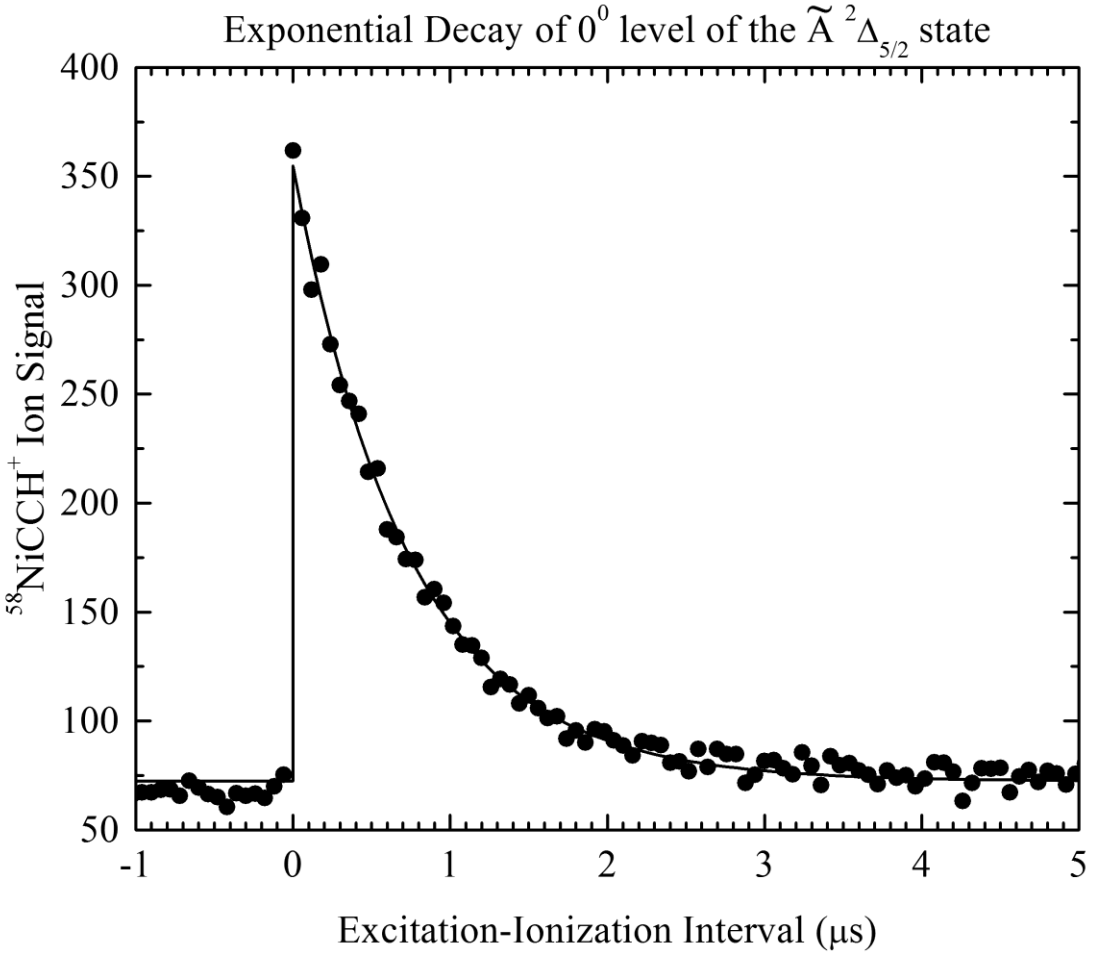

Figure 2.10 Exponential decay of the 0^0 level of the $\tilde{A}\ ^2\Delta_{5/2}$ state of NiCCH, measured by the time-delayed resonant two-photon ionization method. The fit of this decay curve gives $\tau = 0.730$ μs; combined with two other measurements, a value of $\tau = 0.725 \pm 0.015$ μs is obtained.

2.10 References

1. Morse, M. D. Supersonic Beam Sources. In *Methods of Experimental Physics: Atomic, Molecular, and Optical Physics*, Dunning, F. B.; Hulet, R., Eds. Academic Press, Inc.: Orlando, Florida, 1996; Vol. II Atoms and Molecules, pp 21-47.

2. Duncan, M. A. Invited Review Article: Laser Vaporization Cluster Sources. *Rev. Sci. Instrum.* **2012,** *83* (4), 041101/1-041101/19.

3. Airola, M. B.; Morse, M. D. Rotationally Resolved Spectroscopy of Pt_2. *J. Chem. Phys.* **2002,** *116* (4), 1313-1317.

4. Krechkivska, O.; Morse, M. D.; Kalemos, A.; Mavridis, A. Electronic Spectroscopy and Electronic Structure of Diatomic TiFe. *J. Chem. Phys.* **2012,** *137*, 054302/1-12.

5. Matthew, D. J.; Oh, S. H.; Sevy, A.; Morse, M. D. The Bond Length and Bond Energy of Gaseous CrW. *J. Chem. Phys.* **2016,** *144* (21), 214306/1-214306/10.

6. Le, A.; Steimle, T. C.; Morse, M. D.; Garcia, M. A.; Cheng, L.; Stanton, J. F. Hyperfine Interactions and Electric Dipole Moments in the [16.0]1.5(v = 6), [16.0]3.5(v = 7), and $X^2\Delta_{5/2}$ States of Iridium Monosilicide, IrSi. *J. Phys. Chem. A* **2013,** *117* (50), 13292-13302.

7. Garcia, M. A.; Vietz, C.; Ruipérez, F.; Morse, M. D.; Infante, I., Electronic Spectroscopy and Electronic Structure of Diatomic IrSi. *J. Chem. Phys.* **2013,** *138* (15), 154306/1-9.

8. Garcia, M. A.; Morse, M. D. Electronic Spectroscopy and Electronic Structure of Copper Acetylide, CuCCH. *J. Phys. Chem. A* **2013,** *117* (39), 9860-9870.

9. Fu, Z.; Lemire, G. W.; Bishea, G. A.; Morse, M. D. Spectroscopy and Electronic Structure of Jet-cooled Al_2. *J. Chem. Phys.* **1990,** *93* (12), 8420-8441.

10. Fu, Z.; Lemire, G. W.; Hamrick, Y. M.; Taylor, S.; Shui, J.-C.; Morse, M. D. Spectroscopic Studies of the Jet-cooled Aluminum Trimer. *J. Chem. Phys.* **1988,** *88*, 3524-3531.

11. Arrington, C. A.; Morse, M. D. Spectroscopy of Jet-Cooled Bi_3. *J. Phys. Chem. B* **2008,** *112* (50), 16182-16192.

12. Ready, J. F. *Industrial Applications of Lasers*. Academic Press: New York, 1978; p 588.

13. Levy, D. H. Laser Spectroscopy of Cold Gas-Phase Molecules. *Annu. Rev. Phys. Chem.* **1980,** *31*, 197-225.

14. Lin, S. H.; Fujimora, Y.; Neusser, H. J.; Schlag, E. W., *Multiphoton Spectroscopy of Molecules*. Academic Press, Inc.: Orlando, 1984; p 260.

15. Wiley, W. C.; McLaren, I. H. Time-of-Flight Mass Spectrometer with Improved Resolution. *Rev*. *Sci*. *Instrum*. **1955,** *26* (12), 1150 - 1157.

16. Mamyrin, B. A.; Karataev, V. I.; Shmikk, D. V.; Zagulin, V. A. Mass Reflectron. New Nonmagnetic Time-of-flight High-resolution Mass Spectrometer. *Zh*. *Eksp*. *Teor*. *Fiz*. **1973,** *64* (1), 82-9.

17. Beck, G. Photodiode and Holder with 60 psec Response Time. *Rev*. *Sci*. *Instrum*. **1976,** *47*, 849-853.

18. Thomas, M. E.; Tayag, T. J. Refractive Index of Helium, Sulfur Hexafluoride, and Carbon Dioxide at 0.63299 μm as a Function of Temperature and Pressure. *Appl*. *Opt*. **1988,** *27* (16), 3317-18.

19. Cariou, J.; Luc, P. *Atlas du Spectre d'Absorption de la Molécule de Tellure entre 18,500 - 23,800 cm^{-1}*. CNRS: Paris, 1980.

20. Cariou, J.; Luc, P. *Atlas du Spectre d'Absorption de la Molécule Tellure, Partie 5: 21,100 - 23,800 cm^{-1}*. CNRS: Paris, 1980.

21. Gerstenkorn, S.; Luc, P. *Atlas du Spectre d'Absorption de la Molécule d'Iode entre 14,000-15,600 cm^{-1}*. CNRS: Paris, 1978.

22. Gerstenkorn, S.; Luc, P. *Atlas du Spectre d'Absorption de la Molécule d'Iode entre 14,800-20,000 cm^{-1}*. CNRS: Paris, 1978.

23. Gerstenkorn, S.; Verges, J.; Chevillard, J. *Atlas du Spectre d'Absorption de la Molécule d'Iode entre 11,000-14,000 cm^{-1}*. CNRS: Paris, 1982.

24. Moore, C. E. *Atomic Energy Levels*. Natl. Bur. Stand. U.S. Circ. No. 467 ed.; U. S. Government Printing Office: Washington, D. C., 1971.

25. Bevington, P. R. *Data Reduction and Error Analysis for the Physical Sciences*. McGraw-Hill: New York, 1969; p 336.

CHAPTER 3

THE $\tilde{A}\ ^2\Delta_{5/2} \leftarrow \tilde{X}\ ^2\Delta_{5/2}$ ELECTRONIC BAND SYSTEM OF NICKEL ACETYLIDE, NiCCH

Reproduced from Johnson, E. L.; Morse, M. D., The $\tilde{A}\ ^2\Delta_{5/2} \leftarrow \tilde{X}\ ^2\Delta_{5/2}$ electronic band system of nickel acetylide, NiCCH. *Mol. Phys.* **2015**, *113*, 2255-2266., with the permission of Taylor and Francis Publishing.

3.1 Introduction

Nickel and organonickel compounds are critically important as catalytic reagents in modern synthetic organic chemistry.[1] Probably the first example of the use of an organonickel reagent is the Mond process, which was developed in the 1890s and uses volatile nickel tetracarbonyl to purify nickel from impure nickel powder.[2] Another early example of the use of nickel in organic chemistry is Raney nickel, a powdered nickel-aluminum alloy that was developed in 1926 as a catalyst for the hydrogenation of vegetable oil.[3] More recently, nickel has been employed as a more cost-efficient replacement for palladium in the Heck reaction for the benzylation or arylation of alkenes.[4-6] These examples truly just scratch the surface of the uses of nickel in catalytic chemistry. Other examples include the Reppe synthesis of cyclooctatetraene,[7] the

Kumada coupling of organic halides with Grignard reagents,[8-9] and the Negishi cross-coupling reaction.[10] Nickel acetylides, especially those with the $Ni(C{\equiv}CR)_2L_2$ structure, are useful as catalysts in organic chemistry,[11] particularly in the polymerization of methyl methacrylate[12-14] and of alkynes.[15-16] In these catalysts, nickel is typically either zerovalent (Raney nickel and $Ni(CO)_4$) or divalent (as in $Ni(C{\equiv}CR)_2L_2$). Nevertheless, in order to obtain an improved understanding of the nickel-acetylide bond, we have undertaken a study of the electronic spectroscopy of NiCCH, where nickel is monovalent (Ni^+). This work complements and extends our previous studies of the transition metal acetylides CuCCH [17] and CrCCH.[18-19]

Prior to this work, neutralization-reionization mass spectrometric studies had proved that neutral NiCCH is physically stable as a chemically bound molecule with a lifetime greater than 1 μs.[20] Further, fragmentation patterns from the collision-induced dissociation measurements strongly suggested a linear NiCCH structure, rather than a vinylidene structure.[20] This result is confirmed in the present investigation.

Regardless of whether one considers the molecule to be ionic, as Ni^+ CCH^-, or covalent, as Ni-C≡C-H, the singly ligated nickel atom may be considered to have a valence of one and to have an open $3d^9$ subshell. Thus, NiCCH joins a long list of monoligated, monovalent nickel molecules that have been spectroscopically investigated by this group and others.[21-69] In order of increasing electronegativity of the ligand (provided on the Allred-Pauling[70] scale in parentheses), these previously studied species include NiAl (1.61),[21-22] NiCu (1.90),[23-26] NiH (2.20),[27-33] NiAu (2.54),[22, 34] NiI (2.66),[35-39] NiBr (2.96),[40-43] NiCl (3.16),[43-52] and NiF (3.98).[53-67] In addition to these diatomic species, NiCN has also been investigated.[68-69] Nickel acetylide is expected to be similar

to NiCN, as the group electronegativities of CN and CCH are similar, although the precise values of this quantity depend on the procedure employed in its estimation. Both ligands are also similar in having empty π^* orbitals that are available to receive nickel $d\pi$ electron density. In a recent computation and critical evaluation of group electronegativities, the electronegativities of CCH and CN are listed as 3.11 and 3.19 on the Pauling scale, respectively, placing NiCCH and NiCN on either side of NiCl in the ordered list above.[71]

The hole in the nickel $3d^9$ subshell in these molecules can be located in the $3d\sigma$, $3d\pi$, or $3d\delta$ orbitals, leading to $^2\Sigma^+$, $^2\Pi$, or $^2\Delta$ states. The spin-orbit interaction then causes the $^2\Pi$ and $^2\Delta$ states to split into $^2\Pi_{1/2}$, $^2\Pi_{3/2}$, $^2\Delta_{3/2}$, and $^2\Delta_{5/2}$ levels, and spin-orbit mixing between the $^2\Sigma^+$ and $^2\Pi_{1/2}$ states and between the $^2\Pi_{3/2}$ and $^2\Delta_{3/2}$ states causes the Λ value to become ill-defined in these states. It is only in the $^2\Delta_{5/2}$ state that Λ is expected to remain a good quantum number. Previous experiments have shown that the ground state for the systems with relatively electropositive ligands (NiAl through NiI, and NiCN) have $^2\Delta_{5/2}$ ground states while the more electronegative ligands cause NiBr, NiCl, and NiF to have ground states of mixed $^2\Pi$ and $^2\Delta$ character, with Ω=3/2. Theoretical investigations of the splitting of the $3d^9$ core in the field of a ligand have been provided by several research groups.[32, 72-74]

Section 3.2 describes the experimental methods used to investigate NiCCH, while Section 3.3 presents computational and experimental results. These are discussed and compared to related molecules in Section 3.4, and the most important conclusions from this work are summarized in Section 3.5.

3.2 Experimental

In the current work, nickel acetylide, NiCCH, was investigated using resonant two-photon ionization spectroscopy (R2PI). The instrument employed is identical to that used in previous studies.[17-19, 75-77] Molecular NiCCH is produced by focusing the third harmonic radiation from a Q-switched Nd:YAG laser (355 nm) onto a 1:1 nickel-gold sample at a point that is 1.3 cm upstream from the expansion orifice of a pulsed supersonic expansion of helium (40-60 psig backing pressure) that is seeded with 0.0025% acetylene. The NiAu sample was used in previous experiments,[22, 34] and was convenient for the present study; there is no reason why a pure nickel sample would not have worked equally well. The sample is rotated and translated to prevent holes from being drilled; this provides a relatively constant signal intensity. The products of the laser ablation process are entrained in the carrier gas and travel through a 1.3 cm long reaction zone prior to expansion through a 2 mm orifice into a vacuum. The supersonic expansion into the vacuum chamber cools the ablation products to a rotational temperature of approximately 6 K. The molecular beam is then roughly collimated by a 1 cm diameter skimmer and enters the Wiley-McLaren ion source of a reflectron time-of-flight mass spectrometer.[78-79] In the ion source, the molecular beam is exposed to tunable dye laser radiation that is counterpropagated along the beam path. Following a delay of about 20 ns, the molecules are exposed to the output radiation of an F_2 excimer laser (157 nm, 7.87 eV) that intersects the molecular beam at right angles. Any ions produced are accelerated in a static electric field into a time-of-flight tube, and are reflected down a second flight tube to a dual microchannel plate detector. The ion signal is preamplified, digitized, and the ion signals of interest are stored for subsequent analysis on a personal computer. The

entire experiment is repeated at a rate of 10 Hz.

Low-resolution spectra of ^{58}NiCCH (mass 83 Da) and ^{60}NiCCH (mass 85 Da) were recorded from 15400 cm^{-1} to 18800 cm^{-1}. To reveal the rotational structure of the observed bands, high-resolution scans were performed by inserting an air-spaced étalon into the oscillator cavity of the dye laser, which was then pressure scanned using SF_6. Calibration of the rotationally resolved bands was accomplished using two partial reflections of the dye laser light. One was directed through a cell containing gaseous I_2, and the transmission spectrum was recorded using a photodiode detector. The other was directed to a 0.22 cm^{-1} free spectral range étalon, and the transmission fringes were recorded. The spectra obtained were linearized using the transmission fringes and then calibrated using the I_2 atlas of Gerstenkorn and Luc.[80-81] Corrections were made to account for the error in the I_2 atlas, -0.0056 cm^{-1},[81] and for the Doppler shift experienced by the molecules as they approach the radiation source at the beam velocity of helium, 1.77 x 10^5 cm/s.[82] Combined, the two corrections amount to about 0.10 cm^{-1} for the bands examined here.

Along with high-resolution spectra, excited state lifetimes were also collected for selected bands by firing the ionization laser at the time of peak NiCCH signal intensity, while the dye laser was scanned in time as the $NiCCH^+$ ion signal was monitored. The resulting decay curves measure the number of NiCCH molecules that remain in states that are readily ionized as a function of time. The measured curves were fitted to an exponential decay model using the Levenberg-Marquardt nonlinear least-squares algorithm.[83] Three independent lifetime curves were collected and fitted for each band; the standard deviation of the three values is reported as the 1σ error limit.

3.3 Results

3.3.1 Computations on NiCCH

To aid in the assignment of the spectra, density functional calculations employing the B3LYP hybrid density functional method in combination with the aug-cc-pVTC Dunning correlation consistent basis set[84] were undertaken for the $^2\Sigma^+$, $^2\Pi$, and $^2\Delta$ states of NiCCH that arise from the $3d^9$ occupation on nickel. These were performed using the Gaussian 09W suite of programs.[85] At this level of theory, the $^2\Delta$ state was found to be the ground state. The $^2\Sigma^+$ and $^2\Pi$ states are calculated to lie 384 and 1282 cm^{-1} above the $^2\Delta$ state, respectively. Calculated energies, bond lengths, vibrational frequencies, and dipole moments of the three low-lying states are provided in Table 3.1. The vibrational frequencies deduced from the spectra that are described below are also provided for comparison.

When a group of states are as closely spaced as these three states, spin-orbit interaction can be important in determining the absolute ordering of the states. If we treat the partially occupied orbitals as having pure Ni 3d character, it is straightforward to approximate the effects of spin-orbit interaction using the spin-orbit Hamiltonian matrices provided by Spain and Morse.[72] For the $^2\Delta_{5/2}$ level, which undergoes no spin-orbit coupling with the other states, the energy is given by

$$E(^2\Delta_{5/2}) = T(^2\Delta) - \zeta_{3d}(Ni), \qquad (3.1)$$

where $T(^2\Delta)$ is the term energy of the $^2\Delta$ state, as obtained from the computational results, and $\zeta_{3d}(Ni)$ is the atomic spin-orbit parameter for the 3d orbitals of nickel, which

Table 3.1 Computed and measured results on ^{58}NiCCH[a]

Property	$^2\Delta$	$^2\Sigma^+$	$^2\Pi$	$\tilde{X}\ ^2\Delta$ (exp)	$\tilde{A}\ ^2\Delta$ (exp)
Energy[b]	0	383.86	1282.45	0	15940.041(56
r(Ni-C) [c]	1.8312	1.8502	1.8550		
r(C≡C) [c]	1.2121	1.2133	1.2139		
r(C-H) [c]	1.0625	1.0624	1.0628		
ν_1 (σ^+, C-H	3451.09	3451.18	3447.37		
ν_2 (σ^+, C≡C	2080.58	2071.66	2053.08		2001.9(1.4)
ν_3 (σ^+, Ni-C	496.94	476.63	474.17		458.4(1.0)
ν_4 (π, C≡C-H bend)[b]	675.02	667.63	652.30 712.56		636.5(0.9)
ν_5 (π, Ni-C≡C bend)[b]	225.04	207.99	208.72 222.22	209.5(0.6)	221.2(2.2)
dipole moment	3.474 D	3.910 D	3.454 D		

[a] As described in the text, all computations were done using the Gaussian 09W suite of programs. The molecule was found to be linear in all calculations, although the different frequencies for the bending modes in the $^2\Pi$ term indicates that a Renner-Teller effect is expected. See text for details.

[b] Given in cm^{-1} units.

[c] Given in Å units.

is tabulated as 670 cm^{-1}.[86] For the remaining levels, states with the same value of Ω are mixed by the spin-orbit interaction, leading to Hamiltonian matrices that must be diagonalized to obtain the final predicted energy levels. These matrices are

$$\begin{pmatrix} T(\,^2\Pi) - \frac{\zeta_{3d}(Ni)}{2} & -\zeta_{3d}(Ni) \\ -\zeta_{3d}(Ni) & T(\,^2\Delta) + \zeta_{3d}(Ni) \end{pmatrix} \text{ for } \Omega = \tfrac{3}{2} \text{ levels} \qquad (3.2)$$

and

$$\begin{pmatrix} T(\,^2\Sigma^+) & -\sqrt{\frac{3}{2}}\,\zeta_{3d}(Ni) \\ -\sqrt{\frac{3}{2}}\,\zeta_{3d}(Ni) & T(\,^2\Pi) + \frac{\zeta_{3d}(Ni)}{2} \end{pmatrix} \text{ for } \Omega = \tfrac{1}{2} \text{ levels.} \qquad (3.3)$$

Using the term energies obtained from the B3LYP calculations, in combination with the value ζ_{3d}(Ni) = 670 cm^{-1}, we obtain a final predicted set of low-lying states in NiCCH as given in Table 3.2. These bear a striking similarity to the known low-lying states in the closely related NiCN molecule, also listed in Table 3.2. The close correspondence between the calculated levels of NiCCH and the measured levels of NiCN shows that the two molecules are electronically very similar.

From the point of view of analyzing the spectra obtained in this study, the vibrational frequencies calculated in NiCCH are particularly important. As was found in our studies of CuCCH[17] and CrCCH,[18] the calculated vibrational frequencies are well separated and are expected to be readily distinguished in the spectra. This is very helpful for making vibronic assignments.

Table 3.2 Calculated spin-orbit levels of the $3d^9$ states of NiCCH, compared to measured states of NiCN.

Calculated states of NiCCH			Measured states of NiCN[a]	
Ω	Energy (cm^{-1})	Composition	Designation	Energy(cm^{-1})
5/2	0	100% $^2\Delta_{5/2}$	$^2\Delta_{5/2}$	0
1/2	644	80% $^2\Sigma^+$; 20% $^2\Pi_{1/2}$		
3/2	795	60% $^2\Delta_{3/2}$; 40% $^2\Pi_{3/2}$	$^2\Delta_{3/2}$	830
3/2	2163	60% $^2\Pi_{3/2}$; 40% $^2\Delta_{3/2}$	$^2\Pi_{3/2}$	2238
1/2	2697	80% $^2\Pi_{1/2}$; 20% $^2\Sigma^+$		

[a] From Reference [68].

3.3.2 Vibronic Spectrum

The vibronically resolved spectrum of ^{58}NiCCH is displayed in Figure 3.1, and the locations of the observed bands are listed in Table 3.2. The spectrum is dominated by one electronic band system, designated as the $\tilde{A} \leftarrow \tilde{X}$ system, although a few additional features are observed. The most intense feature in the spectrum, near 15910 cm^{-1}, is assigned as the 0_0^0 band based on isotopic shift measurements (see below). A series of bands spaced by roughly 450 cm^{-1} extends toward higher wavenumbers. Based on the correspondence between this value, the computed results for the Ni-CCH stretching mode, and the excited state frequencies of the Cr-CCH (425.6 cm^{-1})[18] and Cu-CCH (479, 466.8, and 462 cm^{-1})[17] stretching modes, the progression is assigned to mode ν_3, the Ni-CCH stretch. A corresponding series of weaker features, shifted to lower wavenumbers by 209.5 cm^{-1}, are assigned as hot bands arising from ground state molecules in which the Ni-C≡C bending mode (ν_5) is singly excited. Because this mode carries one unit of vibrational angular momentum, transitions to levels lacking vibrational angular momentum (as is the case here) have vanishing Franck-Condon factors. Thus, these bands have a different source of oscillator strength than the main progression, gaining intensity by vibronic coupling with another state.

It proved more difficult than expected to measure accurate isotope shifts between the more abundant isotopologue, ^{58}NiCCH (83 Da, 66.75%), and the less abundant one, ^{60}NiCCH (85 Da, 25.53%), because of large fluctuating background signals at the mass of ^{60}NiCCH. These large fluctuating signals also appeared at a significantly reduced intensity in mass 87 Da, leading us to suspect that they may be due to AlNi molecules, for which the abundant species have masses of 85 (68.3% abundance) and 87 Da (26.1%

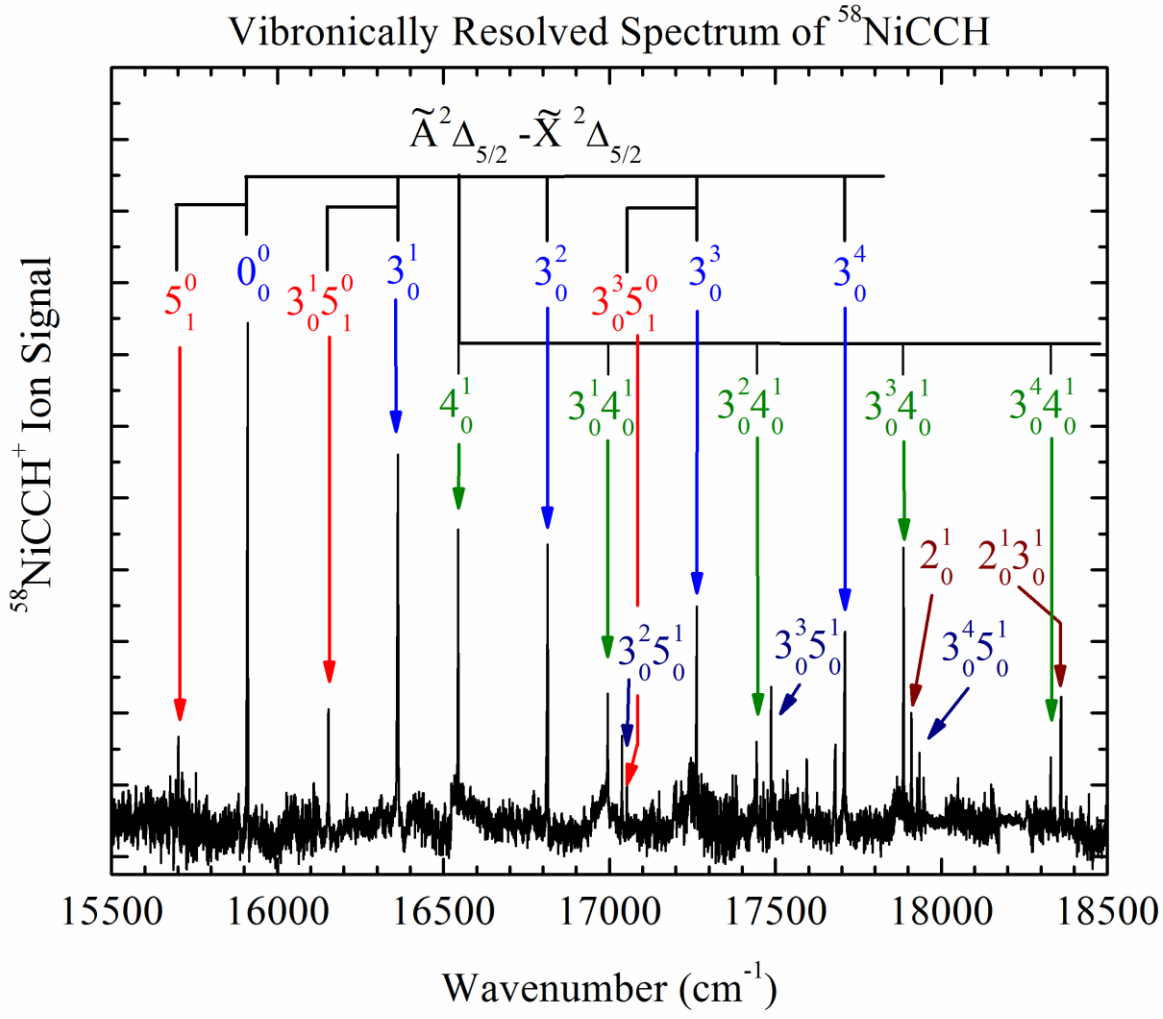

Figure 3.1 Vibronically resolved spectrum of ^{58}NiCCH, showing the $\tilde{A}\ ^2\Delta_{5/2} \leftarrow \tilde{X}\ ^2\Delta_{5/2}$ band system.

abundance). This species has an ionization energy of 6.95±0.09 eV,[21] making it readily one-photon ionized by the F_2 excimer laser (7.89 eV), so even small amounts of AlNi produced via Al impurities can easily overwhelm the signal due to ^{60}NiCCH. The fact that these features became much more intense when we polished the sample with Al_2O_3 sandpaper reinforces this assignment. Apart from the rotationally resolved work on the $\tilde{A} - \tilde{X}\ 3_0^1$ band, all of the isotope shift measurements were obtained from low-resolution scans conducted prior to polishing the sample.

To verify the vibrational assignment, the molecule was treated as a pseudodiatomic, and the isotope shift was modeled by fitting the progression in the ν_3 mode for the ^{58}NiCCH isotopologue to the diatomic formula,

$$\nu_{v'-0} = T_0 + \upsilon' \omega_e' - (\upsilon'^2 + \upsilon') \omega_e' x_e' \ . \quad (3.4)$$

The fitted molecular constants ω_e' and $\omega_e' x_e'$ could then be used to calculate the predicted isotope shift using the formula[87]

$$\nu(^{58}\text{NiCCH}) - \nu(^{60}\text{NiCCH}) = (\rho\text{-}1)[\omega_e'(\upsilon'+½) - \omega_e''(½)] - (\rho^2\text{-}1)[\omega_e' x_e'(\upsilon'+½)^2 - \omega_e'' x_e''(½)^2], \quad (3.5)$$

where the dimensionless parameter, ρ, is given as $\rho = \sqrt{\frac{\mu(^{60}Ni-CCH)}{\mu(^{58}Ni-CCH)}} = 1.00506$. By treating equations (3.1) and (3.2) as functions of a continuous parameter, υ′, it was possible to plot the predicted isotope shift, $\nu(^{58}\text{NiCCH}) - \nu(^{60}\text{NiCCH})$, as a function of the band frequency, $\nu_{v'-0}$, for various assignments of the bands. The resulting curves were then compared to the measured isotope shifts to identify the correct vibrational

numbering. To do so, the ground state vibrational frequency, ω_e'', was taken as 497 cm^{-1} from the DFT calculations using the B3LYP/ cc-pVTZ basis set, and the anharmonicity, $\omega_e''x_e''$, was neglected. The result, displayed in Figure 3.2, shows clearly that the 15910 cm^{-1} band is the 0_0^0 band. This assignment gives a pseudodiatomic vibrational frequency of 454.6 ± 0.4 cm^{-1} and an anharmonicity of 0.98 ± 0.07 cm^{-1} in the excited electronic state.

A weaker series of bands, occurring at 16544.1, 16994.8, 17443.4, 17886.2, and 18329.1 cm^{-1}, also form a progression with a pseudodiatomic vibrational frequency of 453.8 ± 1.3 cm^{-1} and an anharmonicity of 1.5 ± 0.3 cm^{-1}. A plot of the measured isotope shifts is displayed in Figure 3.3, confirming that the first of these bands, at 16544.1 cm^{-1}, has no quanta of the Ni-CCH vibrational mode excited. Although it is possible that these features could correspond to a different excited state of NiCCH, the similarity between the vibrational frequency of this progression (453.8 cm^{-1}) and that of the $\tilde{A}$ state (454.6 cm^{-1}) strongly suggests that the new progression also corresponds to a set of vibrational levels in the $\tilde{A}$ state. The first band in this progression is found 634.0 cm^{-1} to the blue of the $\tilde{A} - \tilde{X}\ 0_0^0$ band, which is in reasonably good agreement with the calculated frequencies of the C≡C-H bending mode, ν_4. Accordingly, we assign these features to the 4_0^1, $3_0^1 4_0^1$, $3_0^2 4_0^1$, $3_0^3 4_0^1$, and $3_0^4 4_0^1$ bands of the $\tilde{A} - \tilde{X}$ system.

As demonstrated in rotationally resolved studies below, the main progression of 3_0^n bands are Ω'=5/2 ← Ω''=5/2 parallel transitions while these $3_0^n 4_0^1$ features have one unit of vibrational angular momentum in the upper state due to the excitation of the π-symmetry ν_4 mode, making them perpendicular transitions. Defining the quantum number P as the combined electronic and vibrational angular momentum around the axis, given

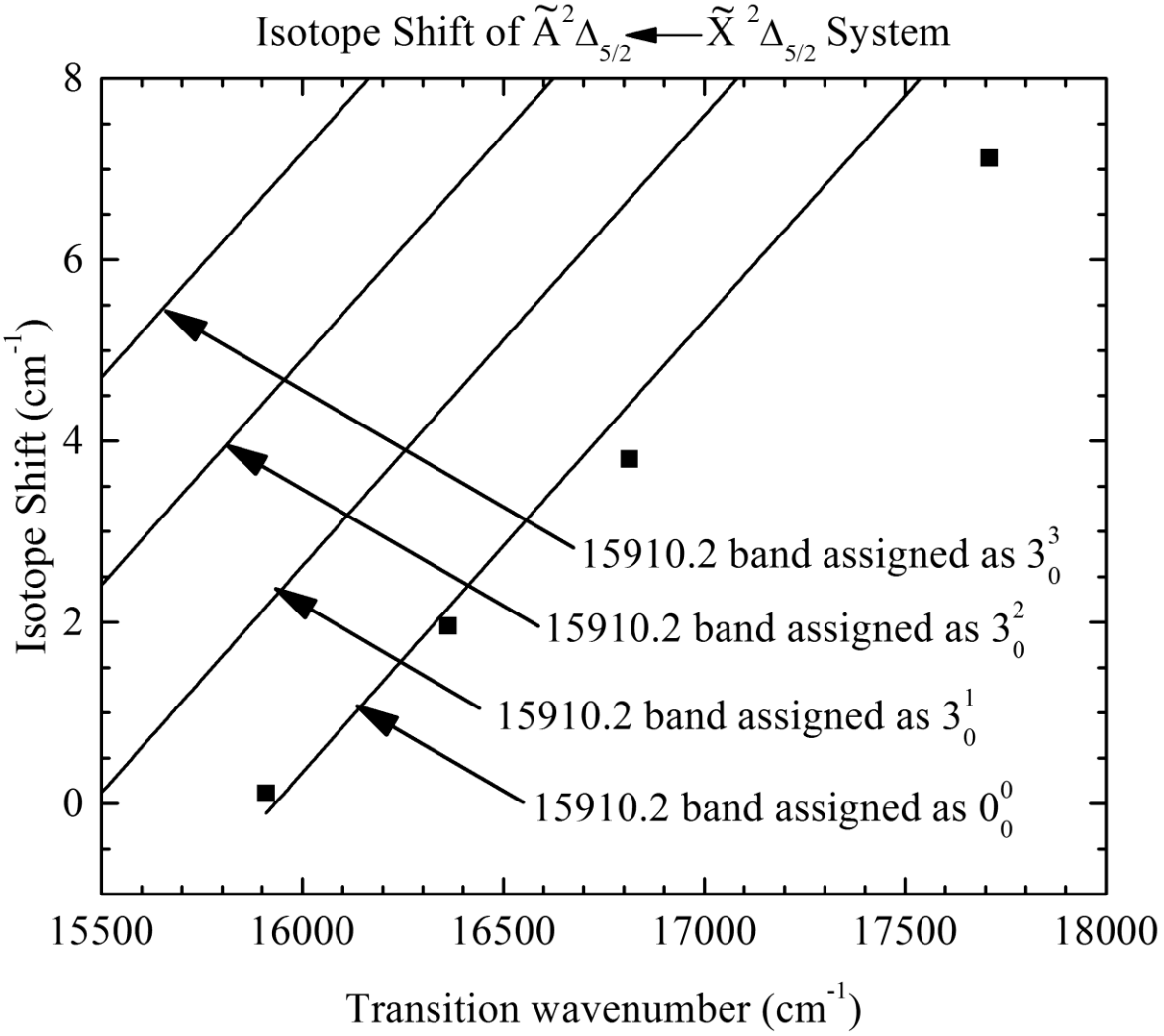

Figure 3.2 Isotope shift of the bands of the $\tilde{A}\,^2\Delta_{5/2} \leftarrow \tilde{X}\,^2\Delta_{5/2}$ band system, demonstrating that the 15 910 cm^{-1} band is the 0_0^0 band of this system.

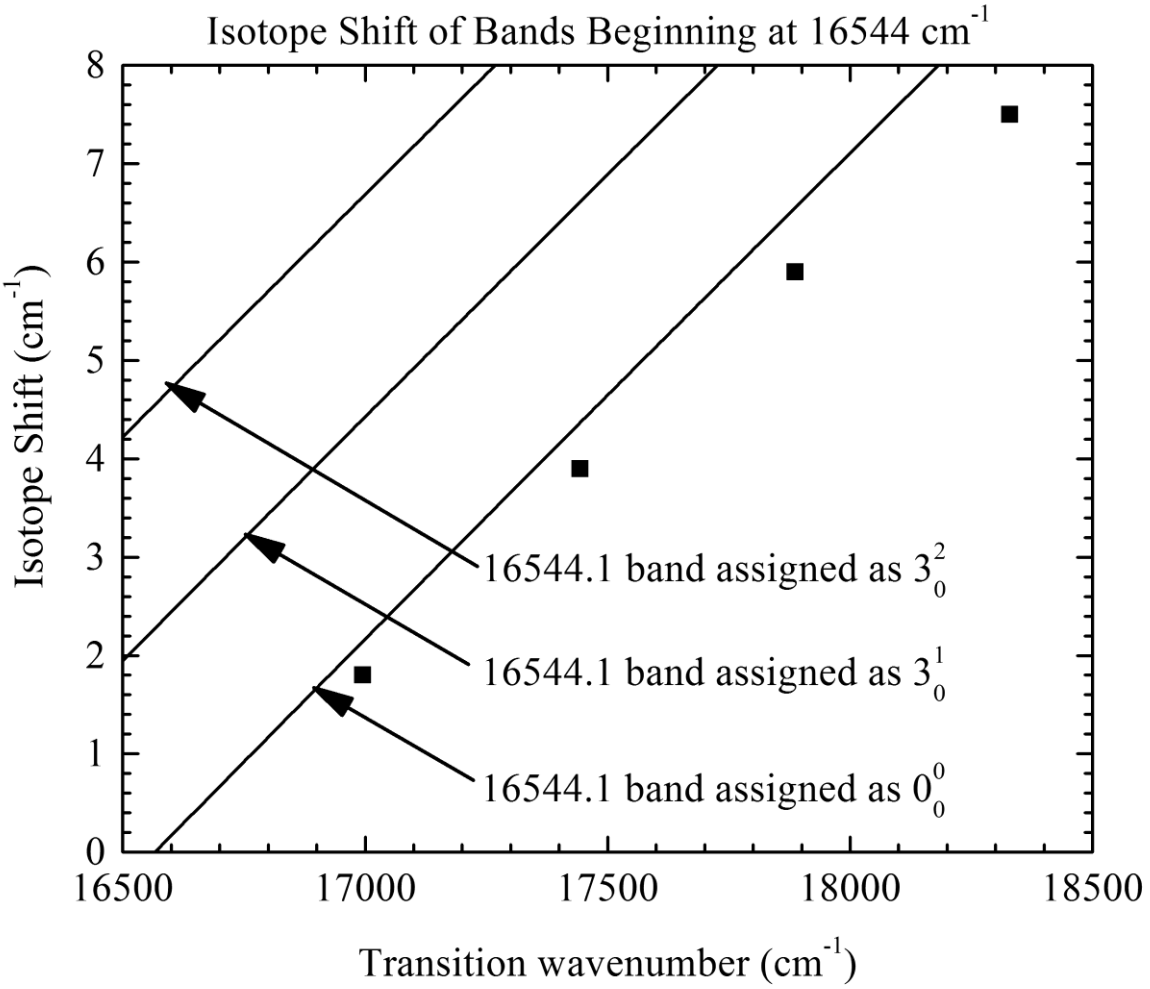

Figure 3.3 Isotope shift of the weak bands beginning at 16 544.1 cm^{-1}. This plot demonstrates that these bands form a progression, and that the 16 544.1 cm^{-1} band has no quanta excited in the Ni-CCH stretching mode, ν_3.

by P ≡ Λ + ℓ + Σ = Ω + ℓ, the $3_0^n 4_0^1$ features are P′=7/2 ← P″=Ω″=5/2 transitions. The other expected set of vibronic levels arising from coupling of the ν_4 bending mode (ℓ = ±1) to the electronic angular momentum of Ω′=5/2, giving an upper state P′= 3/2, is not observed. This implies that the $3_0^n 4_0^1$ progression gains intensity through vibronic coupling with an electronic state with Ω′=7/2, but that vibronic coupling to states with Ω′=3/2 is much weaker, preventing the observation of the P′=3/2 set of vibronic levels.

Another vibrational progression is evident in the data in the weak bands at 17037.8, 17487.0, and 17934.1 cm^{-1}. Fitting these features as the 0_0^0, 3_0^1, and 3_0^2 bands of a new band system yields a pseudodiatomic vibrational frequency and anharmonicity of 451.4 cm^{-1} and 1.07 cm^{-1}, again quite close to that found for the $\tilde{A} - \tilde{X}$ system. Rotational resolution of the weak feature at 17037.8 cm^{-1} shows that this transition has a symmetry of P′=7/2 ← P″=Ω″=5/2. Again, these features could arise from a totally different excited state, but the close similarity in the pseudodiatomic vibrational frequency is evidence that this progression also belongs to the $\tilde{A} - \tilde{X}$ system. These three bands are found 224.5 ± 0.6 cm^{-1} to the blue of the 3_0^2, 3_0^3, and 3_0^4 bands, respectively, consistent with an assignment as combination bands involving one unit of the Ni-C≡C π-bending mode, ν_5. This assignment shows a slight stiffening of the Ni-C≡C bending mode upon electronic excitation, from a frequency of ν_5'' = 209.5 cm^{-1} to ν_5' = 224.5 cm^{-1}, which is not unreasonable. As a comparison, excitation of CuCCH from the $\tilde{X}^1\Sigma^+$ ground state to the $\tilde{A}\ ^1\Sigma^+$ and $\tilde{B}\ ^1\Pi$ states increased the frequency of the ν_5 Cu-C≡C bending mode from 242.9 cm^{-1} to 284.4 and 267 cm^{-1}, respectively.[17] Therefore, these bands are assigned as the $3_0^2 5_0^1$, $3_0^3 5_0^1$, and $3_0^4 5_0^1$ bands of the $\tilde{A} - \tilde{X}$ system. Again, the combination of one unit of vibrational angular momentum (ℓ = ±1) from ν_5' with the

upper state Ω′=5/2 can lead to either P′=3/2 or P′=7/2, but the bands with P′=7/2 show significantly greater oscillator strength, and are observed. The bands with P′=3/2 are presumably too weak to observe in our experiments. This is again presumably due to vibronic coupling with an excited electronic state with Ω′=7/2.

Two features are found at 17910.5 cm^{-1} and 18360.9 cm^{-1} with isotope shifts of -0.1 and 2.0 cm^{-1}, respectively. These are consistent with transitions in which mode 3, the Ni-C stretching mode, has no excitation and one unit of excitation, respectively. These could correspond to the 0_0^0 and 3_0^1 bands of a completely different band system, but their separation, 450.4 cm^{-1}, is again close to that found for other ν_3 excitations in the $\tilde{A}$ state. These bands are separated from the 0_0^0 and 3_0^1 bands by 2000.4 and 1998.0 cm^{-1}, respectively. These intervals are close to what might be expected for excitation of ν_2, the C≡C stretch. Because of the close match between the 450.4 cm^{-1} interval found here and the other ν_3 intervals found in the spectrum, we assign these features to the 2_0^1 and $2_0^1 3_0^1$ bands of the $\tilde{A} - \tilde{X}$ system.

In addition to these 18 bands that are assigned to the $\tilde{A} - \tilde{X}$ system, 5 additional bands were observed that could not be classified into this system. These are also listed in Table 3.3. These weak features likely correspond to excitations to other electronic states that have lower oscillator strength. A large number of excited electronic states are expected for NiCCH in this region, arising from the $3d^8 4s^1$, ^2F and ^4F states of Ni^+ interacting with CCH^-. Although one of these bands was rotationally resolved, we have little additional information about these features. They were generally too weak to warrant further study at this time.

The vibronic bands that are assigned to the $\tilde{A}\ ^2\Delta_{5/2} - \tilde{X}\ ^2\Delta_{5/2}$ system were fitted

to the anharmonic energy expression

$$\nu = T_0 - \omega_2 \mathrm{v}_2 + \omega_2{}' v_2' + \omega_3' v_3' + \omega_4{}' v_4' + \omega_5' v_5' + x_{33}'(v_3{}'^2 + v_3') + x_{23}'\left(v_2' v_3' + \frac{v_2'+v_3'}{2}\right) + x_{34}'\left(v_3' v_4' + \frac{v_3'+v_4'}{2}\right) + x_{35}'\left(v_3' v_5' + \frac{v_3'+v_5'}{2}\right). \quad (3.6)$$

The fitted wavenumbers and residuals in the fit are given in Table 3.3. The resulting molecular constants are provided, along with their 1σ error limits, in Table 3.4.

3.3.3 Rotationally Resolved Spectra of NiCCH

A rotationally resolved scan over the 3_0^1 band of the $\tilde{A} \leftarrow \tilde{X}$ system is displayed in Figure 3.4, along with a negative-going simulation of the spectrum, computed using the PGopher program,[88] in blue. The band shows obvious R, Q, and P branches, with a band head in the R branch, indicating that the rotational constant decreases upon electronic excitation, corresponding to a lengthening of the Ni-C bond. In addition, the large gap between the first R and P lines indicates large Ω values in both the upper and lower states. Analysis of the spectrum shows that it arises from an Ω′ = 5/2 ← Ω″ = 5/2 transition, with first lines of R(2.5), Q(2.5), and P(3.5). Given that the only state with Ω″ = 5/2 that arises from the d^9 configuration is the $^2\Delta_{5/2}$ state, this spectrum proves that the ground state is of $^2\Delta_{5/2}$ symmetry. As should be expected, the ground state of NiCCH is electronically analogous to that of the isoelectronic molecule, NiCN.[68-69] This is also consistent with the B3LYP/aug-cc-pVTZ calculations.

The decay lifetime of the $\tilde{A}$ state, measured for various vibronic levels, varies in the range from 0.72 to 1.8 μs. In a polyatomic molecule such as NiCCH, the decay

Table 3.3 Bands measured for ^{58}NiCCH

Band	Measured ν_0 (cm^{-1})	Fitted ν_0 (cm^{-1})	Residual in fit (cm^{-1})	Isotope shift $\nu(^{58}NiCCH)-\nu(^{60}NiCCH)$ (cm^{-1})	B′ (cm^{-1})	P′	τ (μs)
$\tilde{A}-\tilde{X}\,5_1^0$	15701.2[b]	15701.531	0.669[d]				
$\tilde{A}-\tilde{X}\,0_0^0$	15910.1[b]	15910.041	0.059[d]	0.1			0.725(15)[c]
$\tilde{A}-\tilde{X}\,3_0^1$	16153.6[b]	16153.795	-0.195[d]	1.7			0.739(74)
$\tilde{A}-\tilde{X}\,3_0^1$	16362.8830(27)[c]	16363.305	-0.422[d]	1.96	0.12931(10)[c]	5/2	0.802(18)[c]
$\tilde{A}-\tilde{X}\,4_0^1$	16544.1[b]	16544.817	-0.717[d]				
$\tilde{A}-\tilde{X}\,3_0^2$	16813.8[b]	16814.152	-0.352[d]	3.8			0.820(47)[c]
$\tilde{A}-\tilde{X}\,3_0^1 4_0^1$	16994.7834(27)[c]	16994.578	0.205[d]	1.8	0.12878(11)[c]	7/2	1.243(29)[c]
$\tilde{A}-\tilde{X}\,3_0^2 5_0^1$	17037.7539(30)[c]	17037.709	0.045[d]	1.9	0.12893(8)[c]	7/2	1.456(63)[c]
$\tilde{A}-\tilde{X}\,3_0^3$	17052.6[b]	17053.074	-0.474[d]				
$\tilde{A}-\tilde{X}\,3_0^3$	17262.7[b]	17262.584	0.116[d]	5.9			
U[a]	17437.2[b]						
$\tilde{A}-\tilde{X}\,3_0^2$	17443.4[b]	17441.923	1.477[d]	3.9			
$\tilde{A}-\tilde{X}\,3_0^3$	17487.0[b]	17487.090	-0.090[d]	4.0			1.74(19)
U[a]	17594.2704(68)[c]				0.12820(14)[c]	5/2	7.98(1.08)[c]
U[a]	17680.3[b]			7.1			18.7(1.2)
$\tilde{A}-\tilde{X}\,3_0^4$	17709.2[b]	17708.601	0.599[d]	7.1			
$\tilde{A}-\tilde{X}\,3_0^3 4_0^1$	17886.1530(90)[c]	17886.852	-0.699[d]	5.9	0.12869(14)[c]	7/2	
$\tilde{A}\,2_0^1$	17910.5[b]	17910.500	0.000[d]	-0.1			
U[a]	17927.1[b]						

Table 3.3 Continued

$\tilde{A} - \tilde{X}\ 3_0^4 5_0^1$	17934.1[b]	17934.055	0.045[d]				
U[a]	17946.1[b]						
$\tilde{A} - \tilde{X}\ 3_0^4 4_0^1$	18329.1[b]	18329.365	-0.265[d]	7.5			
$\tilde{A} - \tilde{X}\ 2_0^1 3_0^1$	18360.9[b]	18360.900	0.000[d]	2.0			

[a] Unidentified band

[b] Estimated band origin location, measured in low resolution, expected accuracy ± 1 cm^{-1}.

[c] Error limits (1σ) are provided in parentheses, in units of the last digits quoted.

[d] Residual is defined as measured value minus fitted value. The least-squares fit of the measured vibronic levels to equation (3.3) provides the values listed in Table 3.4.

Table 3.4 Fitted vibrational constants for the $\tilde{A}\ ^2\Delta_{5/2} \leftarrow \tilde{X}\ ^2\Delta_{5/2}$ system of NiCCH.

Constant	Value (cm^{-1})	Constant	Value (cm^{-1})
ν_0	15940.041 ± 0.561	ω_5'	221.184 ± 2.299
ω_5''	209.510 ± 0.576	x_{33}'	-1.208 ± 0.132
ω_2'	2001.891 ± 1.405	x_{23}'	-2.864 ± 1.160
ω_3'	458.388 ± 1.019	x_{34}'	-3.503 ± 0.316
ω_4'	636.528 ± 0.928	x_{35}'	0.949 ± 0.651

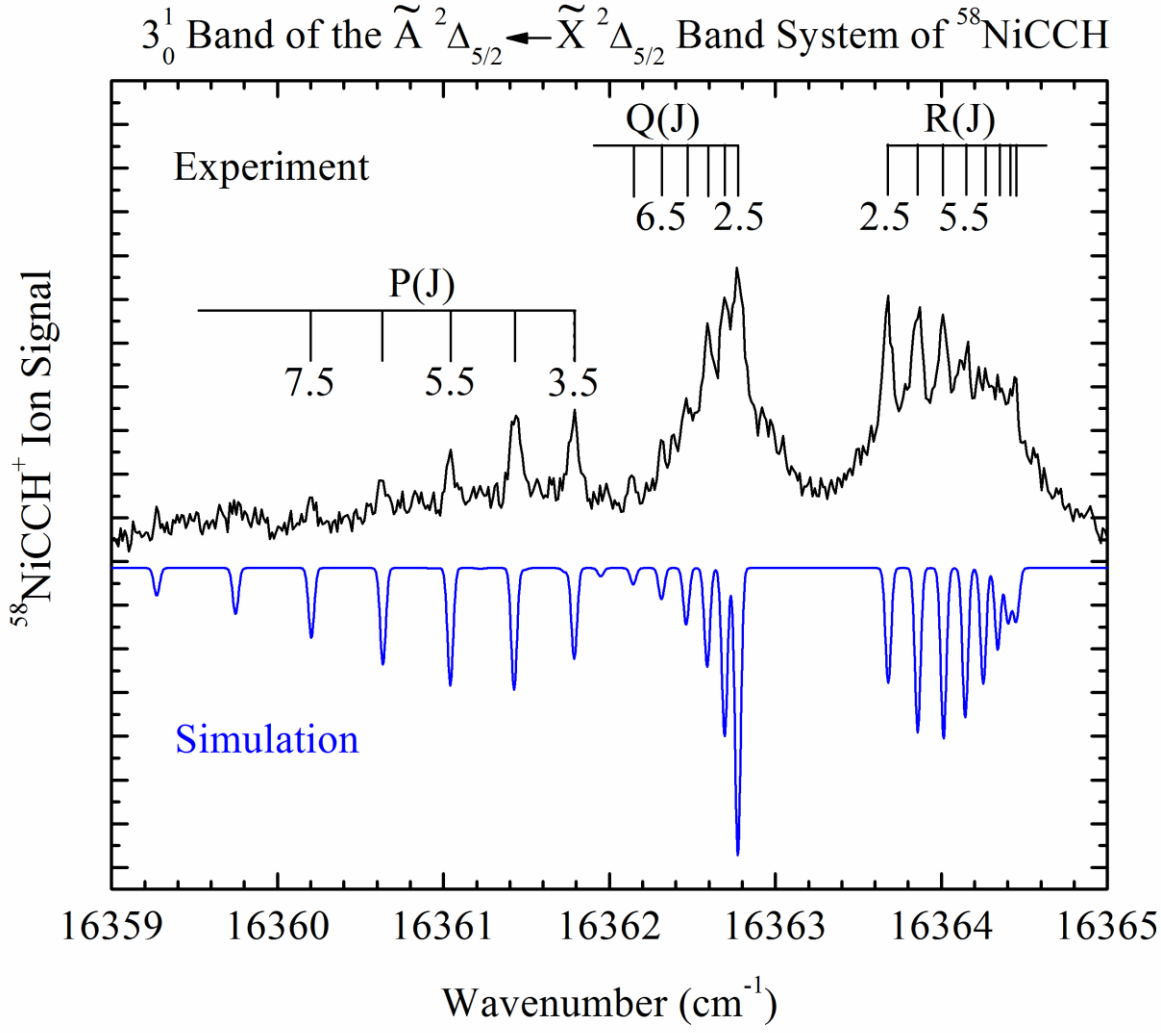

Figure 3.4 Rotationally resolved scan over the 3_0^1 band of the $\tilde{A}\ ^2\Delta_{5/2} \leftarrow \tilde{X}\ ^2\Delta_{5/2}$ band system. The first lines prove that both upper and lower states have Ω=5/2.

process could include nonradiative decay mechanisms in addition to fluorescence. However, under the collision-free conditions of the experiment, nonradiative decay mechanisms would produce a vibrationally hot NiCCH molecule in a lower electronic state; the total energy would be conserved. It is possible that the molecule would remain ionizable using the F_2 laser, but with reduced efficiency. This could lead to a bi-exponential decay curve, with the initial depopulation of the pumped state showing a rapid decay, followed by a slower decay as the nonradiatively populated state decays further. When all of the excitation energy is degraded into vibrational motion on the ground electronic state, poor Franck-Condon factors would likely prevent efficient ionization, giving only background signal levels. For aromatic organic molecules with rapid singlet to triplet intersystem crossing, followed by a slower triplet to ground state singlet intersystem crossing process, this process has been observed. The time-delayed resonant two-photon ionization method has been used to measure the vibrationally excited triplet state lifetime as a function of vibrational energy content.[89-90]

We believe that the measured excited state lifetimes found for NiCCH are true fluorescence lifetimes, without complications due to nonradiative decay. An example of the measured lifetime and the quality of the fit is given in Figure 3.5, which displays no evidence of biexponential behavior. In addition, the measured lifetimes (0.72 to 1.8 μs, depending on vibronic level; 8.0 μs for a level that belongs to a different electronic state) are comparable to those found for diatomic nickel species, where the density of states is certainly inadequate for radiationless decay under collision-free conditions. Examples include molecules whose lifetimes have been measured in the ranges 3.6 to over 40 μs(NiCu, with the longest lifetimes corresponding to quartet states),[23-24] 6 to 10 μs

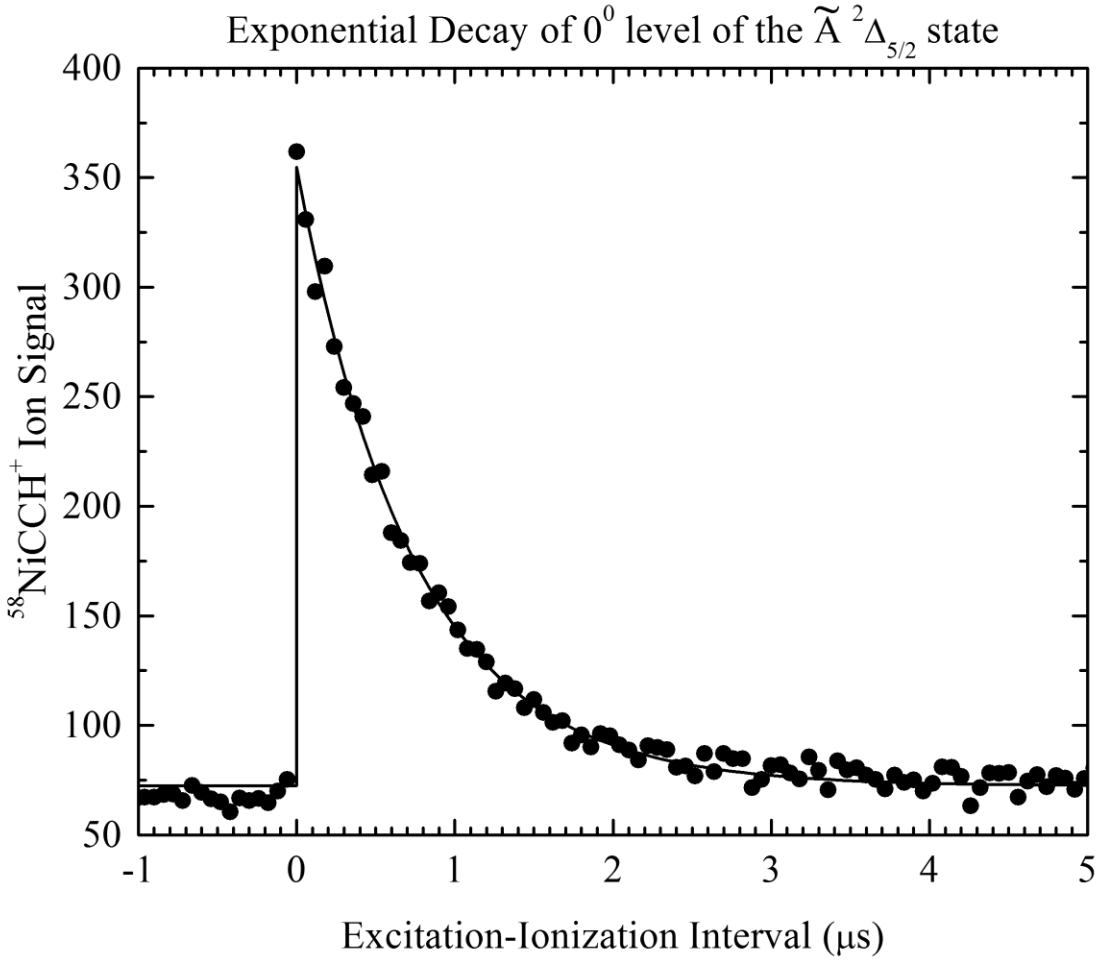

Figure 3.5 Exponential decay of the 0^0 level of the $\tilde{A}\ ^2\Delta_{5/2}$ state, measured by the time-delayed resonant two-photon ionization method. The fit of this decay curve gives $\tau = 0.730$ μs; combined with two other measurements, a value of $\tau = 0.725 \pm 0.015$ μs is obtained.

(NiAu),[34] 0.17 to 10 μs (NiSi),[91] and 0.07 to 0.6 μs (NiC),[92] respectively. It should be noted that the transitions in these diatomic nickel species (and in NiCCH) are primarily 3d ← 3d or 4s ← 3d excitations that are forbidden in the atom, but become allowed through mixing with 4p orbitals in the molecules. As a result, fully allowed excitations in these molecules tend to have lifetimes on the order of 500 ns to 2 μs. Because the 4p orbitals lie significantly above the 3d or 4s orbitals, there is a strong correlation of fluorescence lifetime with the excitation energy of the band system, with higher energy excited states generally having significantly shorter lifetimes. This is due to the greater contribution of 4p character in the higher energy states, along with the shortening of the lifetimes by the ν^3 factor that appears in the Einstein A coefficient.

Given that the low-lying electronic states are all doublets arising from the $3d^9$ configuration on the nickel core, the ~1 μs fluorescence lifetime establishes that the upper state is primarily doublet in character. Doublet states that have $\Omega'=5/2$ are $^2\Delta_{5/2}$ and $^2\Phi_{5/2,}$ but a $^2\Phi_{5/2} \leftarrow \tilde{X}\ ^2\Delta_{5/2}$ transition is forbidden by the $\Delta\Sigma=0$ selection rule. Therefore, the upper state is assigned as a $^2\Delta_{5/2}$ state. The band system is assigned as the $\tilde{A}\ ^2\Delta_{5/2} \leftarrow \tilde{X}\ ^2\Delta_{5/2}$ system.

Figure 3.6 displays the rotationally resolved scan over the $3_0^1 4_0^1$ band near 16695 cm^{-1}. The intense R branch shows that the quantum number P increases in this excitation, and the first lines demonstrate that $P'=7/2$, $P''=\Omega''=5/2$. The upper state P' value includes the vibrational angular momentum of the ν_4 C≡C-H bending mode and provides strong evidence that the band has been properly assigned as having one excitation of a bending mode. A rotationally resolved scan over the $3_0^3 4_0^1$ band near 17886 cm^{-1} displays the same intensity pattern and first lines, as expected, so it is not reproduced here. The scan,

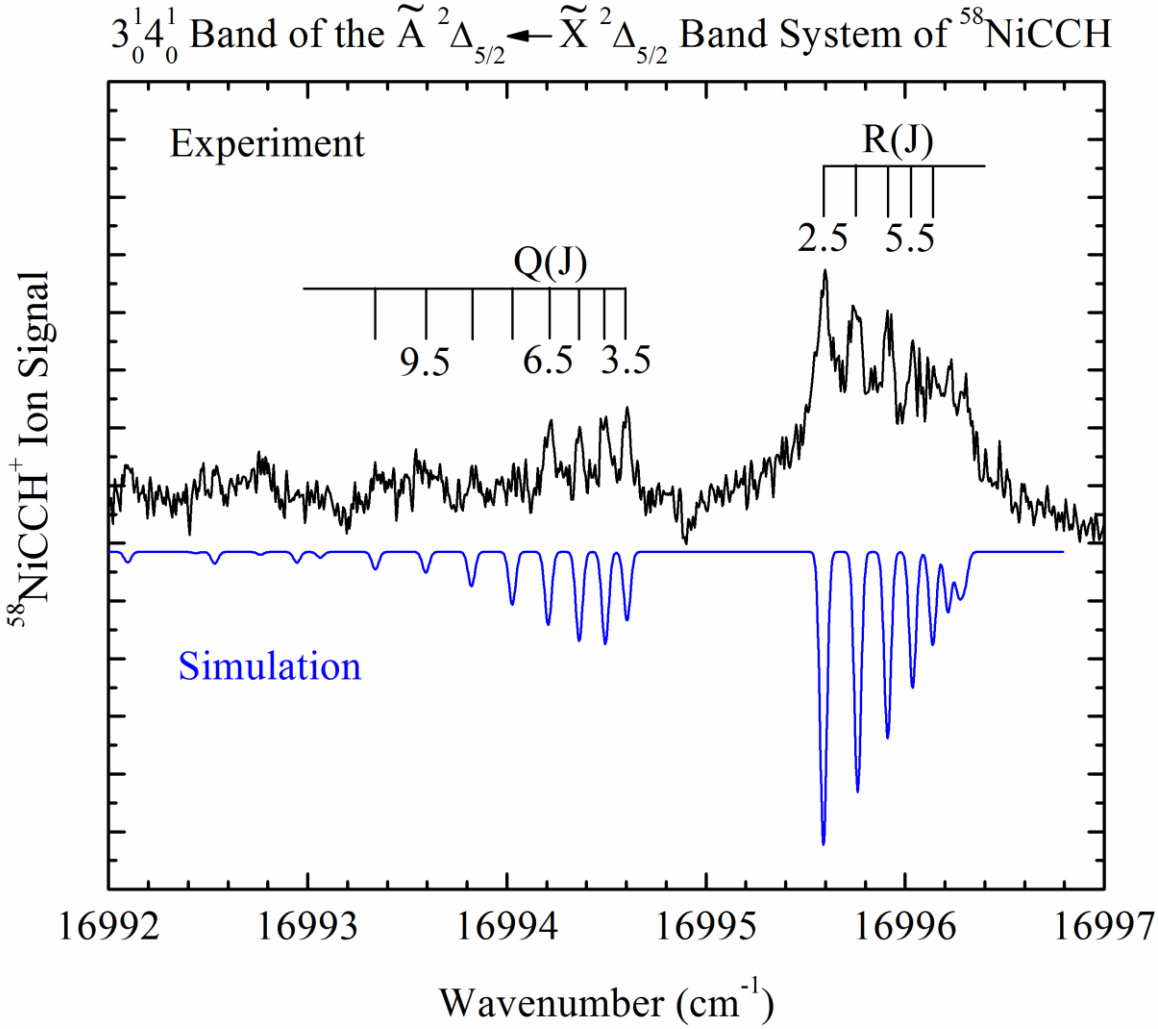

Figure 3.6 Rotationally resolved scan over the $3_0^1 4_0^1$ band of the $\tilde{A}\ ^2\Delta_{5/2} \leftarrow \tilde{X}\ ^2\Delta_{5/2}$ band system. The intense R branch is evidence that $\Delta\Omega = 1$ in this band, and the first lines of R(2.5) and Q(3.5) prove that Ω''=5/2, P'=7/2.

along with a simulated spectrum, is available in Appendix A.

Figure 3.7 displays a scan over the $3_0^2 5_0^1$ band near 17038 cm^{-1}, which is similar in appearance to the $3_0^1 4_0^1$ band shown in Figure 3.6. Again, the band is clearly a P′=7/2 ← Ω″=5/2 band, confirming that a bending mode has been excited in this transition. In this case, it is the low-frequency Ni-C≡C ν_5 mode that is excited in combination with two quanta of the Ni-C stretching vibration.

The remaining band that was rotationally resolved is a band near 17594 cm^{-1} that has a much longer fluorescence lifetime (τ = 7.98 ± 1.08 μs) and appears to belong to a different band system. It is an Ω′=5/2 ←Ω″=5/2 band that probably gains oscillator strength through mixing between its upper state and the $\tilde{A}\ ^2\Delta_{5/2}$ state investigated here. Assuming that the upper state arises from the d^8(^{3}F)s^1, $^{2,\,4}$F configuration of Ni$^+$, as is known in the examples of NiCu and NiH, this state could be of $^2\Phi_{5/2}$, $^4\Phi_{5/2}$, $^4\Delta_{5/2}$, or $^4\Pi_{5/2}$ symmetry.[72] In NiCu,[72] NiH,[72] and NiCN[68] the $^2\Phi_{5/2}$ state lies 1645, 2446, and 2520 cm^{-1} above the $\tilde{A}\ ^2\Delta_{5/2}$ state, respectively. The unknown band in NiCCH lies 1684 cm^{-1} above the $\tilde{A}\ ^2\Delta_{5/2}$ state, which is a bit low in energy if we consider NiCCH to be electronically similar to NiCN. An alternative possibility is a state dominated by $^4\Phi_{5/2}$ character, which lies lower than the equivalent of the $\tilde{A}\ ^2\Delta_{5/2}$ state of NiCu and NiH by 383 and 464 cm^{-1}, respectively.[72] If this is the case, it is likely that the unknown band corresponds to a vibrationally excited level of the $^4\Phi_{5/2}$ state. Further speculation is not warranted at this time. The rotationally resolved spectrum of the 17594 cm^{-1} band, along with a simulated spectrum and measured and fitted line positions, is provided in Appendix A.

All of the rotationally resolved bands originate from a lower level with Ω″=5/2

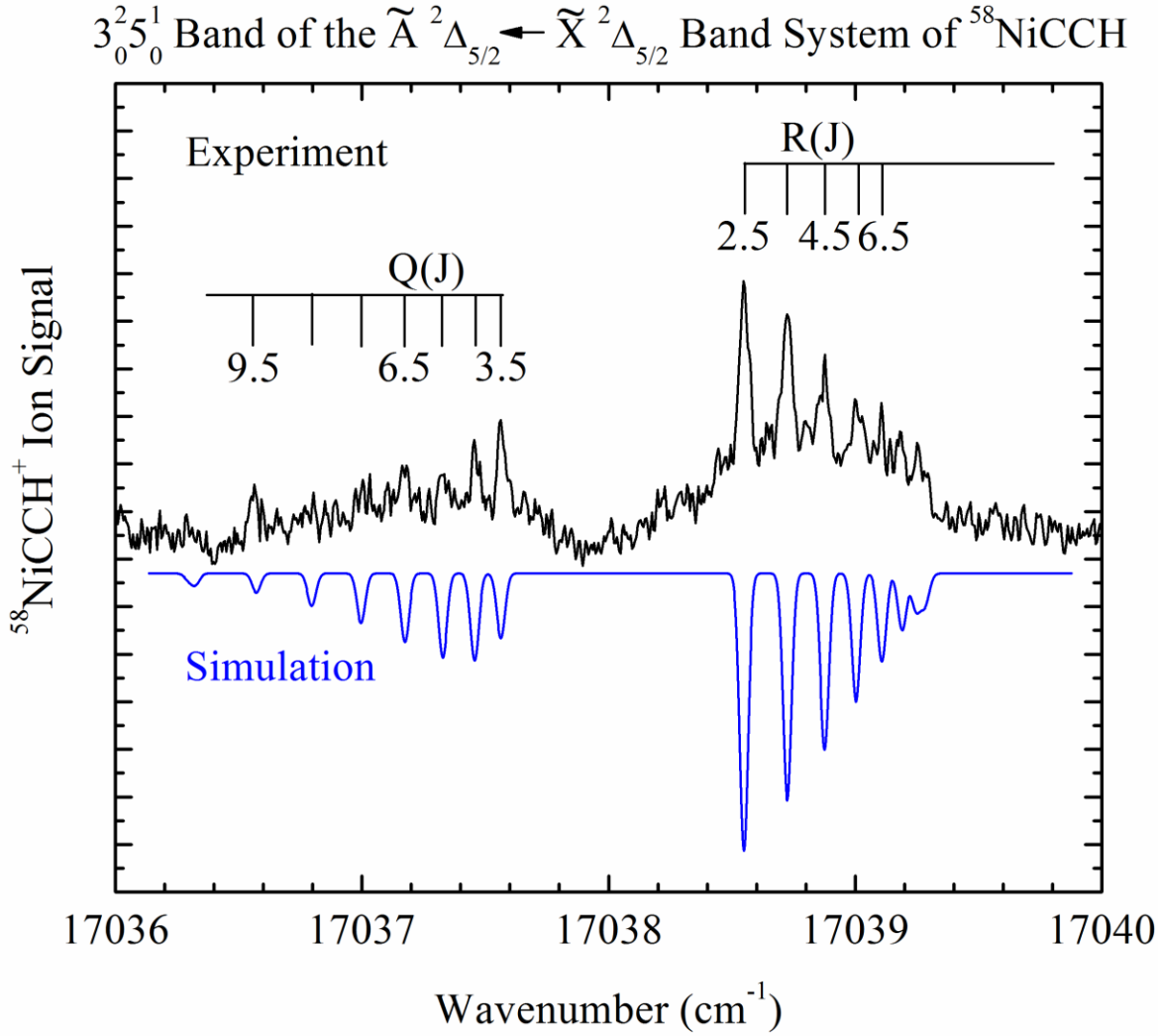

Figure 3.7 Rotationally resolved scan over the $3_0^2 5_0^1$ band of the $\tilde{A}\ ^2\Delta_{5/2} \leftarrow \tilde{X}\ ^2\Delta_{5/2}$ band system. The intense R branch is evidence that $\Delta\Omega = 1$ in this band, and the first lines of R(2.5) and Q(3.5) prove that Ω''=5/2, P′=7/2.

and are found to have very similar rotational constants. Therefore, it seems clear that they arise from the same vibronic level. Although in principle this might be a metastable state that remains populated in the molecular beam, the only example in which we have found a metastable state of a nickel-containing molecule is in Ni_2.[93-94] In our experiments on NiCu,[23-24] NiAu,[34], AlNi,[21] NiC,[92] NiSi,[91] NiPd,[95] and NiPt,[96] we have found only one electronic state to be populated. Thus we assign the ground state as the $\tilde{X}\ ^2\Delta_{5/2}$ state, deriving from a d^9 configuration on the nickel atom.

Accordingly, all rotationally resolved bands were constrained to have the same lower state rotational constant in a combined fit, allowing a more precise value of this quantity to be determined. In the fit, all of the bands were fitted to the Hund's case (a) or (c) formula[87]

$$\nu = \nu_0 + B'J'(J'+1) - B"J"(J"+1)\ . \qquad (3.7)$$

The resulting molecular constants are provided in Table 3.5. The line positions are provided in the Appendix A. The fitted value of B″ obtained for ^{58}NiCCH is 0.14080(11) cm^{-1}. Here, as elsewhere in this report, the value in parentheses represents the 1σ error limit, in units of the last digits quoted.

3.4 Discussion

As in all of the known monovalent, monoligated nickel molecules, the ground state of NiCCH derives from a $3d^9$ configuration on nickel. Like NiAl,[21-22] NiCu,[23-26] NiH,[27-33] NiAu,[22, 34] NiI,[35-39] and NiCN,[68-69] NiCCH preferentially places the 3d hole

Table 3.5 Fitted molecular constants of resolved bands of ^{58}NiCCH.[a]

Band	$\tilde{A} - \tilde{X}\ 3_0^1$	$\tilde{A} - \tilde{X}\ 3_0^1 4_0^1$	$\tilde{A} - \tilde{X}\ 3_0^2 5_0^1$	[17.59]5/2 - $\tilde{A}\ 0_0$	$\tilde{A} - \tilde{X}\ 3_0^3 4_0^1$
T_0	16362.8830(27)	16994.7834(27)	17037.7539(30)	17594.2704(68)	17886.1530(90)
B′	0.12931(10)	0.12878(11)	0.12893(8)	0.12820(14)	0.12869(14)
P′	5/2	7/2	7/2	5/2	7/2
B″	0.14080(11)	0.14080(11)	0.14080(11)	0.14080(11)	0.14080(11)
Ω″	5/2	5/2	5/2	5/2	5/2

[a] All values are in cm^{-1} units; residuals in the fit (calculated – measured) are provided in parentheses, in units of 0.001 cm^{-1}. Error limits in the fitted molecular constants (1σ) are provided in parentheses after each constant, in units of the last digit quoted. In the fit all of the bands were constrained to have the same value of B″.

the 3dδ orbital, leading to an $\tilde{X}\ ^2\Delta_{5/2}$ ground state. This differs from the ground state when more electronegative ligands are present, which has Ω=3/2 for NiCl[43-52] and NiF.[53-67]

If we consider the 3d orbitals of Ni^+ to be too contracted to bond significantly with the orbitals of the ligand, and instead consider the 3d orbital splitting to be governed by electrostatic interactions, it is only possible to obtain a $^2\Delta$ ground term by assigning the ligand a positive effective charge. A negative ligand charge would cause the 3dσ orbital, which points toward the ligand, to be destabilized, causing the Ni 3d orbitals to fall in the order of increasing energy as 3dδ < 3dπ < 3dσ. This favors placement of the 3d hole in the 3dσ orbital, leading to a term ordering of $^2\Sigma^+ < ^2\Pi < ^2\Delta$, in contradiction to experiment, which shows a $^2\Delta_{5/2}$ ground state. Although a positive ligand charge is counterintuitive, reasonably good fits to the calculated[72] or measured[26] electronic levels of the $3d^9$ configuration of NiCu are obtained when a ligand charge of Z_{Cu} = +1 is employed. A positive ligand charge would also be required to account for the energy ordering of the $3d^9$ states in NiH, which follows the same pattern found in NiCu. This result may be rationalized by recognizing that in these molecules, which are more covalent than ionic, the σ bonding electrons lie in a relatively diffuse orbital with substantial $4s_{Ni}$ character. To whatever extent that the σ^2 electrons occupy a diffuse, nearly spherical orbital around the Ni atom, they are not effective in splitting the 3dσ, 3dπ, and 3dδ orbitals. Instead, it is the underlying +1 ion core on the ligand that favors placement of the hole in the 3dδ orbital.

In NiH,[32, 72] NiCN,[68] and NiCu,[72] the manifold of excited states in the 10,000-20000 cm^{-1} range arises from the $3d^84s^1$, ^{2}F, and ^{4}F states of the Ni^+ ion, combined with

an H^-, CN^-, or Cu^- anion. The known electronic states of all three molecules show identical energy orderings, to the extent that they are experimentally known, as displayed in Figure 3.8. For this group of states the energy levels in NiCu and NiH can be well fitted by a ligand field model in which the ligand carries a negative charge of -0.666 for NiCu and -0.439 for NiH.[72] In both NiCu and NiH, the pattern of $3d^8 4s^1$ states is mainly governed by the exchange interaction between the $4s^1$ electron and the $3d^8$ core and by the spin-orbit interaction within the $3d^8$ core.[72] These effects are expected to be largely independent of the ligand, although the exchange effects can be reduced if the ligand is able to delocalize the $4s^1$ electron significantly. To the extent that the CN^- anion acts as a non-interacting negatively charged ligand, a similar pattern of states would be expected. Figure 3.8 shows that this is apparently the case, with the NiCN excited states closely following the NiH pattern of states, as was originally observed by Kingston, Merer, and Varberg.[68] Given that we have only identified one of the expected $3d^8 4s^1$ excited states in the NiCCH molecule, we are unable to prove that it will also follow the same pattern, but we see no reason to expect otherwise.

The NiCCH molecule is isoelectronic with NiCN, differing only by the replacement of the nitrogen atom with a CH group. Thus, the two molecules are not merely isoelectronic; they differ only in the replacement of a triply bonded N atom by a triply bonded CH group. This allows the vibrational motions of the two species to be usefully compared. The Ni-C≡N bending mode in the $\tilde{X}\ ^2\Delta_{5/2}$ ground state exhibits a first excited level that is 243.4 cm^{-1} above the ground level,[68] while in NiCCH the ground state Ni-C≡C bending interval is somewhat reduced from this value, 209.5 cm^{-1}. One might expect the two molecules to have quite similar Ni-C stretching frequencies, but we

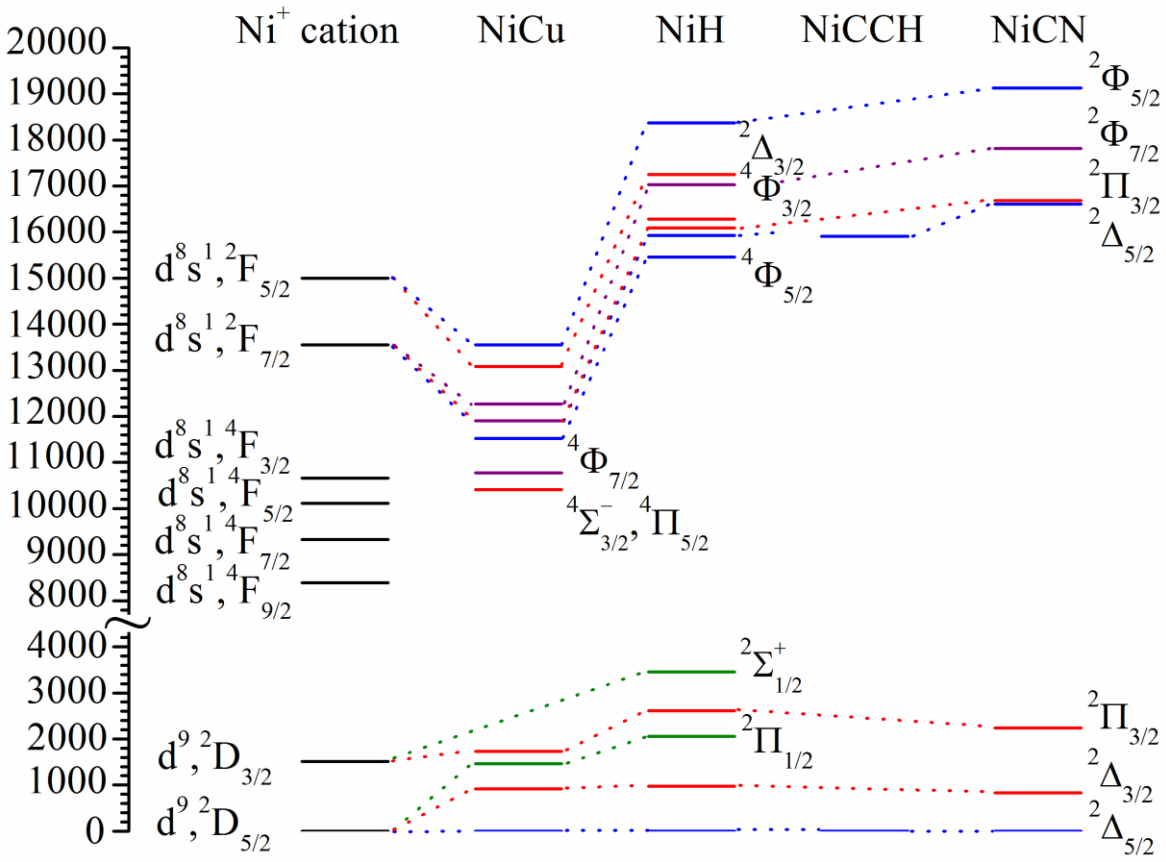

Figure 3.8 Experimentally known electronic states of Ni^+, NiCu, NiH, NiCCH, and NiCN. In this figure, states with Ω=0.5 are displayed using green horizontal lines, while states with Ω=3/2 are indicated in red. States with Ω=5/2 are indicated with blue horizontal lines, and states with Ω=7/2 are indicated by purple. Although many of the states are strongly mixed by spin-orbit interaction, the dominant Hund's case (a) term is listed above. Labels that are provided next to the NiCN column correlate all the way across the table, as shown. Labels provided next to the NiH column correlate in some cases to NiCu, as shown by the dotted correlation lines. The $^4\Phi_{7/2}$ and the nearly degenerate $^4\Pi_{5/2}$ and $^4\Sigma^-_{3/2}$ states are only known in NiCu and are found in the 10,000-11,000 cm^{-1} region.

unfortunately have not measured this quantity for the ground state. The $\tilde{A}\ ^2\Delta_{5/2}$ state of NiCN differs from that of NiCCH, however, in that the vibrational intervals corresponding to excitation of the Ni-CN stretch exhibit a negative anharmonicity, with intervals ranging from 433 cm^{-1} to 450 cm^{-1}. This probably results from perturbations by the nearby $\tilde{B}\ ^2\Pi_{3/2}$ state, which lies only 79 cm^{-1} above the $\tilde{A}\ ^2\Delta_{5/2}$ state. In contrast, the Ni-CCH stretching progression observed in the $\tilde{A}\ ^2\Delta_{5/2} \leftarrow \tilde{X}\ ^2\Delta_{5/2}$ band system is quite regular, with intervals in the 3_0^n progression dropping smoothly from 452.8 cm^{-1} to 446.5 cm^{-1} as one moves from the 0_0^0 band to the 3_0^4 band. Likewise, in the $\tilde{A}\ ^2\Delta_{5/2}$state of NiCN, the Ni-C≡N bending mode is strongly anharmonic, with the first excited level lying 180.2 cm^{-1} above the ground level. This compares to a value of 224 cm^{-1} in the case of NiCCH. These results show that the vibrational frequencies of the two molecules are quite similar, overall.

It is worth noting that the ν_2' excited state C≡C vibrational frequency is now known for two transition metal monoacetylides, NiCCH and CrCCH. In these species the ground state corresponds to a d^9 Ni^+ ion and a d^5 Cr^+ ion, respectively, interacting with a C_2H^- anion. In the excited states, these metal ions are excited to d^8s^1 and d^4s^1 configurations, respectively. The C≡C vibrational frequency in the $\tilde{A}\ ^2\Delta_{5/2}$ and $\tilde{A}\ ^6\Sigma^+$ states of NiCCH and CrCCH are 2001.9 cm^{-1} and 1944.3 cm^{-1}[118], respectively. The large decrease in excited state C≡C vibrational frequency in moving from NiCCH to CrCCH is consistent with a model in which there is a more significant transfer of metal dπ electron density into the C≡C π antibonding orbital in the case of CrCCH as compared to NiCCH, leading to a more significant weakening of the C≡C bond. This would be favored by the more electropositive nature of Cr compared to Ni, and by the larger size and greater

accessibility of the 3d orbitals of Cr as compared to Ni. It would be interesting to see if this trend is followed in the other transition metal acetylides, both in the excited states and in the ground state.

3.5 Conclusions

The first spectroscopic investigation of NiCCH has been performed using the resonant two-photon ionization method. The molecule has been shown to be linear, with a ground state of $\tilde{X}\ ^2\Delta_{5/2}$ symmetry. The electronic transition to the $\tilde{A}\ ^2\Delta_{5/2}$ state has been extensively studied, allowing the rotational constants of both the upper and lower states to be measured, and permitting vibrational levels associated with excitations in the ν_2, ν_3, ν_4, and ν_5 modes in the upper state to be identified. The Ni-C≡C bending frequency in the ground state has also been measured through the observation of hot bands. The $\tilde{A}\ ^2\Delta_{5/2}$-$\tilde{X}\ ^2\Delta_{5/2}$ excitation is found to lie quite close to the corresponding excitation in NiCN, and the vibrational frequencies of NiCCH are found to be similar to the analogous vibrational frequencies of NiCN. Further, it is suggested that the overall pattern of electronic states deriving from the $3d^9$ and $3d^84s^1$ manifolds will be quite similar to that found in NiCN and NiH.

3.6 References

1. Luh, T.-Y.; Huang, L.-F. Functional Organonickel Reagents. *Handb. Funct. Organomet.* **2005,** *2*, 397-449.

2. Mond, L.; Langer, C.; Quincke, F. Action of Carbon Monoxide on Nickel. *J. Chem. Soc., Trans.* **1890,** *57*, 749-753.

3. Yang, T.-K.; Lee, D.-S.; Haas, J. Raney Nickel. *e-EROS Encycl. Reagents Org. Synth.* **2006**, No pp given.

4. Matsubara, R.; Gutierrez, A. C.; Jamison, T. F. Nickel-Catalyzed Heck-Type Reactions of Benzyl Chlorides and Simple Olefins. *J. Am. Chem. Soc.* **2011,** *133* (47), 19020-19023.

5. Goegsig, T. M.; Kleimark, J.; Nilsson Lill, S. O.; Korsager, S.; Lindhardt, A. T.; Norrby, P.-O.; Skrydstrup, T. Mild and Efficient Nickel-Catalyzed Heck Reactions with Electron-rich Olefins. *J. Am. Chem. Soc.* **2012,** *134* (1), 443-452.

6. Tasker Sarah, Z.; Gutierrez Alicia, C.; Jamison Timothy, F. Nickel-catalyzed Mizoroki-Heck Reaction of Aryl Sulfonates and Chlorides with Electronically Unbiased Terminal Olefins: High Selectivity for Branched Products. *Angew. Chem. Int. Ed.* **2014,** *53* (7), 1858-61.

7. Hsieh, J.-C.; Cheng, C.-H. Nickel-catalyzed Cocyclotrimerization of Arynes with Diynes. A Novel Method for Synthesis of Naphthalene Derivatives. *Chem. Commun.* **2005,** (19), 2459-2461.

8. Corriu, R. J. P.; Masse, J. P. Activation of Grignard Reagents by Transition-metal Complexes. New and Simple Synthesis of Trans-stilbenes and Polyphenyls. *J. Chem. Soc., Chem. Commun.* **1972,** (3), 144.

9. Tamao, K.; Sumitani, K.; Kumada, M. Selective Carbon-carbon Bond Formation by Cross-coupling of Grignard Reagents with Organic Halides. Catalysis by Nickel-phosphine Complexes. *J. Amer. Chem. Soc.* **1972,** *94* (12), 4374-6.

10. King, A. O.; Okukado, N.; Negishi, E. Highly General Stereo-, Regio-, and Chemo-selective Synthesis of Terminal and Internal Conjugated Enynes by the Palladium-catalyzed Reaction of Alkynylzinc Reagents with Alkenyl Halides. *J. Chem. Soc., Chem. Commun.* **1977,** (19), 683-4.

11. Melikyan, G. G.; Nicholas, K. M. The Chemistry of metal-alkyne Complexes. *Mod. Acetylene Chem.* **1995**, 99-138.

12. Sun, H.; Shen, Q.; Peng, X.; Yang, M. Neutral Pd(II) and Ni(II) Acetylide Catalysts for the Polymerization of Methyl Methacrylate. *Catal. Lett.* **2002,** *80* (1-2), 11-

18.

13. Sun, H.; Pang, X.; Chen, M.; Shen, Q. Neutral Pd(II) and Ni(II) Acetylide Initiators for Polymerization of (Dimethylamino)ethyl Methacrylate. *Catal. Lett.* **2003,** *90* (1-2), 85-89.

14. Shao, Q.; Sun, H.; Pang, X.; Shen, Q. A Neutral Ni(II) Acetylide-mediated Radical Polymerization of Methyl Methacrylate Using the Atom Transfer Radical Polymerization Method. *Eur. Polym. J.* **2004,** *40* (1), 97-102.

15. Zhan, X.; Yang, M.; Sun, H. Transition Metal Acetylide Catalysts for Polymerization of Polar Alkynes. *Catal. Lett.* **2000,** *70* (1,2), 79-82.

16. Zhan, X.; Yang, M. Transition Metal Acetylide Catalysts for Polymerization of Alkynes 1. Effect of Ligands on Catalytic Activity of Nickel Complexes. *J. Mol. Catal. A Chem.* **2001,** *169* (1-2), 27-31.

17. Garcia, M. A.; Morse, M. D. Electronic Spectroscopy and Electronic Structure of Copper Acetylide, CuCCH. *J. Phys. Chem. A* **2013,** *117* (39), 9860-9870.

18. Brugh, D. J.; Morse, M. D. Rotational Analysis of the 3_0^1 Band of the $\tilde{A}\ ^6\Sigma^+$ - $\tilde{X}\ ^6\Sigma^+$ System of CrCCH. *J. Chem. Phys.* **2014,** *141* (6), 064304/1-9.

19. Brugh, D. J.; DaBell, R. S.; Morse, M. D. Vibronic Spectroscopy of Unsaturated Transition Metal Complexes: CrC_2H, $CrCH_3$, and $NiCH_3$. *J. Chem. Phys.* **2004,** *121* (24), 12379-85.

20. Drewello, T.; Schwarz, H. Generation and Characterization of Stable Monomeric Transition Metal Acetylides MCCH (M = iron, cobalt, nickel) by Neutralization-reionization Mass Spectrometry. *Chem. Phys. Lett.* **1990,** *171* (1-2), 5-8.

21. Behm, J. M.; Arrington, C. A.; Morse, M. D. Spectroscopic Studies of Jet-cooled AlNi. *J. Chem. Phys.* **1993,** *99*, 6409-6415.

22. Fabbi, J. C.; Karlsson, L.; Langenberg, J. D.; Costello, Q. D.; Morse, M. D. Dispersed Fluorescence Spectroscopy of AlNi, NiAu, and PtCu. *J. Chem. Phys.* **2003,** *118* (20), 9247-9256.

23. Fu, Z.; Morse, M. D. Spectroscopy and Electronic Structure of Jet-cooled NiCu. *J. Chem. Phys.* **1989,** *90*, 3417-3426.

24. Spain, E. M.; Morse, M. D. The $3d^8_{Ni}$ (^{3}F) $3d^{10}_{Cu}\ \sigma^2\sigma^{*1}$ Manifold of Excited Electronic States of NiCu. *J. Chem. Phys.* **1992,** *97*, 4633-4640.

25. Dixon-Warren, S. J.; Gunion, R. F.; Lineberger, W. C. Photoelectron Spectroscopy of Mixed Metal Cluster Anions: $NiCu^-$, $NiAg^-$, $NiAg_2^-$, and Ni_2Ag^-. *J.*

Chem. Phys. **1996,** *104* (13), 4902-4910.

26. Rothschopf, G. K.; Morse, M. D. Monoligated Monovalent Ni: the $3d_{Ni}^{9}$ Manifold of States of NiCu and Comparison to the $3d^{9}$ States of AlNi, NiH, NiCl, and NiF. *J. Phys. Chem. A* **2005,** *109* (50), 11358-11364.

27. Gray, J. A.; Rice, S. F.; Field, R. W. The Electric Dipole Moment of Nickel Hydride (NiH) $X^2\Delta_{5/2}$ and $B^2\Delta_{5/2}$. *J. Chem. Phys.* **1985,** *82* (10), 4717-18.

28. Gray, J. A.; Field, R. W. The Zeeman Effect as an aid to Electronic Assignment: the Nickel Hydride (NiH) $A^2\Delta_{5/2}$ state. *J. Chem. Phys.* **1986,** *84* (2), 1041-2.

29. Adakkai Kadavathu, S.; Loefgren, S.; Scullman, R. Rotational Analysis of Some New Transitions in Nickel Deuteride (NiD). A Comparison Between Nickel Hydride (NiH) and Nickel Deuteride (NiD). *Phys. Scr.* **1987,** *35* (3), 277-85.

30. Kadavathu, S. A.; Scullman, R.; Gray, J. A.; Li, M.; Field, R. W. New Low-lying States in Nickel Hydride (NiH): Rotational Analysis with the aid of Laser-induced Dispersed Fluorescence Spectroscopy. *J. Mol. Spectrosc.* **1990,** *140* (1), 126-40.

31. Gray, J. A.; Li, M.; Field, R. W. Zeeman Spectroscopy and Deperturbation of the Low-lying States of Nickel Hydride (NiH). *J. Chem. Phys.* **1990,** *92* (8), 4651-9.

32. Gray, J. A.; Li, M.; Nelis, T.; Field, R. W. The Electronic Structure of NiH: The $\{Ni^+ 3d^9\ ^2D\}$ Supermultiplet. *J. Chem. Phys.* **1991,** *95* (10), 7164-7178.

33. Kadavathu, S. A.; Scullman, R.; Field, R. W.; Gray, J. A.; Li, M. Excited States of Nickel Monohydride and Nickel Monodeuteride in the 15,500-19,000 cm^{-1} Region: Rotational Analysis with the aid of Laser-induced Fluorescence Spectroscopy. *J. Mol. Spectrosc.* **1991,** *147* (2), 448-70.

34. Spain, E. M.; Morse, M. D. Spectroscopic Studies of Jet-cooled NiAu and PtCu. *J. Chem. Phys.* **1992,** *97*, 4605-4615.

35. Tam, W. S.; Leung, J. W. H.; Hu, S.-M.; Cheung, A. S. C. Laser Spectroscopy of NiI: Ground and Low-lying Electronic States. *J. Chem. Phys.* **2003,** *119* (23), 12245-12250.

36. Tam, W. S.; Ye, J.; Cheung, A. S. C. Near-infrared Laser Spectroscopy of NiI. *J. Chem. Phys.* **2004,** *121* (19), 9430-9435.

37. Miyazawa, T.; Okabayashi Emi, Y.; Koto, F.; Tanimoto, M.; Okabayashi, T. The Rotational Spectrum of the NiI Radical in the $X\ ^2\Delta_{5/2}$ and $A\ ^2\Pi_{3/2}$ States. *J. Chem Phys* **2006,** *124* (22), 224321.

38. Cheung, A. S. C.; Pang, H. F.; Tam, W. S.; Leung, J. W. H. Laser Spectroscopy

of NiI: New Electronic States and Hyperfine Structure. *J. Chem. Phys.* **2009,** *131* (19), 194301/1-194301/7.

39. Ayles, V. L.; Muzangwa, L. G.; Reid, S. A. Single Vibronic Level Emission Spectroscopy of the Low-lying Electronic States of NiI. *Chem. Phys. Lett.* **2010,** *497* (4-6), 168-171.

40. Leung, J. W. H.; Wang, X.; Cheung, A. S. C. Laser Spectroscopy of NiBr: Ground and Low-lying Electronic States. *J. Chem. Phys.* **2002,** *117* (8), 3694-3700.

41. Yamazaki, E.; Okabayashi, T.; Tanimoto, M. Perturbation Analysis for the Rotational Spectrum of the NiBr Radical in the X $^2\Pi_{3/2}$ and A $^2\Delta_{5/2}$ States. *J. Chem. Phys.* **2004,** *121* (1), 162-168.

42. Ye, J.; Leung, J. W. H.; Cheung, A. S. C. Laser Spectroscopy of NiBr: New Electronic States and Hyperfine Structure. *J. Chem. Phys.* **2006,** *125* (21), 214308/1-214308/8.

43. Muzangwa, L. G.; Ayles, V. L.; Nyambo, S.; Reid, S. A. Probing the Electronic Structure of the Nickel Monohalides: Spectroscopy of the Low-lying Electronic States of NiBr and NiCl. *J. Mol. Spectrosc.* **2011,** *269* (1), 36-40.

44. Darji, A. B.; Sureshkumar, M. B. Rotational Analysis of $^2\Pi_i$->$^2\Delta_i$ System of Nickel Chloride (NiCl). *Indian J. Pure Appl. Phys.* **1990,** *28* (6), 338-41.

45. Hirao, T.; Dufour, C.; Pinchemel, B.; Bernath, P. F. Laser-induced Fluorescence and Fourier Transform Spectroscopy of the $[21.9]^2\Delta_{5/2}$-$X^2II_{3/2}$ (21910 cm^{-1}) and the $[21.9]^2\Delta_{5/2}$-$[0.16]^2\Delta_{5/2}$ (21750 cm^{-1}) Transitions of NiCl. *J. Mol. Spectrosc.* **2000,** *202* (1), 53-59.

46. Poclet, A.; Krouti, Y.; Hirao, T.; Pinchemel, B.; Bernath, P. F. Laser-Induced Fluorescence and Fourier Transform Spectroscopy of NiCl: Identification of a Low-Lying $^2\Sigma^+$ State (1768 cm^{-1}). *J. Mol. Spectrosc.* **2000,** *204* (1), 125-132.

47. Krouti, Y.; Poclet, A.; Hirao, T.; Pinchemel, B.; Bernath, P. F. The $X^2\Pi_i$, $A^2\Delta_i$, and $B^2\Sigma^+$ Low-Lying States of NiCl: Laser-Induced Fluorescence and Fourier Transform Emission Experiments. *J. Mol. Spectrosc.* **2001,** *210* (1), 41-50.

48. O'Brien, J. J.; Miller, J. S.; O'Brien, L. C. Intracavity Laser Spectroscopy of NiCl System G: Identification of a [13.0] $^2\Pi_{3/2}$ State. *J. Mol. Spectrosc.* **2002,** *211* (2), 248-253.

49. O'Brien, L. C.; Homann, K. M.; Kellerman, T. L.; O'Brien, J. J. Fourier Transform and Intracavity Laser Spectroscopy of NiCl System H: Identification of a [12.3] $^2\Sigma^+$ State. *J. Mol. Spectrosc.* **2002,** *211* (1), 93-98.

50. Rice, C. A.; O'Brien, L. C. Fourier Transform Spectroscopy of NiCl: Identification of the [12.3] $^2\Sigma^+$-$B^2\Sigma^+$ Transition. *J. Mol. Spectrosc.* **2003,** *221* (1), 131-134.

51. Tumturk, S.; O'Brien, L. C.; O'Brien, J. J. Fourier Transform Spectroscopy of NiCl: Identification of a [9.1] $\Omega = 3/2$ State. *J. Mol. Spectrosc.* **2004,** *225* (2), 225-229.

52. Rice, C. A.; Kellerman, T. L.; Owen, B.; O'Brien, L. C.; Cao, H.; O'Brien, J. J. Spectroscopy of NiCl: Identification of the $X^2\Pi_{1/2}$ state. *J. Mol. Spectrosc.* **2006,** *235* (2), 271-274.

53. Pinchemel, B.; Lefebvre, Y.; Schamps, J. Rotational Analysis of a $^2\Delta$-$^2\Pi$ System of Nickel Fluoride (NiF). *J. Mol. Spectrosc.* **1979,** *77* (1), 29-35.

54. Gopal, R.; Joshi, M. M. New Band Systems of the Nickel Fluoride (NiF) Molecule. *Curr. Sci.* **1981,** *50* (12), 530-1.

55. Bai, J.; Hilborn, R. C. Chemiluminescence and Laser-induced Fluorescence of Nickel Fluoride (NiF). *Chem. Phys. Lett.* **1986,** *128* (2), 133-6.

56. Bouddou, A.; Dufour, C.; Pinchemel, B., Laser-induced Fluorescence of a $^2\Pi_{3/2}$-$^2\Sigma$ (18 145 cm^{-1}) Transition of NiF. *J. Mol. Spectrosc.* **1994,** *168* (2), 477-82.

57. Dufour, C.; Hikmet, I.; Pinchemel, B. An Energy Level Diagram of the Known Electronic States of NiF Determined by Radiative and Collisional Transfers. *J. Mol. Spectrosc.* **1994,** *165* (2), 398-405.

58. Dufour, C.; Pinchemel, B. The Blue-violet Transitions of NiF: Identification of a new Low-lying $^2\Sigma$ State (T_0 = 252 cm^{-1}). *J. Mol. Spectrosc.* **1995,** *173* (1), 70-8.

59. Focsa, C.; Dufour, C.; Pinchemel, B. Dispersed Excitation Spectroscopy of Some Weak Transitions of NiF. *J. Mol. Spectrosc.* **1997,** *182* (1), 65-71.

60. Chen, Y.; Jin, J.; Hu, C.; Yang, X.; Ma, X.; Chen, C. Fluorescence Excitation Spectrum of a $^2\Pi_{3/2}$-$^2\Pi_{3/2}$ Transition of NiF. *J. Mol. Spectrosc.* **2000,** *203* (1), 37-40.

61. Jin, J.; Chen, Y.; Yang, X.; Ran, Q.; Chen, C. Identification of the High-lying Π Component of NiF by Laser-induced Fluorescence. *J. Mol. Spectrosc.* **2001,** *208* (1), 18-24.

62. Jin, J.; Ran, Q.; Yang, X.; Chen, Y.; Chen, C. Spectroscopic Investigation of Four Electronic States of NiF in the 17500-25000 cm^{-1} Region. *J. Phys. Chem. A* **2001,** *105* (50), 11177-11182.

63. Tanimoto, M.; Sakamaki, T.; Okabayashi, T. Microwave Spectroscopic Study of NiF in the Electronic Ground and Lowest Excited States. *J. Mol. Spectrosc.* **2001,** *207*

(1), 66-69.

64. Krouti, Y.; Hirao, T.; Dufour, C.; Boulezhar, A.; Pinchemel, B.; Bernath, P. F. High-Resolution Survey of the Visible Spectrum of NiF by Fourier Transform Spectroscopy. *J. Mol. Spectrosc.* **2002,** *214* (2), 152-174.

65. Pinchemel, B.; Hirao, T.; Bernath, P. F. High-Resolution Fourier Transform Spectroscopy of Three Near-Infrared Transitions of NiF. *J. Mol. Spectrosc.* **2002,** *215* (2), 262-268.

66. Benomier, M.; Van Groenendael, A.; Pinchemel, B.; Hirao, T.; Bernath, P. F. Near Infrared Spectroscopy of NiF. *J. Mol. Spectrosc.* **2005,** *233* (2), 244-255.

67. Harris, R. A.; O'Brien, L. C.; O'Brien, J. J. Spectroscopy of NiF by Intracavity Laser Spectroscopy: Identification and Analysis of the (1,0) Band of the [11.1] $^2\Pi_{3/2}$-X $^2\Pi_{3/2}$ Electronic Transition. *J. Mol. Spectrosc.* **2010,** *259* (2), 116-119.

68. Kingston, C. T.; Merer, A. J.; Varberg, T. D. The Electronic Spectrum of NiCN in the Visible Region. *J. Mol. Spectrosc.* **2002,** *215* (1), 106-127.

69. Sheridan, P. M.; Ziurys, L. M. Further Studies of 3d Transition Metal Cyanides: The Pure Rotational Spectrum of NiCN (X $^2\Delta_i$). *J. Chem. Phys.* **2003,** *118* (14), 6370-6379.

70. Allred, A. L. Electronegativity Values from Thermochemical Data. *J. Inorg. Nucl. Chem.* **1961,** *17*, 215-21.

71. Moran, M. D.; Jones, J.-P.; Wilson, A. A.; Houle, S.; Surya Prakash, G. K.; Olah, G. A.; Vasdev, N. "Recharging" Group Electronegativities: Computational Chemistry as a Tool for Estimating Electronegativity. *Chem. Educ.* **2011,** *16*, 164-167.

72. Spain, E. M.; Morse, M. D. Ligand Field Theory Applied to Diatomic Transition Metals: Results for the $d^9_A\ d^9_B\ \sigma^2$ States of Ni_2, the $d^9_{Ni}\ d^{10}_{Cu}\ \sigma^2$ States of NiCu, and the $d^8_{Ni}(^3F)\ d^{10}_{Cu}\sigma^2\sigma^{*1}$ Excited States of NiCu. *J. Chem. Phys.* **1992,** *97*, 4641-4660.

73. Carette, P.; Dufour, C.; Pinchemel, B. Theoretical Interpretation of the Nickel Fluoride Spectrum. *J. Mol. Spectrosc.* **1993,** *161* (2), 323-35.

74. Hougen, J. T. Approximate Theoretical Model for the Five Electronic States (Ω = 5/2, 3/2, 3/2, 1/2, 1/2) Arising from the Ground $3d^9$ Configuration in Nickel Halide Molecules and for Rotational Levels of the two Ω = 1/2 States in that Manifold. *J. Mol. Spectrosc.* **2011,** *267* (1-2), 23-35.

75. Shao, L.; Sickafoose, S. M.; Langenberg, J. D.; Brugh, D. J.; Morse, M. D. Resonant Two-photon Ionization Spectroscopy of Jet-cooled PtSi. *J. Chem. Phys.* **2000,** *112* (9), 4118-4123.

76. Lindholm, N.; Morse, M. D. Rotationally Resolved Spectra of Jet-cooled RuSi. *J. Chem. Phys.* **2007,** *127* (8), 084317/1-5.

77. Martinez, A.; Lindholm, N.; Morse, M. D. Resonant Two-photon Ionization Spectroscopy of Jet-cooled PdSi. *J. Chem. Phys.* **2011,** *135* (13), 134308/1-8.

78. Wiley, W. C.; McLaren, I. H. Time-of-Flight Mass Spectrometer with Improved Resolution. *Rev. Sci. Instrum.* **1955,** *26* (12), 1150 - 1157.

79. Mamyrin, B. A.; Karataev, V. I.; Shmikk, D. V.; Zagulin, V. A. Mass Reflectron. New Nonmagnetic Time-of-flight High-resolution Mass Spectrometer. *Zh. Eksp. Teor. Fiz.* **1973,** *64* (1), 82-9.

80. Gerstenkorn, S.; Luc, P. *Atlas du Spectre d'Absorption de la Molécule d'Iode entre 14,800-20,000 cm^{-1}*. CNRS: Paris, 1978.

81. Gerstenkorn, S.; Luc, P. Absolute iodine (I_2) standards measured by means of Fourier transform spectroscopy. *Revue de Physique Appliquee* **1979,** *14*, 791-794.

82. Morse, M. D. Supersonic Beam Sources. In *Methods of Experimental Physics: Atomic, Molecular, and Optical Physics*, Dunning, F. B.; Hulet, R., Eds. Academic Press, Inc.: Orlando, Florida, 1996; Vol. II Atoms and Molecules, pp 21-47.

83. Bevington, P. R. *Data Reduction and Error Analysis for the Physical Sciences*. McGraw-Hill: New York, 1969; p 336.

84. Dunning, T. H., Jr. Gaussian Basis Sets for use in Correlated Molecular Calculations. I. The Atoms Boron through Neon and Hydrogen. *J. Chem. Phys.* **1989,** *90* (2), 1007-23.

85. Frisch, M. J.; Trucks, G. W.; Schlegel, H. B.; Scuseria, G. E.; Robb, M. A.; Cheeseman, J. R.; Scalmani, G.; Barone, V.; Mennucci, B.; Petersson, G. A.; Nakatsuji, H.; Caricato, M.; Li, X.; Hratchian, H. P.; Izmaylov, A. F.; Bloino, J.; Zheng, G.; Sonnenberg, J. L.; Hada, M.; Ehara, M.; Toyota, K.; Fukuda, R.; Hasegawa, J.; Ishida, M.; Nakajima, T.; Honda, Y.; Kitao, O.; Nakai, H.; Vreven, T.; Montgomery, J. A., Jr.; Peralta, J. E.; Ogliaro, F.; Bearpark, M.; Heyd, J. J.; Brothers, E.; Kudin, K. N.; Staroverov, V. N.; Kobayashi, R.; Normand, J.; Raghavachari, K.; Rendell, A.; Burant, J. C.; Iyengar, S. S.; Tomasi, J.; Cossi, M.; Rega, N.; Millam, N. J.; Klene, M.; Knox, J. E.; Cross, J. B.; Bakken, V.; Adamo, C.; Jaramillo, J.; Gomperts, R.; Stratmann, R. E.; Yazyev, O.; Austin, A. J.; Cammi, R.; Pomelli, C.; Ochterski, J. W.; Martin, R. L.; Morokuma, K.; Zakrzewski, V. G.; Voth, G. A.; Salvador, P.; Dannenberg, J. J.; Dapprich, S.; Daniels, A. D.; Farkas, Ö.; Foresman, J. B.; Ortiz, J. V.; Cioslowski, J.; Fox, D. J. *Gaussian 09, Revision D.01*, Gaussian, Inc.: Wallingford, CT, 2009.

86. Lefebvre-Brion, H.; Field, R. W., *The Spectra and Dynamics of Diatomic Molecules*. Elsevier: Amsterdam, 2004; p 766.

87. Herzberg, G. *Molecular Spectra and Molecular Structure I. Spectra of Diatomic Molecules*. 2nd ed.; Van Nostrand Reinhold: New York, 1950.

88. PGOPHER, *a Program for Simulating Rotational Structure, C. M. Western, University of Bristol,* http://pgopher.chm.bris.ac.uk/.

89. Dietz, T. G.; Duncan, M. A.; Puiu, A. C.; Smalley, R. E. Pyrazine and Pyrimidine Triplet Decay in a Supersonic Beam. *J. Phys. Chem.* **1982,** *86* (20), 4026-9.

90. Dietz, T. G.; Duncan, M. A.; Smalley, R. E. Time Evolution Studies of Triplet Toluene by Two-color Photoionization. *J. Chem. Phys.* **1982,** *76* (3), 1227-32.

91. Lindholm, N. F.; Brugh, D. J.; Rothschopf, G. K.; Sickafoose, S. M.; Morse, M. D. Optical Spectroscopy of Jet-cooled NiSi. *J. Chem. Phys.* **2003,** *118* (5), 2190-2196.

92. Brugh, D. J.; Morse, M. D. Resonant Two-photon Ionization Spectroscopy of NiC. *J. Chem. Phys.* **2002,** *117* (23), 10703-10714.

93. Morse, M. D.; Hansen, G. P.; Langridge-Smith, P. R. R.; Zheng, L.-S.; Geusic, M. E.; Michalopoulos, D. L.; Smalley, R. E. Spectroscopic Studies of the Jet-cooled Nickel Dimer. *J. Chem. Phys.* **1984,** *80*, 5400-5405.

94. Pinegar, J. C.; Langenberg, J. D.; Arrington, C. A.; Spain, E. M.; Morse, M. D. Ni_2 Revisited: Reassignment of the Ground Electronic State. *J. Chem. Phys.* **1995,** *102*, 666-674.

95. Taylor, S.; Spain, E. M.; Morse, M. D. Spectroscopy and Electronic Structure of Jet-cooled NiPd and PdPt. *J. Chem. Phys.* **1990,** *92*, 2710-2720.

96. Taylor, S.; Spain, E. M.; Morse, M. D. Resonant Two-photon Ionization Spectroscopy of Jet-cooled NiPt. *J. Chem. Phys.* **1990,** *92*, 2698-2709.

CHAPTER 4

RESONANT TWO-PHOTON IONIZATION SPECTROSCOPY OF JET-COOLED OsSi

Reproduced from Johnson, E. L.; Morse, M. D., Resonant two-photon ionization spectroscopy of jet-cooled OsSi *J*. *Chem*. *Phys*. **2015**, *143*, 104303/1-104303/12, with the permission of AIP Publishing.

4.1 Introduction

Transition metal silicides have been of interest in the electronics industry for many years due to their hardness, resistance to oxidation, useful electronic properties, and compatibility with silicon-based microelectronics. In particular, osmium silicide has received interest from scientists working with semiconductors[1-4] and thin films.[5-7] Prior to the present study, however, diatomic OsSi had not been spectroscopically investigated.

Although OsSi has not been previously studied, many of the other diatomic transition metal silicides have been investigated. Bond dissociation energies have been measured for ScSi,[8] YSi,[9] FeSi,[10] RuSi,[11] CoSi,[10] RhSi,[11] IrSi,[11] NiSi,[10] PdSi,[11-12] PtSi,[11] CuSi,[13] AgSi,[13] and AuSi[11, 14] using Knudsen effusion mass spectrometry. Guided ion

beam mass spectrometry has been used to determine the bond dissociation energies of $ScSi^+$,[15] YSi^+,[15] $LaSi^+$,[15] $LuSi^+$,[15] $TiSi^+$,[16] VSi^+,[16] $CrSi^+$,[16] $FeSi^+$,[17] $CoSi^+$,[17] $NiSi^+$,[17] $CuSi^+$,[18] and $ZnSi^+$.[18] Diatomic VSi and NbSi have been studied using matrix isolation ESR spectroscopy.[19] Spectra of diatomic transition metal silicides have also been recorded in the gas phase. Cavity ringdown laser spectroscopy was used to record the spectra of CuSi,[20] AgSi,[21] AuSi,[22] and PtSi.[23] Along with cavity ringdown spectroscopy, emission spectroscopy has been used to study CuSi,[24] and the bond length and dipole moment have been determined for PtSi using pure rotational spectroscopy.[25] Photoelectron spectroscopy has also been used to investigate the electronic structure of ZrSi,[26-27] NbSi,[27] MoSi,[27] PdSi,[27] and WSi,[27] by first mass-selecting the anions of these species, then measuring their photoelectron spectra.

Diatomic OsSi is a transition metal molecule with 12 valence electrons, eight from Os and four from Si. A number of other 12-electron transition metal molecules have been previously investigated and a variety of ground states have been found. These ground configurations and terms include the $1\sigma^2 2\sigma^2 1\pi^4 1\delta^4$, X $^1\Sigma_{0+}^+$ term in RuC;[28-31] the $1\sigma^2\ 2\sigma^2\ 1\pi^4\ 1\delta^3\ 3\sigma^1$, X $^3\Delta_3$ term in FeC,[32-36] OsC,[37-38] and RuSi;[39-40] the $1\sigma^2\ 2\sigma^2\ 1\pi^4\ 3\sigma^2\ 1\delta^2$, X $^3\Sigma_{0+}^-$ term in tungsten oxide, WO,[41-49] and ReN;[33, 50-53] and the $1\sigma^2\ 2\sigma^2\ 1\pi^4\ 1\delta^2\ 3\sigma^1\ 2\pi^1$, X $^5\Pi_1$ term in CrO[54-61], CrS[62-63], and MoO.[57, 64-67] One of the purposes of this study was to determine the ground configuration and term of OsSi and to compare the result to the findings for other 12-electron transition metal molecules.

Transition metal silicides have also been extensively investigated by this group using resonant two-photon ionization (R2PI) spectroscopy. For example, the Morse group has performed the first spectroscopic characterizations of NiSi,[68] PdSi,[69] RuSi,[40]

and IrSi,[70-71] and also reported on the spectrum of PtSi.[72] No spectroscopic work has been previously done on OsSi; Wu and Su, however, have calculated that the ground state is of $^3\Sigma^-$ symmetry, deriving from the $1\sigma^2 2\sigma^2 1\pi^4 3\sigma^2 1\delta^2$ electronic configuration.[39]

4.2 Experimental

In the current work, OsSi was investigated using resonant two-photon ionization (R2PI) spectroscopy. The instrument employed is identical to that used in many previous studies.[40, 69, 72-74] The OsSi molecule is produced by focusing the third harmonic radiation from a Q-switched Nd:YAG laser (355 nm) onto a 1:1 osmium-vanadium alloy disk in the path of a pulsed supersonic expansion of helium (160 psig backing pressure) seeded with 0.13% silane, SiH_4. The alloy disk is rotated and translated to prevent the drilling of holes and to maintain a stable source of diatomic OsSi. The products of ablation and subsequent reaction then travel down a 1.3 cm long reaction zone and expand supersonically through a 5 mm orifice into a vacuum chamber, causing them to be cooled to approximately 10 K. The molecular beam is then roughly collimated by a 1 cm diameter skimmer and enters the Wiley-McLaren ion source of a reflectron time of flight mass spectrometer,[75-76] where it is exposed to a pulse of tunable dye laser radiation that is counterpropagated along the molecular beam path. After a delay of about 20 ns, the output radiation of an ArF excimer laser (193 nm, 6.42 eV) intersects the molecular beam at right angles, ionizing molecules that have been excited by the dye laser radiation. The resulting ions are accelerated into the flight tube and enter a reflectron,[76] which causes them to reverse their motion, directing them down a second flight tube to a dual microchannel plate detector. The resulting ion signal is then preamplified, digitized, and

stored for analysis at a later time. The entire experiment is repeated at a rate of 10 Hz.

Low-resolution spectra of OsSi at mass 217 (15.52% natural abundance), 218 (25.51% natural abundance), and 220 (38.63% natural abundance) were recorded from 15 350 cm^{-1} to 20 400 cm^{-1}. The three masses that were monitored are dominated by a single isotopologue: mass 217 consists primarily (95.68%) of $^{189}Os^{28}Si$; mass 218 primarily (95.44%) of $^{190}Os^{28}Si$; and mass 220 primarily (97.88%) of $^{192}Os^{28}Si$. Features due to the minor isotopologues that have these same masses were not observed in the spectrum. To reveal the rotational structure of the observed bands, high resolution scans were performed by inserting an air-spaced intracavity étalon into the dye laser, which was then pressure-scanned using SF_6. To calibrate the rotationally resolved bands, partial reflections of the dye laser radiation were sent through a cell containing gaseous I_2 and through a 0.22 cm^{-1} free spectral range étalon, and the transmitted intensity was monitored with a photodiode. Fringes from the étalon were used to linearize the recorded spectrum, and the recorded I_2 spectrum was compared to the I_2 atlas[77] to obtain an absolute calibration. A correction was made to account for the Doppler shift of the spectrum that results from the fact that the molecules approach the radiation source at the beam velocity of helium (1.77×10^5 cm/s).[78] A final correction for the error in the I_2 atlas (-0.0056 cm^{-1}) was also made.[79] The total correction for these two effects amounted to about 0.10 cm^{-1} for the bands examined.

Excited state lifetimes were also measured for selected bands by firing the ionization laser when OsSi had the greatest signal intensity and scanning the firing time of the dye laser. A plot of the $OsSi^+$ ion signal as a function of the firing time of the dye laser displayed an exponential decay curve that was fitted using the Levenberg-

Marquardt nonlinear least-squares algorithm[80] to extract the exponential decay time, τ. Three independent lifetime curves were collected and fitted for each band and the standard deviation of the three values is reported as the 1σ error limit.

4.3 Results

4.3.1 Vibronic Spectrum

Survey scans of OsSi were recorded in the 15 350 – 20 400 cm^{-1} region, resulting in the observation of 39 vibronic bands. The low-resolution spectrum of $^{192}Os^{28}Si$ is displayed in Figure 4.1; wavenumbers of the observed bands are listed in Table 4.1. Progressions of bands belonging to the same electronic state were identified by finding bands of similar intensity separated by nearly constant intervals, allowing 20 of the bands to be grouped into two band systems, designated as the A-X and B-X systems. The A-X system is quite extensive, while the B-X system only exhibits two bands within the range that was scanned. More detailed vibronically resolved spectra, along with rotationally resolved spectra, vibronic band positions, rotational line positions, and details of the least-squares fits are provided in Appendix B.

To determine the vibrational assignment, the isotope shift was modeled by fitting the progression in $^{192}Os^{28}Si$ to the formula[81]

$$\nu_{v'-0} = T_0 + \upsilon' \omega_e' - (\upsilon'^2 + \upsilon') \omega_e' x_e' . \qquad (4.1)$$

The fitted molecular constants ω_e' and $\omega_e' x_e'$ were then used to calculate the expected isotope shift using[81]

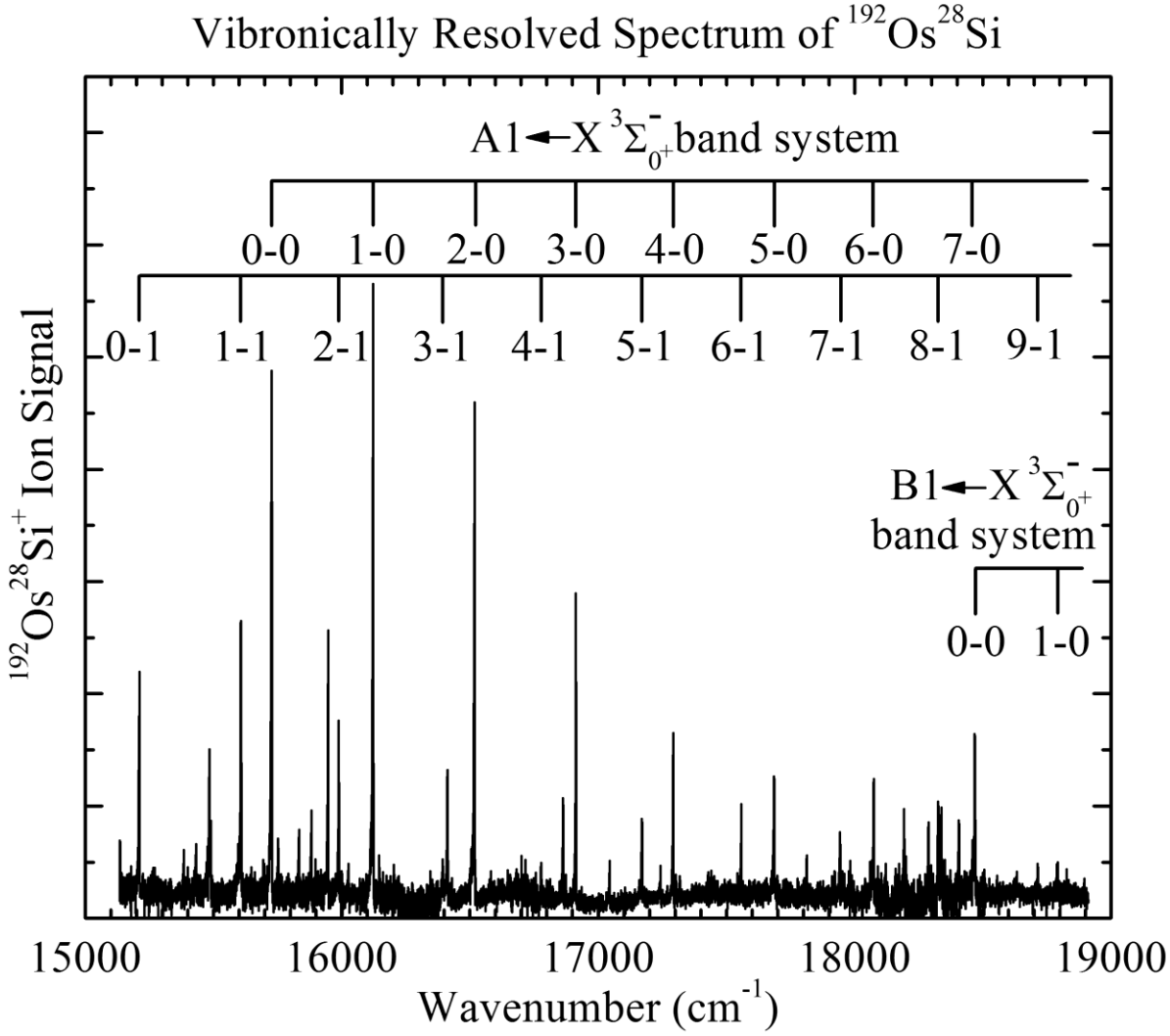

Figure 4.1 Vibronically resolved spectrum of $^{192}Os^{28}Si$, with vibronic transitions belonging to the A1 ← X $^3\Sigma^-_{0^+}$ and B1 ← X $^3\Sigma^-_{0^+}$ band systems indicated.

Table 4.1 Measured vibronic bands of OsSi.[a]

Band	Measured ν_0 for $^{192}Os^{28}Si$ [b]	Isotope shift $\nu(^{190}Os^{28}Si)-\nu(^{192}Os^{28}Si)$ [b]	B′	Ω′	τ (μs) [c]
A-X 0-1	15210.74	-0.19			
A-X 1-1	15607.63	-0.11			
A-X 0-0	15727.2143(20)	-0.0095(26)	0.13783(6)	1	1.07(12)
A-X 2-1	15989.69	1.42			
A-X 1-0	16123.7918(21)	0.2555(25)	0.13709(6)	1	1.06(3)
A-X 3-1	16395.73	0.44			
A-X 2-0	16518.40	0.15			
A-X 4-1	16776.23	0.89			
A-X 3-0	16912.45	0.91			
A-X 5-1	17170.38	1.05			
A-X 4-0	17292.51	1.30			
A-X 6-1	17558.2584(39)	1.2195(48)	0.13432(22)	1	1.05(4)
A-X 5-0	17686.7884(53)	1.3835(65)	0.13888(10)	1	
A-X 7-1	17943.3179(37)	1.4402(47)	0.13382(20)	1	1.18(3)
A-X 6-0	18074.5689(28)	1.5562(39)	0.13442(6)	1	1.14(21)
A-X 8-1	18326.64	1.46			
A-X 7-0	18459.6389(42)	1.7605(59)	0.13306(9)	1	
A-X 9-1	18714.20	1.70			
B-X 0-0	18468.7147(32)	0.0305(41)	0.14263(7)	1	8.31(33)
B-X 1-0	18792.8211(16)	0.1734(26)	0.14174(8)	1	6.16(60)
U[d]	15384.33	0.57			
U[d]	15431.78	0.79			
U[d]	15484.17	0.42			
U[d]	15489.03	-0.17			
U[d]	15753.06	0.18			
U[d]	15833.10	0.65			
U[d]	15882.47	0.08			
U[d]	15947.26	0.90			
U[d]	16026.89	0.13			
U[d]	16412.92	0.90			
U[d]	16863.19	1.36			
U[d]	17044.37	1.30			
U[d]	17242.17	0.49			
U[d]	17813.78	1.30			
U[d]	17922.72	-0.10			
U[d]	18193.66	2.19			
U[d]	18287.99	1.07			
U[d]	18338.03	0.13			
U[d]	18406.75	0.11			

Table 4.1 Continued

[a] All values are in cm^{-1} units unless otherwise specified; 1σ error limits are provided in parentheses, in units of the last digit quoted. [b] Band origins that have been determined in rotationally resolved scans are given to four digits after the decimal, with the 1σ error provided. Band origins quoted to only two digits are estimated from low resolution measurements, and are thought to be accurate to better than 1 cm^{-1}. Similarly, isotope shifts measured in low resolution are quoted to two digits. These are generally accurate to 0.1 cm^{-1}, based on comparisons to high resolution measurements. Weaker features may have larger errors. When four digits and an error estimate are provided, the feature was measured in a well-calibrated high resolution scan. [c] Excited state exponential decay lifetime. [d]Unclassified band.

$$\nu(^{190}Os^{28}Si) - \nu(^{192}Os^{28}Si) = (\rho-1)[\omega_e'(\upsilon'+½)-\omega_e''(½)]-(\rho^2-1)[\omega_e'x_e'(\upsilon'+½)^2-\omega_e''x_e''(½)^2], \quad (4.2)$$

where ρ is given as $\rho = \sqrt{\frac{\mu(^{192}Os^{28}Si)}{\mu(^{190}Os^{28}Si)}} = 1.00067$. By treating equations (4.1) and (4.2) as functions of a continuous parameter, v', it was possible to plot the expected isotope shift, $\nu(^{190}Os^{28}Si) - \nu(^{192}Os^{28}Si)$, as a function of the band frequency, $\nu_{v'-0}$, for various assignments of the bands. The resulting nearly linear curves were compared to the measured isotope shifts to identify the correct vibrational numbering. In equation (4.2), the ground state vibrational frequency, ω_e'', was taken as 516.32 cm^{-1} based on the separation between cold bands and their corresponding hot bands (see below), and the anharmonicity, $\omega_e''x_e''$, was neglected. The result, displayed in Figure 4.2, shows clearly that the 15 927 cm^{-1} band is the 0-0 band of the A-X system. This assignment gives vibrational constants of the A state of ω_e'=396.97(75) and $\omega_e'x_e'$=0.839(95) cm^{-1} for the $^{192}Os^{28}Si$ isotopologue.

Also evident in Figure 4.1 is a progression of weaker features displaced to the red of the main bands of the A-X system by approximately 516 cm^{-1}. To verify that these are hot bands arising from v''=1, the assigned 6-0, 6-1, 7-0, and 7-1 bands were examined with rotational resolution to verify that the $\Delta G_{1/2}''$ values, obtained as $\nu_{6-0} - \nu_{6-1}$ and $\nu_{7-0} - \nu_{7-1}$, were the same. The $\Delta G_{1/2}''(^{192}Os^{28}Si)$ values were in good agreement, 516.3105(48) and 516.3210(56) cm^{-1}, confirming the assignment of the v'-1 hot bands. Similar agreement was found for $\Delta G_{1/2}''(^{190}Os^{28}Si)$, but the quality of the data did not permit similar measurements for $\Delta G_{1/2}''(^{189}Os^{28}Si)$.

Excited state lifetimes were measured for several bands belonging to the A-X system, and all were found to be in the range from 1.05 to 1.18 μs. These values are

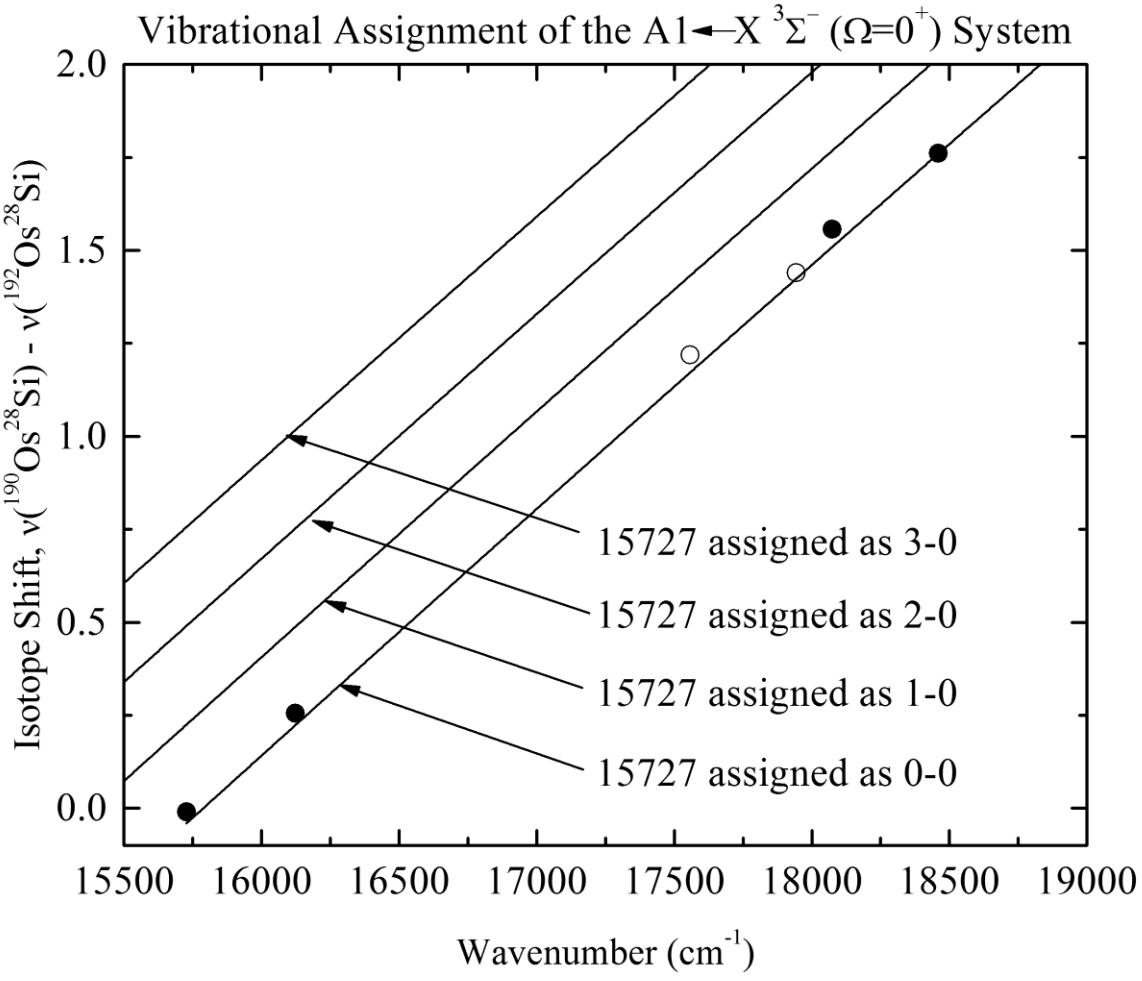

Figure 4.2 Isotope shift plot for the A1 ← X $^3\Sigma^-_{0^+}$ system of OsSi. The lines provide the expected isotope shifts based on various assignments. The filled data points give the measured isotope shifts for v′-0 bands; the open symbols for v′-1 bands. It is apparent that the 15 727 cm^{-1} band is the 0-0 band for this system.

typical of allowed transitions in transition metal diatomics in the red portion of the spectrum. Figure 4.3 displays a measured set of data points for the decay lifetime of the v′=1 level of the A state along with the fitted decay curve.

Near the blue end of the scanned region there are two bands, near 18 469 cm^{-1} and 18 790 cm^{-1}, that are assigned to the B-X system. At first we thought that the 18 469 cm^{-1} band was the 7-0 band of the A-X system, but its band origin is displaced about 10 cm^{-1} from the expected position, and its upper state lifetime is about a factor of 7 longer than the lifetimes of the other bands in the A-X system. The A-X 7-0 band was subsequently found as a much weaker feature, which was successfully rotationally resolved. The two bands near 18 469 and 18 790 cm^{-1} have similar upper state rotational constants and lifetimes, and exhibit isotope shifts that are consistent with assignments as the 0-0 and 1-0 bands of a new system. Therefore, they are assigned as the 0-0 and 1-0 bands of the B-X system. The strong spin-orbit interaction that is operative in this molecule makes it likely that the B-X system borrows its intensity from the nearby A-X system.

4.3.2 Rotationally Resolved Spectra of OsSi

Figure 4.4 displays a rotationally resolved scan over the 1-0 band of the A-X system, along with a negative-going simulation of the spectrum that was computed using the PGopher program,[82] in blue. The band displays P, Q, and R branches with a small gap between the first Q and R lines, indicative of small Ω values in the upper and lower states. There is also a band head in the R branch, establishing that the rotational constant decreases upon electronic excitation, corresponding to a lengthening of the Os-Si bond. The first lines were found to be R(0), Q(1), and P(2), thereby identifying the band as an

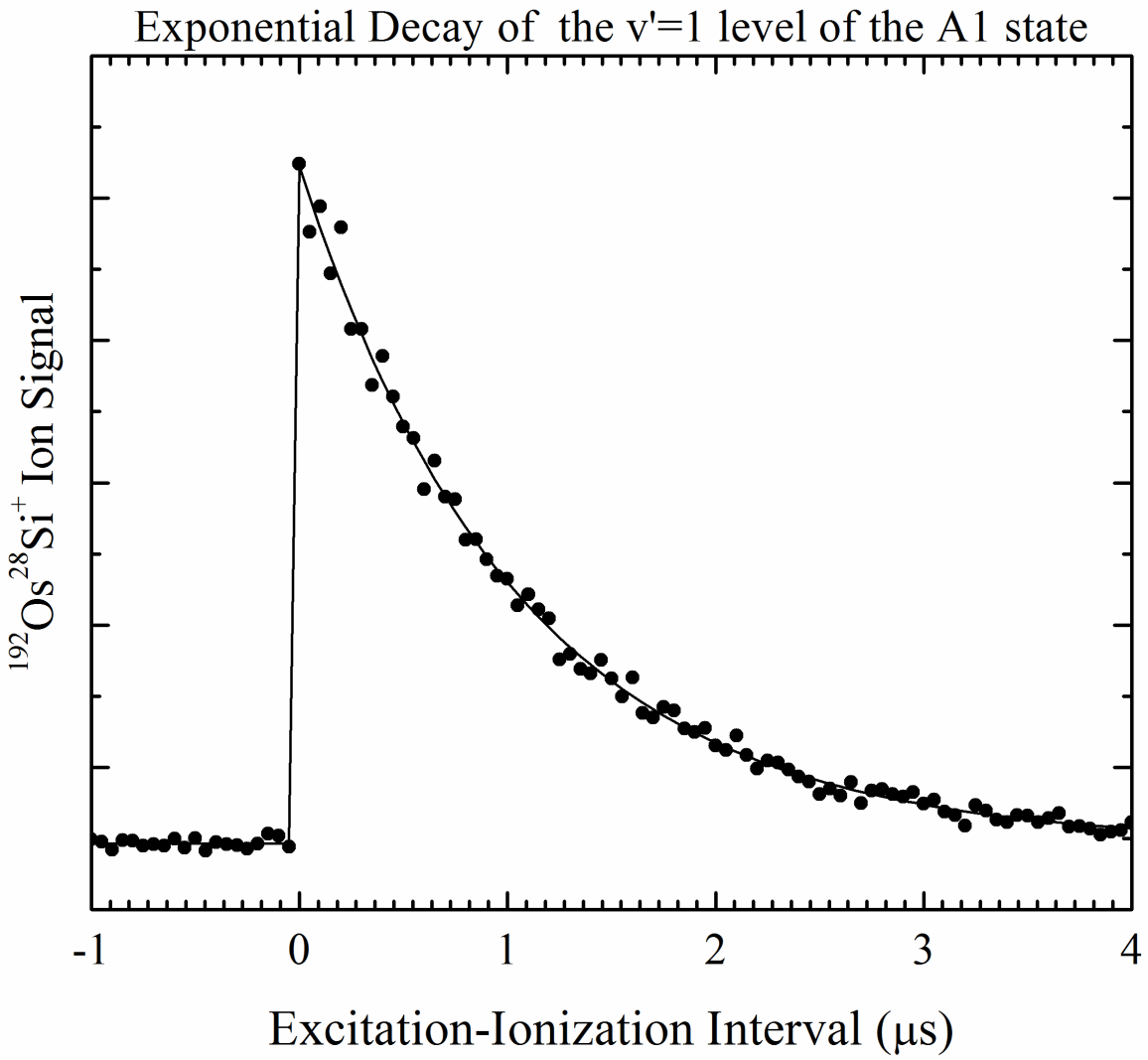

Figure 4.3 Lifetime measurement for the v′=1 level of the A state. From three datasets similar in quality to this one, a value of $\tau = 1.06(3)$ μs is obtained.

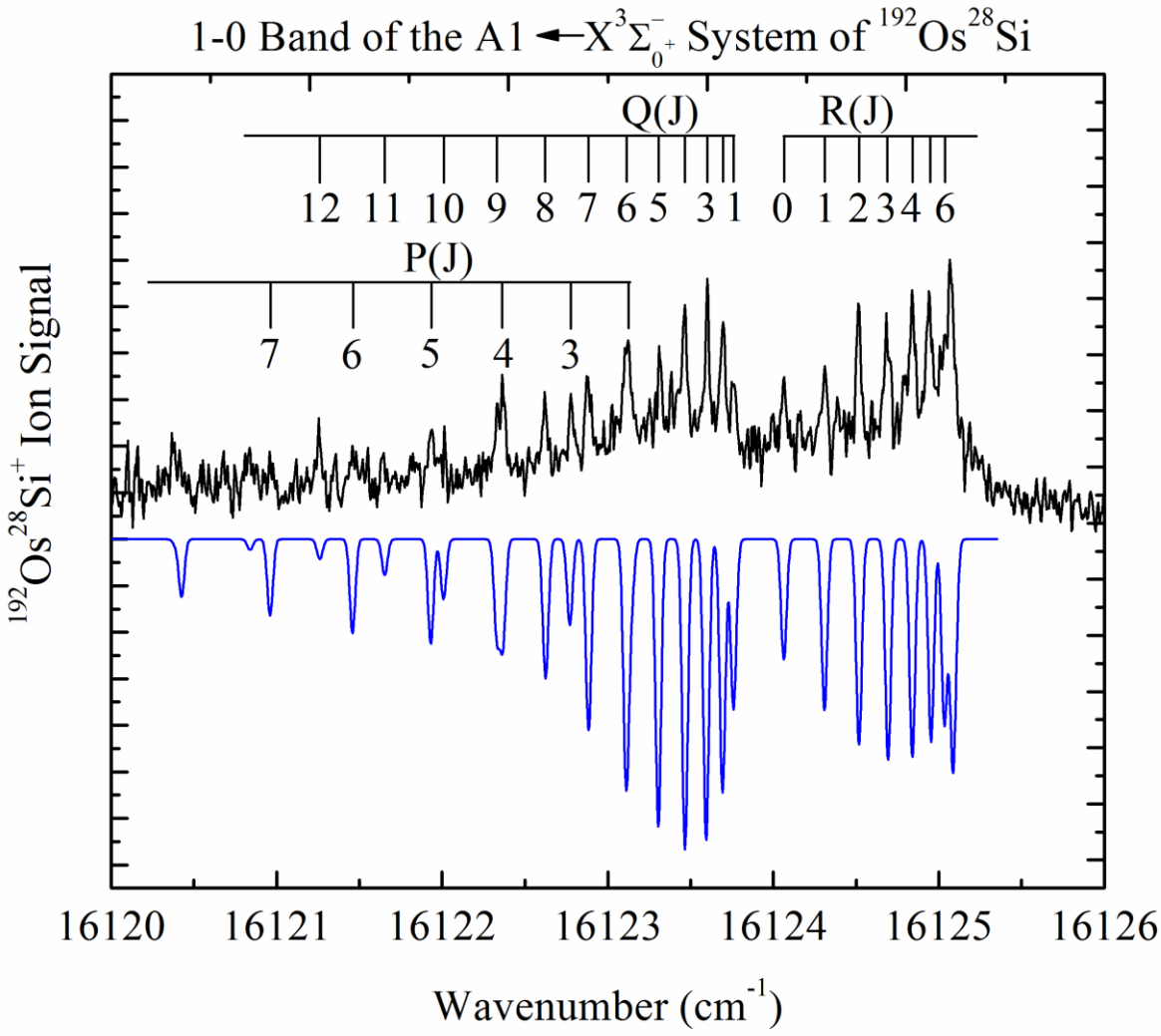

Figure 4.4 Rotationally resolved scan over the 1-0 band of the A1 ← X $^3\Sigma^-_{0^+}$ system of ^{192}Os^{28}Si.

$\Omega' = 1 \leftarrow \Omega'' = 0$ transition, which is consistent with the other rotationally resolved bands of the A-X system.

The 1-0 band of the B-X system, located near 18 793 cm^{-1}, is displayed in Figure 4.5. This band has the same general characteristics as the 1-0 band of the A-X system: a band head in the R-branch and first lines of R(0), Q(1), and P(2). It is likewise an $\Omega'=1 \leftarrow \Omega''=0$ transition, in which the upper state bond length is longer than the ground state bond length.

All bands in the A-X and B-X systems that were rotationally resolved were fitted to the Hund's case (a) or (c) formula[81]

$$\nu = \nu_0 + B'J'(J'+1) - B"J"(J"+1). \quad (4.3)$$

In doing so, bands originating from the same lower level were simultaneously fitted to extract the most accurate values of B_0'' and B_1'' for the ground state. Any lambda doubling that may be present is beyond our ability to resolve, so that equation (4.3) is adequate for the description of the levels. Measured line positions, residuals, and molecular constants are provided in Appendix B, along with graphs of the recorded spectra and band positions measured in low-resolution scans. In Table 4.2 fitted vibronic and rotational constants for the X, A, and B states are provided for the $^{192}Os^{28}Si$, $^{190}Os^{28}Si$, and $^{189}Os^{28}Si$ isotopologues. Here, as elsewhere in this report, the value in parentheses represents the 1σ error limit, in units of the last digits quoted. These error limits reflect the error in the least-squares fitting procedure and do not reflect any other sources of error. During these studies, we noted a significant variation in signal intensity

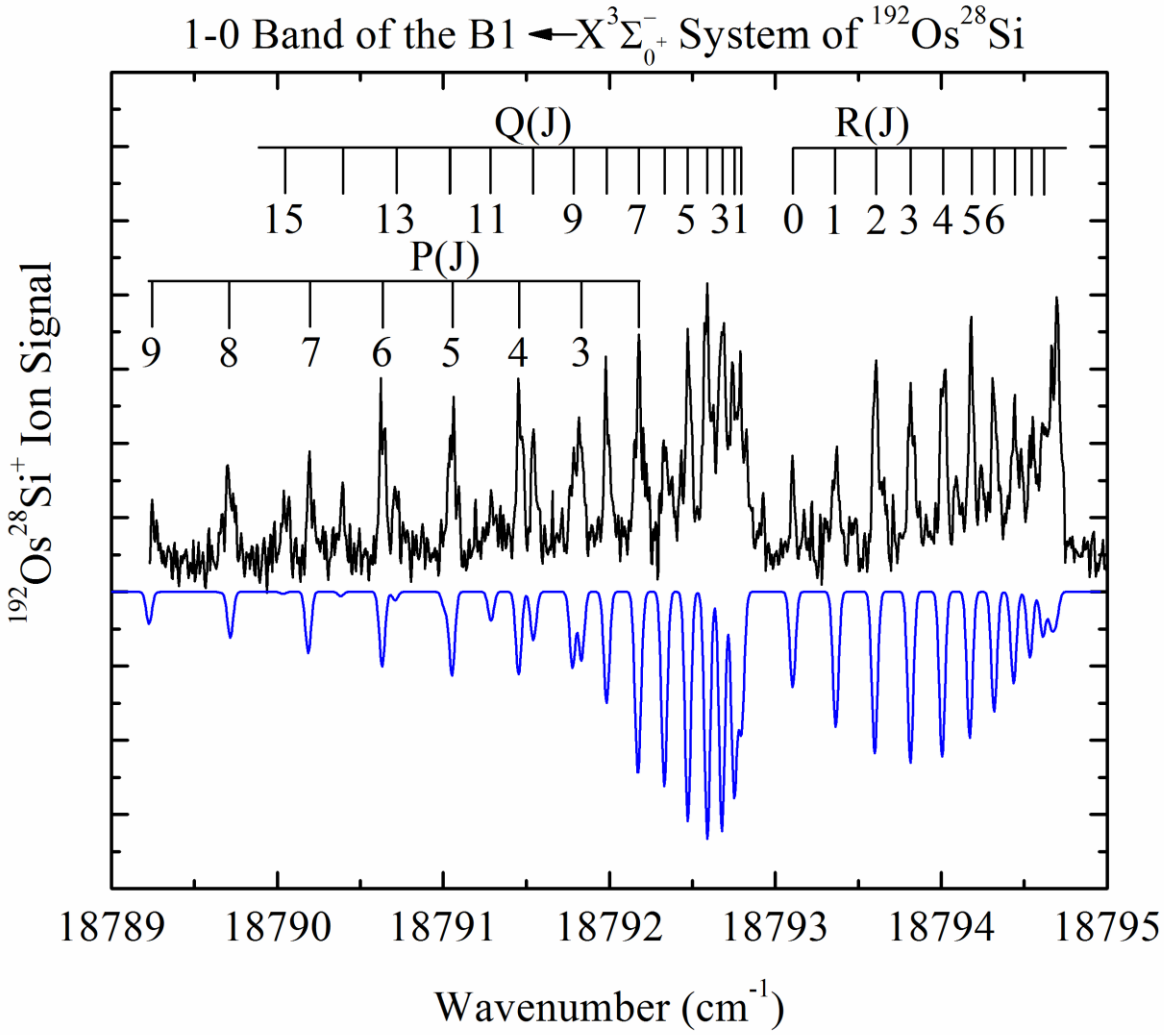

Figure 4.5 Rotationally resolved scan over the 1-0 band of the B1 ← X $^3\Sigma^-_{0^+}$ system of ^{192}Os^{28}Si.

Table 4.2 Molecular constants of OsSi.

Electronic State	Molecular constant	$^{192}Os^{28}Si$	$^{190}Os^{28}Si$	$^{189}Os^{28}Si$
$X\ ^3\Sigma_{0^+}^-$	$\Delta G_{1/2}$	516.3149(36)	516.6450(31)	516.8333(55)
	B_0''	0.15332(8)	0.15317(6)	0.15350(8)
	B_1''	0.15242(21)	0.15297(14)	0.15248(17)
	B_e''	0.15377(14)	0.15327(10)	0.15401(12)
	α_e''	0.00090(22)	0.00020(15)	0.00102(19)
	r_e''	2.1189(10)	2.1238(7)	2.1194(8)
	Recommended r_e''	2.1207(27)		
A1	T_0	15727.734(702)	15727.702(672)	15727.205
	ω_e'	396.97(75)	397.31(72)	399.06
	$\omega_e'x_e'$	0.839(95)	0.849(91)	1.042
	B_e'	0.13804(20)	0.13724(164)	0.13817(18)
	α_e'	0.00035(78)	0.00025(66)	0.00053(7)
	r_e'	2.236(16)	2.244(13)	2.2376(15)
	Recommended r_e'	2.2394(43)		
B1	T_0	18468.7147(32)	18468.7452(26)	18468.7644(24)
	$\Delta G_{1/2}$	324.1064(36)	324.2493(33)	324.3268(31)
	B_e'	0.14308(10)	0.14275(12)	0.14308(9)
	α_e'	0.00089(11)	0.00074(13)	0.00077(11)
	r_e'	2.1966(8)	2.2006(9)	2.1988(7)
	Recommended r_e'	2.1987(20)		

during the scans, which ultimately was determined to result from the build-up of powdered SiO_2 in the body of the pulsed supersonic valve, due to the reaction of $SiH_4$with residual atmosphere. This variation made it more difficult to pick out the rotational lines for some of the bands, due to the lines lying upon a randomly fluctuating background signal. As a result, the variations in r_e bond lengths between the different isotopologues should not be considered significant, and these values have been averaged to provide recommended values of the r_e bond length of the X, A, and B states.

4.4 Discussion

As noted above, all of the rotationally resolved bands arise from the same lower electronic state, characterized by $\Omega'' = 0$. To deduce the molecular configuration and term that leads to this ground level, it is useful to review the valence molecular orbitals of diatomics composed of a transition metal and a p-block element. Considering only the valence 5d and 6s orbitals of osmium, and the 3s and 3p orbitals of silicon, the molecular orbitals, in order of qualitatively increasing energy are the following:

1σ – composed primarily of Si 3s character

2σ – a bonding combination of primarily Si $3p\sigma$ and Os $5d\sigma$ character

1π – a bonding combination of Si $3p\pi$ and Os $5d\pi$ orbitals

3σ – a mostly nonbonding orbital composed primarily of Os 6s character

1δ – nonbonding orbitals of nearly pure Os 5d character

2π – antibonding orbitals composed of Os $5d\pi$ and Si $3p\pi$ character

4σ – antibonding orbital of mainly Os $5d\sigma$ and Si $3p\sigma$ character.

In most of the diatomic molecules composed of a transition metal and a p-block

element, the nonbonding 3σ and 1δ orbitals lie quite close in energy and their ordering varies from molecule to molecule. A major issue in the electronic structure of 12-electron molecules like OsSi centers on the occupation numbers of these orbitals in the ground state.

Comparing to other known 12-electron transition metal-p block diatomic molecules, the possible ground configurations, terms, and levels are $1\sigma^2 2\sigma^2 1\pi^4 1\delta^4$, X $^1\Sigma_{0+}^+$, as found in RuC;[28-31] $1\sigma^2\, 2\sigma^2\, 1\pi^4\, 1\delta^3\, 3\sigma^1$, X $^3\Delta_3$, as found in FeC,[32-36] OsC,[37-38] and RuSi;[39-40] $1\sigma^2\, 2\sigma^2\, 1\pi^4\, 3\sigma^2 1\delta^2$, X $^3\Sigma_{0+}^-$, as found in WO[41-49] and ReN;[33, 50-53] and $1\sigma^2\, 2\sigma^2\, 1\pi^4\, 1\delta^2\, 3\sigma^1\, 2\pi^1$, X $^5\Pi_{-1}$, as found in CrO[54-61], CrS[62-63], and MoO.[57, 64-67] Of these, only the $1\sigma^2\, 2\sigma^2\, 1\pi^4\, 1\delta^4$, X $^1\Sigma_{0+}^+$ and $1\sigma^2\, 2\sigma^2\, 1\pi^4\, 3\sigma^2 1\delta^2$, X $^3\Sigma_{0+}^-$ possibilities are consistent with a ground state Ω″ value of 0. Our experiments do not distinguish between these possibilities, but the relativistic stabilization of the 6s orbital in osmium strongly favors the assignment as the $1\sigma^2\, 2\sigma^2\, 1\pi^4\, 3\sigma^2 1\delta^2$, X $^3\Sigma_{0+}^-$ configuration and term.

This assignment is made even more likely by the strong second-order spin-orbit interaction between the $1\sigma^2\, 2\sigma^2\, 1\pi^4\, 3\sigma^2 1\delta^2$, $^3\Sigma_{0+}^-$ level and the higher-lying $1\sigma^2\, 2\sigma^2\, 1\pi^4\, 3\sigma^2 1\delta^2$, $^1\Sigma_{0+}^+$ level, which causes the $^3\Sigma_{0+}^-$ level to be significantly lowered relative to the $^3\Sigma_1^-$ level. A straightforward two-state treatment of the interaction between these levels using the matrix Hamiltonian[83]

$$\underline{\underline{\mathbf{H}}} = \begin{pmatrix} \mathrm{T}(\,^3\Sigma_{0+}^-) & 2\zeta_{5d}(\mathrm{Os}) \\ 2\zeta_{5d}(\mathrm{Os}) & \mathrm{T}(\,^1\Sigma_{0+}^+) \end{pmatrix} \tag{4.4}$$

using the value $\zeta_{5d}(\mathrm{Os})$ = 3045 cm^{-1} (Ref. 84) shows that for zeroth-order energy

differences between the $^1\Sigma_{0+}^+$ and $^3\Sigma_{0+}^-$ levels, T($^1\Sigma_{0+}^+$) - T($^3\Sigma_{0+}^-$), of 5 000 to 15 000 cm^{-1}, the resulting lowering of the $^3\Sigma_{0+}^-$ level ranges from 4083 to 2161 cm^{-1}. This is a significant drop in the $^3\Sigma_{0+}^-$ energy that is above and beyond the stabilization of the $1\sigma^2$ $2\sigma^2$ $1\pi^4$ $3\sigma^2 1\delta^2$ configuration that results from the relativistic stabilization of the 6s-like 3σ orbital. In the isoelectronic ReN molecule, the lowering of the $^3\Sigma_{0+}^-$ level relative to the $^3\Sigma_1^-$ level is 2616 cm^{-1};[51-52] in OsSi the $^3\Sigma_{0+}^-$ level is expected to be stabilized by a similar amount.

The $1\sigma^2$ $2\sigma^2$ $1\pi^4$ $3\sigma^2 1\delta^2$, X $^3\Sigma_{0+}^-$ state is also calculated to be the ground state in B3LYP density functional calculations using the LANL2DZ basis set by Wu and Su.[39] Their values of r_e (2.139 Å) and ω_e (520 cm^{-1}) are also in good agreement with our measured values of r_e (2.121 Å) and $\Delta G_{1/2}$ (516 cm^{-1}). For all of these reasons, we assign the OsSi ground state to be $1\sigma^2$ $2\sigma^2$ $1\pi^4$ $3\sigma^2 1\delta^2$, X $^3\Sigma_{0+}^-$.

The well-known relativistic stabilization of the 6s orbital in the 5d series of transition metals and in the 6p elements explains many aspects of the chemistry of these heavy metal species. For example, the stabilization of the 6s orbital (i) causes Ir, Pt, and Au to be noble metals with high ionization energies, (ii) is responsible for the stabilization of low-valent oxidation states in the 6p elements, leading to stable oxidation states such as Tl^+, and Pb^{2+}, and (iii) increases the bond energies of systems dominated by 6s-6s bonding so that Au_2 has a much greater bond energy than Ag_2, and gives Hg_2^{2+} a bond energy that is sufficient to stabilize the diatomic dication in aqueous solution.[84-86] The relativistic increase in the 6p ← 6s excitation energy due to the stabilization of the 6s orbital is also responsible for the low melting point of mercury, making it a liquid metal at room temperature.[84-87]

In the diatomic transition metal carbides and silicides, the relativistic stabilization of the 6s atomic orbital leads to a stabilization of the 3σ molecular orbital, which is then preferentially populated in the diatomics composed of 5d series metals. This is illustrated in Tables 4.3 and 4.4, which summarize the current experimental and computational knowledge of the diatomic transition metal silicides and carbides, respectively. In comparing the 4d series to the 5d series, the effect of the relativistic stabilization of the 3σ orbital is obvious. In each of the 5d transition metal molecules TaC, WC, OsC, IrC, AuC, TaSi, IrSi, and now OsSi, the number of electrons in the 3σ orbital in the ground state is found to be one greater than in the isovalent 4d transition metal molecules NbC, MoC, RuC, RhC, AgC, NbSi, RhSi, and RuSi. The preferential population of the 3σ orbital in the 5d series leads to different ground terms in the two groups of molecules.

The A1 electronic state of OsSi displays a fluorescence lifetime that ranges between 1.05 and 1.18 μs, depending on the vibrational level that is probed. Assuming that fluorescence returns the molecule to the X $^3\Sigma^-_{0^+}$ ground state, this lifetime implies an absorption oscillator strength of f ≈ 0.005, a value that is typical of allowed transitions in transition metal diatomics in the red region of the spectrum. If we assume that the $^3\Sigma^-_1$-$^3\Sigma^-_{0^+}$ splitting in OsSi matches the 2616 cm^{-1} splitting found in ReN, analysis of the the two-state matrix Hamiltonian (4.1) provides that the ground $\Omega=0^+$ level has 85% $1\sigma^2\,2\sigma^2\,1\pi^4\,3\sigma^2 1\delta^2$, $^3\Sigma^-_{0^+}$ character and 15% $1\sigma^2\,2\sigma^2\,1\pi^4\,3\sigma^2 1\delta^2$, $^1\Sigma^+_{0^+}$ character. An allowed transition to an upper state with $\Omega'=1$ then suggests that the upper state is primarily of $^3\Pi_1$ symmetry. On this basis we tentatively suggest that the A1 state is dominated by $^3\Pi_1$ character.

Table 4.3 Experimental and [computational] data on the ground states of the diatomic transition metal silicides.[a]

ScSi $[1\pi^2 3\sigma^1, {}^4\Sigma^-]$ [2.519 Å][c] [348 cm^{-1}][d] 2.32(15) eV [8, 39]	TiSi $[1\pi^2 3\sigma^1 1\delta^1, {}^5\Delta]$ [2.447 Å][c] [359 cm^{-1}][d] [2.28 eV] [39, 88]	**VSi**[f] $1\pi^4 1\delta^1, {}^2\Delta$ [2.399 Å][c] [362 cm^{-1}][d] [1.98 eV] [19, 39]	CrSi $[1\pi^3 1\delta^2 3\sigma^1, {}^5\Pi]$ [2.425 Å][c] [294 cm^{-1}][d] [1.54 eV] [39]	MnSi $[1\delta^2 3\sigma^1, {}^4\Sigma^-]$ [2.308 Å][c] [325 cm^{-1}][d] [1.76 eV] [39]	FeSi $[1\delta^2 3\sigma^2, {}^3\Sigma^-]$ [2.170 Å][c] [382 cm^{-1}][d] 3.04(26) eV [10, 39]	CoSi $[1\delta^4 3\sigma^1, {}^2\Sigma^+]$ [2.123 Å][c] [392 cm^{-1}][d] 2.81(18) eV [10, 39]	**NiSi** $1\delta^4 3\sigma^2, {}^1\Sigma^+$ 2.0316(4) Å[b] 467.4 cm^{-1}[d] 3.26(18) eV [10, 39, 68]	CuSi $3\sigma^2 2\pi^1, {}^2\Pi_{1/2}$ [2.242 Å] 330(15) cm^{-1}[e] 2.21(6) eV [13, 20, 24, 39, 89-93]
YSi $[1\pi^2 3\sigma^1, {}^4\Sigma^-]$ [2.677 Å][c] [305 cm^{-1}][d] 2.63(18) eV [9, 39]	ZrSi $[1\pi^2 3\sigma^1 1\delta^1, {}^5\Delta]$ [2.554 Å][c] [350 cm^{-1}][d] [2.72 eV] [26-27, 39, 94]	**NbSi**[f] $1\pi^4 1\delta^1, {}^2\Delta$ [2.365 Å][c] [386 cm^{-1}][d] [2.59 eV] [19, 27, 39]	MoSi $[1\pi^3 1\delta^2 3\sigma^1, {}^5\Pi]$ [2.359 Å][c] [336 cm^{-1}][d] [2.06 eV] [27, 39]	TcSi $[1\delta^2 3\sigma^1, {}^4\Sigma^-]$ [2.177 Å][c] [3.69 eV] [39]	**RuSi** $1\delta^3 3\sigma^1, {}^3\Delta_3$ 2.0921(4) Å[b] [493 cm^{-1}][d] 4.08(22) eV [11, 39-40]	**RhSi** $1\delta^4 3\sigma^1, {}^2\Sigma^+$ 2.0425 Å[b] 522 cm^{-1}[d] 4.05(19) eV [11, 39, 95]	**PdSi** $1\delta^4 3\sigma^2, {}^1\Sigma^+$ 2.0824(3) Å[b] [473 cm^{-1}] 2.66(12) eV [11-12, 27, 39, 69]	AgSi $[3\sigma^2 2\pi^1, {}^2\Pi_{1/2}]$ [2.428 Å] 296.9 cm^{-1}[d] 1.77(10) eV [13, 21, 39, 92-93]
LaSi $[2\sigma^1 1\pi^4, {}^2\Sigma^+]$ [2.532 Å][c] [377 cm^{-1}][d] [2.46 eV] [39]	HfSi $[1\pi^3 3\sigma^1, {}^3\Pi]$ [2.406 Å][c] [390 cm^{-1}][d] [2.68 eV] [39]	TaSi $[1\pi^3 1\delta^1 3\sigma^1, {}^4\Phi]$ [2.356 Å][c] [404 cm^{-1}][d] [2.68 eV] [39]	WSi $[1\pi^3 1\delta^2 3\sigma^1, {}^5\Pi]$ [2.329 Å][c] [391 cm^{-1}][d] [2.96 eV] [27, 39]	ReSi $[1\delta^2 3\sigma^1, {}^4\Sigma^-]$ [2.194 Å][c] [461 cm^{-1}][d] [3.12 eV] [39]	**OsSi** $3\sigma^2 1\delta^2, {}^3\Sigma^-$ 2.121(3) Å[c] 516.3 cm^{-1}[e] [4.14 eV] [39]	**IrSi** $3\sigma^2 1\delta^3, {}^2\Delta_{5/2}$ 2.0899(1) Å[b] 533.4 cm^{-1}[e] 4.76(22) eV [11, 39, 70-71]	**PtSi** $1\delta^4 3\sigma^2, {}^1\Sigma^+$ 2.06149 Å[b] 549.0(3) cm^{-1}[d] 5.15(19) eV [11, 23, 39, 72]	AuSi $[3\sigma^2 2\pi^1, {}^2\Pi_{1/2}]$ [2.290 Å] 400(2) cm^{-1}[d] 3.06(6) eV [11, 14, 22, 39, 92-93, 96-97]

Table 4.3 Continued

[a]Molecules for which the ground configuration and term are experimentally known are indicated in **bold**. Quantities in square brackets are obtained from computational studies. The first entry provides the dominant electronic configuration and term, followed by the bond length (Å), vibrational frequency (cm^{-1}), dissociation energy (D_0, eV), and references. Here, D_0 is defined as the difference in energy between the ground state of the separated atoms and the v=0 level of the ground state of the molecule. When computational results are provided, they are from the DFT study by Wu and Su (reference [39]). [b] r_0 value; [c] r_e value; [d] ω_e value; [e]$\Delta G_{1/2}$ value; [f] In the cases of VSi and NbSi, matrix isolation studies have been interpreted as indicating a $^2\Delta$ ground state in which the orbital angular momentum is significantly quenched by the matrix. This differs from the computational work, which finds a $1\pi^2 3\sigma^1 1\delta^2$, $^6\Sigma^+$ ground term for VSi and a $1\pi^3 1\delta^1 3\sigma^1$, $^4\Phi$ ground term for NbSi. The reported bond lengths, vibrational frequencies, and dissociation energies are for the computed $^6\Sigma^+$ and $^4\Phi$ states, respectively.

Table 4.4 Experimental and [computational] data on the ground states of the diatomic transition metal carbides.

ScC $[2\sigma^2\ 1\pi^3, {}^2\Pi]$ [1.988 Å][c] [690 cm^{-1}][d] <4.47(21) eV 98-102	**TiC** $2\sigma^1\ 3\sigma^1, {}^3\Sigma^+$ 1.695(2) Å[b] 889(1) cm^{-1} [d] 3.82(24) eV 103-107	**VC** $1\pi^4 1\delta^1, {}^2\Delta_{3/2}$ 1.6167(3) Å [925 cm^{-1}][d] [3.97 eV] 108-111	**CrC** $1\delta^2\ 3\sigma^0, {}^3\Sigma^-$ (0^+) 1.6188(6)Å[b] [833 cm^{-1}][d] [4.068 eV] 112-113	MnC $[1\delta^2\ 3\sigma^1, {}^4\Sigma^-]$ [1.640 Å][c] [627 cm^{-1}] [3.03 eV] 114-115	**FeC** $1\delta^3\ 3\sigma^1, {}^3\Delta_3$ 1.58885 Å[c] 863(6) cm^{-1} [d] 3.80(30) eV 32, 35-36, 116-123	**CoC** $1\delta^4\ 3\sigma^1, {}^2\Sigma^+$ 1.5612 Å[b] 955 cm^{-1} [d] 3.75(30) eV 116, 124-130	**NiC** $1\delta^4\ 3\sigma^2, {}^1\Sigma^+$ 1.627 Å[c] 875.2 cm^{-1} [d] [4.048 eV] 127, 131-132	CuC $[3\sigma^2 2\pi^1, {}^2\Pi_{1/2}]$ [1.749 Å][c] [683.2 cm^{-1}][d] [2.56 eV] 133-134
YC $1\pi^3\ 2\sigma^1\ 3\sigma^1, {}^4\Pi_i$ 2.05 Å[b] 686(20) cm^{-1}[d] 4.35(20) eV 30, 135-137	**ZrC** $2\sigma^1\ 3\sigma^1, {}^3\Sigma^+$ 1.8066 Å[b] 888.8(8) cm^{-1} [d] <5.76 eV 30, 103, 138-139	**NbC** $1\pi^4 1\delta^1, {}^2\Delta_{3/2}$ 1.7003 Å[b] 980(15) cm^{-1} [d] 5.39(15) eV 19, 30, 108, 140-141	**MoC** $1\delta^2\ 3\sigma^0, {}^3\Sigma^-$ (0^+) 1.688 Å [b] 1008(7) cm^{-1} [d] 5.01(13) eV 30, 108, 142-144	TcC $[1\delta^2\ 3\sigma^1, {}^4\Sigma^-]$ [1.664 Å][c] [1051 cm^{-1}][d] 6.07(9) eV 30, 145	**RuC** $1\delta^4, {}^1\Sigma^+$ 1.608 Å[b] 1100(2) cm^{-1} [d] 6.22(11) eV 28-31, 144, 146-153	**RhC** $1\delta^4\ 3\sigma^1, {}^2\Sigma^+$ 1.6134 Å [c] 1049.87 cm^{-1} [d] 5.97(4) eV 30, 154-163	**PdC** $1\delta^4\ 3\sigma^2, {}^1\Sigma^+$ 1.712 Å[b] 848(2) cm^{-1} [d] [3.01 eV] 30, 144, 164-167	AgC $[3\sigma^1 2\pi^2, {}^4\Sigma^-]$ [1.936 Å][c] [539.4 cm^{-1}][d] [2.01 eV] 30, 134
LaC $[2\sigma^1, {}^2\Sigma^+]$ [2.030 Å][c] [718 cm^{-1}][d] 4.65(20) eV 37, 168	HfC $[2\sigma^1\ 3\sigma^1, {}^3\Sigma^+]$ [1.739 Å][c] [960 cm^{-1}][d] <5.55 eV 37, 103	**TaC** $2\sigma^2 1\pi^4 3\sigma^1, {}^2\Sigma^+$ 1.7490(1) Å[b] [944 cm^{-1}][d] [4.53 eV] 37, 169	**WC** $1\delta^1\ 3\sigma^1, {}^3\Delta_1$ 1.7143(2) Å[b] 983(4) cm^{-1} [d] [5.16 eV] 37, 170-175	ReC $[1\delta^2\ 3\sigma^1, {}^4\Sigma^-]$ [1.692 Å][c] [1046 cm^{-1}] [5.40 eV] 37	**OsC** $1\delta^3\ 3\sigma^1, {}^3\Delta_3$ 1.6727 Å[b] [1110 cm^{-1}][c] 6.15(14) eV 37-38, 176-177	**IrC** $3\sigma^2 1\delta^3, {}^2\Delta_{5/2}$ 1.6858 Å[b] 1060(1) cm^{-1} [d] 6.50(5) eV 37, 146, 178-184	**PtC** $1\delta^4\ 3\sigma^2, {}^1\Sigma^+$ 1.6767 Å[c] 1051.1 cm^{-1} [d] 6.30(7) eV 37, 156, 185-192	AuC $[3\sigma^2 2\pi^1, {}^2\Pi_{1/2}]$ [1.805 Å][c] [781.7 cm^{-1}][d] [3.36 eV] 37, 134

Table 4.4 Continued

[a] Molecules for which the ground configuration and term are experimentally known are indicated in **bold**. Quantities in square brackets are obtained from computational studies. The first entry provides the dominant electronic configuration and term, followed by the bond length (Å), vibrational frequency (cm^{-1}), dissociation energy (D_0, eV), and references. Here, D_0 is defined as the difference in energy between the ground state of the separated atoms and the v=0 level of the ground state of the molecule. [b] r_0 value; [c] r_e value; [d] ω_e value; [e] $\Delta G_{1/2}$ value

The B1 electronic state exhibits a fluorescence lifetime of 6.1 to 8.3 μs. Again, if we assume that the fluorescence is dominated by fluorescence to the ground state, this implies an absorption oscillator strength of $f \approx 0.0006$, an order of magnitude weaker than the A-X system. This suggests that the B-X transition may be spin-forbidden, induced by the approximately 15% $^1\Sigma_{0+}^+$ character in the ground state wavefunction. If so, this would imply that the B1 state is dominated by $^1\Pi_1$ character.

In the isoelectronic WO molecule, $^3\Pi$ and $^1\Pi$ states arising from the $2\sigma^2\ 1\pi^4\ 3\sigma^2\ 1\delta^1\ 2\pi^1$ configuration have been calculated to lie 12 141 and 16 609 cm^{-1} above the $1\sigma^2\ 2\sigma^2\ 1\pi^4\ 3\sigma^2\ 1\delta^2$, X $^3\Sigma_{0+}^-$ ground state, respectively, neglecting spin-orbit interaction.[193] This is similar to the energies of the A1 and B1 states of OsSi, which are 15728 and 18469 cm^{-1}, respectively. Based on this correspondence, we tentatively suggest that the A1 and B1 states observed in the present study correspond to the $2\sigma^2\ 1\pi^4\ 3\sigma^2\ 1\delta^1\ 2\pi^1$, $^3\Pi_1$ and $^1\Pi_1$ states, respectively.

The transition metal carbides and silicides share a trend of decreasing bond length as one proceeds left to right in the periodic table, until the coinage metal molecules are reached. The major contributor to this trend is the decrease in both nd and (n+1)s orbital size as the nuclear charge of the metal atom is increased. This allows shorter bond lengths to be achieved as one moves to the right, which in turn leads to greater bond energies, in general. A sharp increase in bond length and corresponding decrease in bond energy occurs in the coinage group metal silicides and carbides (CuSi, CuC, and their congeners), because the antibonding 2π orbital is occupied for the first time in this group. For most of the transition metal series, it is the relatively nonbonding 1δ and 3σ orbitals that are being filled in the metal carbide, MC, and metal silicide, MSi, molecules; the fact

that these are primarily nonbonding in character allows the change in bond length to be dominated by the decrease in atomic orbital size rather than by changes in bond order.

In Tables 4.3 and 4.4, experimental results are presented when available; computational results are provided in square brackets when experimental results are absent. Another trend that is readily apparent is that there is much more experimental information available for the metal silicides on the right side of the table than for those on the left. The metal carbides on the right side of the table have likewise been far more thoroughly investigated than those on the left, although at least some experimental information is available for most of the carbides on the left side of the table. There are several reasons for the comparative lack of studies of the species from the left side of the transition metal series (the "early" transition metals). First, the species on the left are not as strongly bound as those on the right, so they are experimentally more difficult to produce. More importantly, however, other species exist that are more strongly bound that compete with the formation of the diatomic carbides and silicides. The "early" transition metals are much more oxophilic than the "late" transition metals, so laser ablation sources tend to produce copious quantities of the early transition metal oxides and far fewer carbides or silicides unless extreme care is taken to exclude oxygen from the source. In the late transition metals, the oxides are less strongly bound due to the occupation of the antibonding 2π and/or 4σ orbitals, and the carbides have similar or greater bond energies than the oxides. Thus, carbides such as FeC, NiC, RuC, RhC, OsC, IrC, and PtC are easily produced.

Another reason for the paucity of studies on the early transition metal carbides is that C_2 has a high electron affinity (3.269(6) eV)[194] and forms highly stable ionic adducts

with the more electropositive metals such as Sc, Y, La, Hf, and Ta. This is evidenced by the successful spectroscopic work that has been published on ScC_2 and YC_2.[195-198] In fact, Knudsen effusion mass spectrometric studies have demonstrated that the electropositive transition metal dicarbides such as ScC_2, TiC_2, and VC_2 (and many others) have M-C_2 bond energies that are typically 85-95% of the corresponding MO bond energy.[199] It is likely that a significant contribution of $M^{2+}C_2^{2-}$ character is present in these strongly bound species, accounting for the similarity of their bond energies to those of the oxides. In contrast, the electron affinity of C is only 1.263 eV.[200] As a result, the diatomic early transition metal carbides can only be formed using highly dilute single carbon sources (such as dilute CH_4) or short reaction times. For these metals, species such as ScC_2 are much more readily produced, severely limiting the concentration of the diatomic carbide (ScC) that can be formed. Experimentally, it is also found that the early transition metal carbides cluster far more readily than the late metal carbides. If the reaction time and concentration of the carbon source are not sufficiently limited, production of large clusters such as the metallocarbohedrenes occurs,[201-203] and this leads to negligible concentrations of the diatomic carbides.

The weaker bond dissociation energies of the transition metal silicides make oxygen impurities even more problematic in studying the diatomic transition metal silicides from the left side of the table. In addition, clustering of silicon atoms around the early transition metals occurs quite readily,[204-205] requiring the use of extremely low concentrations of the silicon source, typically SiH_4. The combination of these effects makes it progressively more difficult to study the diatomic transition metal silicides as one moves to the left in the periodic table.

The lack of experimental data on the early transition metal silicides makes it difficult to judge the quality of computational results, which frequently differ from one calculation to another for the early transition metal silicides. In the cases of ZrSi, NbSi, MoSi, and WSi, photoelectron spectra of the mass-selected negative ions have been used to assign ground states,[26-27] however these studies also differ from the computational results and leave room for uncertainty in the assignments. At this point in time, the ground states of the MSi species to the left of the column headed by FeSi remain rather uncertain. We have not attempted to evaluate the various calculations for these species, but have simply reported the results of the comprehensive DFT calculation by Wu and Su for reference.[39]

4.5 Conclusion

The first spectroscopic investigation of OsSi has been performed using the resonant two-photon ionization method. The molecule has been shown to have a ground state of X $^3\Sigma^-_{0+}$ arising from the $1\sigma^2\ 1\pi^4\ 2\sigma^2\ 3\sigma^2\ 1\delta^2$ electronic configuration. Two electronic band systems have been observed, designated as the A1 ← X $^3\Sigma^-_{0+}$ and the B1 ← X $^3\Sigma^-_{0+}$ systems. By analogy to the isoelectronic WO molecule, the A1 state is tentatively assigned as having primarily $2\sigma^2\ 1\pi^4\ 3\sigma^2\ 1\delta^1\ 2\pi^1$, $^3\Pi_1$ character, while the B1 state is tentatively assigned as having primarily $2\sigma^2\ 1\pi^4\ 3\sigma^2\ 1\delta^1\ 2\pi^1$, $^1\Pi_1$ character. Rotationally resolved spectroscopy has permitted the rotational constants and bond lengths of all three states to be measured, and hot bands have provided the vibrational interval in the X $^3\Sigma^-_{0+}$ ground state.

4.6 References

1. Shaposhnikov, V. L.; Migas, D. B.; Borisenko, V. E.; Dorozhkin, N. N. Features of the Band Structure for Semiconducting Iron, Ruthenium, and Osmium Monosilicides. *Semiconductors* **2009,** *43* (2), 142-144.

2. Migas, D. B.; Borisenko, V. E. Semiconducting Silicides as Potential Candidates for Light Detectors. Ab Initio Predictions. *Physica Status Solidi C: Current Topics in Solid State Physics* **2013,** *10* (12), 1658-1660.

3. Xu, B.; Verstraete, M. J. First-principles Study of Transport Properties in Os and OsSi. *Phys. Rev. B: Condens. Matter Mater. Phys.* **2013,** *87* (13), 134302/1-134302/9.

4. Oliveira, M. I. A.; Rivelino, R.; de Brito Mota, F.; Gueorguiev, G. K. Optical Properties and Quasiparticle Band Gaps of Transition-Metal Atoms Encapsulated by Silicon Cages. *J. Phys. Chem. C* **2014,** *118* (10), 5501-5509.

5. Amir, F. Z.; Cottier, R. J.; Golding, T. D.; Donner, W.; Anibou, N.; Stokes, D. W. X-ray Diffraction Analysis of an Osmium Silicide Epilayer Grown on Si(100) by Molecular Beam Epitaxy. *J. Cryst. Growth* **2006,** *294* (2), 174-178.

6. Cottier, R. J.; Amir, F. Z.; Zhao, W.; Hossain, K.; Gorman, B. P.; Golding, T. D.; Anibou, N.; Donner, W. Molecular Beam Epitaxial Growth of Osmium Silicides. *J. Vac. Sci. Technol., B: Microelectron. Nanometer Struct.--Process., Meas., Phenom.* **2006,** *24* (3), 1488-1491.

7. Yu, Z.-Q. Electronic Structure and Photoelectric Properties of $OsSi_2$ Epitaxially Grown on a Si(111) Substrate. *Wuli Xuebao* **2012,** *61* (21), 217102/1-217102/8.

8. Kingcade, J. E., Jr.; Gingerich, K. A. Thermodynamic Stability of Gaseous Scandium Silicides and Germanides. *J. Chem. Soc. Faraday Trans. 2* **1989,** *85* (3), 195-200.

9. Kingcade, J. E., Jr.; Gingerich, K. A. Thermodynamic Investigation of Gaseous Yttrium Germanides and Silicides. *J. Chem. Phys.* **1986,** *84* (8), 4574-4578.

10. Auwera-Mahieu, A. V.; McIntyre, N. S.; Drowart, J. Mass Spectrometric Determination of the Dissociation Energies of the Gaseous Molecules FeSi, CoSi, and NiSi. *Chem. Phys. Lett.* **1969,** *4* (4), 198-200.

11. Vander Auwera-Mahieu, A.; Peeters, R.; McIntyre, N. S.; Drowart, J. Mass Spectrometric Determination of Dissociation Energies of the Borides and Silicides of Some Transition Metals. *Transactions of the Faraday Society* **1970,** *66* (4), 809-16.

12. Shim, I.; Kingcade, J. E.; Gingerich, K. A. Electronic States and Nature of Bonding of the Molecule PdSi by all Electron *Ab Initio* HF-CI Calculations and Mass

Spectrometric Equilibrium Experiments. *Zeitschrift fur Physik D* **1987,** *7*, 261-269.

13. Riekert, G.; Lamparter, P.; Steeb, S. Mass-spectrometric Determination of the Dissociation Energy of the Gaseous Molecules Copper-silicon (CuSi) and Silver-silicon (AgSi). *Z. Metallkd.* **1981,** *72* (11), 765-8.

14. Gingerich, K. A.; Haque, R.; Kingcade, J. E., Jr. Gaseous Metal Silicides. II. Thermodynamic Study of the Molecules Gold Silicides (AuSi, $AuSi_2$ and Au_2Si) with a Mass Spectrometer. *Thermochim. Acta* **1979,** *30* (1-2), 61-71.

15. Kickel, B. L.; Armentrout, P. B. Guided Ion Beam Studies of the Reactions of Group 3 Metal Ions (Sc^+, Y^+, La^+, and Lu^+) with Silane. Electronic State Effects, Comparison to Reactions with Methane, and M^+-SiH_x (x = 0-3) Bond Energies. *J. Am. Chem. Soc.* **1995,** *117* (14), 4057-70.

16. Kickel, B. L.; Armentrout, P. B. Guided Ion Beam Studies of the Reactions of Ti^+, V^+, and Cr^+ with Silane. Electronic State Effects, Comparison to Reactions with Methane, and M^+-SiH_x (x = 0-3) Bond Energies. *J. Am. Chem. Soc.* **1994,** *116* (23), 10742-50.

17. Kickel, B. L.; Armentrout, P. B. Reactions of Fe^+, Co^+, and Ni^+ with Silane. Electronic State Effects, Comparison to Reactions with Methane, and M^+-SiH_x (x = 0-3) Bond Energies. *J. Am. Chem. Soc.* **1995,** *117* (2), 764-73.

18. Kickel, B. L.; Armentrout, P. B. Guided Ion Beam Studies of the Reactions of Mn^+, Cu^+, and Zn^+ with Silane. M^+-SiH_x (x = 0-3) Bond Energies. *J. Phys. Chem.* **1995,** *99* (7), 2024-32.

19. Hamrick, Y. M.; Weltner, W., Jr. Quenching of Angular Momentum in the Ground States of VC, NbC, VSi, NbSi Molecules. *J. Chem. Phys.* **1991,** *94*, 3371-3380.

20. Scherer, J. J.; Paul, J. B.; Collier, C. P.; Saykally, R. J. Cavity Ringdown Laser Absorption Spectroscopy and Time-of-flight Mass Spectroscopy of Jet-cooled Copper Silicides. *J. Chem. Phys.* **1995,** *102* (13), 5190-5199.

21. Scherer, J. J.; Paul, J. B.; Collier, C. P.; Saykally, R. J. Cavity Ringdown Laser Absorption Spectroscopy and Time-of-flight Mass Spectroscopy of Jet-cooled Silver Silicides. *J. Chem. Phys.* **1995,** *103* (1), 113-120.

22. Scherer, J. J.; Paul, J. B.; Collier, C. P.; O'Keefe, A.; Saykally, R. J. Cavity Ringdown Laser Absorption Spectroscopy and Time-of-flight Mass Spectroscopy of Jet-cooled Gold Silicides. *J. Chem. Phys.* **1995,** *103* (21), 9187-9192.

23. Paul, J. B.; Scherer, J. J.; Collier, C. P.; Saykally, R. J. Cavity Ringdown Laser Absorption Spectroscopy and Time-of-flight Mass Spectroscopy of Jet-cooled Platinum Silicides. *J. Chem. Phys.* **1996,** *104* (8), 2782-2788.

24. Lefebvre, Y.; Schamps, J. Optical Spectroscopy of Diatomic Species: Copper with Group 14 Elements (Si, Ge, Sn, Pb). *J*. *Mol*. *Spectrosc*. **2000,** *201* (1), 128-133.

25. Cooke, S. A.; Gerry, M. C. L.; Brugh, D. J.; Suenram, R. D. The Rotational Spectrum, Nuclear Field Shift Effects, ^{195}Pt Nuclear Spin-rotation Constant, and Electric Dipole Moment of PtSi. *J*. *Mol*. *Spectrosc*. **2004,** *223* (2), 185-194.

26. Gunaratne, K. D. D.; Hazra, A.; Castleman, A. W., Jr. Photoelectron Imaging Spectroscopy and Theoretical Investigation of ZrSi. *J*. *Chem*. *Phys*. **2011,** *134* (20), 204303/1-204303/6.

27. Gunaratne, K. D. D.; Berkdemir, C.; Harmon, C. L.; Castleman, A. W. Probing the Valence orbitals of Transition Metal-silicon Diatomic Anions. ZrSi, NbSi, MoSi, PdSi and WSi. *Phys*. *Chem*. *Chem*. *Phys*. **2013,** *15* (16), 6068-6079.

28. Steimle, T. C.; Virgo, W. L.; Brown, J. M. Permanent Electric Dipole Moments and Hyperfine Interaction in Ruthenium Monocarbide, RuC. *J*. *Chem*. *Phys*. **2003,** *118* (6), 2620-2625.

29. Virgo, W. L.; Steimle, T. C.; Aucoin, L. E.; Brown, J. M. The Permanent Electric Dipole Moments of Ruthenium Monocarbide in the $^3\Pi$ and $^3\Delta$ States. *Chem*. *Phys*. *Lett*. **2004,** *391* (1-3), 75-80.

30. Wang, J.; Sun, X.; Wu, Z. Chemical Bonding and Electronic Structure of 4d-metal Monocarbides. *Chem*. *Phys*. *Lett*. **2006,** *426* (1-3), 141-147.

31. Yang, M.; Ma, T.; Li, B. W.; Chan, M.-C.; Cheung, A. S. C. Near Infrared Laser-induced Fluorescence Spectroscopy of RuC. *J*. *Mol*. *Spectrosc*. **2014,** *297*, 25-31.

32. Balfour, W. J.; Cao, J.; Prasad, C. V. V.; Qian, C. X. Electronic Spectroscopy of Jet-cooled Iron Monocarbide. The $^3\Delta_i$ - $^3\Delta_i$ Transition near 493 nm. *J*. *Chem*. *Phys*. **1995,** *103* (10), 4046-4051.

33. Cao, J. Electronic Structures of Iron Monocarbide (FeC) and Rhenium Mononitride (ReN). Ph.D., University of Victoria, Victoria, 1997.

34. Leung, J. W. H.; Tam, W. S.; Ran, Q.; Cheung, A. S. C. Near Infrared Laser Spectroscopy of FeC. *Chem*. *Phys*. *Lett*. **2001,** *343* (1,2), 64-70.

35. Steimle, T. C.; Virgo, W. L.; Hostutler, D. A. The Permanent Electric Dipole Moments of Iron Monocarbide, FeC. *J*. *Chem*. *Phys*. **2002,** *117* (4), 1511-1516.

36. Tzeli, D.; Mavridis, A. Theoretical Investigation of Iron Carbide, FeC. *J*. *Chem*. *Phys*. **2002,** *116* (12), 4901-4921.

37. Wang, J.; Sun, X.; Wu, Z. Theoretical Investigation of 5d-Metal Monocarbides. *J*.

Cluster Sci. **2007,** *18* (1), 333-344.

38. Krechkivska, O.; Morse, M. D. Resonant Two-photon Ionization Spectroscopy of Jet-cooled OsC. *J*. *Chem*. *Phys*. **2008,** *128* (8), 084314/1-084314/9.

39. Wu, Z. J.; Su, Z. M. Electronic Structures and Chemical Bonding in Transition Metal Monosilicides MSi (M=3d, 4d, 5d Elements). *J*. *Chem*. *Phys*. **2006,** *124* (18), 184306/1-184306/15.

40. Lindholm, N.; Morse, M. D. Rotationally Resolved Spectra of Jet-cooled RuSi. *J*. *Chem*. *Phys*. **2007,** *127* (8), 084317/1-5.

41. Weltner, W., Jr.; McLeod, D., Jr. Spectroscopy of Tungsten Oxide Molecules in Neon and Argon Matrixes at 4 and 20 °K. *J*. *Mol*. *Spectrosc*. **1965,** *17* (2), 276-99.

42. Green, D. W.; Ervin, K. M. Infrared Spectra of Matrix-isolated Tungsten Oxides. *J*. *Mol*. *Spectrosc*. **1981,** *89* (1), 145-58.

43. Samoilova, A. N.; Efremov, Y. M.; Gurvich, L. V. Electronic Spectrum of the Tungsten Oxide ($^{186}W^{16}O$) Molecule. *J*. *Mol*. *Spectrosc*. **1981,** *86* (1), 1-15.

44. Nelin, C. J.; Bauschlicher, C. W., Jr. On the Low-lying States of Tungsten Monoxide: a Comparison with Chromium Monoxide and Molybdenum Monoxide. *Chem*. *Phys*. *Lett*. **1985,** *118* (2), 221-5.

45. Kraus, D.; Saykally, R. J.; Bondybey, V. E. Cavity Ringdown Laser Absorption Spectra of Tungsten Oxide. *Chem*. *Phys*. *Lett*. **1998,** *295* (4), 285-288.

46. Lorenz, M.; Bondybey, V. E. Isotopically Resolved Spectra of Tungsten Oxides in Solid Neon. *Chem*. *Phys*. **1999,** *241* (1), 127-138.

47. Gabrusenoks, J.; Von Czarnowski, A.; Meiwes-Broer, K. H. IR Spectroscopy of Monoclinic Tungsten Oxide. *NATO Sci*. *Ser*., *3* **2000,** *77* (Defects and Surface-Induced Effects in Advanced Perovskites), 151-154.

48. Yao, C.; Guan, W.; Song, P.; Su, Z. M.; Feng, J. D.; Yan, L. K.; Wu, Z. J. Electronic Structures of 5d Transition Metal Monoxides by Density Functional Theory. *Theor*. *Chem*. *Acc*. **2007,** *117* (1), 115-122.

49. Krumrey, C.; Cooke, S. A.; Russell, D. K.; Gerry, M. C. L. Fourier Transform Microwave Spectrum of and Born-Oppenheimer Breakdown Effects in Tungsten Monoxide, WO. *Can*. *J*. *Phys*. **2009,** *87* (5), 567-573.

50. Balfour, W. J.; Cao, J.; Qian, C. X. W.; Rixon, S. J. The Visible Spectrum of Rhenium Mononitride. *J*. *Mol*. *Spectrosc*. **1997,** *183* (1), 113-118.

51. Cao, J.; Balfour, W. J.; Qian, C. X. W. Deperturbation Analysis of the [18.5]1-$X0^+$ System and the Electronic Structure of ReN: A Laser Induced and Dispersed Fluorescence Study. *J*. *Phys*. *Chem*. *A* **1997,** *101* (36), 6741-6745.

52. Ram, R. S.; Bernath, P. F.; Balfour, W. J. Fourier Transform Emission Spectroscopy of some new Bands of ReN. *J*. *Mol*. *Spectrosc*. **2007,** *246* (2), 192-197.

53. Hong, B.; Cheng, L.; Wang, M. Y.; Wu, Z. J. Electronic Structures and Chemical Bonding in 4d- and 5d-transition Metal Mononitrides. *Mol*. *Phys*. **2010,** *108* (1), 25-33.

54. Hocking, W. H.; Merer, A. J.; Milton, D. J.; Jones, W. E.; Krishnamurty, G. Laser-induced Fluorescence and Discharge Emission Spectra of Chromium(II) Oxide. Rotational Analysis of the A $^5\Pi$-X $^5\Pi$ Transition. *Can*. *J*. *Phys*. **1980,** *58* (4), 516-33.

55. Cheung, A. S. C.; Zyrnicki, W.; Merer, A. J. Fourier Transform Spectroscopy of Chromium Monoxide: Rotational Analysis of the A $^5\Sigma$-X $^5\Pi$ (0,0) Band near 8000 cm^{-1}. *J*. *Mol*. *Spectrosc*. **1984,** *104* (2), 315-36.

56. Sassenberg, U.; Cheung, A. S. C.; Merer, A. J. Rotational Line Strengths in a $^5\Sigma$ - $^5\Pi$ Transition with Application to the A - X System of Chromium Monoxide. *Can*. *J*. *Phys*. **1984,** *62* (12), 1610-15.

57. Bauschlicher, C. W., Jr.; Nelin, C. J.; Bagus, P. S. Transition Metal Oxides: Chromium Monoxide, Molybdenum Monoxide, Nickel Monoxide, Palladium Monoxide, and Silver Monoxide. *J*. *Chem*. *Phys*. **1985,** *82* (7), 3265-76.

58. Jasien, P. G.; Stevens, W. J. Theoretical Calculations of Diatomic Metal Oxides. Chromium Oxide (CrO) and CrO^+. *Chem*. *Phys*. *Lett*. **1988,** *147* (1), 72-8.

59. Steimle, T. C.; Nachman, D. F.; Shirley, J. E.; Bauschlicher, C. W., Jr.; Langhoff, S. R. The Permanent Electric Dipole Moment of Chromium Monoxide. *J*. *Chem*. *Phys*. **1989,** *91* (4), 2049-53.

60. Barnes, M.; Hajigeorgiou, P. G.; Merer, A. J. Rotational Analysis of the A'$^5\Delta$-X$^5\Pi$ Transition of Chromium Monoxide. *J*. *Mol*. *Spectrosc*. **1993,** *160* (1), 289-310.

61. Gutsev, G. L.; Jena, P.; Zhai, H.-J.; Wang, L.-S. Electronic Structure of Chromium Oxides, CrO_n^- and CrO_n (n = 1-5) from Photoelectron Spectroscopy and Density Functional Theory Calculations. *J*. *Chem*. *Phys*. **2001,** *115* (17), 7935-7944.

62. Shi, Q.; Ran, Q.; Tam, W. S.; Leung, J. W. H.; Cheung, A. S. C. Laser-induced Fluorescence Spectroscopy of CrS. *Chem*. *Phys*. *Lett*. **2001,** *339* (1,2), 154-160.

63. Pulliam, R. L.; Ziurys, L. M. The Pure Rotational Spectrum of the CrS Radical in its X $^5\Pi_r$ State. *J*. *Chem*. *Phys*. **2010,** *133* (17), 174313/1-174313/6.

64. Hewett, W. D., Jr.; Newton, J. H.; Weltner, W., Jr. Absorption Spectra of Molybdenum Oxide Molecules and Molybdenum Atoms in Neon and Argon Matrices at 4 K. *J*. *Phys*. *Chem*. **1975,** *79* (24), 2640-9.

65. Bates, J. K.; Gruen, D. M. Absorption Spectra of Diatomic Molybdenum Nitride (MoN), Molybdenum Oxide (MoO), and Molybdenum Dimer (Mo_2) Molecules Isolated in Argon, Neon, and Krypton. *J*. *Mol*. *Spectrosc*. **1979,** *78* (2), 284-97.

66. Langhoff, S. R.; Bauschlicher, C. W., Jr.; Pettersson, L. G. M.; Siegbahn, P. E. M. Theoretical Spectroscopic Constants for the Low-lying States of the Oxides and Sulfides of Molybdenum and Technetium. *Chem*. *Phys*. **1989,** *132* (1-2), 49-58.

67. Broclawik, E.; Borowski, T. Time-dependent DFT Study on Electronic States of Vanadium and Molybdenum Oxide Molecules. *Chem*. *Phys*. *Lett*. **2001,** *339* (5,6), 433-437.

68. Lindholm, N. F.; Brugh, D. J.; Rothschopf, G. K.; Sickafoose, S. M.; Morse, M. D. Optical Spectroscopy of Jet-cooled NiSi. *J*. *Chem*. *Phys*. **2003,** *118* (5), 2190-2196.

69. Martinez, A.; Lindholm, N.; Morse, M. D. Resonant Two-photon Ionization Spectroscopy of Jet-cooled PdSi. *J*. *Chem*. *Phys*. **2011,** *135* (13), 134308/1-8.

70. Garcia, M. A.; Vietz, C.; Ruipérez, F.; Morse, M. D.; Infante, I. Electronic Spectroscopy and Electronic Structure of Diatomic IrSi. *J*. *Chem*. *Phys*. **2013,** *138* (15), 154306/1-9.

71. Le, A.; Steimle, T. C.; Morse, M. D.; Garcia, M. A.; Cheng, L.; Stanton, J. F. Hyperfine Interactions and Electric Dipole Moments in the [16.0]1.5(v = 6), [16.0]3.5(v = 7), and $X^2\Delta_{5/2}$ States of Iridium Monosilicide, IrSi. *J*. *Phys*. *Chem*. *A* **2013,** *117* (50), 13292-13302.

72. Shao, L.; Sickafoose, S. M.; Langenberg, J. D.; Brugh, D. J.; Morse, M. D. Resonant Two-photon Ionization Spectroscopy of Jet-cooled PtSi. *J*. *Chem*. *Phys*. **2000,** *112* (9), 4118-4123.

73. Garcia, M. A.; Morse, M. D. Electronic Spectroscopy and Electronic Structure of Copper Acetylide, CuCCH. *J*. *Phys*. *Chem*. *A* **2013,** *117* (39), 9860-9870.

74. Matthew, D. J.; Morse, M. D. Resonant Two-photon Ionization Spectroscopy of Jet-cooled UN: Determination of the Ground State. *J*. *Chem*. *Phys*. **2013,** *138* (18), 184303/1-184303/7.

75. Wiley, W. C.; McLaren, I. H. Time-of-Flight Mass Spectrometer with Improved Resolution. *Rev*. *Sci*. *Instrum*. **1955,** *26* (12), 1150 - 1157.

76. Mamyrin, B. A.; Karataev, V. I.; Shmikk, D. V.; Zagulin, V. A. Mass Reflectron.

New Nonmagnetic Time-of-flight High-resolution Mass Spectrometer. *Zh. Eksp. Teor. Fiz.* **1973,** *64* (1), 82-9.

77. Gerstenkorn, S.; Luc, P. *Atlas du Spectre d'Absorption de la Molécule d'Iode entre 14,800-20,000 cm^{-1}*. CNRS: Paris, 1978.

78. Morse, M. D. Supersonic Beam Sources. In *Methods of Experimental Physics: Atomic, Molecular, and Optical Physics*, Dunning, F. B.; Hulet, R., Eds. Academic Press, Inc.: Orlando, Florida, 1996; Vol. II Atoms and Molecules, pp 21-47.

79. Gerstenkorn, S.; Luc, P. Absolute Iodine (I_2) Standards Measured by Means of Fourier Transform Spectroscopy. *Revue de Physique Appliquee* **1979,** *14*, 791-794.

80. Bevington, P. R. *Data Reduction and Error Analysis for the Physical Sciences*. McGraw-Hill: New York, 1969; p 336.

81. Herzberg, G. *Molecular Spectra and Molecular Structure I. Spectra of Diatomic Molecules*. 2nd ed.; Van Nostrand Reinhold: New York, 1950.

82. PGOPHER, *a Program for Simulating Rotational Structure, C. M. Western, University of Bristol,* http://pgopher.chm.bris.ac.uk/.

83. Lefebvre-Brion, H.; Field, R. W. *The Spectra and Dynamics of Diatomic Molecules*. Elsevier: Amsterdam, 2004; p 766.

84. Pyykko, P.; Desclaux, J. P. Relativity and the Periodic System of Elements. *Acc. Chem. Res.* **1979,** *12* (8), 276-81.

85. Balasubramanian, K. Relativity and Chemical Bonding. *J. Phys. Chem.* **1989,** *93* (18), 6585-96.

86. Schwerdtfeger, P. Relativity and Chemical Bonding. *Chem. Bond* **2014,** *1*, 383-404.

87. Calvo, F.; Pahl, E.; Wormit, M.; Schwerdtfeger, P. Evidence for Low-Temperature Melting of Mercury owing to Relativity. *Angew. Chem., Int. Ed.* **2013,** *52* (29), 7323.

88. Tomonari, M.; Tanaka, K. Ab-initio Study on Low-lying States of the TiSi Molecule. *Theor. Chem. Acc.* **2001,** *106* (3), 188-193.

89. Boldyrev, A. I.; Simons, J.; Scherer, J. J.; Paul, J. B.; Collier, C. P.; Saykally, R. J. On the Ground Electronic States of Copper Silicide and its Ions. *J. Chem. Phys.* **1998,** *108* (14), 5728-5732.

90. Tomonari, M.; Mochizuki, Y.; Tanaka, K. Multireference Coupled-pair

Approximation Study of the CuSi Molecule. *Theor*. *Chem*. *Acc*. **1999,** *101* (5), 332-335.

91. Turski, P.; Barysz, M. Electronic States of the Copper Silicide and its Ions. *J*. *Chem*. *Phys*. **1999,** *111* (7), 2973-2977.

92. Turski, P. On the Ground States of Copper, Silver, and Gold Silicides. *Chem*. *Phys*. *Lett*. **1999,** *315*, 115-118.

93. Turski, P.; Barysz, M. Electronic States of the Copper, Silver, and Gold Silicides and their Ions. *J*. *Chem*. *Phys*. **2000,** *113* (11), 4654-4661.

94. Wang, J.; Han, J.-G. Geometries, Stabilities, and Electronic Properties of Different-sized ZrSi(n) (n=1-16) Clusters: a Density-functional Investigation. *J Chem Phys* **2005,** *123* (6), 64306.

95. Adam, A. G.; Granger, A. D.; Balfour, W. J.; Li, R. A Laser Spectroscopic Investigation of Rhodium Monosilicide. *J*. *Mol*. *Spectrosc*. **2009,** *258* (1-2), 35-41.

96. Gingerich, K. A. Gaseous Metal Silicides. I. Dissociation Energy of the Molecule AuSi. *J*. *Chem*. *Phys*. **1969,** *50* (12), 5426-8.

97. Abe, M.; Nakajima, T.; Hirao, K. A Theoretical Study of the Low-lying States of the AuSi Molecule: An Assignment of the Excited A and D States. *J*. *Chem*. *Phys*. **2002,** *117* (17), 7960-7967.

98. Haque, R.; Gingerich, K. A. Identification and Atomization Energies of Gaseous Molecules ScC_2, ScC_3, ScC_4, ScC_5, and ScC_6 by High Temperature Mass Spectrometry. *J*. *Chem*. *Phys*. **1981,** *74* (11), 6407-6414.

99. Jeung, G. H.; Koutecky, J. Molecular Bonding with Scandium: Diatomics Scandium Hydride, Scandium Oxide, Scandium Carbide, and Scandium Nitride (ScH, ScO, ScC, and ScN). *J*. *Chem*. *Phys*. **1988,** *88* (6), 3747-60.

100. Kalemos, A.; Mavridis, A.; Harrison, J. F. Theoretical Investigation of Scandium Carbide, ScC. *J*. *Phys*. *Chem*. *A* **2001,** *105* (4), 755-759.

101. Gutsev, G. L.; Andrews, L.; Bauschlicher, C. W., Jr. Similarities and Differences in the Structure of 3d-metal Monocarbides and Monoxides. *Theor*. *Chem*. *Acc*. **2003,** *109* (6), 298-308.

102. Goel, S.; Masunov, A. E. Dissociation Curves and Binding Energies of Diatomic Transition Metal Carbides from Density Functional Theory. *Int*. *J*. *Quantum Chem*. **2011,** *111* (15), 4276-4287.

103. Kohl, F. J.; Stearns, C. A. Vaporization and Dissociation Energies of the Molecular Carbides of Titanium, Zirconium, Hafnium, and Thorium. *High Temp*. *Sci*.

1974, *6* (4), 284-302.

104. Gupta, S. K.; Gingerich, K. A. Identification and the Thermodynamic Stabilities of Titanium Carbide Species in the Vapor Above the Titanium-iridium-graphite System. *High Temp. - High Pressures* **1980,** *12* (3), 273-80.

105. Kalemos, A.; Mavridis, A. Theoretical Investigation of Titanium Carbide, TiC: $X^3\Sigma^+$, $a^1\Sigma^+$, $A^3\Delta$, and $b^1\Delta$ States. *J. Phys. Chem. A* **2002,** *106* (15), 3905-3908.

106. Luo, Z.; Huang, H.; Chang, Y.-C.; Zhang, Z.; Yin, Q.-Z.; Ng, C. Y. Rotationally Resolved State-to-state Photoionization and Photoelectron Study of Titanium Carbide and its Cation (TiC/TiC^+). *J. Chem. Phys.* **2014,** *141* (14), 144307/1-144307/9.

107. Matthew, D. J.; DaBell, R.; Erickson, T. J.; Lusk, J. R.; Morse, M. D. Spectroscopic Studies of Jet-cooled TiC. **in preparation**.

108. Gupta, S. K.; Gingerich, K. A. Mass Spectrometric Study of the Stabilities of Gaseous Carbides of Vanadium, Niobium, and Molybdenum. *J. Chem. Phys.* **1981,** *74* (6), 3584-3590.

109. Kalemos, A.; Dunning, T. H., Jr.; Mavridis, A. The Electronic Structure of Vanadium Carbide, VC. *J. Chem. Phys.* **2005,** *123* (1), 014301/1-014301/8.

110. Krechkivska, O.; Morse, M. D. Electronic Spectroscopy of Diatomic VC. *J. Phys. Chem. A* **2013,** *117* (50), 13284-13291.

111. Chang, Y. C.; Luo, Z.; Pan, Y.; Zhang, Z.; Song, Y.-N.; Kuang, S. Y.; Yin, Q. Z.; Lau, K.-C.; Ng, C. Y. Rotationally Resolved State-to-state Photoionization and the Photoelectron Study of Vanadium Monocarbide and its Cations (VC/VC^+). *Phys. Chem. Chem. Phys.* **2015,** *17* (15), 9780-9793.

112. Kalemos, A.; Dunning, T. H., Jr.; Mavridis, A. First Principles Investigation of Chromium Carbide, CrC. *J. Chem. Phys.* **2005,** *123* (1), 014302/1-014302/8.

113. Brugh, D. J.; Morse, M. D.; Kalemos, A.; Mavridis, A. Electronic Spectroscopy and Electronic Structure of Diatomic CrC. *J. Chem. Phys.* **2010,** *133* (3), 034303/1-034303/8.

114. Kalemos, A.; Dunning, T. H., Jr.; Mavridis, A. Ab Initio Study of the Electronic Structure of Manganese Carbide. *J. Chem. Phys.* **2006,** *124* (15), 154308/1-154308/6.

115. Borin, A. C.; Gobbo, J. P. The Lowest Quartet Electronic States of MnC. *Chem. Phys. Lett.* **2006,** *417* (4-6), 334-340.

116. Hettich, R. L.; Freiser, B. S. Gas-phase Photodissociation of $FeCH_2^+$ and $CoCH_2^+$: Determination of the Carbide, Carbyne, and Carbene Bond Energies. *J. Am. Chem. Soc.*

1986, *108* (10), 2537-40.

117. Allen, M. D.; Pesch, T. C.; Ziurys, L. M. The Pure Rotational Spectrum of FeC (X, $^3\Delta_i$). *Astrophys*. *J*. **1996,** *472*, L57-L60.

118. Brugh, D. J.; Morse, M. D. Optical Spectroscopy of Jet-cooled FeC Between 12,000 cm^{-1} and 18,100 cm^{-1}. *J*. *Chem*. *Phys*. **1997,** *107* (23), 9772-9782.

119. Aiuchi, K.; Tsuji, K.; Shibuya, K. The Low-lying Electronic State of FeC Observed 3460 cm^{-1} Above X $^3\Delta_3$. *Chem*. *Phys*. *Lett*. **1999,** *309* ((3,4)), 229-233.

120. Fujitake, M.; Toba, A.; Mori, M.; Miyazawa, F.; Ohashi, N.; Aiuchi, K.; Shibuya, K. Near-Infrared Diode Laser Spectroscopy of FeC in the 0.8-mm Region: A Simultaneous Analysis of the $X^3\Delta_i$ and $[3.8]^1\Delta$ States. *J*. *Mol*. *Spectrosc*. **2001,** *208* (2), 253-270.

121. Tzeli, D.; Mavridis, A. On the Dipole Moment of the Ground State $X^3\Delta$ of Iron Carbide, FeC. *J*. *Chem*. *Phys*. **2003,** *118* (11), 4984-4986.

122. Lau, K.-C.; Chang, Y.-C.; Lam, C.-S.; Ng, C. Y. High-Level Ab Initio Predictions for the Ionization Energy, Bond Dissociation Energies, and Heats of Formations of Iron Carbide (FeC) and Its Cation (FeC^+). *J*. *Phys*. *Chem*. *A* **2009,** *113* (52), 14321-14328.

123. Chang, Y. C.; Lam, C. S.; Reed, B.; Lau, K. C.; Liou, H. T.; Ng, C. Y. Rovibronically Selected and Resolved Two-Color Laser Photoionization and Photoelectron Study of the Iron Carbide Cation. *J*. *Phys*. *Chem*. *A* **2009,** *113* (16), 4242-4248.

124. Van Zee, R. J.; Bianchini, J. J.; Weltner, W., Jr. ESR of the CoC and VC molecules. *Chem*. *Phys*. *Lett*. **1986,** *127* (4), 314-318.

125. Barnes, M.; Merer, A. J.; Metha, G. F. Electronic Transitions of Cobalt Carbide, CoC, Near 750 nm: A Good Example of Case ($b_{\beta S}$) Hyperfine Coupling. *J*. *Chem*. *Phys*. **1995,** *103* (19), 8360-8371.

126. Adam, A. G.; Peers, J. R. D. A Rotational and Hyperfine Analysis of the $[14.0]^2\Sigma^+$ - $X^2\Sigma^+$ Band System of Cobalt Monocarbide. *J*. *Mol*. *Spectrosc*. **1997,** *181*, 24-32.

127. Brewster, M. A.; Ziurys, L. M. The Millimeter-wave Spectrum of NiC ($X\ ^1\Sigma^+$) and CoC ($X\ ^2\Sigma^+$). *Astrophys*. *J*. **2001,** *559* (2, Pt. 2), L163-L166.

128. Borin, A. C.; Gobbo, J. P.; Roos, B. O. The Lowest-lying Doublet Electronic States of CoC - A Theoretical Study. *Chem*. *Phys*. *Lett*. **2006,** *418* (4-6), 311-316.

129. Tzeli, D.; Mavridis, A. Electronic Structure of Cobalt Carbide, CoC. *J*. *Phys*.

Chem. *A* **2006,** *110* (28), 8952-8962.

130. Lau, K.-C.; Pan, Y.; Lam, C.-S.; Huang, H.; Chang, Y.-C.; Luo, Z.; Shi, X.; Ng, C. Y. High-level Ab Initio Predictions for the Ionization Energy, Bond Dissociation Energies, and Heats of Formation of Cobalt Carbide (CoC) and its Cation (CoC^+). *J*. *Chem*. *Phys*. **2013,** *138* (9), 094302/1-094302/7.

131. Brugh, D. J.; Morse, M. D. Resonant Two-photon Ionization Spectroscopy of NiC. *J*. *Chem*. *Phys*. **2002,** *117* (23), 10703-10714.

132. Lau, K.-C.; Chang, Y. C.; Shi, X.; Ng, C. Y. High-level Ab Initio Predictions for the Ionization Energy, Bond Dissociation Energies, and Heats of Formation of Nickel Carbide (NiC) and its Cation (NiC^+). *J*. *Chem*. *Phys*. **2010,** *133* (11), 114304/1-114304/8.

133. Kalemos, A.; Dunning, T. H., Jr.; Mavridis, A. The Electronic Structure of the two Lowest States of CuC. *J*. *Chem*. *Phys*. **2008,** *129* (17), 174306/1-174306/4.

134. Li, Z.; Zhang, J.; Meng, D.; Yu, Y. Electronic Structure and Bonding Characters of the two Lowest States of Copper, Silver, and Gold Monocarbides. *Comput*. *Theor*. *Chem*. **2011,** *966* (1-3), 97-104.

135. Shim, I.; Pelino, M.; Gingerich, K. A. Electronic States and Nature of Bonding in the Molecule YC by all Electron *Ab Initio* Multiconfiguration Self-consistent Field Calculations and Mass Spectrometric Equilibrium Experiments. *J*. *Chem*. *Phys*. **1992,** *97*, 9240-9248.

136. Pelino, M.; Gingerich, K. A. Thermodynamic Stability of Yttrium Carbide at High Temperature. *J*. *Mater*. *Sci*. *Lett*. **1993,** *12* (4), 241-3.

137. Simard, B.; Hackett, P. A.; Balfour, W. J. Jet-cooled Optical Spectroscopy of Yttrium Monocarbide. Evidence for a $^4\Pi_i$ ground state. *Chem*. *Phys*. *Lett*. **1994,** *230*, 103-109.

138. Rixon, S. J.; Chowdhury, P. K.; Merer, A. J. Nuclear Hyperfine Structure in the $X^3\Sigma^+$ State of ^{91}ZrC. *J*. *Mol*. *Spectrosc*. **2004,** *228* (2), 554-564.

139. Rixon, S. J. High Resolution Electronic Spectra of Some New Transition-metal Bearing Molecules. Ph.D., 2004.

140. Simard, B.; Presunka, P. I.; Loock, H. P.; Bérces, A.; Launila, O. Laser Spectroscopy and Density Functional Calculations on Niobium Monocarbide. *J*. *Chem*. *Phys*. **1997,** *107* (2), 307-318.

141. Denis, P. A.; Balasubramanian, K. Theoretical Characterization of the Low-lying Electronic States of NbC. *J*. *Chem*. *Phys*. **2005,** *123* (5), 054318/1-054318/9.

142. Shim, I.; Gingerich, K. A. Electronic States and Nature of Bonding in the Molecule MoC by all Electron *Ab Initio* Calculations. *J*. *Chem*. *Phys*. **1997,** *106* (19), 8093-8100.

143. Brugh, D. J.; Ronningen, T. J.; Morse, M. D. First Spectroscopic Investigation of the 4d Transition Metal Monocarbide MoC. *J*. *Chem*. *Phys*. **1998,** *109*, 7851-7862.

144. DaBell, R. S.; Meyer, R. G.; Morse, M. D. Electronic Structure of the 4d Transition Metal Carbides: Dispersed Fluorescence Spectroscopy of MoC, RuC, and PdC. *J*. *Chem*. *Phys*. **2001,** *114* (7), 2938-2954.

145. Rinehart, G. H.; Behrens, R. G. Mass Spectrometric Determination of the Dissociation Energy of TcC(g). *J*. *Phys*. *Chem*. **1979,** *83* (15), 2052-2053.

146. McIntyre, N. S.; Vander Auwera-Mahieu, A.; Drowart, J. Mass Spectrometric Determination of the Dissociation Energies of Gaseous RuC, IrC and PtB. *Transactions of the Faraday Society* **1968,** *64*, 3006 - 3010.

147. Scullman, R.; Thelin, B. The Spectrum of RuC in the Region 6000-8700 Å. *Phys*. *Scr*. **1971,** *3*, 19-34.

148. Scullman, R.; Thelin, B. The Spectrum of RuC in the Region 4100-4800 Å. *Phys*. *Scr*. **1972,** *5*, 201-208.

149. Shim, I.; Finkbeiner, H. C.; Gingerich, K. A. Electronic States and Nature of Bonding of the RuC Molecule by All-electron *Ab Initio* HF-CI Calculations and Equilibrium Mass Spectrometric Experiments. *J*. *Phys*. *Chem*. **1987,** *91* (12), 3171-3178.

150. Langenberg, J. D.; DaBell, R. S.; Shao, L.; Dreessen, D.; Morse, M. D. Resonant Two-photon Ionization Spectroscopy of Jet-cooled RuC. *J*. *Chem*. *Phys*. **1998,** *109*, 7863-7875.

151. Shim, I.; Gingerich, K. A. All-electron *Ab Initio* Investigations of the Three Lowest-lying Electronic States of the RuC Molecule. *Chem*. *Phys*. *Lett*. **2000,** *317*, 338-345.

152. Lindholm, N. F.; Hales, D. A.; Ober, L. A.; Morse, M. D. Optical Spectroscopy of RuC: 18 000-24 000 cm-1. *J*. *Chem*. *Phys*. **2004,** *121* (14), 6855-6860.

153. Wang, F.; Steimle, T. C.; Adam, A. G.; Cheng, L.; Stanton, J. F. The Pure Rotational Spectrum of Ruthenium Monocarbide, RuC, and Relativistic Ab Initio Predictions. *J*. *Chem*. *Phys*. **2013,** *139* (17), 174318/1-174318/6.

154. Lagerqvist, A.; Neuhaus, H.; Scullman, R. The Band Spectrum of RhC. *Zeitschrift fur Naturforschung* **1965,** *20a*, 751-752.

155. Lagerqvist, A.; Scullman, R. Rotational Analysis of the Spectrum of RhC in the 4000 - 5000 Å Region. *Arkiv för Fysik* **1966,** *32*, 479 - 508.

156. Auwera-Mahieu, A. V.; Drowart, J. The Dissociation Energies of the Molecules PtC and RhC. *Chem*. *Phys*. *Lett*. **1967,** *1*, 311-313.

157. Kaving, B.; Scullman, R. The Spectrum of RhC in the Near Infrared Region. *J*. *Mol*. *Spectrosc*. **1969,** *32*, 475 - 500.

158. Cocke, D. L.; Gingerich, K. A. Determination of the Heats of Atomization of the Molecules Rhodium Dicarbide, Rhodium Carbide, and Titanium Dicarbide by High-temperature Mass Spectrometry. *J*. *Chem*. *Phys*. **1972,** *57* (9), 3654-61.

159. Brom, J. M., Jr.; Graham, W. R. M.; Weltner, W., Jr. ESR and Optical Spectroscopy of the RhC Molecule at 4^{o}K. *J*. *Chem*. *Phys*. **1972,** *57* (10), 4116-4124.

160. Shim, I.; Gingerich, K. A. Electronic Structure and Bonding in the RhC Molecule by All-electron *Ab Initio* HF-CI Calculations and Mass Spectrometric Measurements. *J*. *Chem*. *Phys*. **1984,** *81* (12), 5937-5944.

161. Tan, H.; Liao, M.; Balasubramanian, K. Electronic States and Potential Energy Surfaces of Rhodium Carbide (RhC). *Chem*. *Phys*. *Lett*. **1997,** *280* (5), 423-429.

162. Li, X.; Wang, L.-S. The Chemical Bonding and Electronic Structure of RhC, RhN, and RhO by Anion Photoelectron Spectroscopy. *J*. *Chem*. *Phys*. **1998,** *109* (13), 5264-5268.

163. Balfour, W. J.; Fougère, S. G.; Heuff, R. F.; Qian, C. X. W.; Zhou, C. The Electronic Structure and Spectrum of RhC: New Bands in the 400-500 nm Region, Interacting $^{2}\Sigma^{+}$ and $^{2}\Pi$ States, and Deperturbation. *J*. *Mol*. *Spectrosc*. **1999,** *198* (2), 393-407.

164. Shim, I.; Gingerich, K. A. The Nature of Bonding in PdC. *J*. *Chem*. *Phys*. **1982,** *76* (7), 3833-3834.

165. Tan, H.; Dai, D.; Balasubramanian, K. Spectroscopic Properties and Potential Energy Curves for 16 Electronic States of Palladium Carbide (PdC). *Chem*. *Phys*. *Lett*. **1998,** *286* (5), 375-381.

166. Langenberg, J. D.; Shao, L.; Morse, M. D. Resonant Two-photon Ionization Spectroscopy of Jet-cooled PdC. *J*. *Chem*. *Phys*. **1999,** *111*, 4077-4086.

167. Shim, I.; Gingerich, K. A. All-electron *Ab Initio* Investigation of the Electronic States of the PdC Molecule. *ChemPhysChem* **2001,** *2* (2), 125-130.

168. Pelino, M.; Gingerich, K. A. Atomization Energies of the Gaseous Molecules

Lanthanium Monocarbide and Dilanthanium Monocarbide by High Temperature Equilibrium Measurements. *J*. *Phys*. *Chem*. **1989,** *93* (4), 1581-3.

169. Krechkivska, O.; Morse, M. D. Resonant Two-photon Ionization Spectroscopy of Jet-cooled Tantalum Carbide, TaC. *J*. *Chem*. *Phys*. **2010,** *133* (5), 054309/1-054309/8.

170. Sickafoose, S. M.; Smith, A. W.; Morse, M. D. Optical Spectroscopy of Tungsten Carbide (WC). *J*. *Chem*. *Phys*. **2002,** *116* (3), 993-1002.

171. Lee, J.; Meyer, E. R.; Paudel, R.; Bohn, J. L.; Leanhardt, A. E. An Electron Electric Dipole Moment Search in the $X^3\Delta_1$ Ground State of Tungsten Carbide Molecules. *J*. *Mod*. *Opt*. **2009,** *56* (18-19), 2005-2012.

172. Wang, F.; Steimle, T. C. Communication: Electric Dipole Moment and Hyperfine Interaction of Tungsten Monocarbide, WC. *J*. *Chem*. *Phys*. **2011,** *134* (20), 201106/1-201106/4.

173. Wang, F.; Steimle, T. C. Optical Zeeman Spectroscopy of the [17.6]2-$X^3\Delta_1$(1,0) Band System of Tungsten Monocarbide, WC. *J*. *Chem*. *Phys*. **2011,** *135* (10), 104313/1-104313/3.

174. Wang, F.; Steimle, T. C. Tungsten Monocarbide, WC: Pure Rotational Spectrum and ^{13}C Hyperfine Interaction. *J*. *Chem*. *Phys*. **2012,** *136* (4), 044312/1-044312/6.

175. Lee, J.; Chen, J.; Skripnikov, L. V.; Petrov, A. N.; Titov, A. V.; Mosyagin, N. S.; Leanhardt, A. E. Optical Spectroscopy of Tungsten Carbide for Uncertainty Analysis in Electron Electric-dipole-moment Search. *Phys*. *Rev*. *A At*., *Mol*., *Opt*. *Phys*. **2013,** *87* (2-A), 022516/1-022516/12.

176. Gingerich, K. A.; Cocke, D. L. The Atomization Energies of Gaseous Cerium-osmium (CeOs), Cerium Ruthenium (CeRu), Osmium (IV) Carbide, and Osmium (VIII) carbide. *Inorg*. *Chim*. *Acta* **1978,** *28* (2), L171-L172.

177. Meloni, G.; Thomson, L. M.; Gingerich, K. A. Structure and Thermodynamic Stability of the OsC and OsC_2 Molecules by Theoretical Calculations and by Knudsen Cell Mass Spectrometry. *J*. *Chem*. *Phys*. **2001,** *115* (10), 4496-4501.

178. Jansson, K.; Scullman, R.; Yttermo, B. Spectrum of IrC in the Region 4800 - 5300 Å. *Chem*. *Phys*. *Lett*. **1969,** *4* (4), 188-90.

179. Jansson, K.; Scullman, R. Two New Band Systems of the Spectrum of IrC in the Region 6600 - 8500 Å. *J*. *Mol*. *Spectrosc*. **1970,** *36*, 248 - 267.

180. Gupta, S. K.; Nappi, B. M.; Gingerich, K. A. Thermodynamic Stabilities of Gaseous Carbides of Iridium and Platinum. *J*. *Phys*. *Chem*. **1981,** *85* (8), 971-976.

181. Marr, A. J.; Flores, M. E.; Steimle, T. C. The Optical and Optical/Stark Spectrum of Iridium Monocarbide and Mononitride. *J*. *Chem*. *Phys*. **1996,** *104* (21), 8183-8196.

182. Tan, H.; Liao, M.; Balasubramanian, K. Electronic States and Potential Energy Curves of Iridium Carbide (IrC). *Chem*. *Phys*. *Lett*. **1997,** *280* (3,4), 219-226.

183. Ma, T.; Leung, J. W. H.; Cheung, A. S. C. Cavity Ring-down Laser Absorption Spectroscopy of IrC. *Chem*. *Phys*. *Lett*. **2004,** *385* (3,4), 259-262.

184. Pang, H. F.; Cheung, A. S. C. Laser Spectroscopy of IrC: New Electronic States. *Chem*. *Phys*. *Lett*. **2009,** *471* (4-6), 194-197.

185. Neuhaus, H.; Scullman, R.; Yttermo, B. Band Spectrum of PtC. *Zeitschrift fur Naturforschung* **1965,** *20a*, 162.

186. Scullman, R.; Yttermo, B. The Absorption Spectrum of PtC in the 3100-6400 Å Region. *Arkiv för Fysik* **1966,** *33* (14), 231-254.

187. Appelblad, O.; Barrow, R. F.; Scullman, R. A New Electronic Transition in Gaseous PtC. *Proc*. *Phys*. *Soc*., *London* **1967,** *91* (1), 260-1.

188. Appelblad, O.; Nilsson, C.; Scullman, R. Vibrational and Rotational Analysis of Some Band Systems of the Molecule PtC. *Phys*. *Scr*. **1973,** *7*, 65-71.

189. Steimle, T. C.; Jung, K. Y.; Li, B.-Z. A Supersonic Molecular Beam Spectroscopic Study of Platinum Monocarbide, PtC. *J*. *Chem*. *Phys*. **1995,** *102* (15), 5937-5941.

190. Steimle, T. C.; Jung, K. Y.; Li, B.-Z. The Permanent Electric Dipole Moment of PtO, PtS, PtN, and PtC. *J*. *Chem*. *Phys*. **1995,** *103* (5), 1767-1772.

191. Beaton, S. A.; Steimle, T. C. Laser-induced Fluorescence and Optical/Stark Spectroscopy of PtC. *J*. *Chem*. *Phys*. **1999,** *111* (24), 10876-10882.

192. Qin, C.; Zhang, R.; Wang, F.; Steimle, T. C. The Pure Rotational Spectrum of Platinum Monocarbide, PtC. *Chem*. *Phys*. *Lett*. **2012,** *535*, 40-43.

193. Ram, R. S.; Lievin, J.; Bernath, P. F. Fourier Transform Emission Spectroscopy and Ab Initio Calculations on WO. *J*. *Mol*. *Spectrosc*. **2009,** *256* (2), 216-227.

194. Ervin, K. M.; Lineberger, W. C. Photoelectron Spectra of C_2^- and C_2H^-. *J*. *Phys*. *Chem*. **1991,** *95*, 1167-1177.

195. Bousquet, R. R.; Steimle, T. C. The Permanent Electric Dipole Moment of Yttrium Dicarbide, YC_2. *J*. *Chem*. *Phys*. **2001,** *114* (3), 1306-1311.

196. Steimle, T. C.; Bousquet, R. R.; Namiki, K. C.; Merer, A. J. Rotational Analysis of the A^2A_1-X^2A_1 Band System of Yttrium Dicarbide, YC_2. *J*. *Mol*. *Spectrosc*. **2002,** *215* (1), 10-28.

197. Halfen, D. T.; Min, J.; Ziurys, L. M. The Fourier Transform Microwave Spectrum of YC_2 ($\widetilde{X}^2A_1$) and its ^{13}C Isotopologues: Chemical Insight into Metal Dicarbides. *Chem*. *Phys*. *Lett*. **2013,** *555*, 31-37.

198. Min, J.; Halfen, D. T.; Ziurys, L. M. Fourier Transform Microwave/Millimeter-wave Spectroscopy of the ScC_2 ($\widetilde{X}^2A_1$) Radical: A Model System for Endohedral Metallofullerenes. *Chem*. *Phys*. *Lett*. **2014,** *609*, 70-75.

199. De Maria, G.; Balducci, G. Equilibrium Studies at High Temperatures. *MTP (Med*. *Tech*. *Publ*. *Co*.*) Int*. *Rev*. *Sci*. *Phys*. *Chem*., *Ser*. *One* **1972,** *10*, 209-30.

200. Hotop, H.; Lineberger, W. C. Binding Energies in Atomic Negative Ions: II. *J*. *Phys*. *Chem*. *Ref*. *Data* **1985,** *14* (3), 731-750.

201. Castleman, A. W., Jr.; Guo, B.; Wei, S. Metallo-carbohedrenes: a New Class of Molecular Clusters. *Int*. *J*. *Mod*. *Phys*. *B* **1992,** *6*, 3587-3594.

202. Guo, B. C.; Castleman, A. W., Jr. Metallo-carbohedrenes:a New Class of Molecular Clusters. *Adv*. *Met*. *Semicond*. *Clusters* **1994,** *2*, 137-164.

203. Castleman, A. W., Jr.; Guo, B. The Production and Properties of Met-cars. *Adv*. *Sci*. *Technol*. **1995,** *4*, 125-133.

204. Beck, S. M. Studies of Silicon Cluster-metal Atom Compound Formation in a Supersonic Molecular Beam. *J*. *Chem*. *Phys*. **1987,** *87* (7), 4233-4.

205. Beck, S. M. Mixed Metal-silicon Clusters Formed by Chemical Reaction in a Supersonic Molecular Beam: Implications for Reactions at the Metal/Silicon Interface. *J*. *Chem*. *Phys*. **1989,** *90* (11), 6306-12.

CHAPTER 5

PREDISSOCIATION MEASUREMENTS OF BOND DISSOCIATION ENERGIES: VC, VN, AND VS

Reproduced from Johnson, E. L.; Davis, Q. C.; Morse, M. D., Predissociation measurements of bond dissociation energies: VC, VN, and VS. *J*. *Chem*. *Phys*. **2016**, *144*, 234306/1-234306/9, with the permission of AIP Publishing.

5.1 Introduction

Chemical bonding between transition metals and main group elements is of great interest to many fields of chemistry, including catalysis, bioinorganic chemistry, and organometallic chemistry. Much of the interest in these species derives from their ability to catalyze chemical rearrangements, allowing synthetic organic chemists to produce the molecules they desire selectively, and permitting living organisms to do likewise. In such processes, chemical bonds between main group elements and transition metals are broken and new ones are formed, so bond dissociation energies lie at the heart of these phenomena.

An important goal of computational chemistry is to predict accurately the thermochemistry and activation energy of chemical reactions, in order to develop a better

understanding of reaction kinetics and mechanisms and to enable the design of better catalysts. To model reactions accurately, computational methods are needed that provide the energies of the reactants and products, as well as the energies of transition states that occur along the reaction path. At the transition state, bonds are partially formed and partially broken, and methods that can accurately calculate the energetics of these processes are crucial for this. An analog to the transition state, with its partially formed and partially broken bonds, is the dissociation process, in which bonds are completely broken. One would expect that a computational method that fails to obtain accurate bond dissociation energies (BDEs) might also be unlikely to obtain accurate transition state energies, at least in some cases.

Among the most important quantities that computational chemistry can provide are BDEs, but these are also among the most difficult to calculate to high accuracy. This is because of the need to treat electron correlation to the same level of accuracy in the initial molecule and in its dissociated fragments. While current computational methods succeed well for the main group elements, the *d*- and *f*-block metals still present difficulties.[1-22] To make solid advances toward accurate computational chemistry of transition metal species, precise measurements of BDEs are needed. These precise values can provide a set of benchmarks that may be used to test the accuracy of various theoretical methods.[7-22] Theoretical methods have improved so much in recent years that "chemical accuracy" may now be regularly obtained for many main group molecules. "Chemical accuracy" for main-group-containing molecules has been defined as when the computed thermochemical property is within 1.0 kcal mol^{-1} (0.04 eV) of the experimental value.[11] For the more difficult transition-metal-containing molecules, "chemical

accuracy" is considered achieved when the error is 3.0 kcal mol^{-1} (0.13 eV) or less.[11]

In addition to computational methods, several experimental methods have been used to measure BDEs. A useful review of methods that have been employed for main group metals is provided in reference 23. For transition metal molecules, one method that is frequently used employs high-temperature Knudsen effusion mass spectrometry to measure equilibrium constants for gas phase reactions. The equilibrium constants are determined from the partial pressures of the reactants and products under equilibrium conditions. The equilibrium constants are then used to calculate thermodynamic properties using either second- or third-law methods.[24] The second-law method uses the relationship

$$d \ln K_{eq}(T)/d(1/T) = -\Delta H_T^0/R, \tag{5.1}$$

where T is the temperature, $K_{eq}(T)$ is the equilibrium constant at temperature T, ΔH_T^0 is the standard enthalpy change of the reaction at temperature T, and R is the gas constant. From the measured temperature dependence of the equilibrium constant, ΔH_T^0 may be determined. The third-law method uses

$$\Delta H_0^0 = -RT \ln K_{eq}(T) + T\Delta[(G_T^0 - H_0^0)/T], \tag{5.2}$$

where ΔH_0^0 is the standard enthalpy change of the reaction at 0 K and $(G_T^0 - H_0^0)/T$ is the free energy function, which is closely related to the entropy.[25-26] In both methods, statistical thermodynamics is required. In the second-law method, it is used to

extrapolate ΔH_T^0 to 0 K to find the BDE. In the third-law method, it is used to obtain the absolute entropies and free energy functions of the reactants and products as functions of temperature. As a result, the third-law method is sometimes called the absolute entropy method. In either case, information about the electronic states of the reactants and products is required in order to complete the statistical thermodynamic calculations.

Another method that has been used to derive BDEs utilizes the ionization energy of the molecule, which can be measured either by monitoring the ion signal while scanning in the vacuum ultraviolet (VUV) to observe the photoionization threshold or by using more sophisticated pulsed-field ionization zero electron kinetic energy (PFI-ZEKE) methods. A thermochemical cycle then relates the BDEs of the neutral and ionized molecules to the ionization energies of the molecule and its fragment, according to

$$IE(AB) + D_0(A^+—B) = D_0(A—B) + IE(A). \quad (5.3)$$

Here D_0(A—B) is the BDE of the neutral molecule, $D_0(A^+—B)$ is the BDE of the molecular ion dissociating to the fragments A^+ + B, IE(A) is the ionization energy of fragment A, and IE(AB) is the adiabatic ionization energy of the neutral molecule at 0 K.[27-28] Solving for D_0(A—B) gives

$$D_0(A—B) = D_0(A^+—B) + IE(AB) - IE(A), \quad (5.4)$$

which demonstrates that knowledge of the two ionization energies may be combined with the BDE of the ion to obtain the BDE of the neutral molecule. For MX molecules such

as the VC, VN, and VS species studied here, the lowest dissociation pathway of the molecular ion produces the metal atomic cation, so (5.4) becomes

$$D_0(M-X) = D_0(M^+-X) + IE(MX) - IE(M). \quad (5.5)$$

Ionization energies of the atoms are known to extremely high precision,[29] and many MX species have now been studied by PFI-ZEKE methods, giving ionization energies to an accuracy of 0.001 eV or better. Thus, if the BDE of the cation is known, this relation allows the BDE of the neutral molecule to be determined, often to the same accuracy as that of the cationic bond energy.

One of the most effective methods of determining the BDE of cations such as MX^+ employs guided ion beam mass spectrometry, in combination with collision-induced dissociation (CID) or endothermic reaction. In CID, ions are created and collisionally thermalized, accelerated to a desired kinetic energy, and then radially trapped by an octopole ion guide. The ions are then passed through a cell containing a gaseous collision partner. The fragment ions and unreacted ions then travel through a quadrupole mass filter and are detected. From the ion intensities, the cross section, σ, for dissociation is determined as a function of the collision energy, E. Analysis of the resulting σ(E) curves permits the BDE of the MX^+ cation to be determined, often to an uncertainty in the range of 0.05-0.15 eV.[30-31] Similar methods are used to obtain the endothermic reaction cross section as a function of collision energy, and these data may be used to extract the BDE of the ion of interest. Although guided ion beam mass spectrometry can give accurate BDEs, the internal energy of the parent molecular ion

must be well known, which is not always the case.

In this article, we advocate the use of predissociation thresholds in a dense manifold of vibronic states observed in the spectrum of a jet-cooled molecule as a means of providing precise BDEs for *d*-block and *f*-block metal-containing molecules, and illustrate its application with the vanadium-main group molecules VC, VN, and VS. The use of photodissociation thresholds for the measurement of BDEs in transition-metal-containing ions was pioneered by C. J. Cassidy, R. L. Hettich, and B. S. Freiser, who employed a low-resolution (arc-lamp and monochromator) light source and ion cyclotron resonance mass spectrometry to measure the photodissociation threshold for a number of different M^+-X systems.[32-35] Their results were unfortunately limited by the low resolution and low fluence of the light source. Since then, the method has been used to measure bond energies in diatomic transition metal molecules such as V_2,[36-37] Ni_2,[38-39] Pt_2,[40] VNi,[36-37] NiPt,[41] TiV,[37] TiCo,[37] Zr_2,[42] YCo,[42] YNi,[42] ZrCo,[42] ZrNi,[42] NbCo,[42] NbNi,[42] TiZr,[43] TiNb,[43] ZrV,[43] Rh_2,[44] NbCr,[45] and VNb.[46] It has also been used to obtain the BDEs of the main group-transition metal molecules AlV,[47] AlCr,[47] AlCo,[47] and AlNi,[48] and Al_3,[49] a *p*-block metal trimer. It has been similarly applied to transition metal cations to measure the bond energies of Co_2^+,[50] Ti_2^+,[51] V_2^+,[51] Co_3^+,[51] TiO^+-Mn,[49] V_2^+-V,[49] Zr_2^+,[52] Nb_2^+,[52] and Nb_3^+-Nb.[52]

The onset of predissociation provides in all cases an upper limit to the BDE, provided the molecule under examination is cold. When there is a sharp, well-defined predissociation threshold in a dense vibronic spectrum, however, it is very likely that the threshold corresponds to the true thermochemical dissociation energy, that is, the difference between the energy of the ground state separated atoms and the zero-point

ground level of the molecule. Two criteria have been proposed for predissociation thresholds to correspond to the thermochemical BDE: (1) the molecule must have a sufficiently large density of electronic states, and (2) the lowest separated atom limit must generate repulsive potential energy curves.[36, 37] In addition, it is required that the spin-orbit coupling between the various potential curves must be sufficiently large to allow the molecule to hop readily from one potential curve to another. These conditions are readily satisfied for the vast majority of transition metal MX molecules.

To validate the idea that transition metal species rapidly dissociate as soon as the dissociation limit is exceeded, we may consider the example of V_2, for which all of the quantities appearing in Eqns (5.3)-(5.5) have been independently measured to high accuracy. The BDE of V_2 was measured by the onset of predissociation and found to be 2.753(1) eV.[36, 37] In independent studies the BDE of V_2^+ was found to be 3.140(2) eV,[51] the ionization energy of V_2 was measured as 6.3568(1) eV,[53] and the ionization energy of vanadium atom is 6.74619(2) eV.[46] Employing Eqn. (5.5), the dissociation energy of V_2 may be calculated from the three remaining quantities to be 2.751(2) eV. Such superb agreement between the directly measured $D_0(V_2)$ and that calculated by the thermochemical cycle shows that when the density of states is sufficiently high, and repulsive states correlate to the ground separated atom limit (both of which occur in V_2), predissociation does occur promptly as soon as the ground separated atom limit is exceeded.

Although in the past we have concentrated on the BDEs of diatomic transition metals, the need to calibrate computational methods for transition metal-main group bonds impels us to attempt this method on these types of molecules. In this article, we

present results on VC, VN, and VS. In the case of VC, the BDE has been measured using Knudsen effusion mass spectrometry,[54] the ionization energy is known through PFI-ZEKE studies,[55] and a number of computational studies have been performed.[4, 56-60] The first spectroscopic study of the molecule was a matrix isolation ESR study, which found the ground state to be of $^2\Sigma^+$ symmetry.[61] In a subsequent ESR reinvestigation, the ground state assignment was revised to $^2\Delta_{3/2}$.[62] The ground state has now been confirmed as $1\delta^1$, $^2\Delta_{3/2}$ by theoretical[58, 63] and spectroscopic methods.[55, 64] For VN, the BDE has been measured using Knudsen effusion mass spectrometry,[65-66] proton-transfer experiments,[67] and has been obtained using computational chemistry.[5, 9, 68] The electronic structure of VN is very well known through spectroscopic studies, which have determined the ground electronic state to be $^3\Delta_1$, deriving from the $1\delta^1 3\sigma^1$ configuration.[69-79] The ground state of VN has also been calculated to be $^3\Delta_1$ using density functional theory (DFT)[5, 9] and multireference configuration interaction methods.[68, 80] Although VS is not as thoroughly studied as VC and VN, the BDE of VS has been measured by Knudsen effusion mass spectrometry[81-84] and has been estimated computationally.[2, 6, 85-88] One electronic band system has been observed using laser-induced fluorescence,[89] and this has demonstrated that the ground state is of $^4\Sigma^-$ symmetry, deriving from the $1\delta^2 3\sigma^1$ electronic configuration. The electric dipole moment has been measured by Steimle et al.,[90] and DeVore and Franzen have reported the matrix isolation infrared and near-infrared spectra.[91] Multiple computational studies confirm that the ground electronic state of VS is $1\delta^2 3\sigma^1$, $^4\Sigma^-$.[2, 6, 85, 88]

5.2 Experimental

In the current work, VC, VN, and VS were investigated using resonant two-photon ionization spectroscopy (R2PI). The instrument employed is identical to that used in previous studies.[92-93] The molecules are produced by focusing the third harmonic radiation from a Q-switched Nd:YAG laser (355 nm) onto a 1:1 vanadium-molybdenum alloy disk in the path of a pulsed supersonic expansion of helium (20 psig backing pressure) seeded with 0.1% CH_4 for VC, 0.8% NH_3 for VN, and 0.67% H_2S for VS. The alloy disk is rotated and translated to prevent the drilling of holes and to maintain a stable source of the desired diatomic molecule. The products of ablation and subsequent reaction then travel down a 1.3 cm long reaction zone and expand supersonically through a 5 mm orifice into a vacuum chamber, causing them to be cooled to approximately 10 K. The molecular beam is then roughly collimated by a 1 cm diameter skimmer and enters the Wiley-McLaren ion source of a reflectron time-of-flight mass spectrometer.[94-95] In the ion source the molecules are exposed to a pulse of tunable UV radiation generated by an OPO laser, which is counterpropagated along the molecular beam path. After a delay of about 20 ns, the output radiation of a KrF excimer laser (248 nm, 5.00 eV) intersects the molecular beam at right angles, ionizing molecules that have been excited by the OPO laser radiation. Some ions are also produced by the absorption of two UV photons produced by the OPO laser, but these show up slightly earlier in the mass spectrum due to the time delay between the two lasers. Thus, ion signals produced by the absorption of two OPO laser photons are distinguishable from those produced by one OPO photon and one KrF excimer photon. Although ionization by absorption of two KrF photons is another ionization mechanism, this process is greatly inhibited by filtering the KrF

excimer output to reduce its fluence. This leads to background ion signals that are nearly zero. Ions produced by either process are accelerated into the flight tube and enter the reflectron,[95] which causes them to reverse their motion, directing them down a second flight tube to a dual microchannel plate detector. The resulting ion signal is then preamplified, digitized, and stored for subsequent analysis. The entire experiment is repeated at a rate of 10 Hz.

Vibronic spectra of $^{51}V^{12}C$ at mass 63 (98.65% natural abundance) were recorded from 25 000 cm^{-1} to 34 247 cm^{-1}. In separate experiments, vibronic spectra of $^{51}V^{32}S$ (mass 83; 94.78% abundance) and $^{51}V^{34}S$ (mass 85; 4.20% abundance) were recorded from 25 000 cm^{-1} to 38 168 cm^{-1} and spectra of $^{51}V^{14}N$ at mass 65 (99.39% abundance) were recorded from 35 086 cm^{-1} to 42 736 cm^{-1}. To calibrate the spectra, the simultaneously recorded atomic transitions of vanadium and molybdenum were compared to the known transition wavenumbers to obtain an absolute calibration.[29]

Excited-state lifetimes were also measured for selected transitions to verify that levels just below the sharp predissociation threshold exhibit lifetimes that are similar to those of levels at lower wavenumbers. This was done to verify that predissociation sets in at a sharply defined threshold, rather than occurring with a gradual onset. The lifetimes were collected by firing the KrF ionization laser when VC, VN, or VS had the greatest signal intensity and scanning the firing time of the OPO laser. A plot of the VC^+, VN^+, or VS^+ ion signal as a function of the firing time of the OPO laser displayed an exponential decay curve that was fitted using the Levenberg-Marquardt nonlinear least-square algorithm[96] to extract the exponential decay time, τ. Because we are only interested in verifying a sharp drop in lifetime at the predissociation threshold, and not in obtaining a

particularly accurate measurement of the lifetime, only one lifetime curve was collected and fitted for each excitation energy that was measured.

5.3 Results

5.3.1 The Bond Dissociation Energy of VC

The R2PI spectrum of VC is displayed in Figure 5.1, along with the R2PI spectra of atomic vanadium and molybdenum, which were used for calibration. The VC spectrum below 33 138 cm^{-1} is a modulated continuous absorption; nowhere in the spectrum below 33 138 cm^{-1} does the intensity drop to the background level that is observed above 33 138 cm^{-1}. The sharp drop in signal to background levels indicates that a predissociation threshold occurs at this energy.

Kalemos et al. has conducted high-level MRCI calculations on 29 molecular terms of VC, all of which lie below 20 000 cm^{-1}.[58] When spin-orbit interaction is considered, these 29 molecular terms lead to 108 different Ω-levels, and this is still more than 13 000 cm^{-1} below the observed predissociation threshold. Far more Ω potential curves will be accessible at 33 138 cm^{-1}. Clearly, VC satisfies the criterion of having a large density of states at the observed predissociation threshold. The abrupt termination of the spectrum cannot be due to a lack of accessible states above 33 138 cm^{-1}, but instead must be due to the onset of rapid predissociation at this wavenumber. The ground separated atom limit for VC is is V, d^3s^2, $^4F_{3/2g}$ + C, s^2p^2, , $^3P_{0g}$,[29] from which molecular levels arise with Ω = 1/2 and 3/2. The ground term of VC is $1\delta^1$, $^2\Delta_{3/2}$,[64] which can undergo excitations to dipole-allowed states with Ω′ = 1/2, 3/2, and 5/2. Of these, the Ω′ = 1/2 and 3/2 states can undergo nonadiabatic coupling to potential curves that dissociate

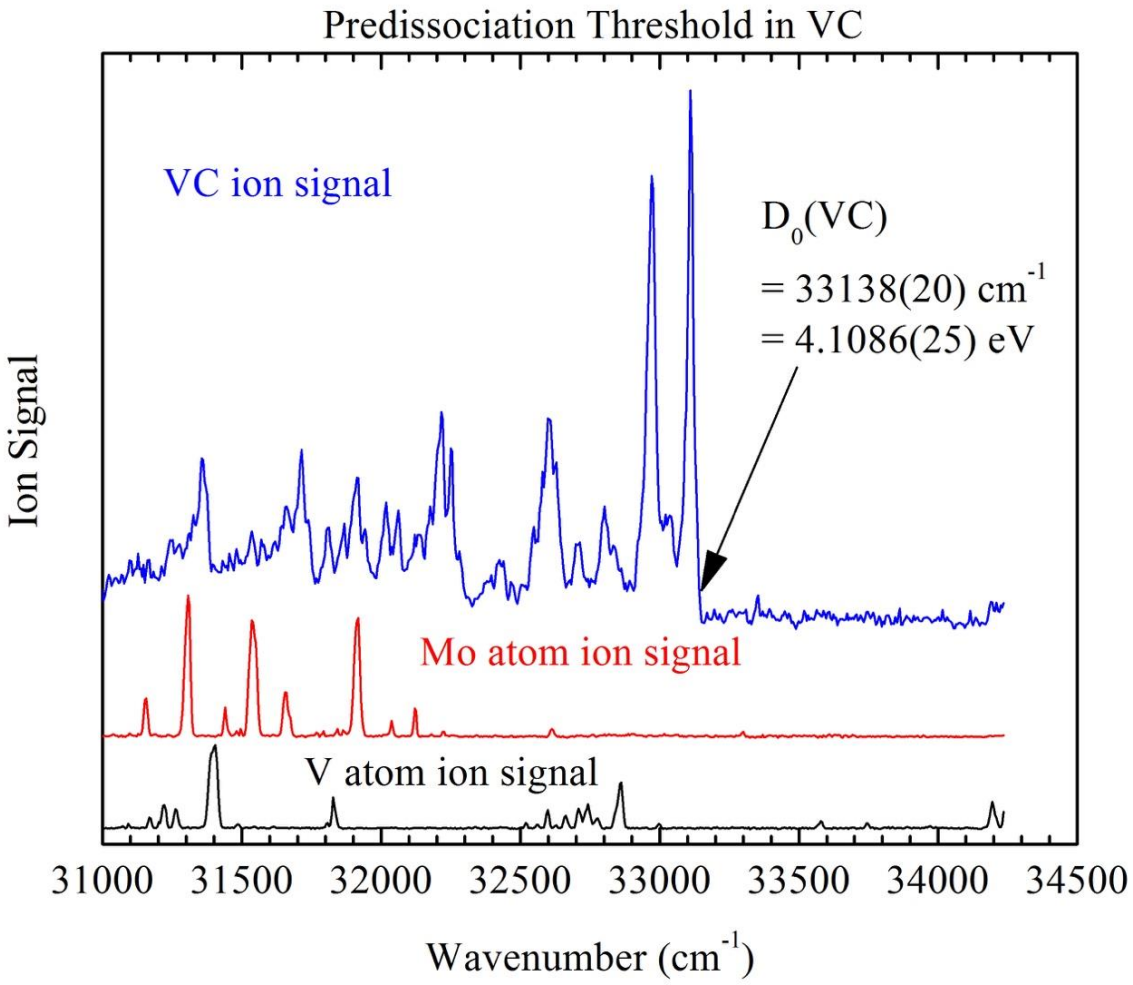

Figure 5.1 Predissociation threshold in VC (blue), Mo atomic signal (red), and V atomic signal (black). The dense continuum of transitions terminates at 33 138 cm^{-1}, giving $D_0(VC) = 4.1086(25)$ eV and $\Delta_{f,\,0\,K}H°(VC(g)) = 827.0 \pm 8$ kJ · mol^{-1}.

to ground state atoms, but the $\Omega' = 5/2$ states may have difficulty in doing so. It is conceivable that the $\Omega' = 5/2$ states that are excited may be unable to predissociate until the first spin-orbit excited separated atom limit, V, d^3s^2, $^4F_{3/2g}$ + C, s^2p^2, $^3P_{1g}$, is reached, 16.40 cm^{-1} above ground-state atoms.[29] No evidence of a second predissociation threshold is observed, however. The V, d^3s^2, $^4F_{3/2g}$ + C, s^2p^2, $^3P_{1g}$ limit generates the required potential curves with Ω=5/2, allowing predissociation by nonadiabatic coupling to occur. Rotationally induced coupling of the $\Omega' = 5/2$ levels to curves with $\Omega = 3/2$ is possible, however, through the **L**- and **S**-uncoupling operators,[97] and this process will permit the $\Omega' = 5/2$ states to predissociate to ground-state atoms. Thus, it is likely that any states with $\Omega' = 5/2$ that are excited will also be able to predissociate as soon as the ground separated atom limit is exceeded in energy.

In order to verify that the states observed just below the sharp predissociation threshold are not predissociating with a slow rate that still permits them to be observed via the R2PI process, the time-delayed R2PI technique was used to measure their lifetimes. Lifetimes for the intense features at 32 972 and 33 110 cm^{-1} were found to be 479 and 536 ns, respectively. These are typical values for allowed transitions in this spectral range, and show no evidence of predissociation below the observed threshold.

Based on these considerations, we assign the observed sharp predissociation threshold as the true bond dissociation energy of VC. Consideration of the errors obtained in the calibration of the atomic transitions, combined with the line width of the ultraviolet laser, forces us to place an uncertainty of ±20 cm^{-1} on this result. Our final assigned BDE for VC is D_0(VC) = 33 138(20) cm^{-1} or 4.1086(25) eV. Employing the standard enthalpy of formation values, $\Delta_{f,\,0\,K}H^o$(V(g)) and $\Delta_{f,\,0\,K}H^o$(C(g)), from the fourth

edition JANAF tables,[98] 512.2 ± 8 and 711.19 ± 0.45 kJ · mol^{-1}, respectively, this value of the bond dissociation energy provides the enthalpy of formation of VC(g) as $\Delta_{f,\,0\ K}H°(VC(g)) = 827.0 \pm 8$ kJ · mol^{-1}. Employing Eqn (5.5) and the precisely measured ionization energies IE(V) and IE(VC),[46, 55] we obtain a value of $D_0(V^+\text{-}C) = 3.7242(25)$ eV.

5.3.2 The Bond Dissociation Energy of VN

The R2PI spectrum of VN near the predissociation threshold is displayed in Figure 5.2, along with the spectra of atomic V and Mo, which were used for calibration. As was found for VC, a structured continuous absorption is found below 40 302 cm^{-1}, followed by a sharp drop to baseline at this wavenumber. In this case, the ground level of VN is known to be of $^3\Delta_1$ symmetry, so upper states with $\Omega' = 0^+$, 0^-, 1, and 2 may be reached in dipole-allowed transitions. The ground separated atom limit of V, d^3s^2, $^4F_{3/2g}$ + N, s^2p^3, $^4S_{3/2u}$, however, generates Ω values of 0^+, 0^-, 1, 2, and 3, so all states reached in dipole-allowed transitions can dissociate to ground-state atoms while preserving Ω. This leads us to suspect that again, the sharp drop to baseline occurs at the thermochemical threshold for dissociation to ground-state atoms.

In the case of VN, there is a gradual diminution in transition intensity as the threshold is approached, so we again checked to see if the observed features showed shortened lifetimes as the threshold was approached. The lifetimes of 9 features lying between 37 800 and 40 300 cm^{-1} were measured; all were found to lie in the range of 350 to 900 ns. No evidence of predissociation below the apparent threshold was found.

Based on these results, the BDE of VN is assigned as $D_0(VN) = 40\ 302(16)$ cm^{-1}

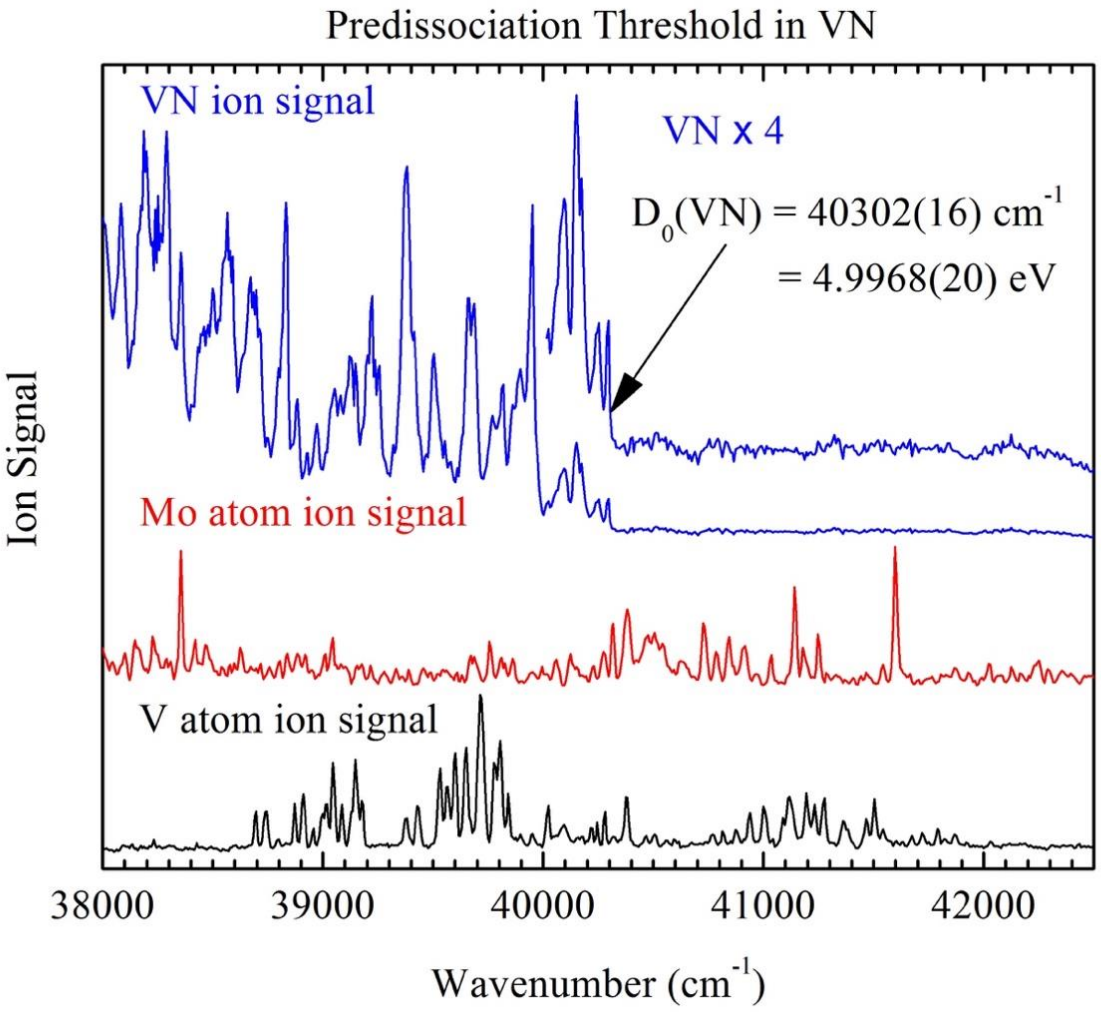

Figure 5.2 Predissociation threshold in VN (blue), Mo atomic signal (red), and V atomic signal (black). The dense continuum of transitions terminates at 40 302(16) cm^{-1}, giving $D_0(VN) = 4.9968(20)$ eV and $\Delta_{f,\,0\,K}H^{o}(VN(g)) = 500.9 \pm 8$ kJ · mol^{-1}.

or 4.9968(20) eV. Again, employing the JANAF tables,[98] this corresponds to an enthalpy of formation of $\Delta_{f,\,0\,K}H^{o}(VN(g)) = 500.9 \pm 8$ kJ · mol^{-1}. Employing Eqn (5.5) and the precisely measured ionization energies of IE(V) and IE(VN),[46, 78] we obtain a value of $D_0(V^+\text{-}N) = 4.6871(20)$ eV.

5.3.3 The Bond Dissociation Energy of VS

The R2PI spectrum of VS is displayed in Figure 5.3 over the range from 34 000 to 38 000 cm^{-1}, along with the spectrum of atomic vanadium that was used for calibration. The VS spectrum exhibits a continuous absorption that gradually decreases in intensity as one moves to higher wavenumbers, and abruptly terminates at 36 580 cm^{-1}. Because the gradual decrease in intensity could result from a predissociation process that sets in gradually, excited state lifetimes were measured at seven different wavenumbers between 34 361 cm^{-1} and 36 486 cm^{-1}. All of the measured upper state lifetimes fall within the range of 380 to 550 ns, with no obvious trend. These lifetimes are much longer than expected if predissociation were occurring. Instead, the observed pattern of decreasing signal intensity with increasing wavenumber must be a result of either reduced electronic transition moments or reduced Franck-Condon factors as the predissociation threshold is approached, or both.

The ground state of VS is $1\delta^2\ 3\sigma^1$, $^4\Sigma^-$,[89] which has $\Omega'' = 1/2$ and 3/2. Therefore, excited states may be populated under dipole selection rules having $\Omega' = 1/2$, 3/2, or 5/2. The ground separated atom limit, V d^3s^2, $^4F_{3/2g}$ + S s^2p^4, $^3P_{2g}$, generates molecular potential curves with $\Omega = 1/2$, 3/2, 5/2, and 7/2, so any states excited from the VS ground term can predissociate to ground-state atoms while preserving Ω. Therefore, given the

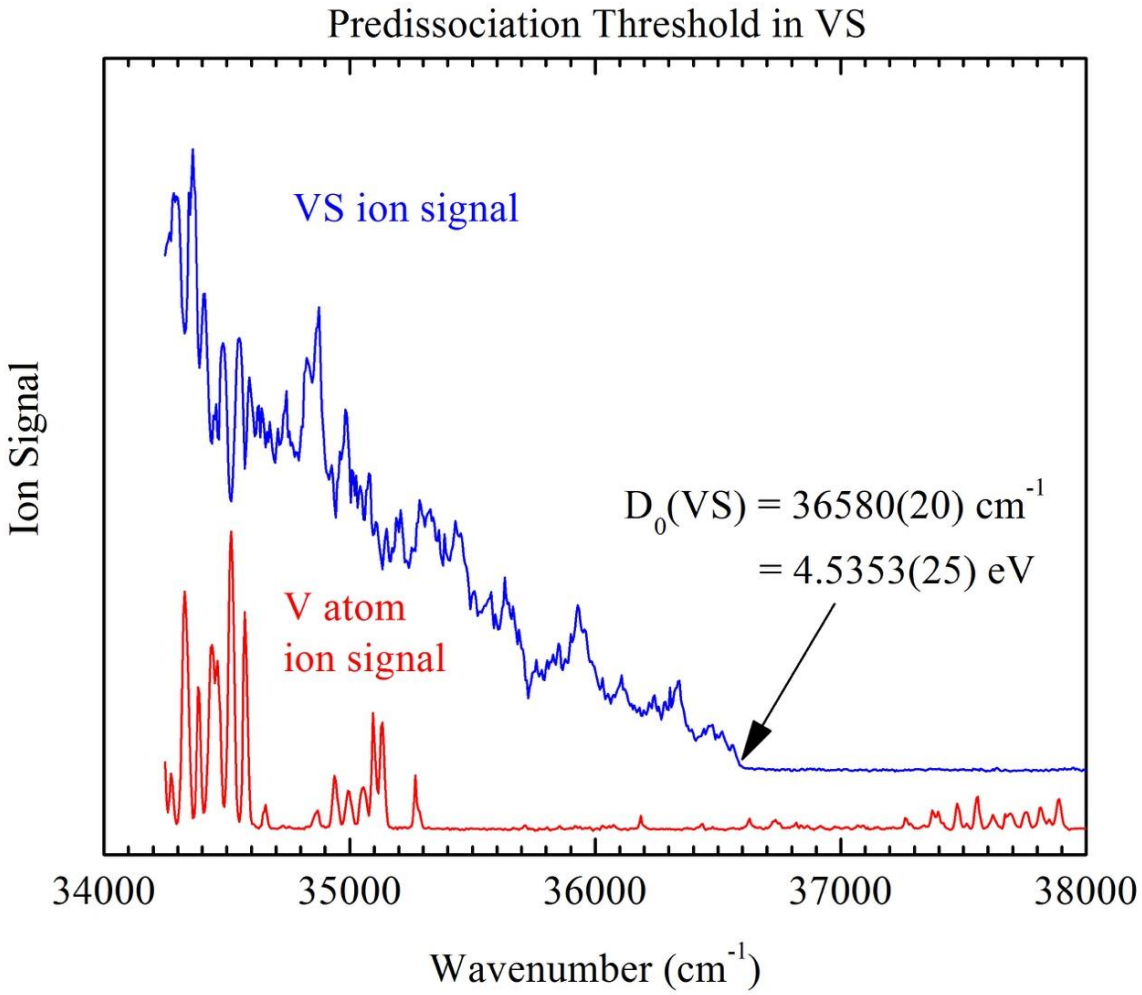

Figure 5.3 Predissociation threshold in VS (blue) and V atomic signal (red). The dense continuum of transitions terminates at 36 580(20) cm^{-1}, giving $D_0(VS) = 4.5353(25)$ eV and $\Delta_{f,\,0\,K}H°(VS(g)) = 349.3 \pm 8$ kJ · mol^{-1}.

high density of states expected in this molecule, we expect predissociation to occur as soon as the energy of the ground separated atom limit is exceeded. On this basis, we assign the sharp drop in signal at 36 580 cm^{-1} as the bond dissociation energy of VS. Adopting a similar error limit as in the other molecules, again based on the errors in the fits of the atomic lines and the linewidth of the ultraviolet laser, leads to a BDE of VS of $D_0(VS)$ = 36 580(20) cm^{-1} or 4.5353(25) eV. Employing the enthalpies of formation of V(g) and S(g) from the JANAF tables,[98] this gives a 0 K enthalpy of formation of VS(g) of $\Delta_{f,\ 0\ K}H°(VS(g))$ = 349.3 ± 8 kJ · mol^{-1}. Employing Eqn (5.5) and the precisely measured ionization energy of IE(V) and the precisely measured dissociation energy of $D_0(V^+\text{-}S)$,[46, 99] we obtain a value of IE(VS) = 7.50(10) eV.

5.4 Discussion

5.4.1 D_0(VC) – Comparison to Previous Experimental and Computational Results

Previously measured or calculated BDEs of gaseous VC are listed in Table 5.1, with experimental results in **bold**. To our knowledge, there has been only one direct measurement of the BDE of VC, a third-law measurement of the high-temperature equilibrium

$$V(g) + C(g) \rightleftharpoons VC(g), \tag{4.6}$$

which provided the value $D_0(VC)$ = 4.34(25) eV.[54] Our result, 4.1086(25) eV, is within the error limit of this value, but reduces the error limit by a factor of 100. An indirect measurement is provided via the thermochemical cycle, Eqn. (5.5), using the

Table 5.1 Bond dissociation energies measured or calculated for VC.[a]

Investigators	Reference	Method	D_0(VC) (eV)
This work		Predissociation threshold	**4.1086 (25)**
Gupta and Gingerich (1981)	54	High-temperature equilibria	**4.34(25)**
Mattar (1993)	56	LDA-LCAO DFT calculation	6.70
Maclagan and Scuseria (1996)	57	MRCI calculation	2.87[b]
Gutsev, Andrews, and Bauschlicher (2003)	4	BPW91 DFT calculation	4.39
Majumdar and Balasubramanian (2003)	63	CASMCSCF-MRSDCI	3.29[c]
Kalemos, Dunning, and Mavridis (2005)	58	MRCI – very large basis	4.04
Redondo, Barrientos, and Largo (2006)	59	B3LYP DFT calculation	3.84
Goel and Masunov (2011)	60	M05-2x:DKH DFT calculation	4.43
Ng et al. (2015)	55	CCSDTQ/CBS calculation	4.023
Ng et al. (2015); Aristov (1984)	55, 100	$D_0(V^+\text{-C})+IE(VC)-IE(V)$	**4.20(21)**
Ng et al. (2015); Aristov (1986)	55, 101	$D_0(V^+\text{-C})+IE(VC)-IE(V)$	**4.33(4)**
Ng et al. (2015); Clemmer (1991)	55, 102	$D_0(V^+\text{-C})+IE(VC)-IE(V)$	**4.25(14)**

[a] Experimental values are given in **boldface.**
[b] Corrected from D_e to D_0 using the calculated vibrational frequency.
[c] Corrected from D_e to D_0 using the calculated vibrational frequency, and corrected for spin-orbit effects.

independently measured values of $D_0(V^+-C)$, IE(VC), and IE(V). The ionization energy of vanadium is 6.76.746187(21) eV,[46] and the ionization energy of VC has been measured by PFI-ZEKE spectroscopy as IE(VC) = 7.13058(10) eV.[55] The BDE of V^+-C has been measured in three different experiments using guided ion beam CID methods, providing $D_0(V^+-C)$ = 3.82(21) eV,[100] 3.95(4) eV,[101] and 3.87(14) eV.[102] Using the thermochemical cycle, these results give D_0(VC) = 4.20(21), 4.33(4), and 4.25(14) eV, respectively. Our result lies within the error limits of the first and last of these, but is substantially less than the 4.33(4) eV value. It appears that the error limit for this measurement may have been underestimated, because in the very worst case, our result is an upper limit on the true BDE.

Two computational studies stand out as the highest-level calculations on the VC molecule. The multireference configuration interaction study by Kalemos et al.[58] obtained D_0(VC) = 4.04 eV when the estimated effects of core-valence correlation, scalar relativistic, and basis set superposition errors were included. The CCSDTQ/CBS result of Ng et al.[55] obtained D_0(VC) = 4.023 eV. Both results are within 0.1 eV of our measurement.

5.4.2 D_0(VN) – Comparison to Previous Experimental and Computational Results

Previous experimental and computational results for the BDE of VN are provided in Table 5.2. A study of the high-temperature equilibria over a heated sample of solid VN has provided a value of D_0(VN) = 4.91(9) eV,[66] in agreement with our value of 4.9968(20) eV. In another study, the proton affinity of VN has been bracketed using ioncyclotron resonance mass spectrometry, and this result has been combined with other

Table 5.2 Bond dissociation energies measured or calculated for VN.[a]

Investigators	Reference	Method	D_0(VN) (eV)
This work		Predissociation threshold	**4.9968 (20)**
Gingerich (1968)	65	Estimated by comparison to UN, ThN, and ZrN	**4.99** [b]
Farber and Srivastava (1973)	66	High-temperature equilibria	**4.91(9)** [b]
Buckner, Gord, and Freiser (1988)	67	Proton affinity bracketing	**5.42(39)**
Harrison (1996)	68	MCSCF calculation	3.68[c]
Furche and Perdew (2006)	9	TPSSh DFT calculation	4.741[c]
Wu (2006)	5	B3LYP DFT calculation	4.62 [c]
Huang (2013); Clemmer (1993)	78, 103	$D_0(V^+\text{-}N)+IE(VN)-IE(V)$	**4.96(6)**

[a] Experimental values are given in **boldface.**
[b] Corrected from D_T^o, as provided in the original work, to D_0^o.
[c] Corrected from D_e to D_0 using the calculated vibrational frequency.

data to give $D_0(VN) = 5.42(39)$ eV.[67] Our value falls slightly below the range spanned by the uncertainty in this measurement. Using the observation that the BDEs of the diatomic nitrides UN, ThN, and ZrN are proportional to the atomization energy of the bulk solid metal nitrides, the BDE of molecular VN has been estimated to be 4.99 eV,[65] matching our result nearly exactly. Finally, the BDE of VN may also be derived using the thermochemical cycle (5.5), combined with the ionization energy of VN, obtained using PFI-ZEKE spectroscopy as IE(VN)= 7.05588(10) eV,[78] the BDE of VN^+, obtained through a guided ion beam mass spectrometric study as 4.65(6) eV,[103] and the previously cited IE(V). The result is 4.96(6) eV, in good agreement with our result.

On the computational side, an MCSCF calculation has significantly underestimated the bond energy at 3.68 eV.[68] Density functional theory using either the B3LYP functional or the TPSSh functional give significantly better values,[5, 9] but still underestimate the bond energy of VN by 0.25 eV or more. Other functionals gave a wide range of values, many of which are in error by more than 0.5 eV.[5, 9]

5.4.3 D_0(VS) – Comparison to Previous Experimental and Computational Results

Previous measurements and computations of the BDE of VS are given in Table 5.3. Four different studies of high-temperature equilibria have provided values of $D_0(VS)$ ranging from 4.61(15) eV to 5.03(17) eV.[81-84] All are higher than our result, $D_0(VS) = 4.5353(25)$ eV. For three of the four measurements, our value lies outside of the quoted error limit. We do not believe that the error lies in our study, which at the very least provides an upper limit on $D_0(VS)$.

A number of computational studies on VS have also been undertaken, providing

Table 5.3 Bond dissociation energies measured or calculated for VS.[a]

Investigators	Reference	Method	D_0(VS) (eV)
This work		Predissociation threshold	**4.5353(25)**
Drowart, Pattoret, and Smoes (1967)	81	High-temperature equilibria	**4.61(15)**
Owzarski and Franzen (1974)	82	High-temperature equilibria	**5.03(17)**
Edwards, Pelino, and Starzynski (1983)	83	High-temperature equilibria	**4.966(34)** [b]
Botor and Edwards (1984)	84	High-temperature equilibria	**4.898(20)** [b]
Bauschlicher and Langhoff (1986)	85	CPF calculation	3.90
Anderson, Hong, and Smialek (1987)	86	ASED-MO calculation	5.86 or 4.60
Bauschlicher and Maitre (1995)	2	RCCSDT calculation	4.02
Bridgeman and Rothery (2000)	87	Non-local DFT calculation	5.36
Wu, Wang, and Su (2006)	6	B3LYP DFT calculation	4.21[c]
Petz and Lüchow (2011)	88	DMC/PPII calculation	4.482(7)

[a] Experimental values are given in **boldface.**

[b] Corrected from D^o_T, as provided in the original work, to D^o_0.

[c] Corrected from D_e to D_0 using the calculated vibrational frequency.

values of D_0(VS) ranging from 3.90 to 5.86 eV.[2, 6, 85-88] The most accurate result is obtained using the diffusion quantum Monte Carlo method, employing pseudopotentials to model the core electrons.[88] With this method, a value of D_0(VS) = 4.482(7) eV is obtained, a value that differs from our result by only 0.053 eV.

5.4.4 Recommended Bond Dissociation Energies for Vanadium Species

Table 5.4 provides a list of dissociation energies for vanadium-containing species that have been determined by the observation of predissociation thresholds, in some cases combined with the thermochemical cycle (5.5). These are the most precisely known BDEs for vanadium-containing species, and are reproduced here to provide a set of benchmark molecules for the testing of computational methods. As we continue our work measuring BDEs by the onset of predissociation for other transition metal species, we will continue to compile lists of the most accurately known BDEs for a variety of transition metal molecules, in the hope that this effort will be useful to computational chemists in honing their methods to obtain greater accuracy.

5.5 Conclusion

Abrupt predissociation thresholds have been observed in the resonant two-photon ionization spectra of VC, VN, and VS. This has allowed bond dissociation energies and enthalpies of formation to be obtained for these molecules as follows: D_0(VC) = 4.1086(25) eV and $\Delta_{f,\,0\,K}H^o$(VC(g)) = 827.0 ± 8 kJ · mol^{-1}; D_0(VN) = 4.9968(20) eV and $\Delta_{f,\,0\,K}H^o$(VN(g)) = 500.9 ± 8 kJ · mol^{-1}; D_0(VS) = 4.5353(25) eV and $\Delta_{f,\,0\,K}H^o$(VS(g)) =

349.3 ± 8 kJ $\cdot$ mol^{-1}. These values have been compared to previous bond dissociation measurements and the results of calculations.

Table 5.4 Recommended bond dissociation energies of vanadium-containing molecules and ions

Molecule	Reference	Method	BDE (eV)
VC	This work	Predissociation threshold	4.1086(25)
VN	This work	Predissociation threshold	4.9968(20)
VS	This work	Predissociation threshold	4.5353(25)
AlV	47	Predissociation threshold	1.489(10)
V_2	36-37	Predissociation threshold	2.753(1)
TiV	37	Predissociation threshold	2.068(2)
VNi	36-37	Predissociation threshold	2.100(1)
ZrV	43	Predissociation threshold	2.663(3)
VNb	46	Predissociation threshold	3.7892(12)
V^+-C	46, 78, this work	D_0(VC)-IE(VC)+IE(V)	3.7424(25)
V^+-N	46, 55, this work	D_0(VN)-IE(VN)+IE(V)	4.687(20)
V_2^+	36-37, 46, 51, 51	Predissociation or $D_0(V_2)$-IE(V_2)+IE(V)	3.140(2) 3.142(1)
V^+-Nb	46	D_0(VNb)-IE(VNb)+IE(V)	4.1433(17)

5.6 References

1. Siegbahn, P. E. M. A Comparative Study of the Bond Strengths of The Second Row Transition Metal Hydrides, Fluorides, and Chlorides. *Theor*. *Chim*. *Acta* **1993,** *86* (3), 219-28.

2. Bauschlicher, C. W., Jr.; Maitre, P. Theoretical Study of the First Transition Row Oxides and Sulfides. *Theor*. *Chim*. *Acta* **1995,** *90* (2/3), 189-203.

3. Harrison, J. F. Electronic Structure of Diatomic Molecules Composed of a First-row Transition Metal and Main-group Element (H-F). *Chem*. *Rev*. **2000,** *100* (2), 679-716.

4. Gutsev, G. L.; Andrews, L.; Bauschlicher, C. W., Jr. Similarities and Differences in the Structure of 3d-metal Monocarbides and Monoxides. *Theor*. *Chem*. *Acc*. **2003,** *109* (6), 298-308.

5. Wu, Z. Electronic Structures of 3d-metal Mononitrides. *J*. *Comput*. *Chem*. **2006,** *27* (3), 267-276.

6. Wu, Z. J.; Wang, M. Y.; Su, Z. M. Electronic Structures and Chemical Bonding in Diatomic ScX to ZnX (X = S, Se, Te). *J*. *Comput*. *Chem*. **2007,** *28* (3), 703-714.

7. Cundari, T. R.; Arturo Ruiz Leza, H.; Grimes, T.; Steyl, G.; Waters, A.; Wilson, A. K. Calculation of the Enthalpies of Formation for Transition Metal Complexes. *Chem*. *Phys*. *Lett*. **2005,** *401* (1-3), 58-61.

8. Schultz, N. E.; Zhao, Y.; Truhlar, D. G. Density Functionals for Inorganometallic and Organometallic Chemistry. *J*. *Phys*. *Chem*. *A* **2005,** *109* (49), 11127-11143.

9. Furche, F.; Perdew, J. P. The Performance of Semilocal and Hybrid Density Functionals in 3d Transition-metal Chemistry. *J*. *Chem*. *Phys*. **2006,** *124* (4), 044103/1-044103/27.

10. Zhao, Y.; Truhlar, D. G. Comparative Assessment of Density Functional Methods for 3d Transition-metal Chemistry. *J*. *Chem*. *Phys*. **2006,** *124* (22), 224105/1-224105/6.

11. DeYonker, N. J.; Peterson, K. A.; Steyl, G.; Wilson, A. K.; Cundari, T. R. Quantitative Computational Thermochemistry of Transition Metal Species. *J*. *Phys*. *Chem*. *A* **2007,** *111* (44), 11269-11277.

12. Jensen, K. P.; Roos, B. O.; Ryde, U. Performance of Density Functionals for First Row Transition Metal Systems. *J*. *Chem*. *Phys*. **2007,** *126* (1), 014103/1-014103/14.

13. Riley, K. E.; Merz, K. M., Jr. Assessment of Density Functional Theory Methods for the Computation of Heats of Formation and Ionization Potentials of Systems

Containing Third Row Transition Metals. *J*. *Phys*. *Chem*. *A* **2007,** *111* (27), 6044-6053.

14. DeYonker, N. J.; Williams, T. G.; Imel, A. E.; Cundari, T. R.; Wilson, A. K. Accurate Thermochemistry for Transition Metal Complexes from First-principles Calculations. *J*. *Chem*. *Phys*. **2009,** *131* (2), 024106/1-024106/9.

15. Mayhall, N. J.; Raghavachari, K.; Redfern, P. C.; Curtiss, L. A. Investigation of Gaussian4 Theory for Transition Metal Thermochemistry. *J*. *Phys*. *Chem*. *A* **2009,** *113* (17), 5170-5175.

16. Tekarli, S. M.; Drummond, M. L.; Williams, T. G.; Cundari, T. R.; Wilson, A. K. Performance of Density Functional Theory for 3d Transition Metal-Containing Complexes: Utilization of the Correlation Consistent Basis Sets. *J*. *Phys*. *Chem*. *A* **2009,** *113* (30), 8607-8614.

17. Kulik, H. J.; Marzari, N. Systematic Study of First-row Transition-metal Diatomic Molecules: A Self-consistent DFT + U approach. *J*. *Chem*. *Phys*. **2010,** *133* (11), 114103/1-114103/16.

18. Jiang, W.; DeYonker, N. J.; Determan, J. J.; Wilson, A. K. Toward Accurate Theoretical Thermochemistry of First Row Transition Metal Complexes. *J*. *Phys*. *Chem*. *A* **2012,** *116* (2), 870-885.

19. Laury, M. L.; Wilson, A. K. Performance of Density Functional Theory for Second Row (4d) Transition Metal Thermochemistry. *J*. *Chem*. *Theory Comput*. **2013,** *9* (9), 3939-3946.

20. Luo, S.; Averkiev, B.; Yang, K. R.; Xu, X.; Truhlar, D. G. Density Functional Theory of Open-Shell Systems. The 3d-Series Transition-Metal Atoms and Their Cations. *J*. *Chem*. *Theory Comput*. **2014,** *10* (1), 102-121.

21. Manivasagam, S.; Laury, M. L.; Wilson, A. K. Pseudopotential-Based Correlation Consistent Composite Approach (rp-ccCA) for First- and Second-Row Transition Metal Thermochemistry. *J*. *Phys*. *Chem*. *A* **2015,** *119* (26), 6867-6874.

22. Xu, X.; Zhang, W.; Tang, M.; Truhlar, D. G. Do Practical Standard Coupled Cluster Calculations Agree Better than Kohn-Sham Calculations with Currently Available Functionals When Compared to the Best Available Experimental Data for Dissociation Energies of Bonds to 3d Transition Metals? *J*. *Chem*. *Theory Comput*. **2015,** *11* (5), 2036-2052.

23. Lau, K.-C.; Ng, C.-Y. Benchmarking State-of-the-Art ab Initio Thermochemical Predictions with Accurate Pulsed-Field Ionization Photoion-Photoelectron Measurements. *Acc*. *Chem*. *Res*. **2006,** *39* (11), 823-829.

24. Drowart, J.; Chatillon, C.; Hastie, J.; Bonnell, D.; Alairo Franco, M. A.; Alcock,

C. B.; Alves, O. L.; Anthony, A. M.; Badri, M. B.; Balducci, G.; Baran, E. J.; Baumard, J. F.; Bayer, G.; Boehm, H. P.; Brook, R. J.; Carlsson, J. O.; Chadwick, A. V.; Chatillon, C. B. J.; Choy, J. H.; Clark, J. B.; Corish, J.; Costa, F. M.; Coutures, J. P.; De Maria, G.; de Waal, D.; Drabik, M.; Drowart, J. D.; Echegut, P.; Edwards, J. G.; El-Sewefy, M. S. E.; Ettmayer, P.; Fitzer, E.; Gilles, P. W.; Gopalakrishnan, J.; Gorokhov, L. N.; Grieveson, G. P.; Gurvich, L. V.; Hanic, F.; Hastic, J. W.; Hausner, H.; Hocking, M. G.; Holland, D.; Hyde, B. G.; Jafelicci, M., Jr.; Kihlborg, L.; Kim, C. H.; Kizilyalli, M.; Kniep, R.; Kolar, D.; Komarek, K. L.; Koumoto, K.; Leskela, M.; Lewis, M. H.; Lieber, C. M.; Livage, J.; Lux, B.; MacKenzie, K. J. D.; Magneli, A.; Mathews, C. K.; Matousek, J.; Matzke, H. J.; McCartney, E. R.; Metselaar, R.; Mintmire, J.; Mocellin, A.; Mrowee, S.; Ng, W. L.; Nygren, M.; Ohse, R. W.; Peshev, P.; Petzow, G.; Rand, M. H.; Ristic, M. M.; Rosenblatt, G. M.; Saha, P.; Saito, T.; Sata, T.; Sersale, R.; Solymosi, F.; Somiya, S.; Spear, K. E.; Subba Rao, G. V.; Sinha, A. P. B.; Thackeray, M.; Tichy, L.; Tilley, R. J. D.; Van Tendeloo, G.; Vernerkar, R.; Verweij, H.; Voronin, G. F.; Walso de Reca, N. E.; Worrell, W. L.; Yan, D. S.; Yanagida, H.; Yen, T. S.; Ziokowski, J. J. High-temperature Mass Spectrometry: Instrumental Techniques, Ionization Cross-sections, Pressure Measurements, and Thermodynamic Data. *Pure and Applied Chemistry* **2005,** *77* (4), 683-737.

25. Drowart, J.; Goldfinger, P. Inorganic Systems Investigated at High Temperature by Mass Spectrometry. *Angew*. *Chem*., *Int*. *Ed*. *Engl*. **1967,** *6* (7), 581-96.

26. Gingerich, K. A. Mass Spectrometric Investigation of Gas Phase Reactions During Sublimation. *J*. *Cryst*. *Growth* **1971,** *9* (1), 31-45.

27. Ng, C.-Y. Vacuum Ultraviolet Spectroscopy and Chemistry by Photoionization and Photoelectron Methods. *Annu*. *Rev*. *Phys*. *Chem*. **2002,** *53*, 101-140.

28. Ng, C.-Y. State-to-state Spectroscopy and Dynamics of Ions and Neutrals by Photoionization and Photoelectron Methods. *Annu*. *Rev*. *Phys*. *Chem*. **2014,** *65*, 197-224.

29. Kramida, A. E.; Ralchenko, Y.; Reader, J.; Team, a. N. A. *NIST Atomic Spectra Database (version 5.3)*. National Institute of Standards and Technology, Gaithersburg, MD: 2015.

30. Armentrout, P. B. Threshold Collision-induced Dissociations for the Determination of Accurate Gas-phase Binding Energies and Reaction Barriers. *Topics in Current Chemistry* **2003,** *225* (Modern Mass Spectrometry), 233-262.

31. Armentrout, P. B. Fifty Years of Ion and Neutral Thermochemistry by Mass Spectrometry. *Int*. *J*. *Mass Spectrom*. **2015,** *377*, 54-63.

32. Cassady, C. J.; Freiser, B. S. Determination of the Fe^+-OH and Co^+-H Bond Energies by Deprotonation Reactions and by Photodissociation. *J*. *Am*. *Chem*. *Soc*. **1984,** *106* (21), 6176-9.

33. Hettich, R. L.; Freiser, B. S. Heteronuclear Transition-metal Cluster Ions in the Gas Phase. Photodissociation and Reactivity of Vanadium-iron Cluster Ion (VFe^+). *J*. *Am*. *Chem*. *Soc*. **1985,** *107* (22), 6222-6.

34. Hettich, R. L.; Freiser, B. S. Gas-phase Photodissociation of Transition Metal Ion Complexes and Clusters. *ACS Symposium Series* **1987,** *359* (Fourier Transform Mass Spectrom.), 155-74.

35. Hettich, R. L.; Freiser, B. S. Determination of Carbide, Carbyne, and Carbene Bond Energies by Gas-phase Photodissociation of $RhCH_2^+$, $NbCH_2^+$, and $LaCH_2^+$. *J*. *Am*. *Chem*. *Soc*. **1987,** *109* (12), 3543-8.

36. Spain, E. M.; Morse, M. D. Bond Strengths of Transition Metal Diatomics: VNi and V_2. *Int*. *J*. *Mass*. *Spectrom*. *Ion Proc*. **1990,** *102*, 183-197.

37. Spain, E. M.; Morse, M. D. Bond Strengths of Transition Metal Dimers: TiV, V_2, TiCo, and VNi. *J*. *Phys*. *Chem*. **1992,** *96*, 2479-2486.

38. Morse, M. D.; Hansen, G. P.; Langridge-Smith, P. R. R.; Zheng, L.-S.; Geusic, M. E.; Michalopoulos, D. L.; Smalley, R. E. Spectroscopic Studies of the Jet-cooled Nickel Dimer. *J*. *Chem*. *Phys*. **1984,** *80*, 5400-5405.

39. Pinegar, J. C.; Langenberg, J. D.; Arrington, C. A.; Spain, E. M.; Morse, M. D. Ni_2 Revisited: Reassignment of the Ground Electronic State. *J*. *Chem*. *Phys*. **1995,** *102*, 666-674.

40. Taylor, S.; Lemire, G. W.; Hamrick, Y. M.; Fu, Z.; Morse, M. D. Resonant Two-photon Ionization Spectroscopy of Jet-cooled Pt_2. *J*. *Chem*. *Phys*. **1988,** *89*, 5517-5523.

41. Taylor, S.; Spain, E. M.; Morse, M. D. Resonant Two-photon Ionization Spectroscopy of Jet-cooled NiPt. *J*. *Chem*. *Phys*. **1990,** *92*, 2698-2709.

42. Arrington, C. A.; Blume, T.; Morse, M. D.; Doverstål, M.; Sassenberg, U. Bond Strengths of Transition Metal Diatomics: Zr_2, YCo, YNi, ZrCo, ZrNi, NbCo, and NbNi. *J*. *Phys*. *Chem*. **1994,** *98*, 1398-1406.

43. Langenberg, J. D.; Morse, M. D. Bond Energies of Transition Metal Dimers: TiZr, TiNb, and ZrV. *Chem*. *Phys*. *Lett*. **1995,** *239*, 24-30.

44. Langenberg, J. D.; Morse, M. D. The Bond Energy of Rh_2. *J*. *Chem*. *Phys*. **1998,** *108* (6), 2331-2335.

45. Sickafoose, S. M.; Langenberg, J. D.; Morse, M. D. Rotationally Resolved Spectra of Isovalent NbCr and VCr. *J*. *Phys*. *Chem*. *A* **2000,** *104* (16), 3521-3527.

46. James, A. M.; Kowalczyk, P.; Langlois, E.; Campbell, M. D.; Ogawa, A.; Simard,

B. Resonant Two Photon Ionization Spectroscopy of the Molecules V_2, VNb, Nb_2. *J*. *Chem*. *Phys*. **1994,** *101* (6), 4485-4495.

47. Behm, J. M.; Brugh, D. J.; Morse, M. D. Spectroscopic Analysis of the Open 3d Subshell Transition Metal Aluminides: AlV, AlCr, and AlCo. *J*. *Chem*. *Phys*. **1994,** *101*, 6487-6499.

48. Behm, J. M.; Arrington, C. A.; Morse, M. D. Spectroscopic Studies of Jet-cooled AlNi. *J*. *Chem*. *Phys*. **1993,** *99*, 6409-6415.

49. Fu, Z.; Russon, L. M.; Morse, M. D.; Armentrout, P. B. Photodissociation Measurements of Bond Dissociation Energies: $D_0(Al_2\text{-}Al)$, $D_0(TiO^+\text{-}Mn)$, and $D_0(V_2^+\text{-}V)$. *Int*. *J*. *Mass Spectrom*. **2001,** *204* (1-3), 143-157.

50. Russon, L. M.; Heidecke, S. A.; Birke, M. K.; Conceicao, J.; Armentrout, P. B.; Morse, M. D. The Bond Strength of Co_2^+. *Chem*. *Phys*. *Lett*. **1993,** *204*, 235-240.

51. Russon, L. M.; Heidecke, S. A.; Birke, M. K.; Conceicao, J.; Morse, M. D.; Armentrout, P. B. Photodissociation Measurements of Bond Dissociation Energies: Ti_2^+, V_2^+, Co_2^+, and Co_3^+. *J*. *Chem*. *Phys*. **1994,** *100*, 4747-4755.

52. Aydin, M.; Lombardi, J. R. Multiphoton Fragmentation Spectra of Zirconium and Niobium Cluster Cations. *Int*. *J*. *Mass Spectrom*. **2004,** *235* (1), 91-96.

53. Yang, D. S.; James, A. M.; Rayner, D. M.; Hackett, P. A. Pulsed Field Ionization Zero Kinetic Energy Photoelectron Spectroscopy of the Vanadium Dimer Molecule. *J*. *Chem*. *Phys*. **1995,** *102* (8), 3129-34.

54. Gupta, S. K.; Gingerich, K. A. Mass Spectrometric Study of the Stabilities of Gaseous Carbides of Vanadium, Niobium, and Molybdenum. *J*. *Chem*. *Phys*. **1981,** *74* (6), 3584-3590.

55. Chang, Y. C.; Luo, Z.; Pan, Y.; Zhang, Z.; Song, Y.-N.; Kuang, S. Y.; Yin, Q. Z.; Lau, K.-C.; Ng, C. Y. Rotationally Resolved State-to-state Photoionization and the Photoelectron Study of Vanadium Monocarbide and its Cations (VC/VC^+). *Phys*. *Chem*. *Chem*. *Phys*. **2015,** *17* (15), 9780-9793.

56. Mattar, S. M. Electronic Structure, Spectroscopic Properties, and State Ordering of the Isoelectronic ScO, TiN, and VC Diatomics. *J*. *Phys*. *Chem*. **1993,** *97* (13), 3171-3175.

57. Maclagan, R. G. A. R.; Scuseria, G. E. An *Ab Initio* Study of VC: a Comparison of Different Levels of Theory Including Density Functional Methods. *Chem*. *Phys*. *Lett*. **1996,** *262*, 87-90.

58. Kalemos, A.; Dunning, T. H., Jr.; Mavridis, A. The Electronic Structure of

Vanadium Carbide, VC. *J*. *Chem*. *Phys*. **2005,** *123* (1), 014301/1-014301/8.

59. Redondo, P.; Barrientos, C.; Largo, A. Small Carbon Clusters Doped with Vanadium Metal: A Density Functional Study of VC_n (n = 1-8). *J*. *Chem*. *Theory Comput*. **2006,** *2* (3), 885-893.

60. Goel, S.; Masunov, A. E. Dissociation Curves and Binding Energies of Diatomic Transition Metal Carbides from Density Functional Theory. *Int*. *J*. *Quantum Chem*. **2011,** *111* (15), 4276-4287.

61. Van Zee, R. J.; Bianchini, J. J.; Weltner, W., Jr. ESR of the CoC and VC Molecules. *Chem*. *Phys*. *Lett*. **1986,** *127* (4), 314-318.

62. Hamrick, Y. M.; Weltner, W., Jr. Quenching of Angular Momentum in the Ground States of VC, NbC, VSi, NbSi Molecules. *J*. *Chem*. *Phys*. **1991,** *94*, 3371-3380.

63. Majumdar, D.; Balasubramanian, K. A Theoretical Study of Potential Energy Curves and Spectroscopic Constants of VC. *Mol*. *Phys*. **2003,** *101* (9), 1369-1376.

64. Krechkivska, O.; Morse, M. D. Electronic Spectroscopy of Diatomic VC. *J*. *Phys*. *Chem*. *A* **2013,** *117* (50), 13284-13291.

65. Gingerich, K. A. Gaseous Metal Nitrides. III. On the Dissociation Energy of Thorium Mononitride and Predicted Dissociation Energies of Diatomic Group III-VI Transition-metal Nitrides. *J*. *Chem*. *Phys*. **1968,** *49* (1), 19-24.

66. Farber, M.; Srivastava, R. D. Effusion-mass Spectrometric Study of Thermodynamic Properties of Vanadium and Vanadium Nitride. *J*. *Chem*. *Soc*., *Faraday Trans*. *1* **1973,** *69* (2), 390-8.

67. Buckner, S. W.; Gord, J. R.; Freiser, B. S. Gas-phase Chemistry of Transition Metal-imido and -nitrene Ion Complexes. Oxidative Addition of Nitrogen-hydrogen Bonds in Ammonia and Transfer of NH from a Metal Center to an Alkene. *J*. *Am*. *Chem*. *Soc*. **1988,** *110* (20), 6606-12.

68. Harrison, J. F. Electronic Structure of the Transition Metal Nitrides TiN, VN, and CrN. *J*. *Phys*. *Chem*. **1996,** *100*, 3513-3519.

69. Peter, S. L.; Dunn, T. M. Rotational Analysis of the 7000 Å (A $3\Phi \rightarrow$ X 3Δ) Electronic Emission System of Diatomic Vanadium Mononitride (VN). *J*. *Chem*. *Phys*. **1989,** *90* (10), 5333-6.

70. Simard, B.; Masoni, C.; Hackett, P. A. Spectroscopy and Photophysics of Refractory Molecules at Low Temperature: the $d^1\Sigma^+ - X^3\Delta_1$ Intercombination System of Vanadium Nitride. *J*. *Mol*. *Spectrosc*. **1989,** *136* (1), 44-55.

71. Balfour, W. J.; Merer, A. J.; Niki, H.; Simard, B.; Hackett, P. A. Rotational, Fine, and Hyperfine Analyses of the (0,0) Band of the D $^3\Pi$ - X $^3\Delta$ System of Vanadium Mononitride. *J*. *Chem*. *Phys*. **1993,** *99* (5), 3288-3303.

72. Andrews, L.; Bare, W. D.; Chertihin, G. V. Reactions of Laser-Ablated V, Cr, and Mn Atoms with Nitrogen Atoms and Molecules. Infrared Spectra and Density Functional Calculations on Metal Nitrides and Dinitrogen Complexes. *J*. *Phys*. *Chem*. *A* **1997,** *101* (45), 8417-8427.

73. Andrews, L. Reactions of Laser-ablated First-row Transition Metal Atoms with Nitrogen: Matrix Infrared Spectra of the MN, NMN and $(MN)_2$ Molecules. *J*. *Electron Spectrosc*. *Relat*. *Phenom*. **1998,** *97* (1-2), 63-75.

74. Steimle, T. C.; Robinson, J. S.; Goodridge, D. The Permanent Electric Dipole Moments of Chromium and Vanadium Mononitride: CrN and VN. *J*. *Chem*. *Phys*. **1999,** *110* (2), 881-889.

75. Ram, R. S.; Bernath, P. F.; Davis, S. P Emission Spectroscopy of the d $^1\Sigma^+$-b $^1\Sigma^+$, d $^1\Sigma^+$-X $^3\Delta_1$, and e $^1\Pi$-a $^1\Delta$ Systems of VN. *J*. *Mol*. *Spectrosc*. **2001,** *210* (1), 110-118.

76. Ram, R. S.; Bernath, P. F.; Davis, S. P. Fourier Transform Emission Spectroscopy of the f$^1\Phi$-a$^1\Delta$ System of VN. *J*. *Mol*. *Spectrosc*. **2002,** *215* (1), 163-164.

77. Flory, M. A.; Ziurys, L. M. Submillimeter-wave Spectroscopy of VN ($X^3\Delta_r$) and VO ($X^4\Sigma^-$): A Study of the Hyperfine Interactions. *J*. *Mol*. *Spectrosc*. **2008,** *247* (1), 76-84.

78. Huang, H.; Luo, Z.-H.; Chang, Y. C.; Lau, K.-C.; Ng, C. Y. State-to-state Photoionization Dynamics of Vanadium Nitride by Two-color Laser Photoionization and Photoelectron Methods†. *Chin*. *J*. *Chem*. *Phys*. **2013,** *26* (6), 669-678.

79. Fan, Q.; Hu, S.; Sun, W.; Wang, Q. The Emission Spectroscopy of the e$^1\Pi$-a$^1\Delta$ System of VN Molecule. *Spectrochim*. *Acta, Part A* **2013,** *114*, 357-359.

80. Mattar, S. M.; Doleman, B. J. MRSD-CI and LDF Studies of the VN X $^3\Delta$ and D $^3\Pi$ States. *Chem*. *Phys*. *Lett*. **1993,** *216* (3-6), 369-74.

81. Drowart, J.; Pattoret, A.; Smoes, S. Mass Spectrometric Studies of the Vaporization of Refractory Compounds. *Ogneupory* **1967,** *No*. *8*, 67-89.

82. Owzarski, T. P.; Franzen, H. F. High-temperature Mass Spectrometry, Vaporization, and Thermodynamics of Vanadium Monosulfide. *J*. *Chem*. *Phys*. **1974,** *60* (3), 1113-17.

83. Edwards, J. G.; Pelino, M.; Starzynski, J. S. Vapor Pressure, Vaporization Reactions, and Thermodynamics of Vaporization of Vanadium Sulfide (VS)(s). *J*. *Chem*.

Phys. **1983,** *79* (5), 2351-5.

84. Botor, J. P.; Edwards, J. G. Thermodynamics of Solid Vanadium Monosulfide and its Equilibrium Vapor by Knudsen-cell Mass Spectrometry. *J*. *Chem*. *Phys*. **1984,** *81* (4), 2185-6.

85. Bauschlicher, C. W., Jr.; Langhoff, S. R. Theoretical Studies of the Low-lying States of Scandium Oxide (ScO), Scandium Sulfide (ScS), Vanadium Oxide (VO), and Vanadium Sulfide (VS). *J*. *Chem*. *Phys*. **1986,** *85* (10), 5936-42.

86. Anderson, A. B.; Hong, S. Y.; Smialek, J. L. Comparison of Bonding in First Transition-metal Series: Diatomic and Bulk Sulfides and Oxides. *J*. *Phys*. *Chem*. **1987,** *91* (16), 4250-4.

87. Bridgeman, A. J.; Rothery, J. Periodic Trends in the Diatomic Monoxides and Monosulfides of the 3d Transition Metals. *Dalton* **2000,** (2), 211-218.

88. Petz, R.; Lüchow, A. Energetics of Diatomic Transition Metal Sulfides ScS to FeS with Diffusion Quantum Monte Carlo. *ChemPhysChem* **2011,** *12* (10), 2031-2034.

89. Ran, Q.; Tam, W. S.; Cheung, A. S. C.; Merer, A. J. Laser Spectroscopy of VS: Hyperfine and Rotational Structure of the $C^4\Sigma^-$-$X^4\Sigma^-$ Transition. *J*. *Mol*. *Spectrosc*. **2003,** *220* (1), 87-106.

90. Zhuang, X.; Steimle, T. C. The Permanent Electric Dipole Moment of Vanadium Monosulfide. *J*. *Chem*. *Phys*. **2010,** *132* (23), 234304/1-234304/8.

91. DeVore, T. C.; Franzen, H. F. First Period Transition Metal Sulfide Gaseous Molecules. Matrix Spectra, Oxide-sulfide Correlation, and Trends. *High Temp*. *Sci*. **1975,** *7* (3), 220-35.

92. Johnson, E. L.; Morse, M. D. The $\tilde{A}\ ^2\Delta_{5/2}$-$\widetilde{X}\ ^2\Delta_{5/2}$ Electronic Band System of Nickel Acetylide, NiCCH. *Mol*. *Phys*. **2015,** *113* (15-16), 2255-2266.

93. Johnson, E. L.; Morse, M. D. Resonant Two-photon Ionization Spectroscopy of Jet-cooled OsSi. *J*. *Chem*. *Phys*. **2015,** *143* (10), 104303/1-104303/12.

94. Wiley, W. C.; McLaren, I. H. Time-of-Flight Mass Spectrometer with Improved Resolution. *Rev*. *Sci*. *Instrum*. **1955,** *26* (12), 1150 - 1157.

95. Mamyrin, B. A.; Karataev, V. I.; Shmikk, D. V.; Zagulin, V. A. Mass Reflectron. New Nonmagnetic Time-of-flight High-resolution Mass Spectrometer. *Zh*. *Eksp*. *Teor*. *Fiz*. **1973,** *64* (1), 82-9.

96. Bevington, P. R. *Data Reduction and Error Analysis for the Physical Sciences*. McGraw-Hill: New York, 1969; p 336.

97. Lefebvre-Brion, H.; Field, R. W. *Perturbations in the Spectra of Diatomic Molecules*. 1 ed.; Academic Press: Orlando, 1986; p 420.

98. Chase, M. W., Jr. *NIST-JANAF Thermochemical Tables, Fourth Edition*. American Institute of Physics for the National Institute of Standards and Technology: Washington, D.C., 1998.

99. Kretzschmar, I.; Schroeder, D.; Schwarz, H.; Rue, C.; Armentrout, P. B. Experimental and Theoretical Studies of Vanadium Sulfide Cation. *J. Phys. Chem. A* **1998,** *102* (49), 10060-10073.

100. Aristov, N.; Armentrout, P. B. Bond Energy-bond Order Relations in Transition-metal Bonds: Vanadium. *J. Am. Chem. Soc.* **1984,** *106* (14), 4065-6.

101. Aristov, N.; Armentrout, P. B. Reaction Mechanisms and Thermochemistry of Vanadium Ions with Ethane, Ethene and Ethyne. *J. Am. Chem. Soc.* **1986,** *108* (8), 1806-19.

102. Clemmer, D. E.; Elkind, J. L.; Aristov, N.; Armentrout, P. B. Reaction of Sc^+, Ti^+, and V^+ with CO. MC^+ and MO^+ Bond Energies. *J. Chem. Phys.* **1991,** *95* (5), 3387-3393.

103. Clemmer, D. E.; Sunderlin, L. S.; Armentrout, P. B. Ammonia Activation by Vanadium(1+): Electronic and Translational Energy Dependence. *J. Phys. Chem.* **1990,** *94* (1), 208-17.

CHAPTER 6

CONCLUSION

6.1 Introduction

In this dissertation, resonant two-photon ionization spectroscopy was used to investigate NiCCH, OsSi, VC, VN, and VS. For NiCCH, the molecule has a ground state of $\widetilde{X}\ ^2\Delta_{5/2}$ symmetry. The electronic transition to the $\widetilde{A}\ ^2\Delta_{5/2}$ state has been extensively studied. The rotational constant for the ground state is 0.14080(11) cm^{-1} for ^{58}NiCCH and the rotational constant for the excited level was approximately 0.129 cm^{-1}. The vibrational frequencies for the ν_2, ν_3, ν_4, and ν_5 modes were determined for the upper state and the vibrational frequency for the ν_5 mode was determined for the ground state. The $\widetilde{A}\ ^2\Delta_{5/2} \leftarrow \widetilde{X}\ ^2\Delta_{5/2}$ excitation is found to lie quite close to the corresponding excitation in NiCN, and the vibrational frequencies of NiCCH are found to be similar to the analogous vibrational frequencies of NiCN. These results suggest that the interactions between transition metals and acetylide (or cyanide) ligands are dominated by ionic interactions, a result that was demonstrated clearly in the previous work on CuCCH.[1] However, covalent effects are not completely absent. A comparison of the C≡C stretching frequency in the $\widetilde{A}\ ^2\Delta_{5/2}$ excited state of NiCCH to that of the $\widetilde{A}\ ^6\Sigma^+$ state of CrCCH shows a significant reduction in vibrational frequency, from 2001.9 cm^{-1} to

1944.3 cm^{-1}.[2-3] This result suggests that a significant π-backbonding interaction is weakening the C≡C π-bond in CrCCH compared to NiCCH. Such an effect makes sense, given that the 3d orbitals of Cr are significantly larger than those of Ni. Since the interaction between nickel and the acetylide ligand is dominated by ionic interactions, the results can be compared to previous experiments performed on NiCu, NiH, and NiCN. The energy of the $\tilde{A}\ ^2\Delta_{5/2}$ state in NiCCH is similar to the energy of the $^2\Delta_{5/2}$ excited state in NiH and NiCN. This proves that the main interaction in NiCCH is ionic. Therefore, despite the fact that only one excited state was found in NiCCH, the placement of other excited states can be predicted based on their locations in NiH and NiCN.

For OsSi, the molecule has been shown to have a ground state of X $^3\Sigma_{0+}^-$. Two electronic band systems have been observed, designated as the A1 ← X $^3\Sigma_{0+}^-$ and the B1 ← X $^3\Sigma_{0+}^-$ systems. The bond length for the ground state was found to be 2.1207(27) Å, 2.236(16) Å for the A1 state, and 2.1987(20) Å for the B1 state. My work on OsSi provides rotationally resolved spectroscopic data and the ground electronic state determination of only the third 5d metal silicide ever studied. Together with previous work on IrSi, the present study shows that the diatomic silicides of the 4d and 5d transition metals have significantly different properties. In particular, their ground states are different. While RuSi has a $1\delta^3 3\sigma^1$, $^3\Delta_3$ ground state, OsSi has a $3\sigma^2 1\delta^2$, $^3\Sigma^-$ ground state.[4] Similarly, RhSi has a $1\delta^4 3\sigma^1$, $^2\Sigma^+$ ground state,[5] while its isovalent analog IrSi has a $1\delta^3 3\sigma^2$, $^2\Delta_{5/2}$ ground state.[6] These results demonstrate the relativistic stabilization of the 6s-dominated 3σ orbital, a result that will certainly affect the chemistry of the 5d metals in other contexts. The results from the OsSi investigation also demonstrate the importance of spin-orbit interaction. All of the rotationally resolved bands I studied in

OsSi arose from the same electronic state, characterized by Ω" = 0. Since OsSi is a 12-electron transition metal-p block diatomic molecule, there were two possible ground-state configurations: $1\sigma^2 2\sigma^2 1\pi^4 1\delta^4$, X $^1\Sigma_{0+}^+$ or $1\sigma^2 2\sigma^2 1\pi^4 3\sigma^2 1\delta^2$, X $^3\Sigma_{0+}^-$. Although the relativistic stablilization of the 6s orbital favors the $1\sigma^2 2\sigma^2 1\pi^4 1\delta^4$, X $^1\Sigma_{0+}^+$ configuration and term, the second-order spin-orbit interaction between $1\sigma^2 2\sigma^2 1\pi^4 3\sigma^2 1\delta^2$, $^3\Sigma_{0+}^-$ level and the higher-lying $1\sigma^2 2\sigma^2 1\pi^4 3\sigma^2 1\delta^2$, $^1\Sigma_{0+}^+$ level causes the $^3\Sigma_{0+}^-$ level to be significantly lowered and further confirms that it is the ground electronic state.

Abrupt predissociation thresholds have been observed in the resonant two-photon ionization spectra of VC, VN, and VS. This has allowed bond dissociation energies for these molecules to be measured as follows: D_0(VC) = 4.1086(25) eV; D_0(VN) = 4.9968(20) eV; and D_0(VS) = 4.5353(25) eV. Although the values for VC and VN are close to previous measurements performed on these molecules, the results of this investigation are much more precise. In the case of VS, our results demonstrate that the previously accepted value of the bond dissociation energy is in error by 0.36 eV, a quite significant amount. Given that computational chemists are using dissociation energies to select appropriate parameterizations of density functional theories, it is crucial that accurate values are available for these comparisons. Otherwise, an optimized density functional theory will be optimized to give erroneous results.

6.2 Research Outlook

The work performed in this dissertation naturally leads in a number of new and promising directions. For example, a natural direction to take the studies of NiCCH would be to investigate other excited electronic states of the molecule, to further confirm

(or deny) its electronic similarity to NiH and NiCN. If enough of the expected excited electronic states could be found, it might be possible to develop a ligand field model to predict additional electronic states, as has been done for NiH and NiCu.[7-8] Another natural extension of the work on NiCCH would be to move to FeCCH. This is a molecule that could reasonably be expected to be present in the interstellar medium, in regions where carbon clusters are abundant and Fe compounds have been found. To identify FeCCH in the interstellar medium would of course require that a high-quality terrestrial spectrum be available. Resonant two-photon ionization studies can provide such a spectrum, along with values of the rotational constants that could be refined in microwave/millimeter wave studies.

The investigation of OsSi shows that there can be significant differences between the 4d and 5d diatomic silicides, owing to the relativistic stabilization of the 6s orbital. Our work has identified the ground state as $3\sigma^2 1\delta^2$, $^3\Sigma^-$, but it has not measured the energy of the $1\delta^3 3\sigma^1$, $^3\Delta_3$ state that is the ground state of RuSi. To understand the magnitude of the relativistic stabilization of the 3σ orbital, the energy of the $1\delta^3 3\sigma^1$, $^3\Delta_3$ state should be measured. This, and similar measurements for related molecules, would permit the electronic structures of the 5d compounds to be more precisely understood. In addition, the diatomic transition metal silicides are a poorly understood class of transition metal molecules in general, despite their potential relevance to the bulk metallic silicides that have useful electronic properties. A large number of molecules of this type have never been spectroscopically investigated, and these would be natural follow-up studies to the present work.

Finally, the bond dissociation energy measurements on VC, VN, and VS represent

the first time the Morse group has applied predissociation threshold measurements to transition-metal main group compounds (except for the previous studies of transition-metal aluminum diatomics). Here there is a real opportunity to make a major advance in our knowledge of bond energies, since a great many transition-metal main group bond energies are unknown or poorly characterized. We anticipate that the 0.36 eV error found in the bond dissociation energy of VS will recur in many other small molecules. By amassing a database of accurate bond dissociation energies of small molecules such as these, we will provide computational chemists with the data they need to develop more accurate methods for computational thermochemistry of the transition metals. Our future contributions to this effort may be the most significant result of the present work. Along these lines, since the completion of experimental work on the bond dissociation energies of VC, VN, and VS in January, 2016, subsequent studies in the Morse group have already led to precise determinations of the bond dissociation energies of TiC, TiN, TiS, TiSi, ZrSi, HfSi, VSi, NbSi, and TaSi. This is a powerful experimental method that can be extended to a broad set of molecules.

As mentioned above, the OPO laser is a new addition to the Morse lab that allows convenient access to a broad range of wavelengths, enabling the group to study species that could not previously be investigated. Of particular interest are studies of the R2PI spectra of boron and silicon clusters. These have received a great deal of interest following the discovery of C_{60} in 1985.[9] The boron clusters are particularly interesting because they exhibit aromaticity akin to some aromatic hydrocarbons,[10-11] even though the clusters are thought to be built on an architecture of equilateral (or nearly equilateral) B_3 units that share edges in common. Another interesting aspect is that the boron clusters

are calculated to remain planar up to quite large cluster sizes, unlike the better known boron hydrides.[12-13] Although photoelectron spectra are known of many of the boron clusters, we anticipate that the OPO laser will permit much better resolved spectra to be recorded, allowing computational predictions of these species to be better verified. This will be the work of future Morse group members.

6.3 References

1. Garcia, M. A.; Morse, M. D. Electronic Spectroscopy and Electronic Structure of Copper Acetylide, CuCCH. *J*. *Phys*. *Chem*. *A* **2013,** *117* (39), 9860-9870.

2. Brugh, D. J.; DaBell, R. S.; Morse, M. D. Vibronic Spectroscopy of Unsaturated Transition Metal Complexes: CrC_2H, $CrCH_3$, and $NiCH_3$. *J*. *Chem*. *Phys*. **2004,** *121* (24), 12379-85.

3. Brugh, D. J.; Morse, M. D. Rotational Analysis of the 3_0^1 Band of the A $^6\Sigma^+$ - X $^6\Sigma^+$ System of CrCCH. *J*. *Chem*. *Phys*. **2014,** *141* (6), 064304/1-9.

4. Lindholm, N.; Morse, M. D. Rotationally Resolved Spectra of Jet-cooled RuSi. *J*. *Chem*. *Phys*. **2007,** *127* (8), 084317/1-5.

5. Adam, A. G.; Granger, A. D.; Balfour, W. J.; Li, R. A Laser Spectroscopic Investigation of Rhodium Monosilicide. *J*. *Mol*. *Spectrosc*. **2009,** *258* (1-2), 35-41.

6. Garcia, M. A.; Vietz, C.; Ruipérez, F.; Morse, M. D.; Infante, I. Electronic Spectroscopy and Electronic Structure of Diatomic IrSi. *J*. *Chem*. *Phys*. **2013,** *138* (15), 154306/1-9.

7. Gray, J. A.; Li, M.; Nelis, T.; Field, R. W. The Electronic Structure of NiH: The $\{Ni^+ 3d^9\ ^2D\}$ Supermultiplet. *J*. *Chem*. *Phys*. **1991,** *95* (10), 7164-7178.

8. Spain, E. M.; Morse, M. D. Ligand Field Theory Applied to Diatomic Transition Metals: Results for the $d^9_A\ d^9_B\ \sigma^2$ States of Ni_2, the $d^9_{Ni}\ d^{10}_{Cu}\ \sigma^2$ States of NiCu, and the $d^8_{Ni}(^3F)\ d^{10}_{Cu}\sigma^2\sigma^{*1}$ Excited States of NiCu. *J*. *Chem*. *Phys*. **1992,** *97*, 4641-4660.

9. Pettiette, C. L.; Yang, S. H.; Craycraft, M. J.; Conceicao, J.; Laaksonen, R. T.; Cheshnovsky, O.; Smalley, R. E. Ultraviolet Photoelectron Spectroscopy of Copper Clusters. *J*. *Chem*. *Phys*. **1988,** *88* (9), 5377-5382.

10. Alexandrova, A. N.; Boldyrev, A. I.; Zhai, H.-J.; Wang, L.-S. All-boron Aromatic Clusters as Potential New Inorganic Ligands and Building Blocks in Chemistry. *Coord*. *Chem*. *Rev*. **2006,** *250* (21+22), 2811-2866.

11. Sergeeva, A. P.; Popov, I. A.; Piazza, Z. A.; Li, W.-L.; Romanescu, C.; Wang, L.-S.; Boldyrev, A. I. Understanding Boron through Size-Selected Clusters: Structure, Chemical Bonding, and Fluxionality. *Acc*. *Chem*. *Res*. **2014,** *47* (4), 1349-1358.

12. Alexandrova, A. N.; Zhai, H.-J.; Wang, L.-S.; Boldyrev, A. I. Molecular Wheel B_8^{2-} as a New Inorganic Ligand. Photoelectron Spectroscopy and Ab Initio Characterization of LiB_8. *Inorg*. *Chem*. **2004,** *43* (12), 3552-3554.

13. Alexandrova, A. N.; Boldyrev, A. I.; Zhai, H.-J.; Wang, L.-S. Photoelectron Spectroscopy and Ab Initio Study of the Doubly Antiaromatic B_6^{2-} Dianion in the LiB_6^- Cluster. *J*. *Chem*. *Phys*. **2005,** *122* (5), 054313/1-054313/8.

APPENDIX A

ROTATIONALLY RESOLVED SPECTRA, TABULATED LINE POSITIONS, AND FITTED PARAMETERS OF NiCCH

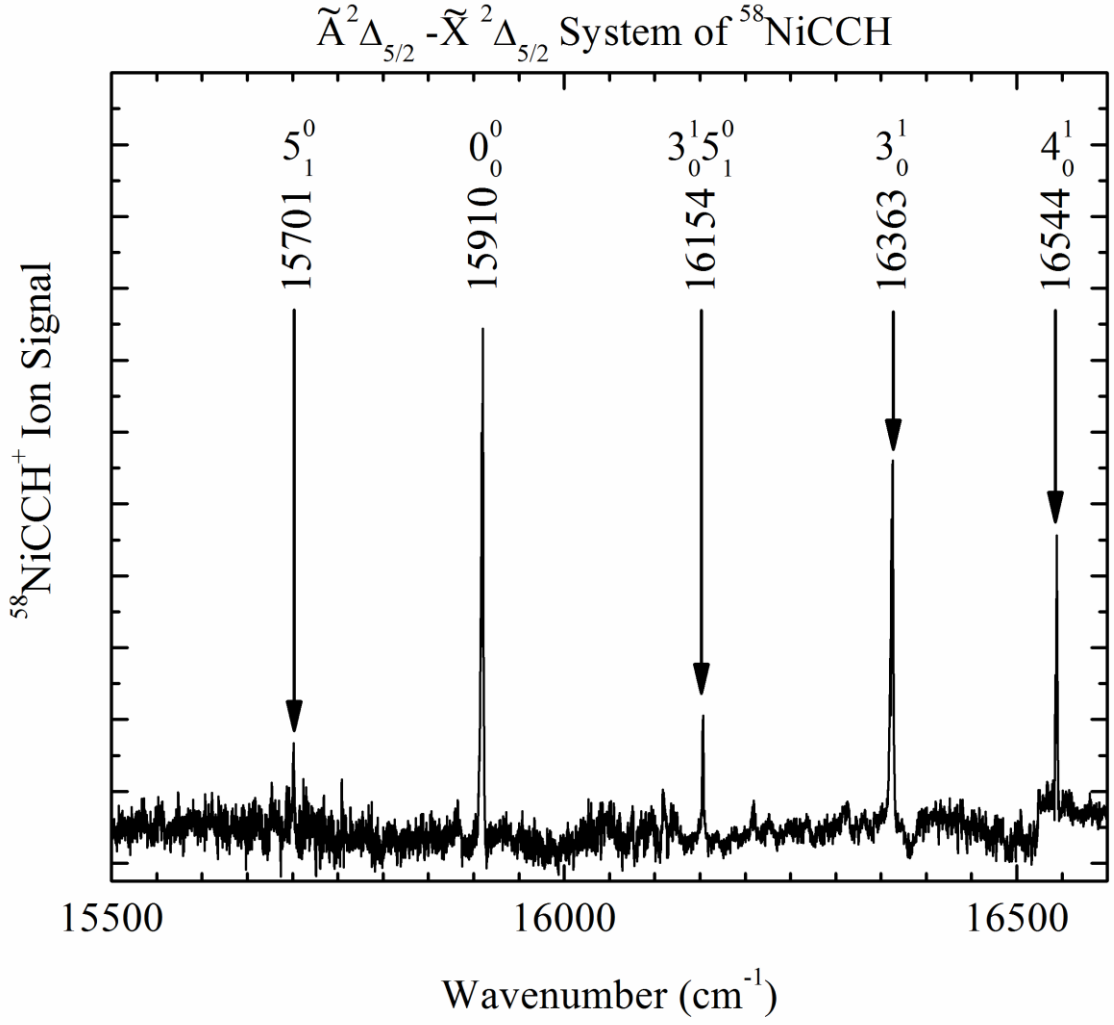

Figure A.1 Vibronically resolved spectrum of the $\tilde{A}\,^2\Delta_{5/2} \leftarrow \tilde{X}\,^2\Delta_{5/2}$ band system of ^{58}NiCCH over the 15500-16600 cm^{-1} range. The bands are identified by wavenumber and vibronic assignment.

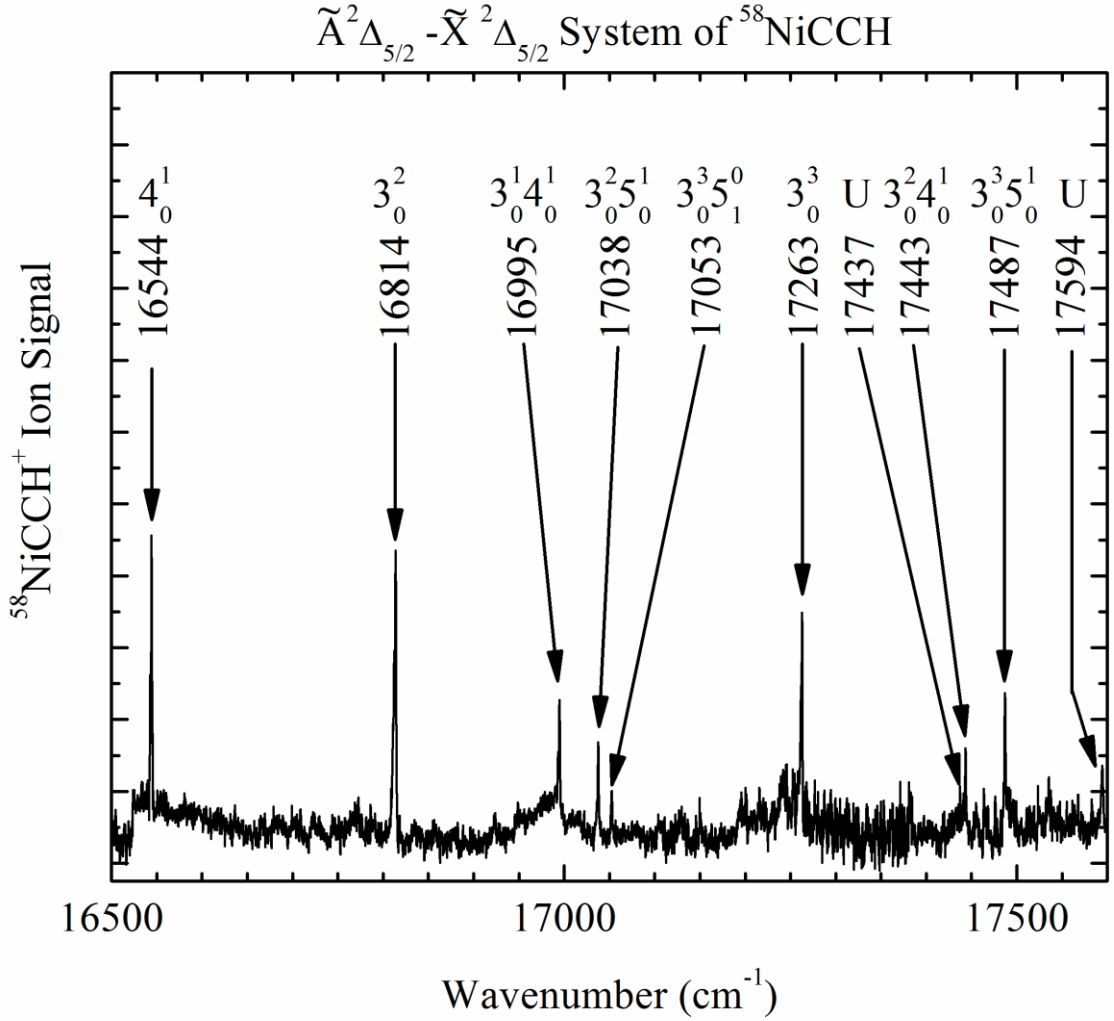

Figure A.2 Vibronically resolved spectrum of the $\tilde{A}\,^2\Delta_{5/2} \leftarrow \tilde{X}\,^2\Delta_{5/2}$ band system of ^{58}NiCCH over the 16500-17600 cm^{-1} range. The bands are identified by wavenumber and vibronic assignment. Unidentified bands are labeled "U".

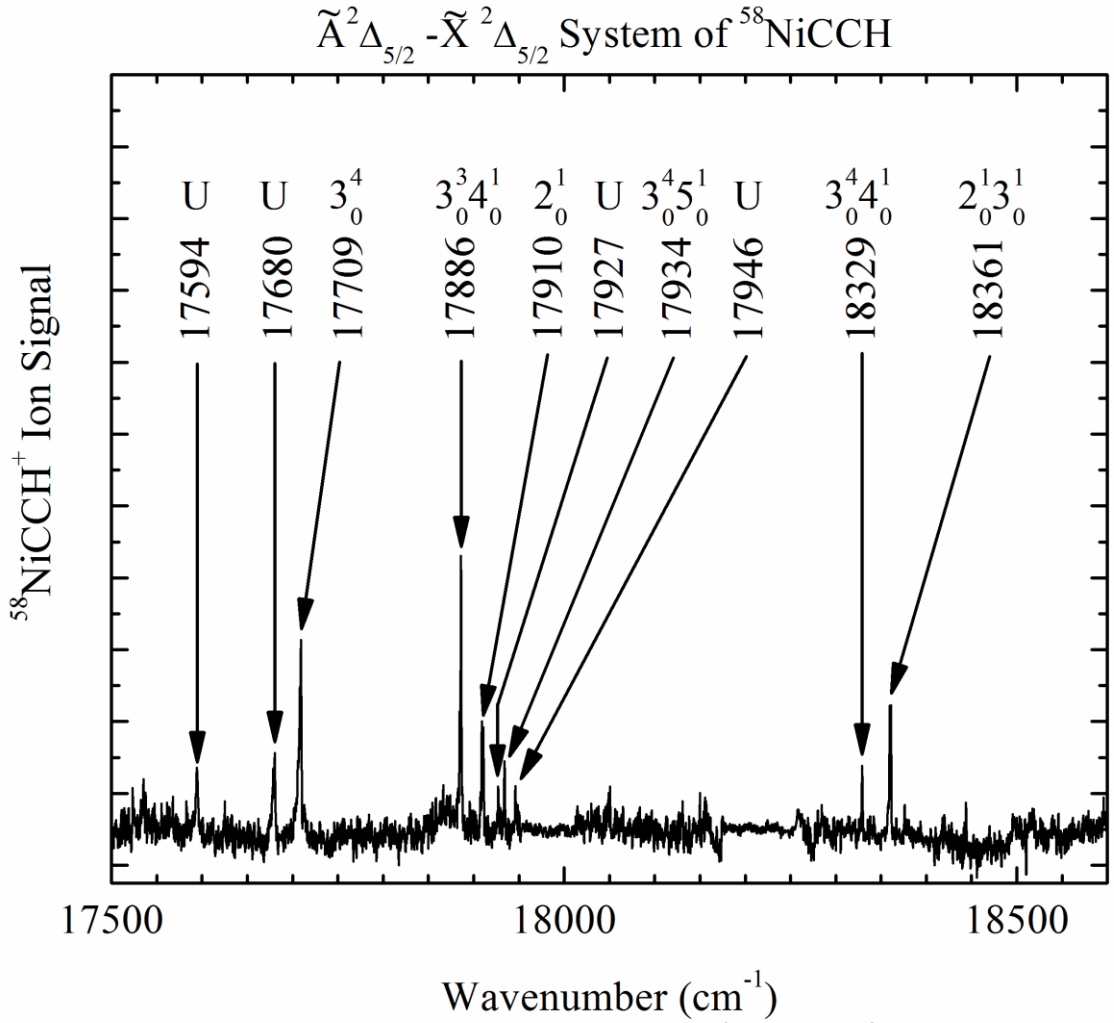

Figure A.3 Vibronically resolved spectrum of the $\tilde{A}\,^2\Delta_{5/2} \leftarrow \tilde{X}\,^2\Delta_{5/2}$ band system of ^{58}NiCCH over the 17500-18600 cm^{-1} range. The bands are identified by wavenumber and vibronic assignment. Unidentified bands are labeled "U".

Table A.1 Bands measured for ^{58}NiCCH

Band	Measured ν_0 (cm^{-1})	Fitted ν_0 (cm^{-1})	Residual in fit (cm^{-1})	Isotope shift $\nu(^{58}NiCCH)-\nu(^{60}NiCCH)$ (cm^{-1})	B′ (cm^{-1})	P′	τ (μs)
$\tilde{A} - \tilde{X}\ 5_1^0$	15701.2[b]	15701.531	0.669[d]				
$\tilde{A} - \tilde{X}\ 0_0^0$	15910.1[b]	15910.041	0.059[d]	0.1			0.725(15)[c]
$\tilde{A} - \tilde{X}\ 3_0^1 5_1^0$	16153.6[b]	16153.795	-0.195[d]	1.7			0.739(74)
$\tilde{A} - \tilde{X}\ 3_0^1$	16362.8830(27)[c]	16363.305	-0.422[d]	1.96	0.12931(10)[c]	5/2	0.802(18)[c]
$\tilde{A} - \tilde{X}\ 4_0^1$	16544.1[b]	16544.817	-0.717[d]				
$\tilde{A} - \tilde{X}\ 3_0^2$	16813.8[b]	16814.152	-0.352[d]	3.8			0.820(47)[c]
$\tilde{A} - \tilde{X}\ 3_0^1 4_0^1$	16994.7834(27)[c]	16994.578	0.205[d]	1.8	0.12878(11)[c]	7/2	1.243(29)[c]
$\tilde{A} - \tilde{X}\ 3_0^2 5_0^1$	17037.7539(30)[c]	17037.709	0.045[d]	1.9	0.12893(8)[c]	7/2	1.456(63)[c]
$\tilde{A} - \tilde{X}\ 3_0^3 5_1^0$	17052.6[b]	17053.074	-0.474[d]				
$\tilde{A} - \tilde{X}\ 3_0^3$	17262.7[b]	17262.584	0.116[d]	5.9			
U[a]	17437.2[b]						
$\tilde{A} - \tilde{X}\ 3_0^2 4_0^1$	17443.4[b]	17441.923	1.477[d]	3.9			
$\tilde{A} - \tilde{X}\ 3_0^3 5_0^1$	17487.0[b]	17487.090	-0.090[d]	4.0			1.74(19)
U[a]	17594.2704(68)[c]				0.12820(14)[c]	5/2	7.98(1.08)[c]
U[a]	17680.3[b]			7.1			18.7(1.2)
$\tilde{A} - \tilde{X}\ 3_0^4$	17709.2[b]	17708.601	0.599[d]	7.1			
$\tilde{A} - \tilde{X}\ 3_0^3 4_0^1$	17886.1530(90)[c]	17886.852	-0.699[d]	5.9	0.12869(14)[c]	7/2	
$\tilde{A}\ 2_0^1$	17910.5[b]	17910.500	0.000[d]	-0.1			
U[a]	17927.1[b]						

Table A. 1 Continued

$\tilde{A} - \tilde{X}\ 3_0^4 5_0^1$	17934.1[b]	17934.055	0.045[d]				
U[a]	17946.1[b]						
$\tilde{A} - \tilde{X}\ 3_0^4 4_0^1$	18329.1[b]	18329.365	-0.265[d]	7.5			
$\tilde{A} - \tilde{X}\ 2_0^1 3_0^1$	18360.9[b]	18360.900	0.000[d]	2.0			

[a] Unidentified band

[b] Estimated band origin location, measured in low resolution, expected accuracy ± 1 cm^{-1}.

[c] Error limits (1σ) are provided in parentheses, in units of the last digits quoted.

[d] Residual is defined as measured value minus fitted value. The least-squares fit of the measured vibronic levels to equation (3.3) provides the values listed in Table 3.3.

Table A.2 Fitted vibrational constants for the $\tilde{A}\ ^2\Delta_{5/2} \leftarrow \tilde{X}\ ^2\Delta_{5/2}$ system of NiCCH.

Constant	Value (cm^{-1})	Constant	Value (cm^{-1})
ν_0	15940.041 ± 0.561	ω_5'	221.184 ± 2.299
ω_5''	209.510 ± 0.576	x_{33}'	-1.208 ± 0.132
ω_2'	2001.891 ± 1.405	x_{23}'	-2.864 ± 1.160
ω_3'	458.388 ± 1.019	x_{34}'	-3.503 ± 0.316
ω_4'	636.528 ± 0.928	x_{35}'	0.949 ± 0.651

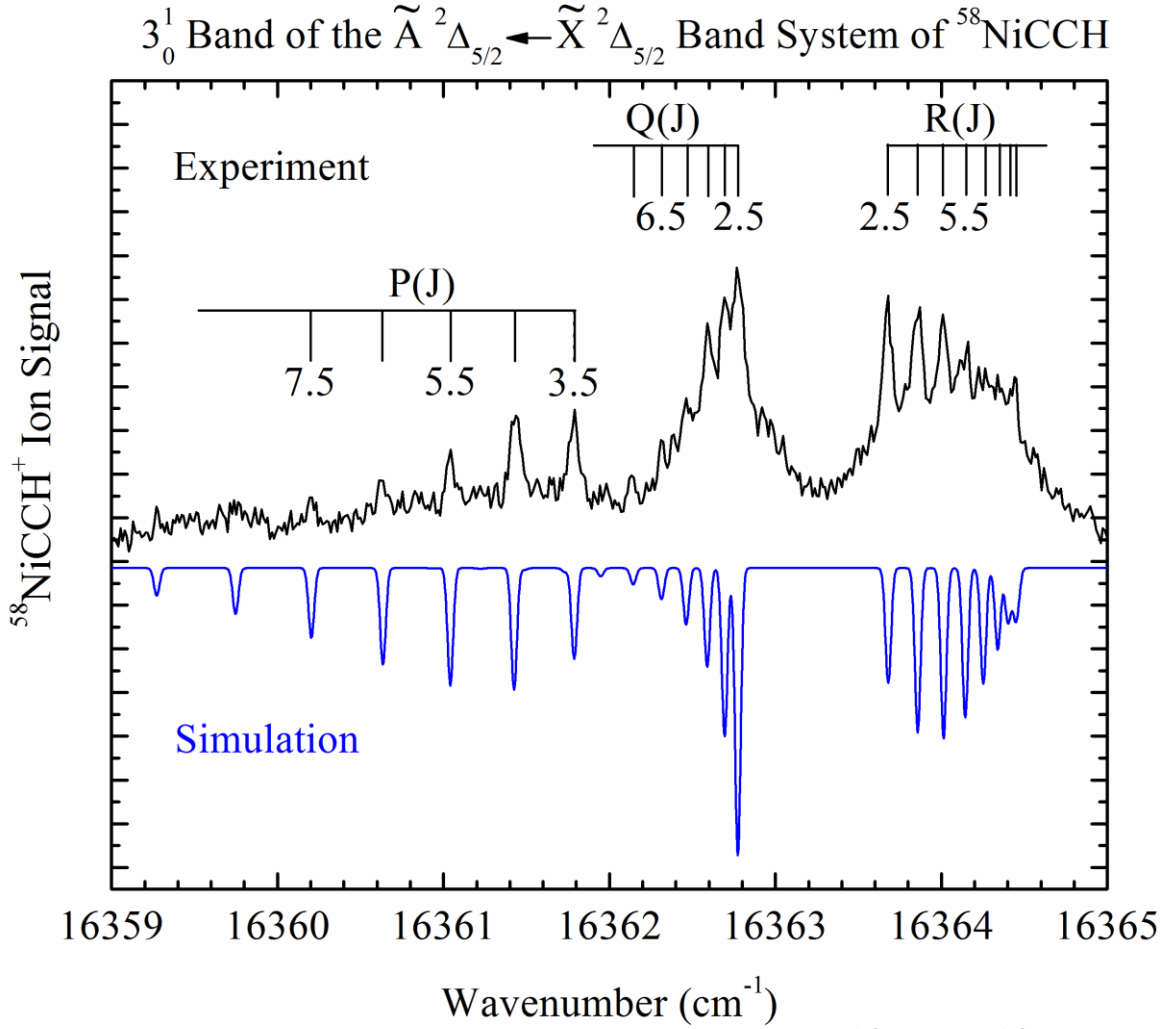

Figure A.4 Rotationally resolved spectrum of the 3_0^1 band of the $\tilde{A}\ ^2\Delta_{5/2} \leftarrow \tilde{X}\ ^2\Delta_{5/2}$ band system of ^{58}NiCCH. The simulated spectrum is provided in blue.

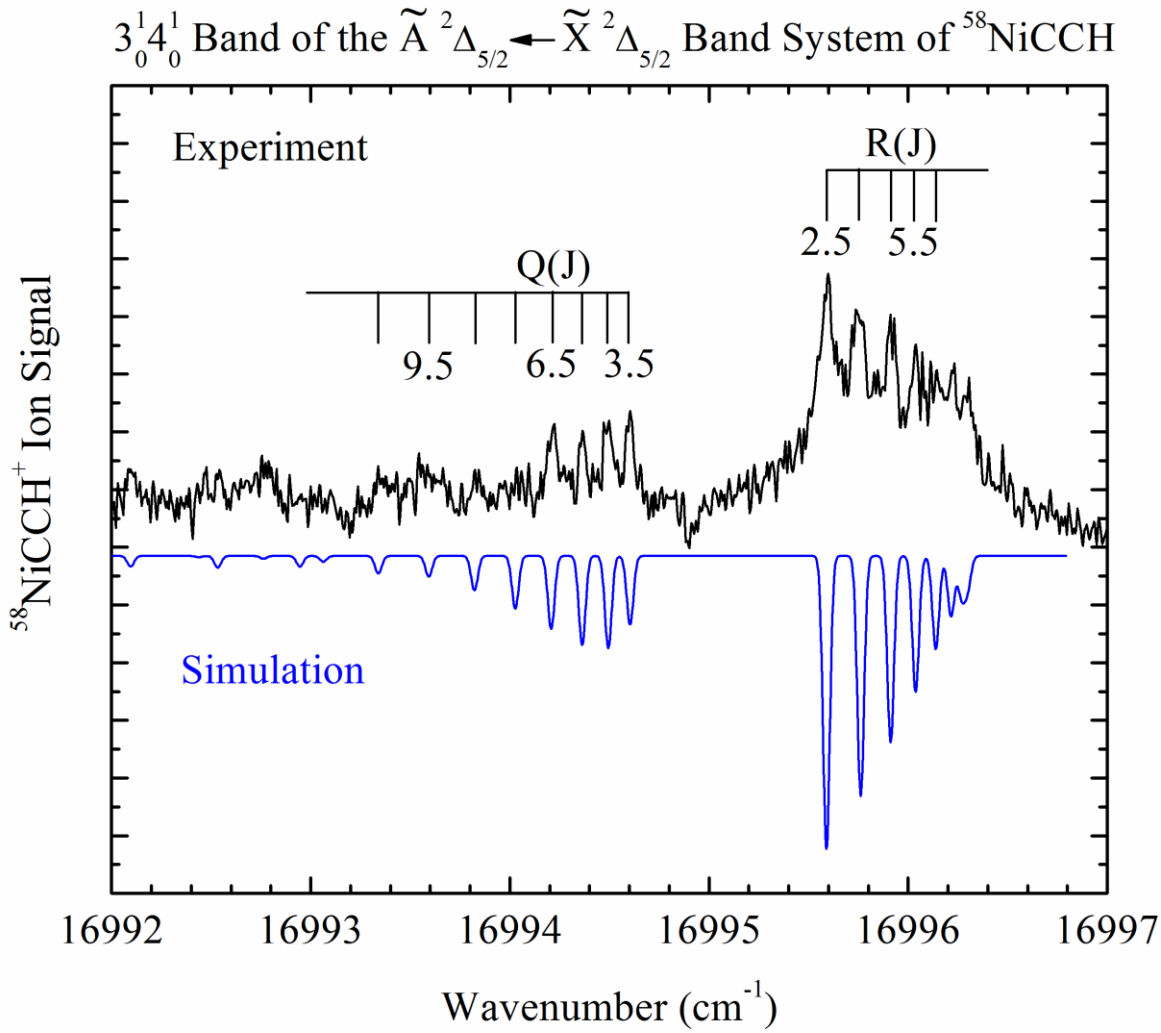

Figure A.5 Rotationally resolved spectrum of the $3_0^1 4_0^1$ band of the $\tilde{A}\ ^2\Delta_{5/2} \leftarrow \tilde{X}\ ^2\Delta_{5/2}$ band system of ^{58}NiCCH. The simulated spectrum is provided in blue.

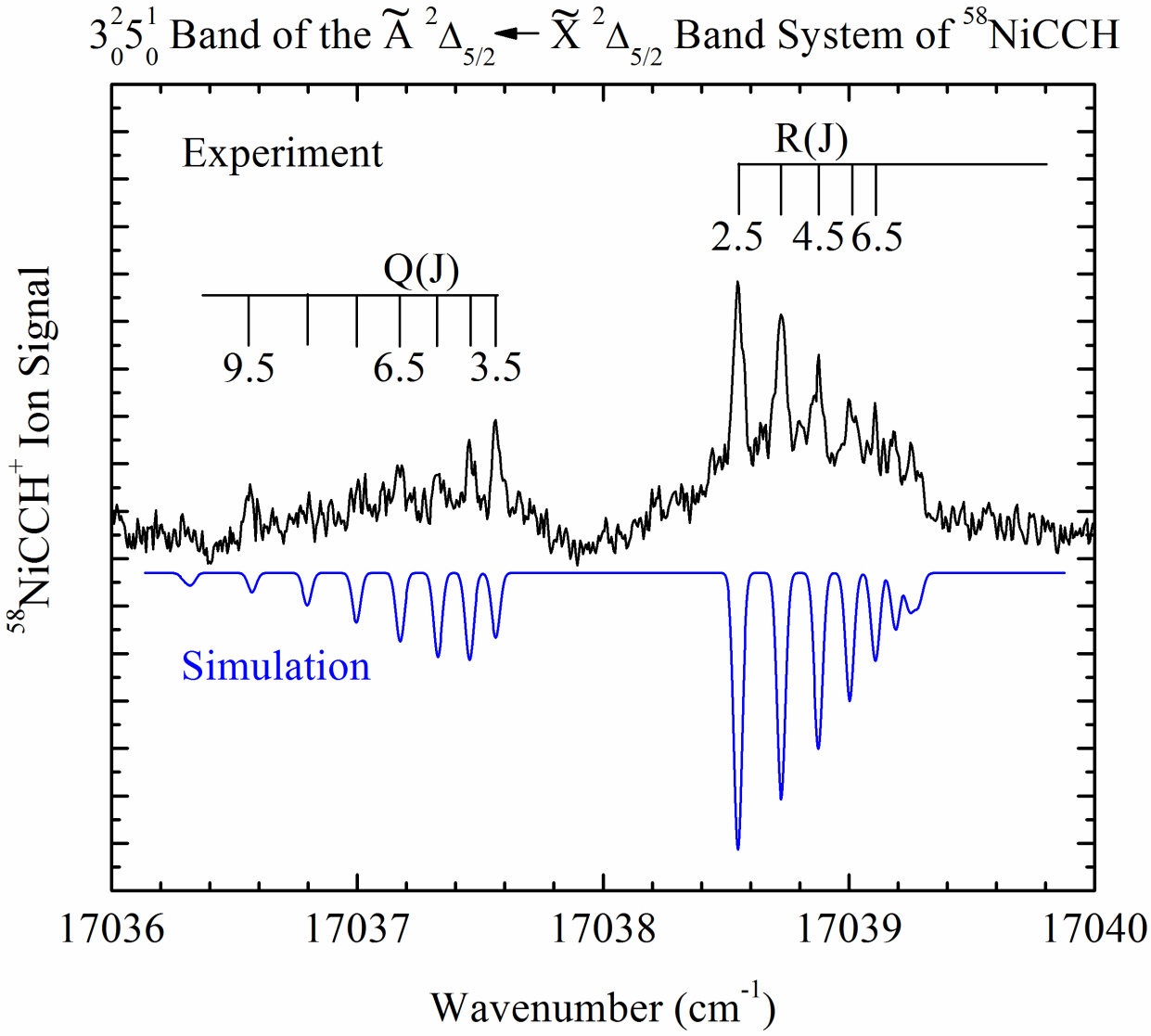

Figure A.6 Rotationally resolved spectrum of the $3_0^2 5_0^1$ band of the $\tilde{A}\ ^2\Delta_{5/2} \leftarrow \tilde{X}\ ^2\Delta_{5/2}$ band system of ^{58}NiCCH. The simulated spectrum is provided in blue.

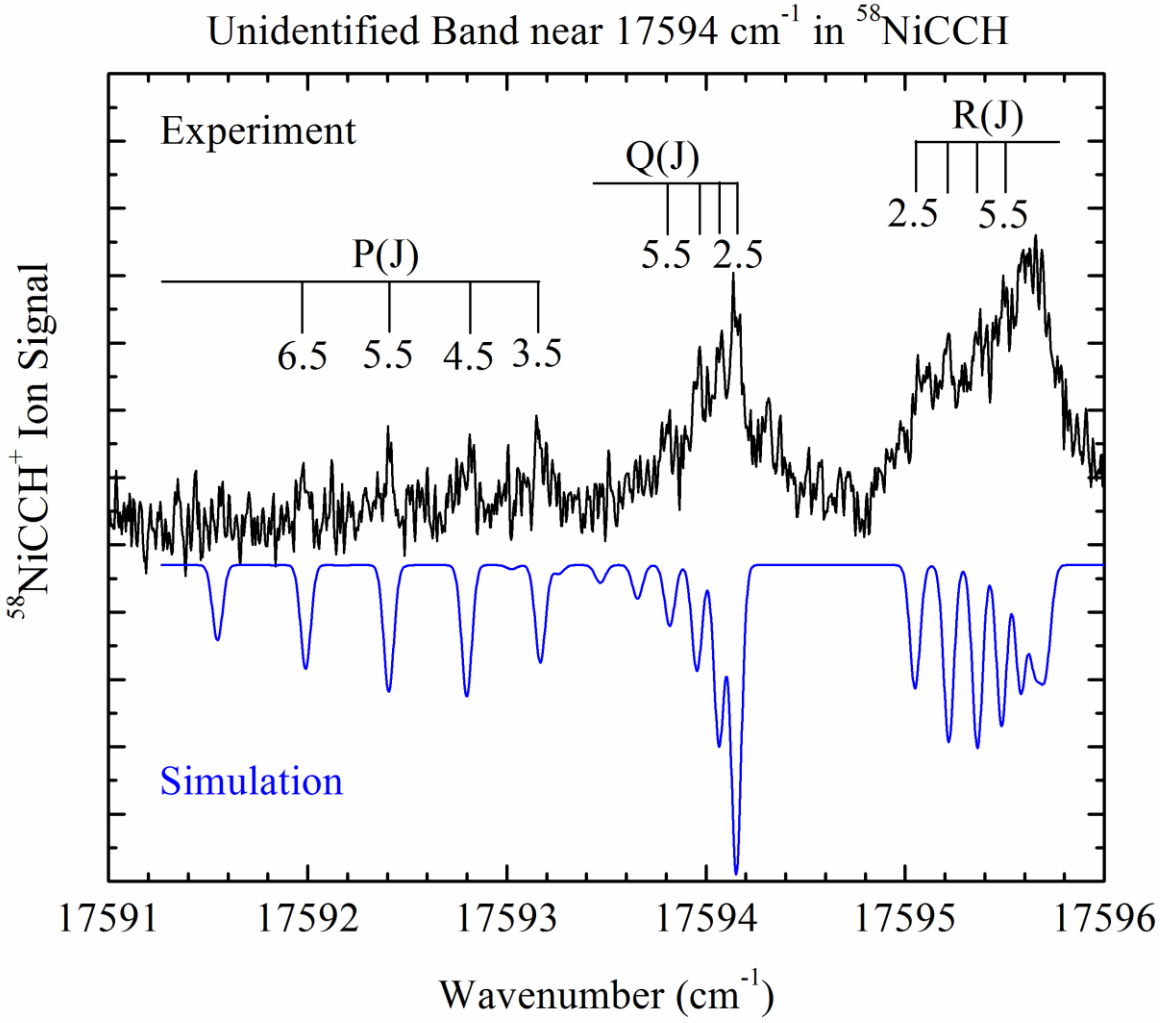

Figure A.7 Rotationally resolved spectrum of the unidentified band of ^{58}NiCCH near 17594 cm^{-1}. The simulated spectrum is provided in blue.

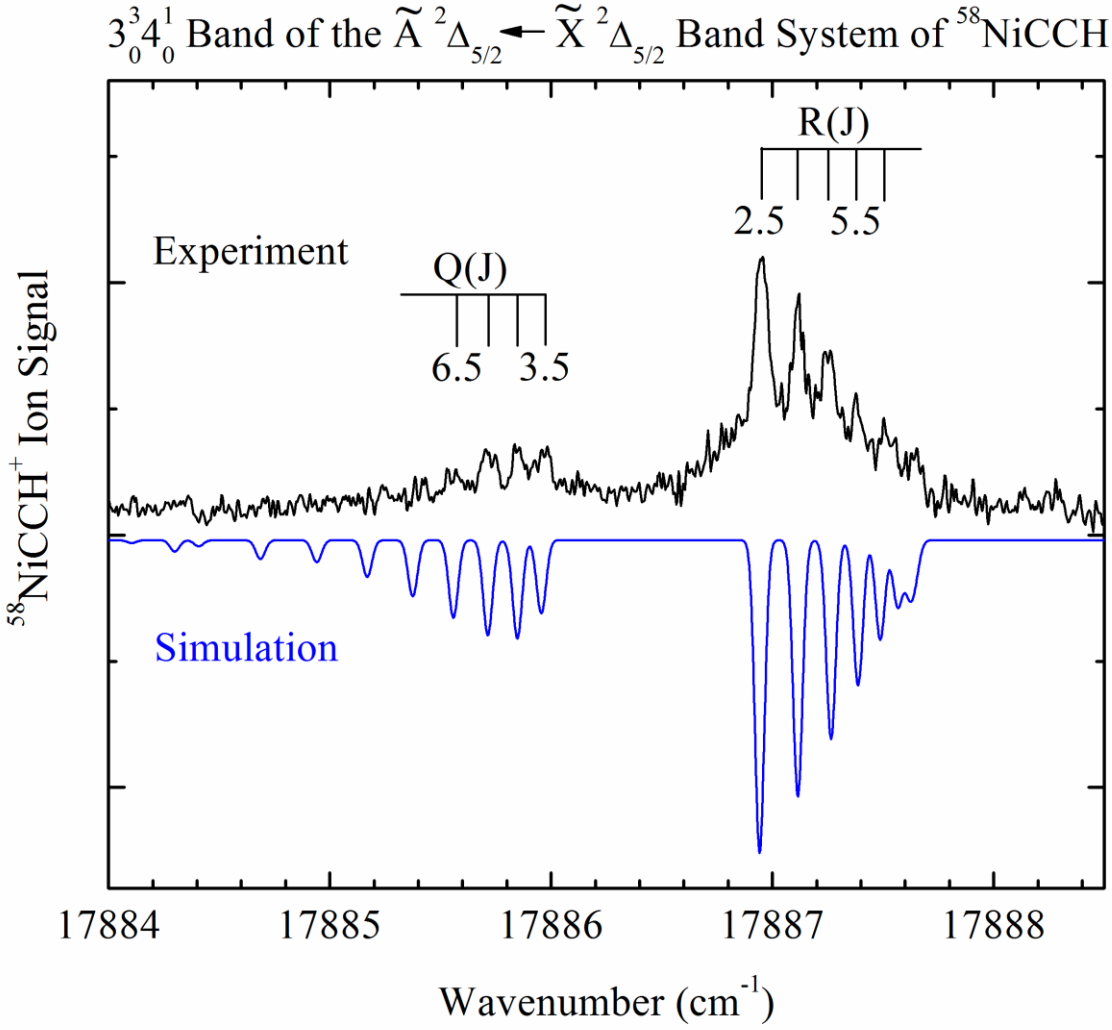

Figure A.8 Rotationally resolved spectrum of the $3_0^3 4_0^1$ band of the $\tilde{A}\ ^2\Delta_{5/2} \leftarrow \tilde{X}\ ^2\Delta_{5/2}$ band system of ^{58}NiCCH. The simulated spectrum is provided in blue.

Table A.3 Rotational lines of resolved bands of ^{58}NiCCH.[a]

Rotational Line	$\tilde{A}-\tilde{X}\ 3_0^1$	$\tilde{A}-\tilde{X}\ 3_0^1 4_0^1$	$\tilde{A}-\tilde{X}\ 3_0^2 5_0^1$	[17.59]5/2 - $\tilde{A}\ 0_0$	$\tilde{A}-\tilde{X}\ 3_0^3 4_0^1$
P(3.5)	16361.800(-3)			17593.165(9)	
P(4.5)	16361.434(1)			17592.816(-11)	
P(5.5)	16361.056(-7)		17035.925(-14)	17592.413(-3)	
P(6.5)	16360.660(-18)		17035.497(2)	17591.972(17)	
P(7.5)	16360.193(18)		17035.061(2)		
P(10.5)	16358.779(1)				
Q(2.5)	16362.778(5)			17594.162(-1)	
Q(3.5)	16362.701(0)	16994.591(3)	17037.565(2)	17594.076(-4)	17885.977(-15)
Q(4.5)	16362.595(4)	16994.487(-1)	17037.456(4)	17593.970(-12)	17885.849(4)
Q(5.5)	16362.474(-2)	16994.359(-6)	17037.325(4)	17593.812(8)	17885.715(5)
Q(6.5)	16362.323(0)	16994.205(-8)	17037.174(1)		17885.571(-8)
Q(7.5)	16362.146(5)	16994.014(2)	17037.005(-8)		
Q(9.5)		16993.581(3)	17036.561(8)		
Q(11.5)		16993.055(-1)			
R(2.5)	16363.687(1)	16995.578(2)	17038.551(1)	17595.059(-2)	17886.951(-3)
R(3.5)	16363.866(0)	16995.752(1)	17038.727(0)	17595.218(8)	17887.117(4)
R(4.5)	16364.020(1)	16995.905(-2)	17038.878(0)	17595.363(6)	17887.254(15)
R(5.5)	16364.150(4)	16996.016(11)	17039.004(1)	17595.501(-15)	17887.382(11)
R(6.5)	16364.261(1)	16996.132(-4)	17039.108(1)		17887.504(-12)
R(7.5)	16364.356(-7)		17039.185(4)		
R(8.5)	16364.416(-4)		17039.254(-10)		
R(9.5)	16364.450(2)				
Fitted spectroscopic constants (cm^{-1})					
T_0	16362.8830(27)	16994.7834(27)	17037.7539(30)	17594.2704(68)	17886.1530(90)
B′	0.12931(10)	0.12878(11)	0.12893(8)	0.12820(14)	0.12869(14)
P′	5/2	7/2	7/2	5/2	7/2
B″	0.14080(11)	0.14080(11)	0.14080(11)	0.14080(11)	0.14080(11)
Ω″	5/2	5/2	5/2	5/2	5/2

[a] All values are in cm^{-1} units; residuals in the fit (calculated – measured) are provided in parentheses, in units of 0.001 cm^{-1}. Error limits in the fitted spectroscopic constants (1σ) are provided in parentheses after each constant, in units of the last digit quoted.

APPENDIX B

ROTATIONALLY RESOLVED SPECTRA, TABULATED LINE POSITIONS, AND FITTED PARAMETERS OF OsSi

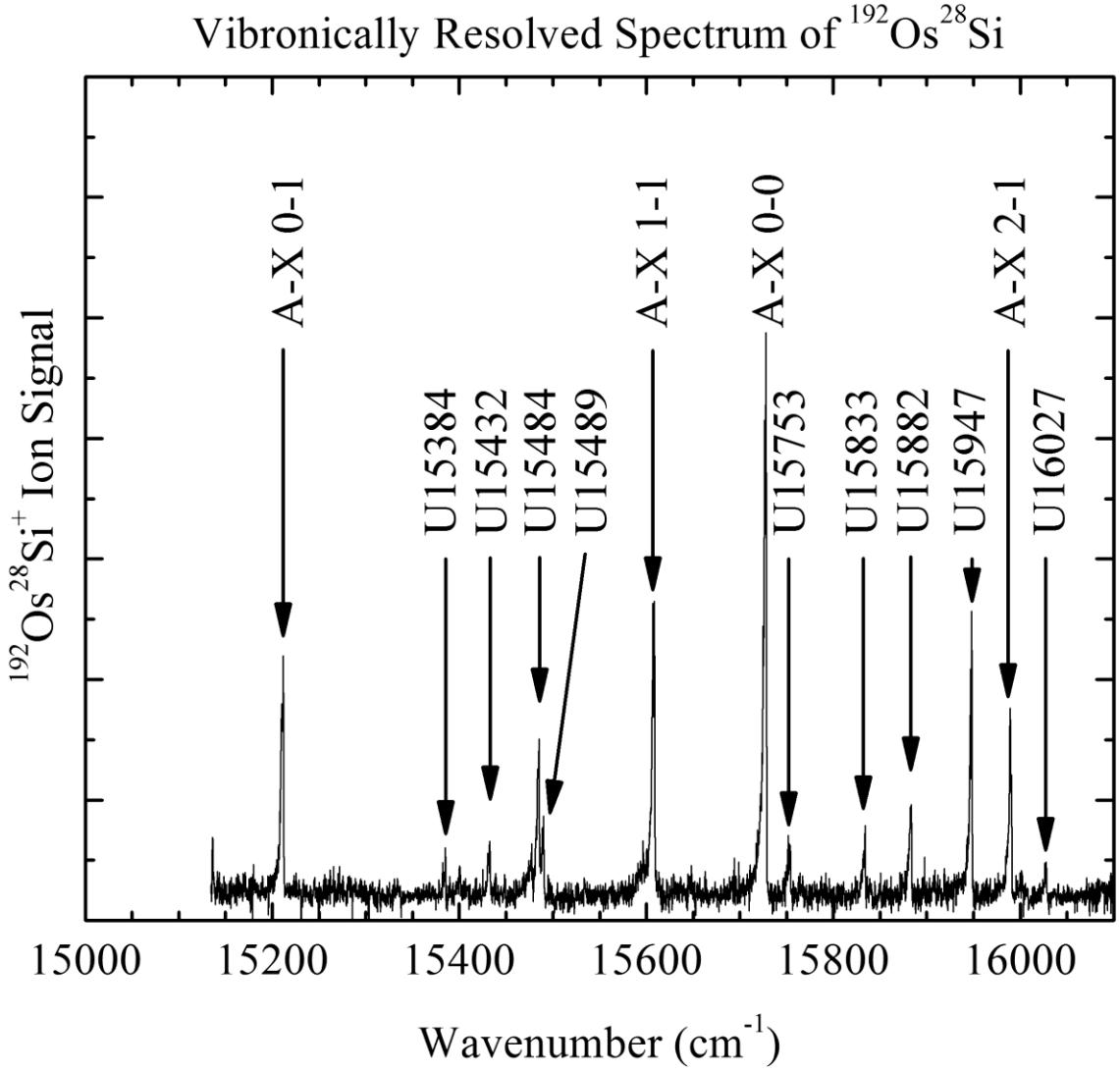

Figure B.1 Vibronically resolved spectrum of OsSi over the 15000-16100 cm^{-1} range. The bands are identified by wavenumber and vibronic assignment. Unclassified bands are labeled "U" followed by the estimated band origin in cm^{-1} units.

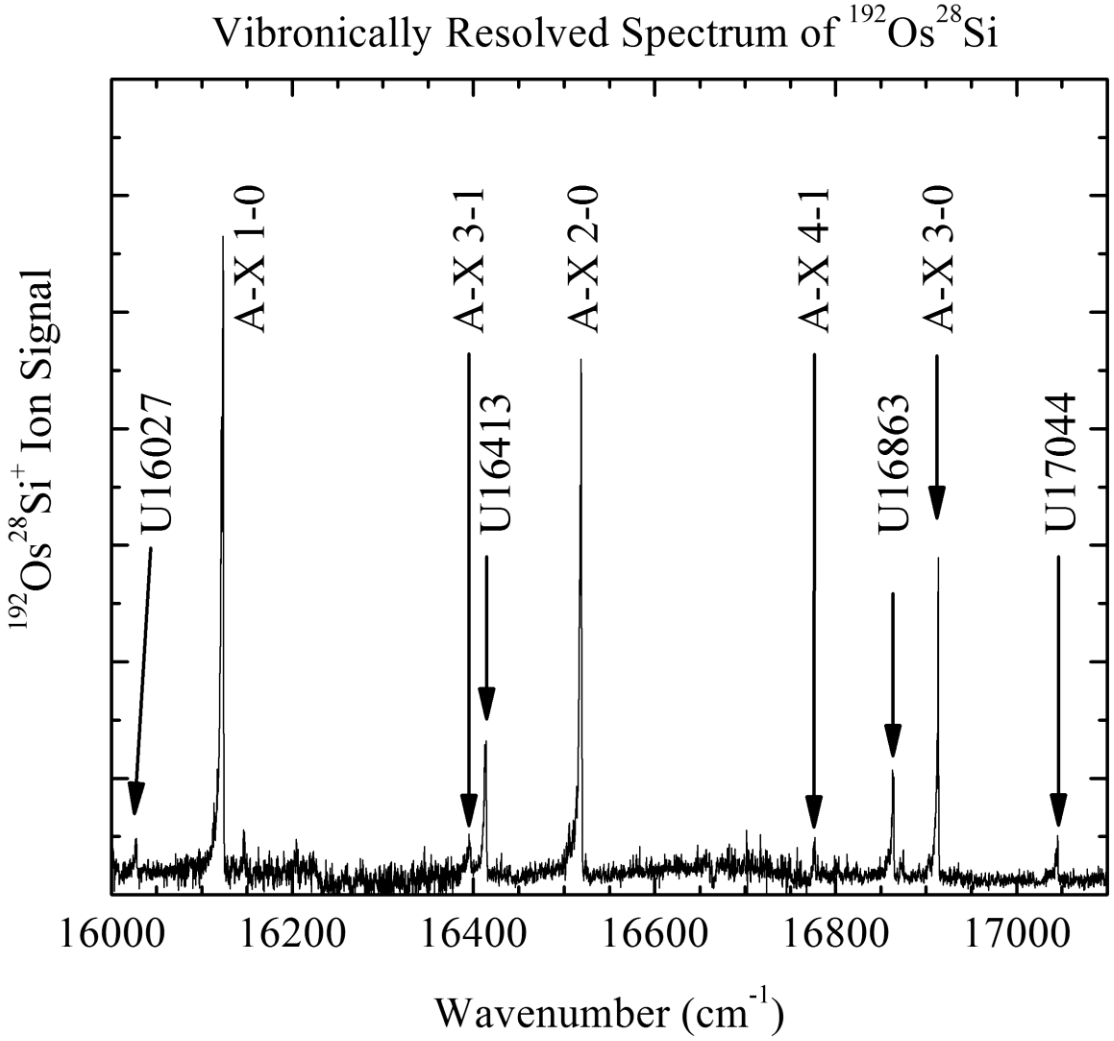

Figure B.2 Vibronically resolved spectrum of OsSi over the 16000-17100 cm^{-1} range. The bands are identified by wavenumber and vibronic assignment. Unclassified bands are labeled "U" followed by the estimated band origin in cm^{-1} units.

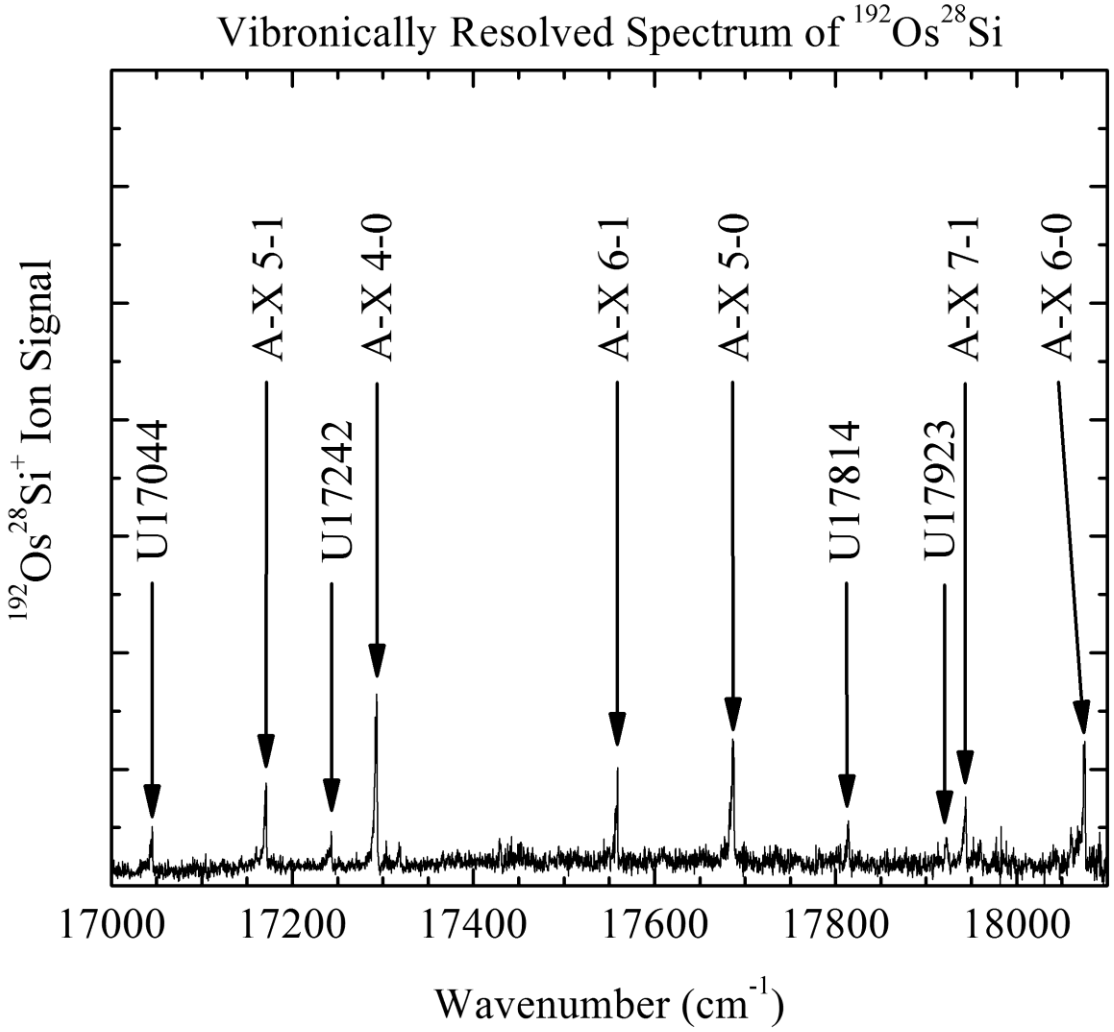

Figure B.3 Vibronically resolved spectrum of OsSi over the 17000-18100 cm^{-1} range. The bands are identified by wavenumber and vibronic assignment. Unclassified bands are labeled "U" followed by the estimated band origin in cm^{-1} units.

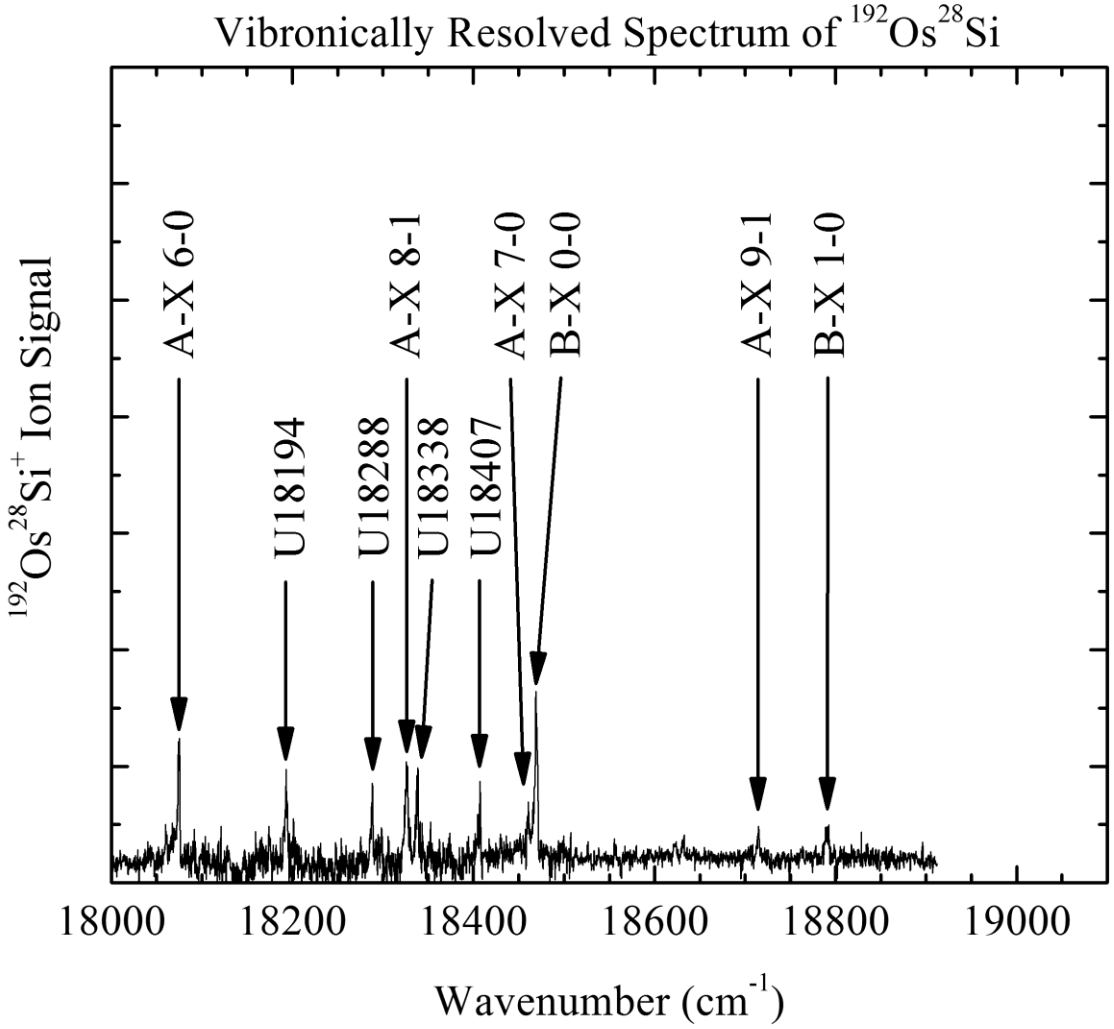

Figure B.4 Vibronically resolved spectrum of OsSi over the 18000-19100 cm^{-1} range. The bands are identified by wavenumber and vibronic assignment. Unclassified bands are labeled "U" followed by the estimated band origin in cm^{-1} units.

Table B.1 Measured vibronic bands of OsSi.[a]

Band	Measured ν_0 for $^{192}Os^{28}Si$ [b]	Isotope shift $\nu(^{190}Os^{28}Si)-\nu(^{192}Os^{28}Si)$ [b]	B′	Ω′	τ (μs) [c]
A-X 0-1	15210.74	-0.19			
A-X 1-1	15607.63	-0.11			
A-X 0-0	15727.2143(20)	-0.0095(26)	0.13783(6)	1	1.07(12)
A-X 2-1	15989.69	1.42			
A-X 1-0	16123.7918(21)	0.2555(25)	0.13709(6)	1	1.06(3)
A-X 3-1	16395.73	0.44			
A-X 2-0	16518.40	0.15			
A-X 4-1	16776.23	0.89			
A-X 3-0	16912.45	0.91			
A-X 5-1	17170.38	1.05			
A-X 4-0	17292.51	1.30			
A-X 6-1	17558.2584(39)	1.2195(48)	0.13432(22)	1	1.05(4)
A-X 5-0	17686.7884(53)	1.3835(65)	0.13888(10)	1	
A-X 7-1	17943.3179(37)	1.4402(47)	0.13382(20)	1	1.18(3)
A-X 6-0	18074.5689(28)	1.5562(39)	0.13442(6)	1	1.14(21)
A-X 8-1	18326.64	1.46			
A-X 7-0	18459.6389(42)	1.7605(59)	0.13306(9)	1	
A-X 9-1	18714.20	1.70			
B-X 0-0	18468.7147(32)	0.0305(41)	0.14263(7)	1	8.31(33)
B-X 1-0	18792.8211(16)	0.1734(26)	0.14174(8)	1	6.16(60)
U[d]	15384.33	0.57			
U[d]	15431.78	0.79			
U[d]	15484.17	0.42			
U[d]	15489.03	-0.17			
U[d]	15753.06	0.18			
U[d]	15833.10	0.65			
U[d]	15882.47	0.08			
U[d]	15947.26	0.90			
U[d]	16026.89	0.13			
U[d]	16412.92	0.90			
U[d]	16863.19	1.36			
U[d]	17044.37	1.30			
U[d]	17242.17	0.49			
U[d]	17813.78	1.30			
U[d]	17922.72	-0.10			
U[d]	18193.66	2.19			
U[d]	18287.99	1.07			
U[d]	18338.03	0.13			
U[d]	18406.75	0.11			

Table B.1 Continued

[a] All values are in cm^{-1} units unless otherwise specified; 1σ error limits are provided in parentheses, in units of the last digit quoted. [b] Band origins that have been determined in rotationally resolved scans are given to four digits after the decimal, with the 1σ error provided. Band origins quoted to only two digits are estimated from low resolution measurements, and are thought to be accurate to better than 1 cm^{-1}. Similarly, isotope shifts measured in low resolution are quoted to two digits. These are generally accurate to 0.1 cm^{-1}, based on comparisons to high resolution measurements. Weaker features may have larger errors. When four digits and an error estimate are provided, the feature was measured in a well-calibrated high resolution scan. [c] Excited state exponential decay lifetime. [d]Unclassified band.

Table B.2 Molecular constants of OsSi.

Electronic State	Molecular constant	$^{192}Os^{28}Si$	$^{190}Os^{28}Si$	$^{189}Os^{28}Si$
$X\ ^3\Sigma_{0+}^-$	$\Delta G_{1/2}$	516.3149(36)	516.6450(31)	516.8333(55)
	B_0''	0.15332(8)	0.15317(6)	0.15350(8)
	B_1''	0.15242(21)	0.15297(14)	0.15248(17)
	B_e''	0.15377(14)	0.15327(10)	0.15401(12)
	α_e''	0.00090(22)	0.00020(15)	0.00102(19)
	r_e''	2.1189(10)	2.1238(7)	2.1194(8)
	Recommended r_e''	2.1207(27)		
A1	T_0	15727.734(702)	15727.702(672)	15727.205
	ω_e'	396.97(75)	397.31(72)	399.06
	$\omega_e'x_e'$	0.839(95)	0.849(91)	1.042
	B_e'	0.13804(20)	0.13724(164)	0.13817(18)
	α_e'	0.00035(78)	0.00025(66)	0.00053(7)
	r_e'	2.236(16)	2.244(13)	2.2376(15)
	Recommended r_e'	2.2394(43)		
B1	T_0	18468.7147(32)	18468.7452(26)	18468.7644(24)
	$\Delta G_{1/2}$	324.1064(36)	324.2493(33)	324.3268(31)
	B_e'	0.14308(10)	0.14275(12)	0.14308(9)
	α_e'	0.00089(11)	0.00074(13)	0.00077(11)
	r_e'	2.1966(8)	2.2006(9)	2.1988(7)
	Recommended r_e'	2.1987(20)		

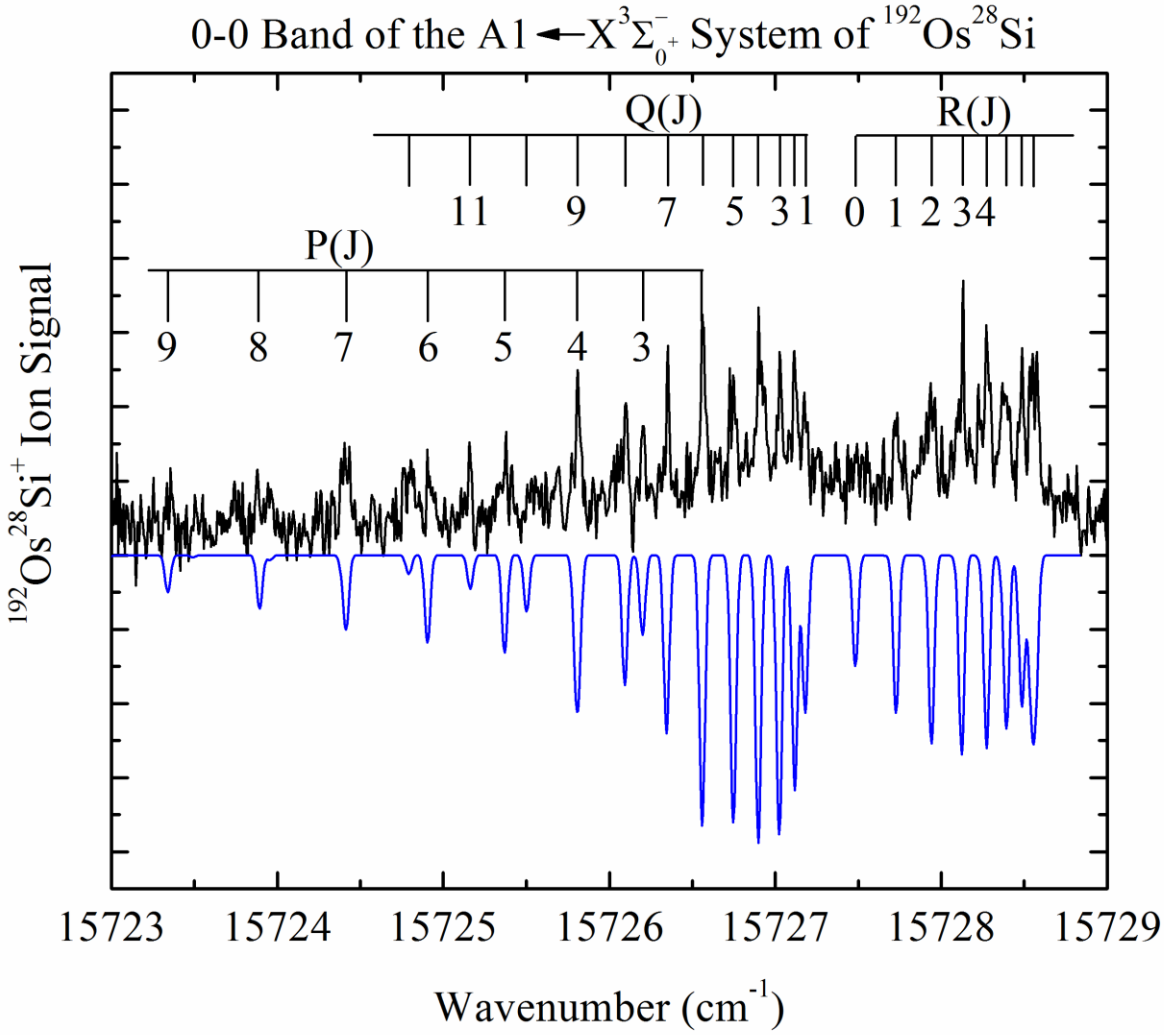

Figure B.5 Rotationally resolved spectrum of the 0-0 band of the A1 ← X $^3\Sigma^-_{0^+}$ band system of ^{192}Os^{28}Si. The simulated spectrum is provided in blue.

Table B.3 Rotational Lines of the 0-0 band of the A1 – X $^3\Sigma^-$ (0^+) system of OsSi.

Rotational Line	$^{192}Os^{28}Si$	$^{190}Os^{28}Si$	$^{189}Os^{28}Si$
P(2)	15726.565(5)	15726.563(-2)	15726.559(0)
P(3)	15726.202(-1)	15726.186(6)	15726.185(6)
P(4)	15725.810(-8)	15725.790(3)	15725.786(5)
P(5)	15725.379(-7)	15725.354(7)	15725.364(-4)
P(6)	15724.920(-10)		
P(7)	15724.411(7)		
P(8)	15723.879(15)	15723.876(7)	15723.878(3)
P(9)	15723.358(-19)	15723.327(1)	15723.324(3)
P(10)	15722.754(0)	15722.743(-1)	
P(11)	15722.141(-4)		15722.131(-7)
Q(1)	15727.180(3)	15727.174(0)	15727.173(1)
Q(2)	15727.118(4)	15727.113(-2)	15727.108(3)
Q(3)	15727.031(-2)	15727.020(-2)	15727.026(-7)
Q(4)	15726.912(-7)	15726.898(-5)	15726.902(-7)
Q(5)	15726.746(3)	15726.738(0)	15726.735(5)
Q(6)	15726.565(-1)	15726.563(-11)	15726.559(-5)
Q(7)	15726.353(-6)	15726.339(-6)	15726.326(12)
Q(8)	15726.100(-1)	15726.098(-13)	15726.098(-8)
Q(11)	15725.162(8)	15725.159(-7)	15725.163(-4)
Q(12)	15724.807(-9)		
Q(13)		15724.387(-13)	15724.377(9)
R(1)	15727.727(7)		15727.723(3)
R(2)	15727.949(-1)	15727.937(0)	15727.934(6)
R(3)	15728.131(0)	15728.120(0)	15728.128(-5)
R(4)	15728.276(7)	15728.272(-3)	15728.268(7)
R(5)		15728.374(15)	15728.410(-13)
R(6)	15728.488(5)	15728.481(-3)	15728.489(-3)
R(7)	15728.552(0)	15728.531(5)	
R(8)	15728.577(3)	15728.553(9)	
R(9)	15728.577(0)	15728.553(4)	
R(10)	15728.534(9)		
R(13)		15728.226(1)	
R(14)		15728.059(8)	
R(15)		15727.877(-1)	
R(16)		15727.650(3)	
Spectroscopic Constants (cm^{-1})			
ν_0	15727.2143(20)	15727.2048(17)	15727.2047(19)
B_0'(A1)	0.13783(6)	0.13762(5)	0.13801(8)
B_0''(X)	0.15333(8)	0.15317(6)	0.15350(8)
χ^2	9.92E-05	7.37E-05	5.97E-05

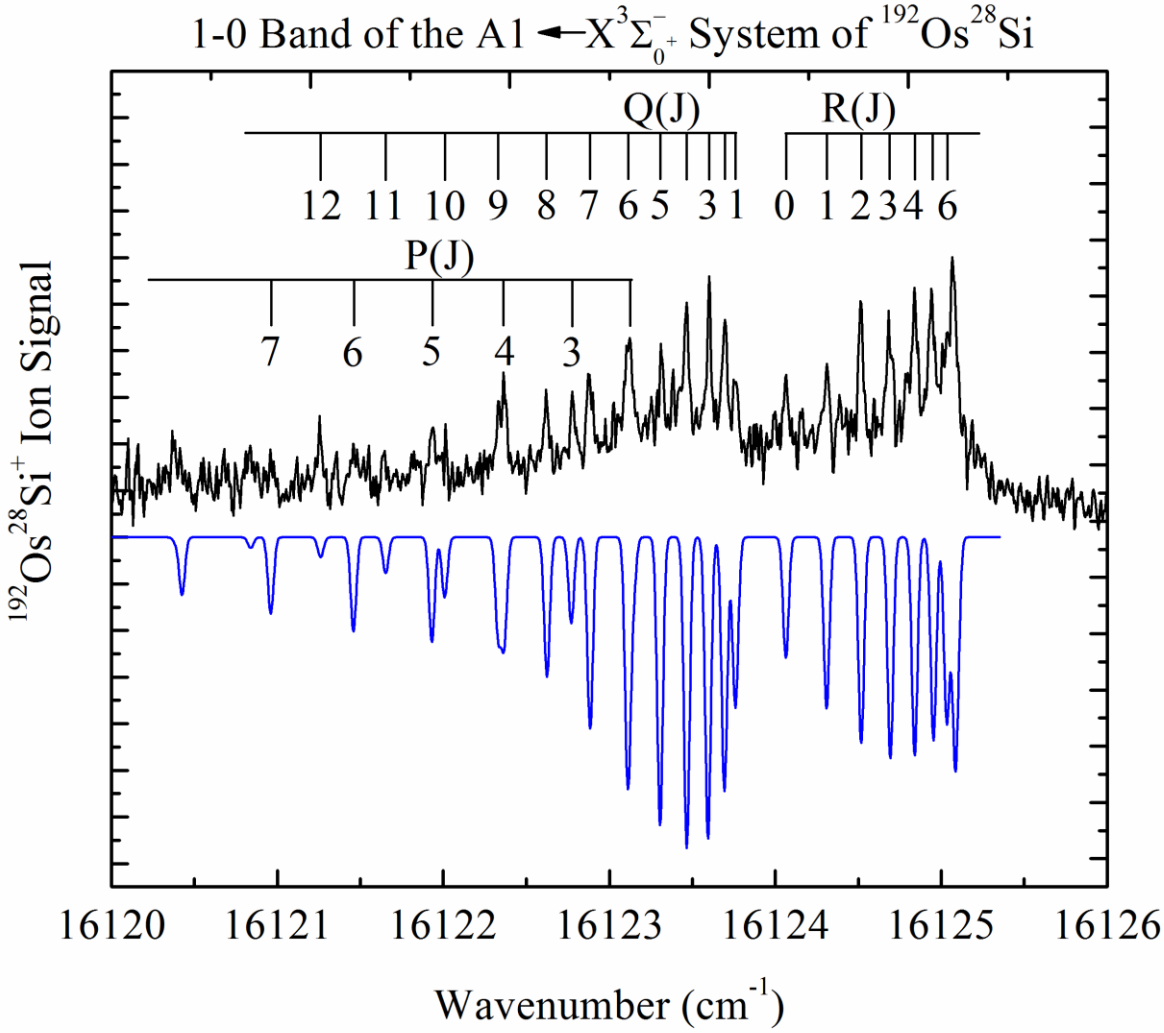

Figure B.6 Rotationally resolved spectrum of the 1-0 band of the A1 ← X $^3\Sigma^-_{0^+}$ band system of $^{192}Os^{28}Si$. The simulated spectrum is provided in blue.

Table B.4 Rotational Lines of the 1-0 band of the A1 – X $^3\Sigma^-$ (0^+) system of OsSi.

Rotational Line	$^{192}Os^{28}Si$	$^{190}Os^{28}Si$	$^{189}Os^{28}Si$
P(2)		16123.401(1)	
P(3)	16122.778(-3)	16123.027(4)	16123.169(-4)
P(4)	16122.366(4)	16122.625(2)	16122.768(-8)
P(5)	16121.937(-2)	16122.179(10)	16122.323(0)
P(6)	16121.459(7)	16121.720(0)	
P(7)	16120.960(4)	16121.219(-1)	16121.356(-5)
P(8)	16120.415(15)	16120.679(5)	
P(9)	16119.860(4)	16120.119(-3)	16120.245(3)
P(10)	16119.267(-1)		
P(11)		16118.884(0)	
P(12)	16117.965(6)		
Q(1)	16123.760(0)	16124.013(2)	16124.152(0)
Q(2)	16123.696(-2)	16123.955(-5)	16124.090(-4)
Q(3)	16123.602(-5)	16123.853(-1)	16123.987(1)
Q(4)	16123.462(5)	16123.716(6)	16123.860(-2)
Q(5)	16123.315(-10)	16123.557(1)	16123.690(5)
Q(6)	16123.121(-11)	16123.369(-6)	16123.490(10)
Q(7)	16122.899(-15)	16123.134(1)	16123.268(3)
Q(8)	16122.620(4)	16122.873(1)	16123.023(-12)
Q(9)	16122.335(-3)	16122.577(3)	
Q(10)	16122.015(-8)	16122.263(-8)	16122.408(-15)
Q(11)	16121.641(9)	16121.897(0)	
Q(12)	16121.258(3)	16121.512(-7)	16121.636(8)
Q(13)	16120.835(4)		
Q(14)	16120.376(9)	16120.610(15)	
Q(15)	16119.892(7)	16120.141(-5)	
Q(16)	16119.380(0)		
R(0)	16124.065(1)	16124.324(-3)	16124.455(3)
R(1)	16124.313(-5)	16124.568(-6)	16124.696(4)
R(2)	16124.516(1)	16124.775(-4)	16124.914(-5)
R(3)	16124.684(10)	16124.940(7)	16125.077(9)
R(4)	16124.839(-1)	16125.097(-7)	16125.234(-4)
R(5)	16124.942(8)	16125.191(10)	16125.331(11)
R(6)	16125.038(-9)	16125.286(-7)	16125.419(2)
R(7)			16125.467(0)
R(8)		16125.336(1)	16125.480(1)
R(12)		16125.068(-4)	16125.211(0)
R(13)	16124.705(-27)	16124.924(-10)	
R(15)		16124.508(8)	
Spectroscopic Constants (cm^{-1})			
ν_0	16123.7918(21)	16124.0473(14)	16124.1836(19)
B_1'(A1)	0.13709(6)	0.13688(5)	0.13722(7)
B_0''(X)	0.15332(8)	0.15317(6)	0.15350(8)
χ^2	9.92E-05	7.37E-05	5.97E-05

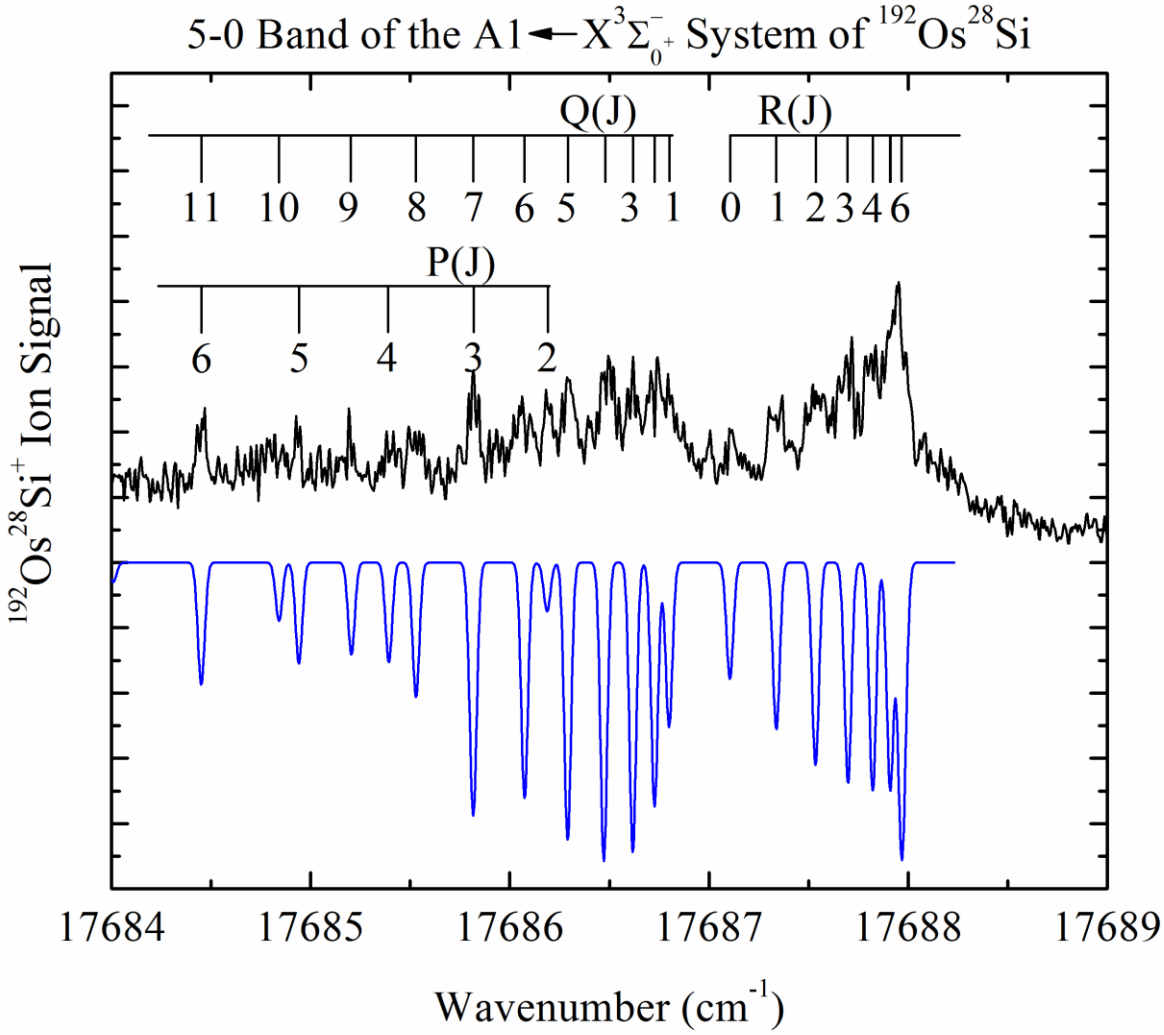

Figure B.7 Rotationally resolved spectrum of the 5-0 band of the A1 ← X $^3\Sigma^-_{0^+}$ band system of $^{192}Os^{28}Si$. The simulated spectrum is provided in blue.

Table B.5 Rotational Lines of the 5-0 band of the A1 – X $^3\Sigma^-$ (0^+) system of OsSi.

Rotational Line	$^{192}Os^{28}Si$	$^{190}Os^{28}Si$	$^{189}Os^{28}Si$
P(3)		17687.147(-2)	
P(4)		17686.749(-18)	
P(5)		17686.283(-2)	
P(8)		17684.700(17)	
Q(1)	17686.747(13)	17688.115(21)	
Q(2)	17686.712(-10)	17688.055(9)	
Q(3)	17686.618(-3)	17687.956(0)	
Q(4)	17686.498(1)	17687.801(12)	
Q(5)		17687.643(-9)	
Q(6)		17687.419(-1)	
Q(7)		17687.176(-8)	
Q(8)		17686.874(7)	
Q(9)	17685.497(-7)		
Q(10)	17685.195(6)	17686.188(11)	
R(2)		17688.889(-13)	
R(3)		17689.036(2)	
R(4)		17689.174(-9)	
R(5)		17689.275(-19)	
R(6)		17689.304(8)	
R(7)		17689.331(0)	
R(11)		17689.058(-8)	
Spectroscopic Constants (cm^{-1})			
ν_0	17686.7884(53)	17688.1719(38)	
B_5'(A1)	0.13888(10)	0.13524(5)	
B_0''(X)	0.15332(8)	0.15317(6)	0.15350(8)
χ^2	9.92E-05	7.37E-05	5.97E-05

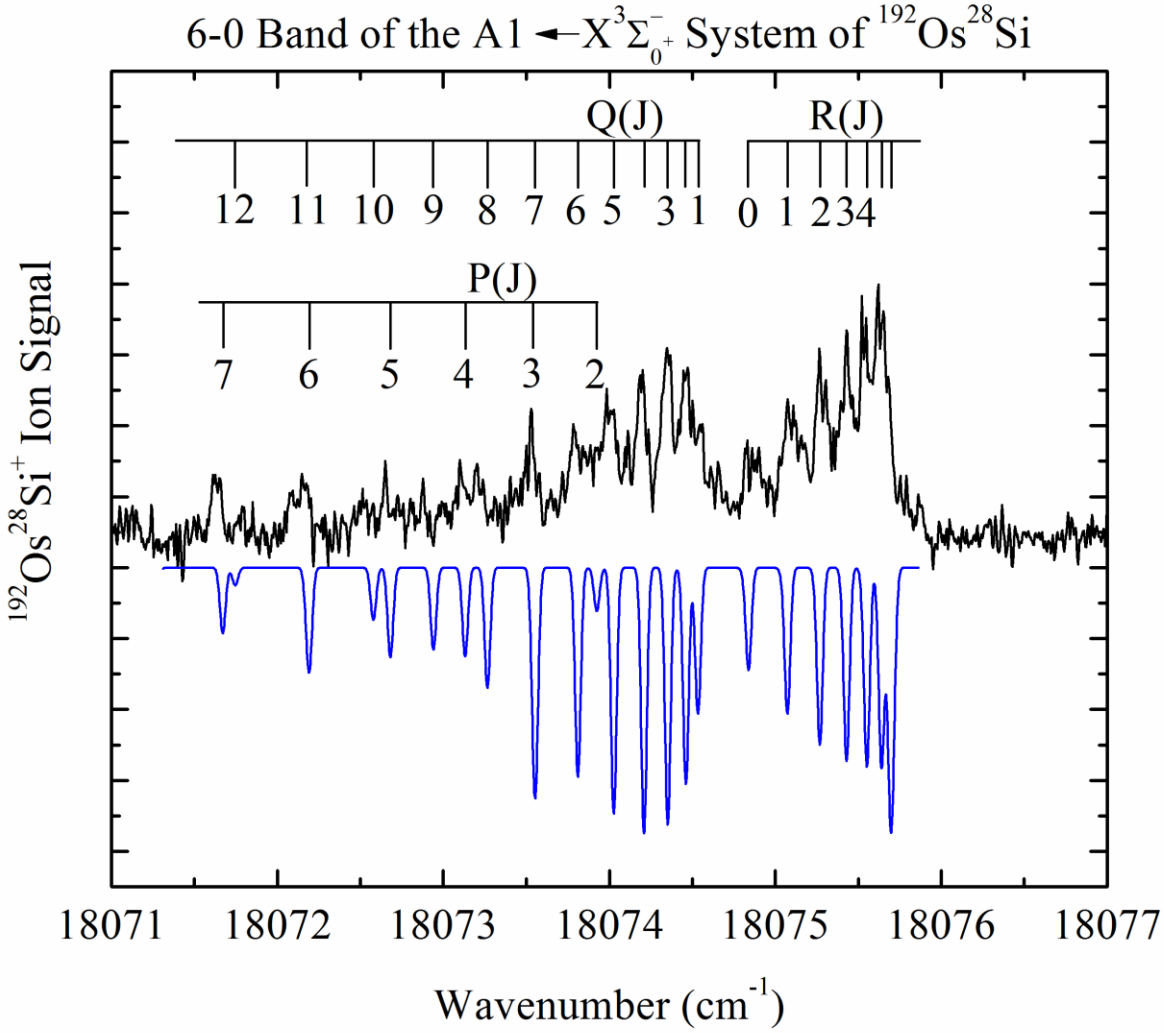

Figure B.8 Rotationally resolved spectrum of the 6-0 band of the A1 ← X $^3\Sigma^-_{0^+}$ band system of $^{192}Os^{28}Si$. The simulated spectrum is provided in blue.

Table B.6 Rotational Lines of the 6-0 band of the A1 – X $^3\Sigma^-$ (0^+) system of OsSi.

Rotational Line	$^{192}Os^{28}Si$	$^{190}Os^{28}Si$	$^{189}Os^{28}Si$
P(2)		18075.479(-4)	
P(3)	18073.531(4)	18075.097(-4)	
P(4)	18073.102(13)	18074.664(10)	
P(5)	18072.652(5)	18074.209(8)	
P(6)	18072.151(11)	18073.726(-3)	
P(7)	18071.637(-8)	18073.190(1)	
P(8)		18072.647(-25)	
P(9)	18070.426(23)		
P(10)		18071.369(0)	
Q(1)	18074.551(-20)	18076.078(10)	
Q(2)	18074.463(-7)	18076.001(12)	
Q(3)	18074.350(-8)	18075.886(13)	
Q(4)	18074.195(-4)	18075.754(-5)	
Q(5)	18074.016(-14)	18075.568(-7)	
Q(6)	18073.789(-13)	18075.328(7)	
Q(7)	18073.502(8)	18075.076(-4)	
Q(8)	18073.200(8)	18074.790(-19)	
Q(9)	18072.877(-9)	18074.429(4)	
Q(11)		18073.629(14)	
Q(12)	18071.622(-1)		
R(0)	18074.825(13)	18076.394(0)	
R(1)	18075.074(-5)	18076.628(-3)	
R(2)	18075.267(-5)	18076.818(0)	
R(3)	18075.430(-13)	18076.987(-13)	
R(4)	18075.523(12)	18077.088(5)	
R(5)	18075.618(-3)		
R(6)	18075.650(7)		
R(7)	18075.650(11)		
R(9)	18075.548(8)	18077.119(1)	
R(11)	18075.303(-3)		
R(12)	18075.117(-2)		
R(13)	18074.902(-9)	18076.463(2)	
Spectroscopic Constants (cm^{-1})			
ν_0	18074.5689(28)	18076.1251(27)	
B_6'(A1)	0.13442(6)	0.13437(5)	
B_0''(X)	0.15332(8)	0.15317(6)	
χ^2	9.92E-05	7.37E-05	

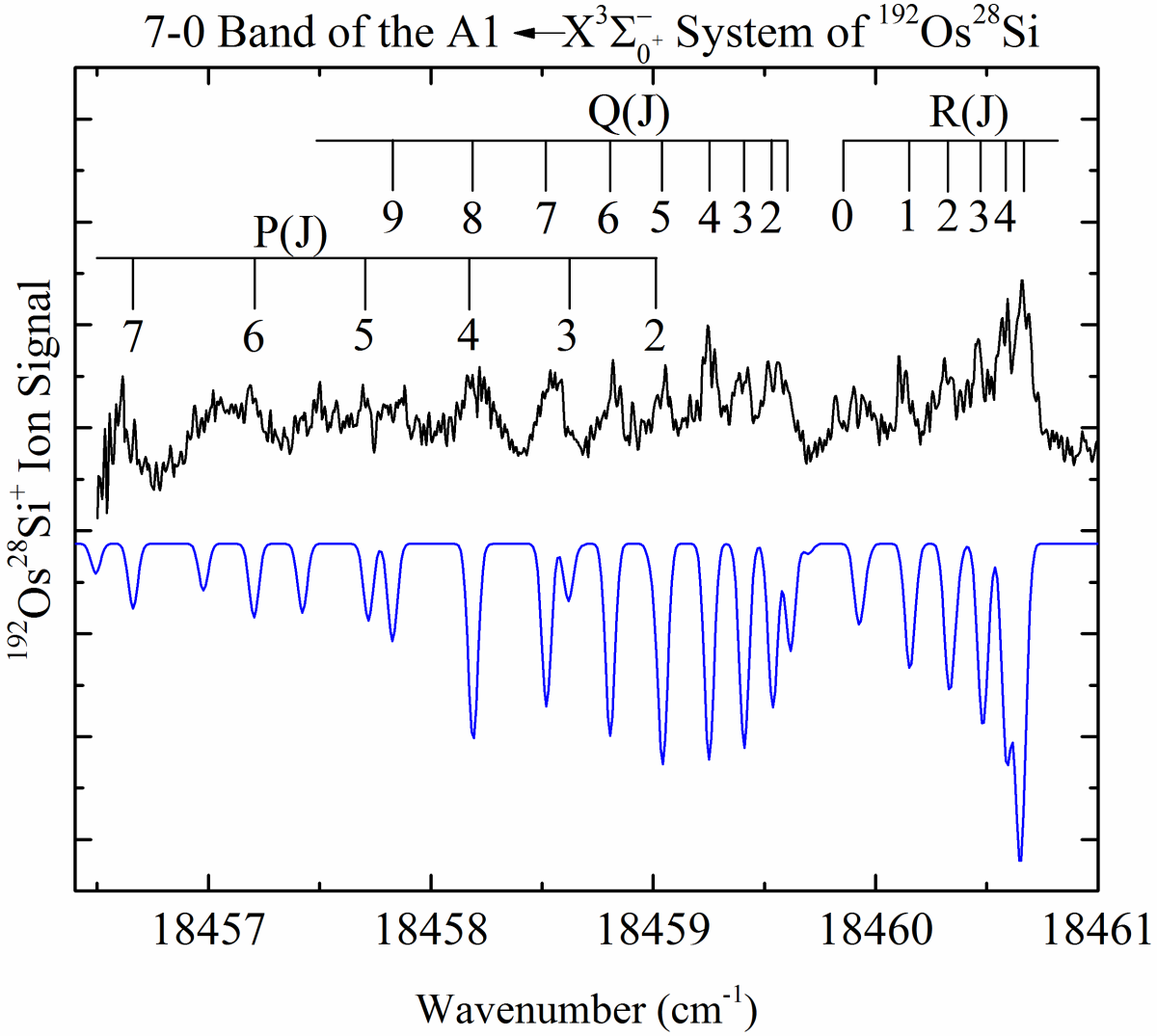

Figure B.9 Rotationally resolved spectrum of the 7-0 band of the A1 ← X $^3\Sigma^-_{0^+}$ band system of $^{192}Os^{28}Si$. The simulated spectrum is provided in blue.

Table B.7 Rotational Lines of the 7-0 band of the A1 – X $^3\Sigma^-$ (0^+) system of OsSi.

Rotational Line	$^{192}Os^{28}Si$	$^{190}Os^{28}Si$	$^{189}Os^{28}Si$
P(3)	18458.581(16)		18461.265(-10)
P(4)	18458.177(-8)	18459.969(-26)	
P(5)	18457.696(5)	18459.480(2)	
P(6)	18457.185(6)		
P(7)	18456.607(34)		
P(8)		18457.861(8)	
P(10)		18456.619(-18)	
Q(1)	18459.601(-2)	18461.361(0)	18462.253(0)
Q(2)	18459.520(-3)	18461.290(-7)	18462.185(-9)
Q(3)	18459.398(-2)	18461.149(19)	18462.061(0)
Q(4)	18459.247(-13)	18461.010(4)	
Q(5)	18459.041(-10)	18460.826(-5)	18461.700(16)
Q(6)	18458.819(-31)	18460.581(9)	18461.485(0)
Q(7)		18460.327(-7)	
Q(8)	18458.177(3)		
Q(9)		18459.660(5)	
R(0)	18459.900(5)		
R(1)	18460.137(-7)	18461.905(-8)	18462.783(8)
R(2)	18460.310(6)	18462.088(-1)	18462.986(-4)
R(3)	18460.462(-2)	18462.230(10)	18463.127(8)
R(4)	18460.568(-4)	18462.344(9)	
R(5)		18462.431(-3)	18463.332(-5)
R(6)	18460.642(9)	18462.458(6)	18463.371(-6)
R(7)		18462.458(4)	
R(10)	18460.341(-3)		
Spectroscopic Constants (cm^{-1})			
ν_0	18459.6389(42)	18461.3994(41)	18462.2921(39)
B_7'(A1)	0.13306(9)	0.13390(13)	0.13429(12)
B_0''(X)	0.15332(8)	0.15317(6)	0.15350(8)
χ^2	9.92E-05	7.37E-05	5.97E-05

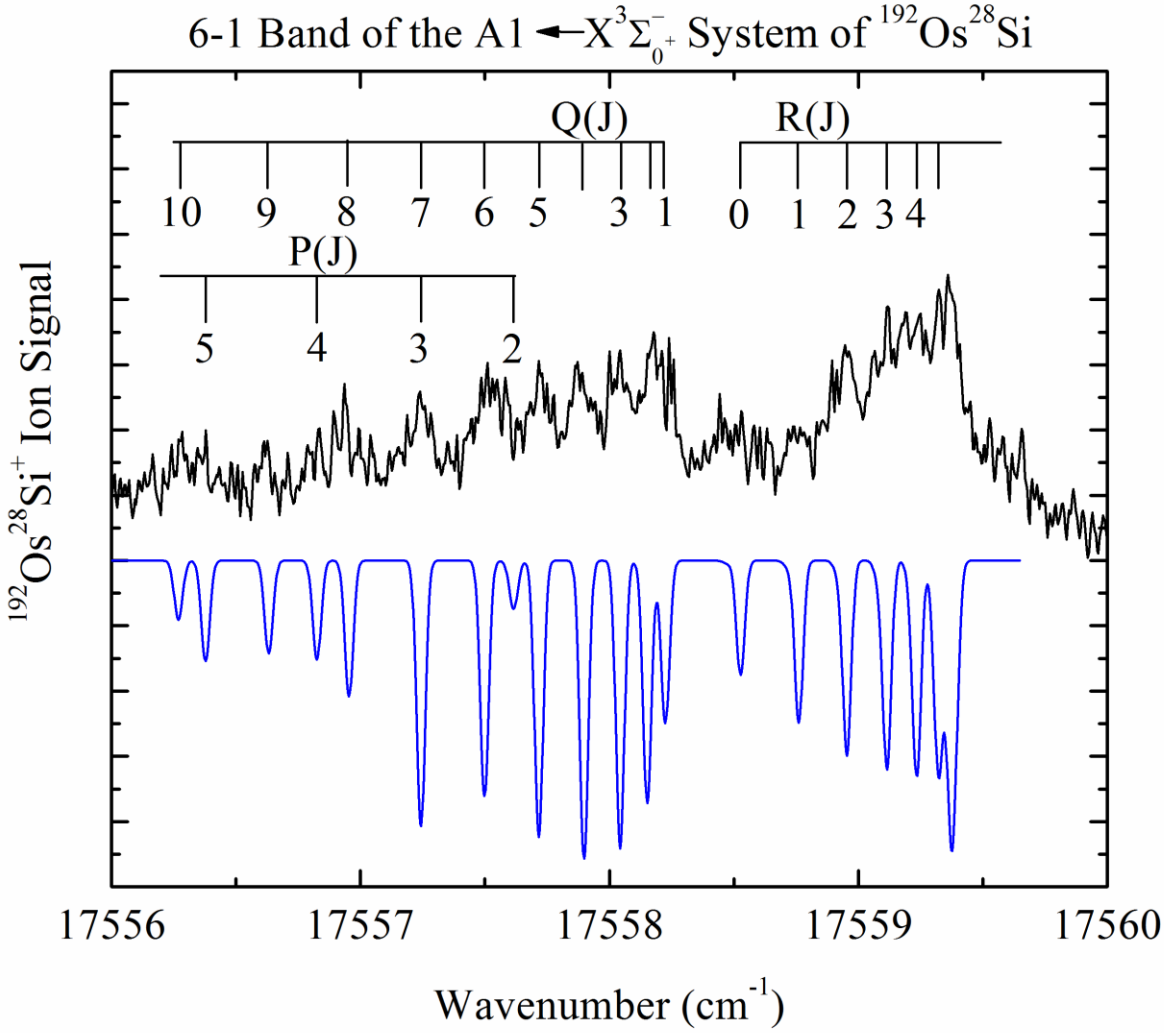

Figure B.10 Rotationally resolved spectrum of the 6-1 band of the A1 ← X $^3\Sigma^-_{0^+}$ band system of ^{192}Os^{28}Si. The simulated spectrum is provided in blue.

Table B.8 Rotational Lines of the 6-1 band of the A1 – X $^3\Sigma^-$ (0^+) system of OsSi.

Rotational Line	$^{192}Os^{28}Si$	$^{190}Os^{28}Si$	$^{189}Os^{28}Si$
P(3)		17558.446(4)	
P(4)	17556.835(-13)		17558.630(3)
P(5)	17556.380(-8)	17557.584(-2)	
P(6)	17555.897(-11)		17557.697(10)
P(7)	17555.362(3)		
P(8)			17556.607(33)
P(9)			17556.041(12)
Q(1)	17558.207(15)	17559.430(11)	
Q(2)	17558.168(-18)	17559.360(8)	
Q(3)		17559.256(2)	17559.867(-14)
Q(4)	17557.871(26)	17559.105(7)	17559.727(-14)
Q(5)	17557.723(-8)	17558.945(-16)	17559.554(-17)
Q(6)	17557.511(-13)		17559.324(1)
Q(7)	17557.245(0)	17558.446(7)	
Q(8)	17556.940(15)	17558.173(-13)	
Q(9)	17556.622(7)		
Q(10)	17556.278(-11)	17557.480(-15)	
Q(11)		17557.054(9)	
Q(13)	17554.968(-4)	17556.160(-12)	
Q(14)		17555.637(-1)	
R(1)		17559.985(-5)	
R(2)	17558.951(4)	17560.175(1)	
R(3)	17559.118(-2)	17560.326(9)	17560.943(-11)
R(4)	17559.239(0)	17560.455(4)	17561.048(14)
R(5)	17559.325(2)	17560.557(-12)	17561.162(-7)
R(6)	17559.370(9)	17560.603(-9)	17561.218(-4)
R(7)	17559.386(8)		17561.227(10)
R(8)			17561.218(7)
R(9)		17560.519(5)	17561.183(-5)
R(10)		17560.425(3)	17561.103(-7)
R(11)			17560.990(-11)
R(14)		17559.662(14)	
Spectroscopic Constants (cm^{-1})			
ν_0	17558.2584(39)	17559.4779(28)	17560.0645(57)
B_6'(A1)	0.13432(22)	0.13467(13)	0.13488(17)
B_1''(X)	0.15242(21)	0.15297(14)	0.15248(17)
χ^2	1.38E-04	1.00E-04	1.62E-04

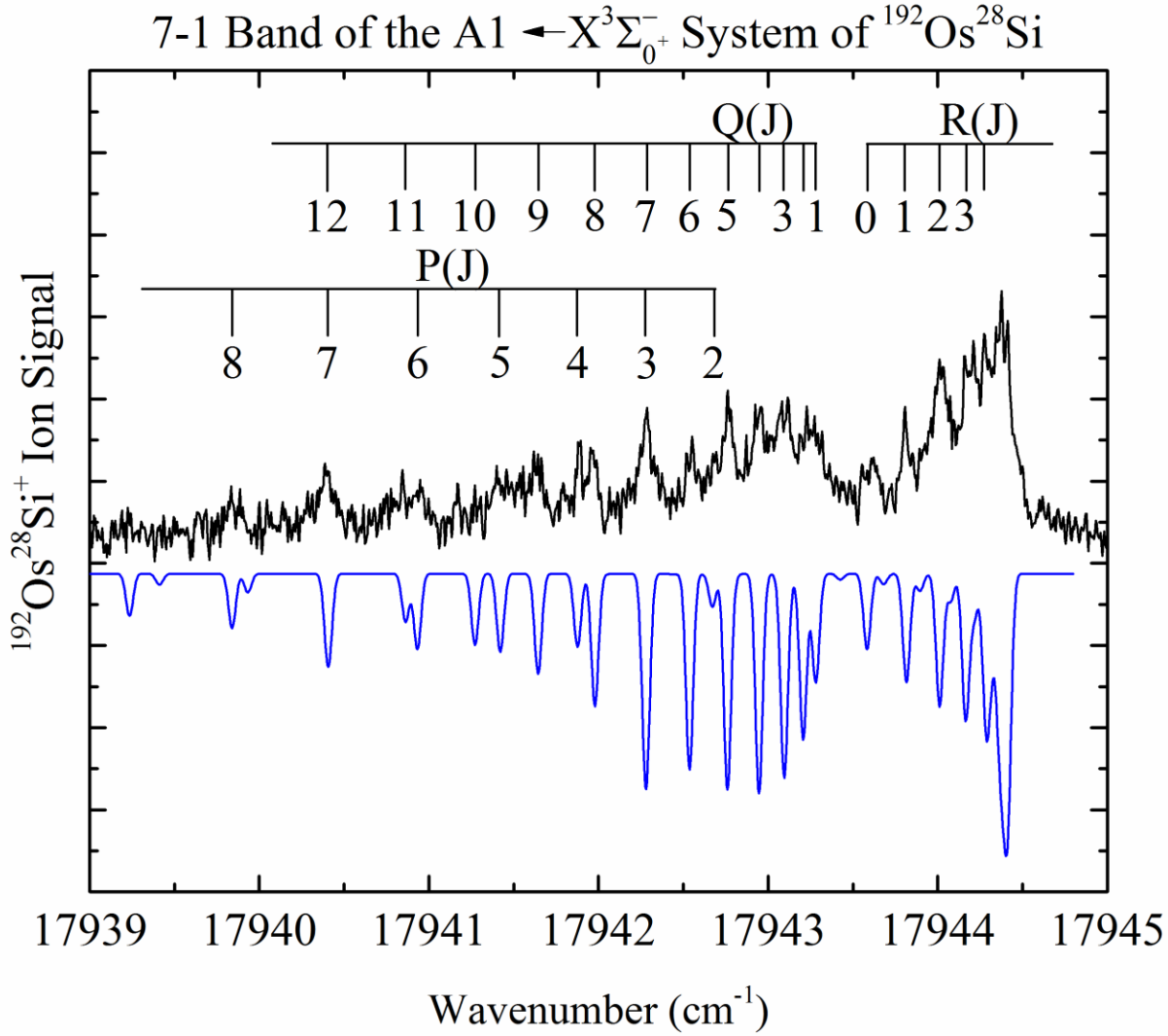

Figure B.11 Rotationally resolved spectrum of the 7-1 band of the A1 ← X $^3\Sigma^-_{0^+}$ band system of ^{192}Os^{28}Si. The simulated spectrum is provided in blue.

Table B.9 Rotational Lines of the 7-1 band of the A1 – X $^3\Sigma^-$ (0^+) system of OsSi.

Rotational Line	$^{192}Os^{28}Si$	$^{190}Os^{28}Si$	$^{189}Os^{28}Si$
P(2)	17942.685(-14)		17944.818(-7)
P(3)	17942.285(7)	17943.719(9)	17944.413(19)
P(4)	17941.889(-13)	17943.301(8)	17944.010(6)
P(5)	17941.400(21)	17942.859(-7)	
P(6)		17942.350(8)	17943.067(6)
P(7)	17940.399(3)	17941.815(12)	17942.560(-14)
P(8)	17939.835(3)	17941.270(-12)	17941.967(14)
P(9)			17941.393(-13)
P(10)		17940.007(-1)	17940.756(-14)
P(11)		17939.316(8)	
Q(1)	17943.264(17)	17944.711(10)	
Q(2)		17944.648(-2)	
Q(3)	17943.096(-1)	17944.526(7)	17945.241(-4)
Q(4)	17942.951(-5)	17944.368(14)	17945.076(12)
Q(5)	17942.766(-6)	17944.211(-17)	17944.919(-16)
Q(6)	17942.554(-18)	17943.984(-16)	17944.676(5)
Q(7)	17942.285(-9)	17943.719(-14)	17944.413(7)
Q(8)	17941.976(3)	17943.410(-6)	17944.128(-4)
Q(9)	17941.639(5)	17943.062(4)	17943.794(-3)
Q(10)		17942.674(15)	17943.433(-13)
Q(11)	17940.844(18)	17942.274(1)	
Q(12)		17941.829(-5)	17942.560(8)
Q(13)			17942.105(-19)
R(0)		17945.036(-9)	
R(1)	17943.808(7)	17945.240(17)	17945.977(-19)
R(2)	17944.010(-1)	17945.458(-8)	
R(3)	17944.161(4)	17945.604(2)	17946.312(-4)
R(4)	17944.275(9)	17945.726(-2)	17946.422(6)
R(5)	17944.376(-11)	17945.817(-13)	17946.521(-11)
R(6)	17944.411(-1)	17945.850(-3)	17946.550(5)
R(7)		17945.850(2)	17946.550(14)
R(8)		17945.836(-17)	17946.521(14)
R(9)	17944.344(-24)	17945.737(12)	17946.469(1)
R(10)	17944.211(4)		17946.367(0)
R(11)		17945.492(3)	17946.206(21)
Spectroscopic Constants (cm^{-1})			
ν_0	17943.3179(37)	17944.7581(29)	17945.4588(38)
B_7'(A1)	0.13382(20)	0.13416(13)	0.13394(18)
B_1''(X)	0.15242(21)	0.15297(14)	0.15248(17)
χ^2	1.38E-04	1.00E-04	1.62E-04

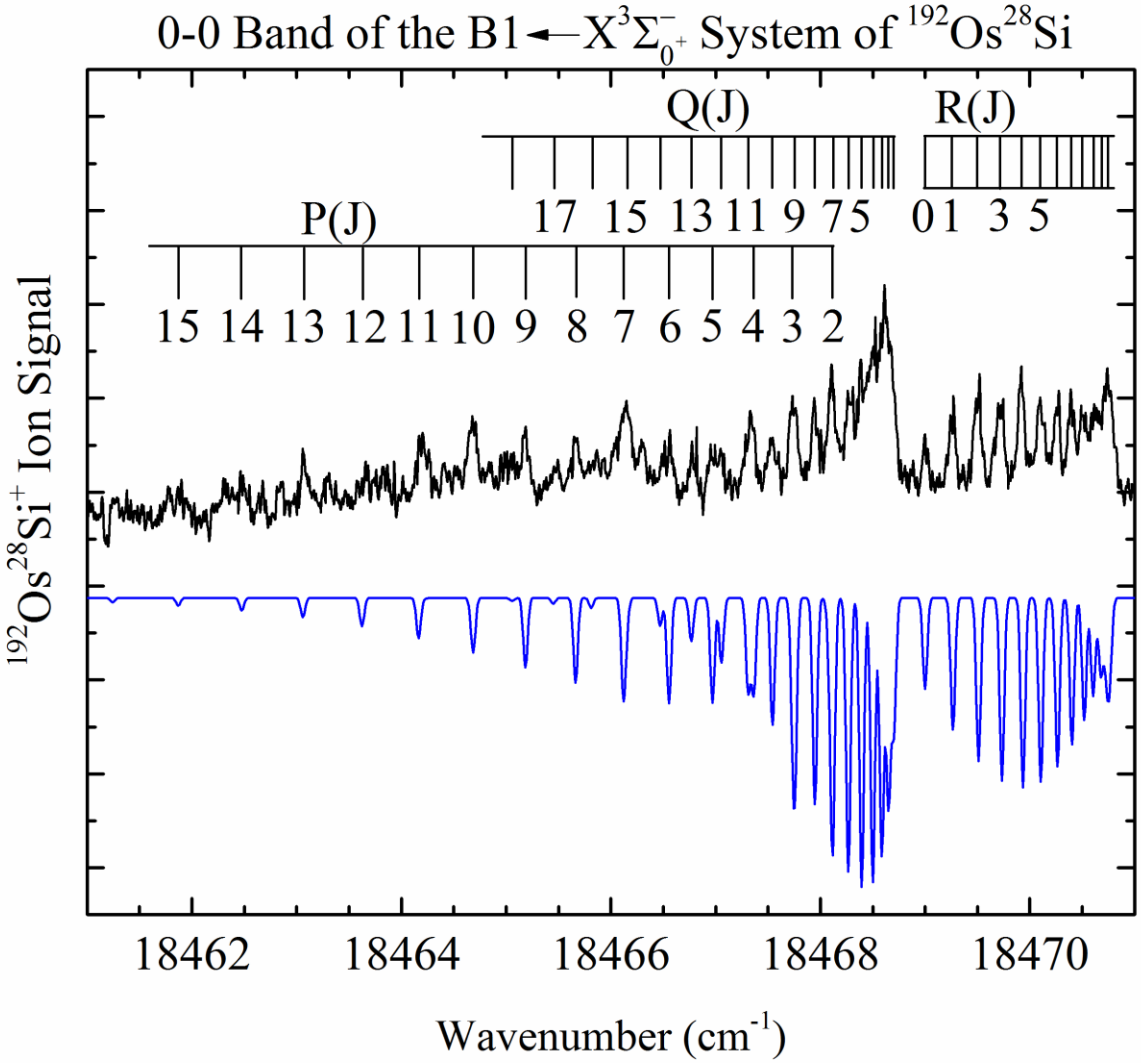

Figure B.12 Rotationally resolved spectrum of the 0-0 band of the B1 ← X $^3\Sigma^-_{0^+}$ band system of $^{192}Os^{28}Si$. The simulated spectrum is provided in blue.

Table B.10 Rotational Lines of the 0-0 band of the B1 – X $^3\Sigma^-$ (0^+) system of OsSi.

Rotational Line	$^{192}Os^{28}Si$	$^{190}Os^{28}Si$	$^{189}Os^{28}Si$
P(2)			18468.115(14)
P(3)		18467.769(-8)	18467.782(-3)
P(4)	18467.346(14)	18467.382(9)	18467.407(-1)
P(5)	18467.007(-39)	18467.030(-33)	18467.024(-11)
P(6)	18466.561(-7)	18466.577(7)	18466.592(6)
P(7)	18466.149(-29)	18466.156(-9)	18466.170(-8)
P(8)	18465.666(-3)	18465.691(-1)	18465.704(-1)
P(9)	18465.176(10)	18465.206(4)	18465.215(8)
P(10)	18464.708(-21)	18464.696(14)	18464.715(7)
P(11)			18464.216(-18)
P(12)		18463.645(-1)	18463.651(3)
P(13)	18463.067(-6)	18463.072(6)	
Q(1)	18468.670(23)	18468.719(4)	
Q(2)		18468.680(0)	
Q(3)		18468.614(2)	
Q(4)		18468.523(7)	18468.567(-19)
Q(5)	18468.384(10)	18468.432(-10)	18468.448(-8)
Q(6)	18468.281(-15)	18468.296(-4)	18468.323(-12)
Q(7)	18468.109(7)	18468.133(8)	18468.168(-9)
Q(8)	18467.943(2)	18467.973(-5)	18467.985(1)
Q(9)	18467.743(10)	18467.769(4)	18467.782(10)
Q(10)	18467.535(4)		18467.563(13)
Q(11)		18467.335(-15)	
Q(12)	18467.050(-3)		
Q(13)	18466.775(-6)	18466.778(3)	18466.806(-9)
Q(14)			18466.491(3)
Q(15)	18466.143(6)		18466.170(1)
Q(17)			18465.455(2)
Q(19)	18464.656(-3)		
Q(22)	18463.301(5)		
R(0)	18469.001(-1)	18469.023(7)	18469.045(5)
R(1)	18469.261(3)	18469.288(5)	18469.309(4)
R(2)	18469.500(7)	18469.534(1)	18469.551(4)
R(3)	18469.718(9)	18469.755(0)	18469.773(3)
R(4)	18469.920(7)	18469.948(5)	18469.960(15)
R(5)	18470.098(7)	18470.130(0)	18470.154(-2)
R(6)	18470.264(-1)	18470.279(6)	18470.296(13)
R(7)	18470.393(6)	18470.419(0)	18470.453(-11)
R(8)	18470.504(8)	18470.523(8)	
R(9)		18470.635(-14)	
Spectroscopic Constants (cm^{-1})			
ν_0	18468.7147(32)	18468.7452(26)	18468.7644(24)
B_0'(B1)	0.14263(7)	0.14238(10)	0.14269(7)
B_0''(X)	0.15332(8)	0.15317(6)	0.15350(8)
χ^2	9.92E-05	7.37E-05	5.97E-05

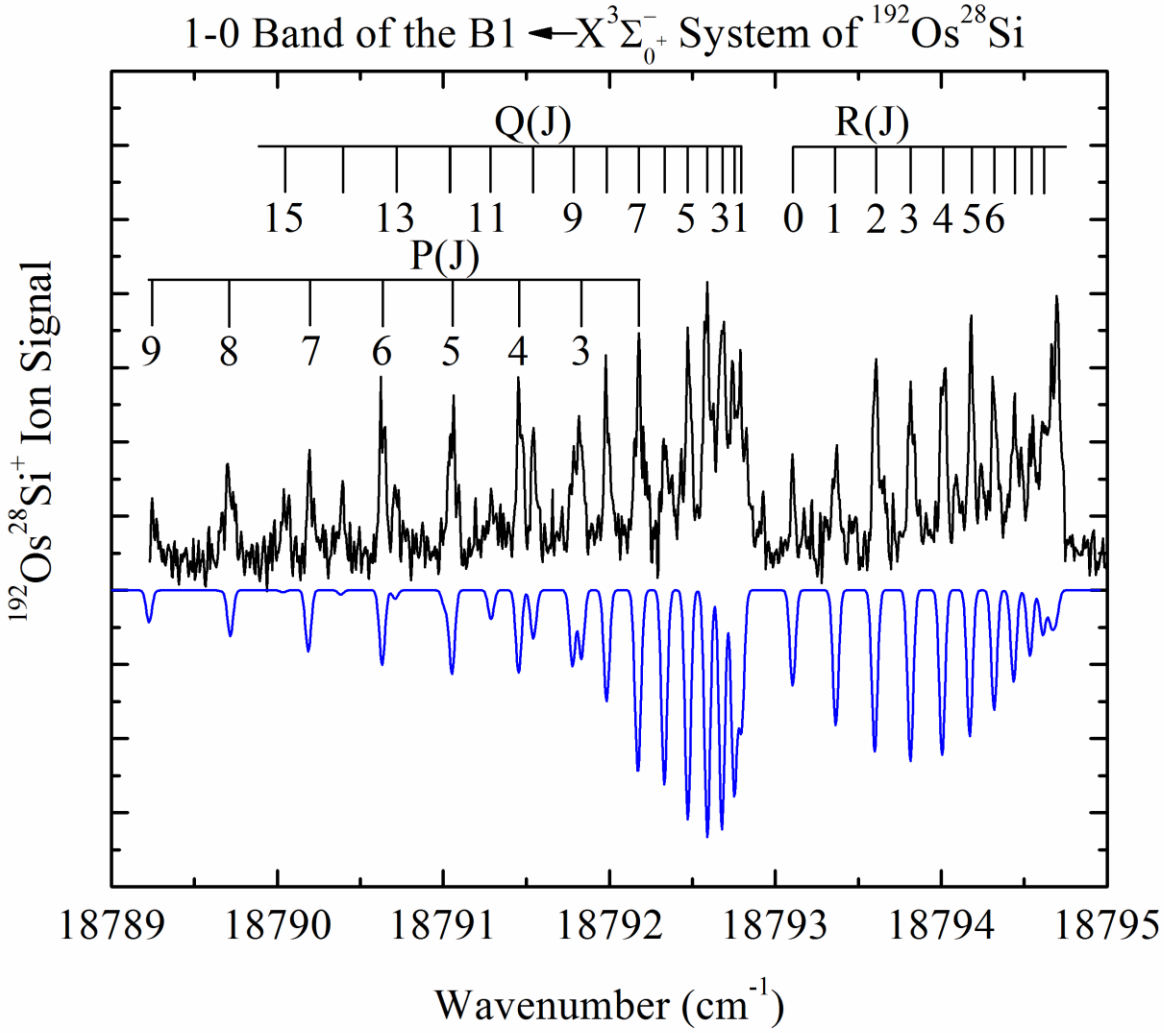

Figure B.13 Rotationally resolved spectrum of the 1-0 band of the B1 ← X $^3\Sigma^-_{0^+}$ band system of $^{192}Os^{28}Si$. The simulated spectrum is provided in blue.

Table B.11 Rotational Lines of the 1-0 band of the B1 – X $^3\Sigma^-$ (0^+) system of OsSi.

Rotational Line	$^{192}Os^{28}Si$	$^{190}Os^{28}Si$	$^{189}Os^{28}Si$
P(2)	18792.178(7)	18792.362(-3)	18792.443(11)
P(3)	18791.819(12)	18791.996(10)	18792.095(6)
P(4)	18791.465(-10)	18791.635(-5)	18791.716(8)
P(5)	18791.052(4)	18791.235(-3)	18791.319(6)
P(6)	18790.634(0)	18790.813(-2)	18790.905(-3)
P(7)	18790.193(-5)	18790.359(7)	18790.451(4)
P(8)	18789.700(20)	18789.884(14)	18789.980(7)
P(9)	18789.247(-20)	18789.411(-4)	18789.494(1)
Q(1)	18792.790(8)	18792.962(10)	18793.065(3)
Q(2)	18792.742(10)	18792.925(0)	18793.036(-14)
Q(3)	18792.679(3)	18792.850(6)	18792.968(-16)
Q(4)	18792.585(5)	18792.765(-1)	18792.855(5)
Q(5)	18792.474(0)	18792.647(1)	18792.743(1)
Q(6)	18792.340(-5)	18792.505(5)	18792.603(2)
Q(7)	18792.178(-5)	18792.362(-13)	18792.443(-1)
Q(8)	18791.979(9)	18792.164(0)	
Q(9)	18791.787(-8)	18791.947(9)	
Q(10)	18791.543(4)	18791.717(9)	18791.813(4)
Q(11)	18791.290(2)	18791.479(-6)	
Q(13)	18790.713(1)		18790.985(-1)
Q(14)	18790.392(-2)		
Q(15)	18790.049(-7)		
R(0)	18793.105(0)	18793.272(6)	18793.380(-5)
R(1)	18793.370(-5)	18793.547(-9)	18793.643(-7)
R(2)	18793.604(-2)	18793.782(-7)	18793.871(2)
R(3)	18793.816(0)	18793.994(-5)	18794.091(-3)
R(4)	18794.012(-5)	18794.190(-10)	18794.282(-3)
R(5)	18794.180(-5)	18794.352(-3)	18794.446(0)
R(6)	18794.317(2)	18794.491(3)	18794.587(4)
R(7)	18794.442(-1)	18794.616(-1)	18794.713(1)
R(8)	18794.553(-14)	18794.721(-7)	18794.827(-15)
R(9)	18794.618(-4)	18794.784(5)	18794.876(11)
R(10)	18794.666(0)	18794.846(-4)	18794.948(-8)
R(11)	18794.697(-3)		
R(16)	18794.483(8)		
R(18)	18794.241(6)		
R(19)	18794.091(0)		
Spectroscopic Constants (cm^{-1})			
ν_0	18792.8211(16)	18792.9945(20)	18793.0912(20)
B_1'(B1)	0.14174(8)	0.14164(8)	0.14192(8)
B_0''(X)	0.15332(8)	0.15317(6)	0.15350(8)
χ^2	9.92E-05	7.37E-05	5.97E-05